TECHNISCHE UNIVERSITÄT MÜNCHEN
Fakultät für Chemie
Lehrstuhl I für Technische Chemie

# Investigation of sulfur poisoning of Ni-Al catalysts for the methanation of carbon dioxide

Moritz René Philipp Wolf

Vollständiger Abdruck der von der Fakultät für Chemie der Technischen Universität München zur Erlangung des akademischen Grades eines

Doktor-Ingenieurs (Dr.-Ing.)

genehmigten Dissertation.

Vorsitzender: Prof. Dr. Sebastian Günther

Prüfer der Dissertation: 1. Prof. Dr.-Ing. Kai-Olaf Hinrichsen
2. Prof. Dr.-Ing. Hartmut Spliethoff

Die Dissertation wurde am 25.09.2019 bei der Technischen Universität München eingereicht und durch die Fakultät für Chemie am 22.01.2020 angenommen.

# Acknowledgements

First and foremost I would like to thank Prof. Dr.-Ing. Kai-Olaf Hinrichsen for having me in his group and giving me the opportunity to work on a very interesting and challenging topic. I appreciate his trust in me, the provided freedom to follow my own research ideas, his scientific supervision and the steady support during my thesis and beyond.

Also, I would like to express my gratitude to Prof. Dr.-Ing. Hartmut Spliethoff for joining the examination board as a secondary examiner.

Furthermore, I would like to thank Prof. Dr. Sebastian Günther for his scientific and technical expertise in X-ray photoelectron spectroscopy, for granting me access to his XPS instrument and for a long-lasting and fruitful scientific cooperation. Thanks also to Prof. Dr. Techn. Jens Rostrup-Nielsen for sharing his knowledge on sulfur poisoning during my short but very valuable stay in Stockholm.

My time at the university would not have been the same without the strong company and great working atmosphere. Hence, I would like to thank all of my colleagues at the Hinrichsen and Günther group for an extremely enjoyable time, especially during coffee and lunch breaks, barbecues and after-work beer or pizza. Thanks to Conny, Daniel, David, Flo, Franz K., Heidi, Jennie, Johanna, Julia, Jürgen, Matthias, My, Patrick, Paul, Thomas B., Thomas M. and Yefei. Special thanks to Chris and Tim for outstanding teamwork, literally 24/7, Stefan and Thomas B. for fruitful discussions and technical expertise, Sebastian and Tassilo for a never-ending coffee supply, Philipp for LaTeX and MATLAB support and Franz H. for lending me 10 € at the precise moment.

Next to my direct colleagues, I would also like to express my gratitude to some employees of the central department. Thanks to Ulrike Ammari, Bircan Dilki and Petra Ankenbauer for countless of elemental analysis and trusting me with the ultra micro balance. Thanks to Marc and his team for manufacturing several mechanical work pieces. Thanks to Daniel and his colleagues for the constant supply with good mood, gases and consumables.

I am also very grateful that a range of students have decided to work with me in the context of their Term Paper, Bachelor's Thesis or Master's Thesis. Thanks to Agnes, Brian, Carmen, Christian, Daniel, Elena, Eva, Filipp, Ladislaus, Ling, Lion, Martina, Patrick, Rosmalinda, Terence, Teresa, Tobias and Yang. I would like to emphasize Tabea in particular for her outstanding contribution.

Last but not least, I would like to thank my family and Johanna for their everlasting support and confidence.

# Abstract

The $CO_2$ methanation has gained renewed interest over the last years because it might become a crucial building block in the energy transition towards an energy supply which relies 100 % on renewable energy sources. As the key step in the Power-to-Gas concept, the $CO_2$ methanation reaction converts 'green hydrogen', which is produced from renewable energy via water electrolysis, into methane, which can be stored (and transported) more easily and in larger quantities within the existing natural gas infrastructure. Prior to the $CO_2$ methanation reaction, the second reactant, which is $CO_2$, needs to be separated from industrial $CO_2$ point sources. As industrial grade $CO_2$ is commonly derived from biogenic or fossil feedstocks, it is primarily contaminated with $H_2S$ and $SO_2$, which are both known to act as severe catalyst poisons in methanation reactions. Despite this obvious challenge for an industrial $CO_2$ methanation process, there is still a lack of systematic poisoning studies conducted with relevant catalysts under relevant operation conditions. This thesis aims to close this gap of knowledge and provides a deep understanding of the prevailing mechanism and kinetics on the macroscopic scale of a fixed-bed microreactor but also on the atomic scale of the catalyst surface.

In the first contribution, a new methodology for studying *in situ* poisoning reactions in a fixed-bed microreactor is presented. Near infrared thermography is applied to spatially resolve the temperature profile along the reactor axis of a fixed-bed microreactor. Upon switching from cold-flow to reactants, a hot spot, caused by the exothermal character of the $CO_2$ methanation reaction, evolves at the reactor entrance. Upon introducing 5 ppm $H_2S$ to the feed, the hot spot migrates through the fixed-bed and dies out at the reactor outlet. As the reaction is run in thermodynamic equilibrium (400 °C, 1 bar, $H_2/CO_2/Ar$ = 4/1/5), the product gas composition is not affected by the poisoning reaction until the hot spot has reached the reactor outlet. Afterwards, however, a rapid and complete loss of the catalyst's ability to form the desired product ($CH_4$) is observed. The results indicate that $H_2S$ is gradually and quantitatively adsorbed by the employed Ni-Al catalyst until the fixed-bed is completely saturated. A basic theoretical model is derived to correlate the lifetime of the catalyst and the active metal surface area of the fresh catalyst.

In the second contribution, the results from the first contribution are validated for a broad range of co-precipitated Ni-Al catalysts with different Ni loadings. Hereby, not only $H_2S$

but also $SO_2$ poisoning is considered, as both sulfur components are major contaminants in biogenic and fossil $CO_2$ sources. Activated, aged and poisoned catalysts are characterized thoroughly by means of X-ray diffraction (XRD), temperature programmed reduction (TPR), $N_2$ physisorption, $H_2$ and $CO_2$ chemisorption and CHNS analysis. The obtained results suggest the blockage of Ni surface atoms by S atoms as the reason for poisoning. The adsorption stoichiometry upon saturation was found to be $0.73 \pm 0.02$ S atoms per surface Ni atom. Under the applied conditions, $H_2S$ and $SO_2$ poisoning proceed via the same mechanism. Based on these data, a model for predicting catalyst lifetimes of Ni-Al catalysts was developed and extrapolated to lower $H_2S$ partial pressures. It was found, that homogeneous sulfur poisoning of catalytic fixed-beds, which is essential for kinetic experiments, is excessively time consuming when carried out via *in situ* poisoning. In addition, sulfur coverages below $\theta_S = 0.5$ cannot be adjusted at $CO_2$ methanation conditions, as $H_2S$ partial pressures below the detection limit of even sophisticated sulfur analyzers (0.1 ppb) are required. Hence, an *ex situ* poisoning approach, i.e. impregnation with $(NH_4)_2S$, was applied to adjust sulfur coverages between $0 < \theta_S < 0.73$. Activity measurements of these samples under differential conditions reveal a strong non-linear dependency between activity and sulfur coverage, suggesting structure-sensitive poisoning. The activity versus $\theta_S$ plot could be fitted to a Maxted-type correlation of the following kind: $a_{rel} = a^0_{rel} \cdot (1-\theta)^{10 \pm 0.57}$. The surprisingly strong dependence of activity on sulfur coverage, as indicated by the comparably high exponent, can be explained by a similarly strong decrease of $CO_2$ adsorption on $Ni^0$. Activation energies of poisoned and non-poisoned catalysts are similar and in the range of 80 to 87 kJ/mol. Sulfur poisoning is therefore ascribed to physical blockage of active sites instead of electronic effects.

In the third contribution, the sulfur resistance of transition metal promoters is evaluated. Therefore, a co-precipitated benchmark catalyst, comprising a Ni/Al molar ratio of 1/1, is doped with up to 5 wt% of Fe, Mn, Co, Cu and Zn. Catalysts are subsequently poisoned *in situ* by $H_2S$ and *ex situ* by $(NH_4)_2S$ and thoroughly characterized. The obtained results suggest an increase in sulfur resistance independent of the promoter material. This effect is traced back to the adsorption of $H_2S$ on promoter phases, causing the protection of active Ni sites. Based on the adsorption properties of spent *in situ* poisoned samples, different $CO_2$ adsorption sites were distinguished, i.e. $CO_2$ adsorbed on $Ni^0$, on the Al-rich mixed-oxide and on the promoter phase. Thus, a correlation between $CO_2$ adsorbed on $Ni^0$ and the promoter phase and the $CO_2$ methanation activity of *ex situ* poisoned catalysts was revealed. Activity enhancement of Mn- and Fe-doped samples was thus ascribed to $CO_2$ adsorption on promoter phases and subsequent conversion to $CH_4$. In contrast, the Cu-doped catalyst suffered from severe deactivation, since $CO_2$ adsorbed on Cu was converted to CO instead of $CH_4$. With regards to activity, Co and Zn were observed to have negligible impact.

The forth contribution is dedicated to the development of a novel method for quantitative analysis of technical catalysts by X-ray photoelectron spectroscopy (XPS). As XPS is a very powerful

technique to probe the outermost layers of surfaces, it is of certain benefit for the investigation of surface phenomena such as sulfur poisoning. Conclusive quantification of technical samples is however often impeded due to an unknown surface geometry. An internal standard would make up for this shortcoming. It is shown, that common catalyst supports such as $Al_2O_3$ and $TiO_2$ are mixed with an internal standard with sufficient accuracy, if both powders show a maximum particle size of 10 µm and are mixed either by grinding or dispersing the powders in ethanol. It is further shown, that internal standards of identical particle size distributions as the catalyst are obtained by coating the catalyst's support material with $MoO_3$ or $Cr_2O_3$. These tailor-made standards are introduced with sufficient precision to the corresponding analyte independent of the particle size and the applied mixing technique. Thus, the introduction of the standard material by mere shaking becomes possible. However, it was observed that mixing the coated standards may cause a systematic quantification error. The origin of this bias could not be entirely resolved. It is however suggested, that grinding and dispersing powders in ethanol trigger the re-dispersion of $MoO_3$ and $Cr_2O_3$.

# Contents

# List of Figures

# List of Tables

# Nomenclature

## Latin Symbols

| | | |
|---|---|---|
| $A$ | (surface) area | $m^2$ |
| $B$ | spectral radiance | $W/(m^2\,\mu m)$ |
| $C$ | BET constant | - |
| $D$ | dispersion | % |
| $D$ | detector efficiency | - |
| $E_A$ | activation energy | kJ/mol |
| $E_{bind}$ | binding energy | eV |
| $E_{kin}$ | kinetic energy | eV |
| $G$ | Gibbs free energy | J/mol |
| $H$ | enthalpy | J/mol |
| $I$ | intensity | arbitrary units |
| $J$ | photon flux | $1/(m^2\,s)$ |
| $K$ | shape factor (Scherrer) | - |
| $L$ | angular asymmetry | - |
| $M$ | molar mass | kg/mol |
| $N$ | number | - |
| $N_A$ | Avogadro's constant | 1/mol |
| $P$ | total energy of thermal radiation | $W/m^2$ |
| $P$ | fraction | - |
| $R$ | universal gas constant | J/(mol K) |
| $S$ | entropy | J/(mol K) |
| $S$ | sensitivity factor (Wagner) | Mb |
| $S_{BET}$ | BET surface area | $m^2/g_{cat}$ |
| $T$ | temperature | °C |
| $T$ | transfer function of the electron analyzer | - |
| $U$ | adsorption capacity | $\mu mol/g_{cat}$ |
| $V$ | volume | $m^3$ |
| $\dot{V}_{feed}$ | feed gas volume stream | $cm^3/min$ |
| $W$ | work function | eV |
| $WTY$ | weight time yield | mol/(kg h) |

| | | |
|---|---|---|
| $X$ | conversion | % |
| $Y$ | yield | % |
| $a$ | activity | mol/(kg h) |
| $c$ | speed of light | m/s |
| $c$ | concentration | μmol/cm$^3$ |
| $d$ | interplanar distance | Å |
| $d$ | mean crystallite size | nm |
| $d$ | film thickness | μm |
| $h$ | Planck constant | J s |
| $m$ | mass | kg |
| $n$ | number | - |
| $n$ | molar amount | mol |
| $p$ | (partial) pressure | bar |
| $s$ | standard deviation | depends |
| $t$ | time | min |
| $u$ | uncertainty | depends |
| $w$ | mass fraction | wt% |
| $y$ | volume fraction | - |
| $z$ | sample depth | m |

## Greek Symbols

| | | |
|---|---|---|
| $\Sigma$ | sum | depends |
| $\Delta$ | difference | depends |
| $\beta$ | line broadening | - |
| $\beta$ | heating rate | K/s |
| $\gamma$ | angle between incident and ejected and detected photoelectrons | ° |
| $\varepsilon$ | emissivity | - |
| $\theta$ | grazing angle | ° |
| $\theta$ | coverage | - |
| $\lambda$ | wavelength | nm |
| $\lambda$ | inelastic mean free path | m |
| $\nu$ | frequency | 1/s |
| $\bar{\nu}$ | arithmetic mean | depends |
| $\xi$ | mass ratio of analyte to internal standard | - |
| $\rho$ | density | kg/m$^3$ |
| $\sigma$ | Stefan-Boltzmann constant | J/(m$^2$ s K$^4$) |
| $\sigma$ | photoionization cross section | Mb |
| $\sigma$ | true standard deviation | depends |

| | | |
|---|---|---|
| $\tau$ | mean crystallite size | nm |

### Superscript

| | |
|---|---|
| 0 | standard or initial state |
| $\infty$ | final state |
| i | species i |

### Subscript

| | |
|---|---|
| 0 | standard or initial state |
| 2D | per area |
| 3D | per volume |
| A | analyte compound |
| M | molar |
| M | matrix |
| P | pore |
| R | reaction |
| S | internal standard compound |
| bt | breakthrough |
| deac | deactivation |
| cat | catalyst |
| i | species i |
| m | monolayer |
| max | maximum |
| rel | relative |

### Abbreviations

| | |
|---|---|
| AHM | ammonium heptamolybdate |
| BET | Brunauer, Emmett and Teller |
| CAS | compressed air storage |
| CHNS | carbon, hydrogen, nitrogen and sulfur |
| DFT | density functional theory |
| EA | elemental analysis |
| ELS | elastic light scattering |
| IEA | International Energy Agency |
| FWHM | full width at half-maximum |

| | |
|---|---|
| GC | gas chromatography |
| ICDD | International Centre for Diffraction Data |
| ICP | inductively coupled plasma |
| IMFP | inelastic mean free path |
| IR | infrared |
| IUPAC | International Union of Pure and Applied Chemistry |
| JCPDS | Joint Committee on Powder Diffraction Standards |
| LEED | low-energy electron diffraction |
| MOF | metal organic framework |
| NIR | near infrared |
| NIST | National Institute of Standards and Technology |
| NPS | New Policies Scenario |
| OES | optical emission spectroscopy |
| PHS | pumped hydroelectric storage |
| PIDS | polarization intensity differential scanning |
| PTFE | Polytetrafluoroethylene |
| PtG | Power-to-Gas |
| SNG | synthetic natural gas |
| TCD | thermal conductivity detector |
| TGA | thermogravimetric analysis |
| TOS | time on stream |
| TPD | temperature programmed desorption |
| TPP | Tanuma, Powell and Penn |
| TPR | temperature programmed reduction |
| UHV | ultra high vacuum |
| WTY | weight time yield |
| XPS | X-ray photoelectron spectroscopy |
| XRD | X-ray diffraction |

# 1 Introduction

## 1.1 Motivation

Today, energy systems worldwide are facing radical changes. The human made climate change has induced concerted actions of a majority of countries around the world to cut the extensive usage of conventional energy carriers such as coal, oil and gas and change to more environmentally friendly and sustainable technologies, i.e. solar and wind power. Next to the complexity associated with individual interests of policymakers worldwide, one of the key challenges of the evolving energy transition is to ensure a continuous growth of renewable energy generation, which not only makes up for the decline in conventional generation but also keeps pace with the ever-growing demand for energy.

Historical and predictive data from the international energy agency (IEA) [1], which are visualized in figure 1.1, suggest that we are currently entering a new era. After most industrialized countries signed the Kyoto Protocol in 1997 [2] (entered into force in 2005) and paved the way to legally binding reductions in greenhouse gas emissions, the share of wind and solar in the energy mix began to increase from below 1 % prior to 2005 to 4.5 % in 2015 on a global scale. Although today, coal is still the most abundant primary energy carrier with 40 % share, it begins to stagnate in absolute numbers, leading to a predicted decrease in share to 30 % in 2030 and 25 % in 2040. At the same time, wind and solar will continue to take over the market with 16 % share in 2030 and 22 % in 2040. As a lot of developing countries, e.g. China and India, will continue to rely primarily on coal to cover their increasing energy demand, the turnaround from conventional to renewables is already more pronounced in industrialized parts of the world, as for example the European Union, which can be regarded as a pioneer in implementing legal frameworks for reaching the Kyoto goals. In the European Union, the share of coal as the former bestseller with 40 % market share in 1990 has already decreased to 25 % in 2015. Simultaneously, wind and solar power, which have not played a role before the year 2000, have already increased to 13 % share in 2015. These trends will continue in the next decades, leading to a predicted decrease of coal energy to 8 % in 2030 and 4 % in 2040. Simultaneously, wind and solar power will increase to 24 % in 2025 and will then have the largest share in primary energy consumption of all energy carriers, followed by gas and nuclear with around

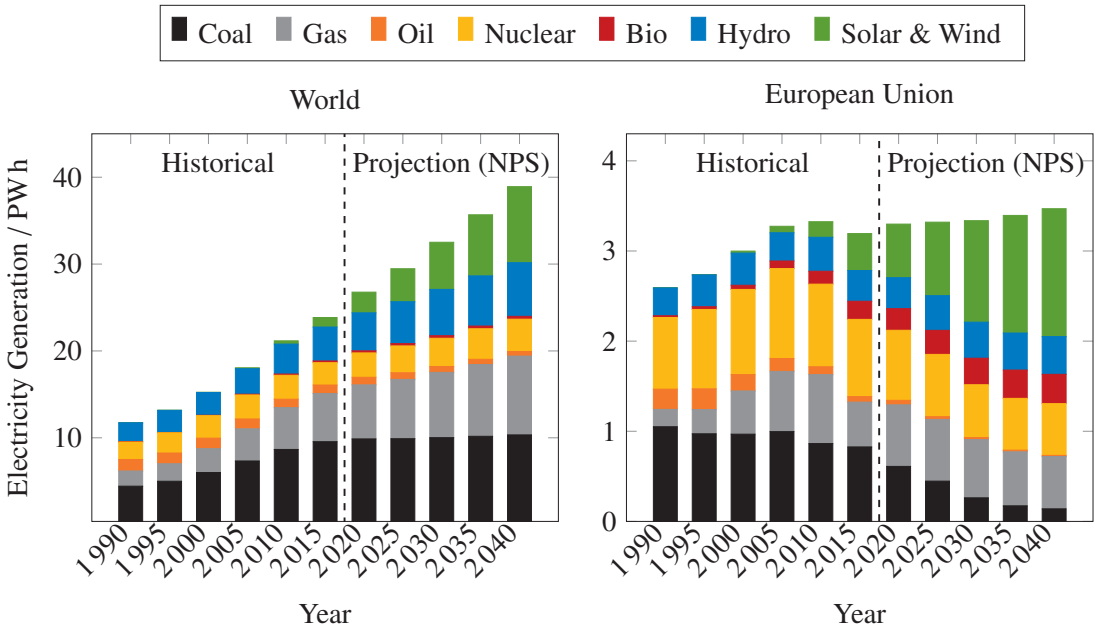


**Figure 1.1:** Historical and projected energy generation of the world and the European Union broken down to the type of energy source. Historical data are based on the World Energy Outlook 2017 [1]. Projected data are based on the New Policies Scenario (NPS) [1].

20 %. In 2040, wind and solar are predicted to have over 40 % market share as compared to only 16 % for gas and nuclear. In summary, the discussed trends show, that energy generation in the European Union, and more slowly worldwide, faces a radical change from fossil-based towards renewable power generation.

One great challenge involved with the increasing share of renewable energy in electricity generation is the steady and stable operation of national electric grids. Hereby, a sensitive balance between supply and demand of electrical energy has to be maintained at each day- and nighttime. Current balancing tools primarily comprise electrical measures for short-term fluctuations and supply-side management (i.e. ramping up and down suppliers) for long-term fluctuations. In a renewable based energy system, however, the complexity of balancing strongly increases, as the output of wind and solar power depends on weather conditions, the time of the day and the time of the year. Hence, fluctuations occur on different time scales, become more severe and are harder to predict. Under these conditions, more sophisticated balancing tools, such demand-side management (i.e. ramping up and down consumers), and additional capacities for energy storage are needed. Today, demand-side management is solely used in exceptional situations, as it primarily comprises large scale consumers. In the future, so-called smart grids shall be established, where an increasing amount of small- and medium-sized consumers, such as industrial and household devices or electrical vehicles contribute to grid management. In selected regions, this concept has already been tested successfully, e.g. on the German island Pellworm [3]. It is assumed that nationwide smart grids may tolerate high shares of renewable energy generation without the need of additional energy storage. In Germany, for example, two modeling studies agree that between 40 and 80 %, solely short-time storage with capacities

of several GW h is required [4, 5]. Above 80 %, however, the demand for long-term storage increases [5, 6]. Predicted capacities are 7 TW h at 85 % [5] and 26 TW h [5] or 75 TW h [6] at 100 % renewable energy generation. As Germany only makes up for about 0.25 % of worldwide energy generation, global storage demands scale accordingly.

In figure 1.2, technical relevant storage technologies are plotted as a function of storage time versus storage capacity. Nowadays, primarily pumped hydroelectric storage (PHS), with a worldwide capacity of 127 GW, is employed [7]. This is i.a. due to high cost-effectiveness, high flexibility, high storage capacities and black start capability [8]. With a large gap, compressed air storage (CAS) and sodium/sulfur batteries follow with global storage capacities of 440 and 315 MW, respectively [7]. Despite the growth potential of these techniques, the increasing demand for energy storage will hardly be covered in the long run. Hence, in future energy systems, a portfolio of electrical, mechanical, thermal and chemical storage is required [8]. A specific problem is the lack of long-term storage of large amounts of electricity, which today is only partly provided by PHS. Hence, chemical energy storage needs to be developed.

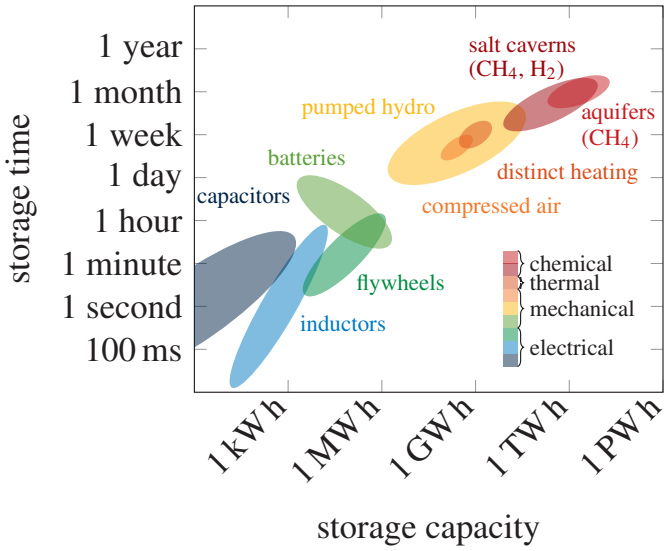


**Figure 1.2:** Comparison of technical relevant storage technologies. Adapted from [8].

Apart from time-dependent fluctuations on the supply side, the transition towards renewable energy also results in a spatial redistribution of suppliers. Hereby, the conventional mechanism of site selection, which was primarily driven by local energy needs, is continuously replaced by an accumulation of renewable power stations, specifically wind and solar, in areas of favorable climatic conditions. This results in the spatial separation of suppliers and customers and triggers the need for new transportation pathways. The necessary expansion of the electrical grid, which exhibits comparably low transportation losses, is frequently not approved of by the local population [9].

A combined solution, which covers energy storage as well as transportation needs, is the Power-to-Gas (PtG) technology. It primarily comprises the conversion of renewable energy (power) into methane (gas) and the subsequent storage and/or transportation in existing infrastructure. Hereby, excess energy, which arises for example on very windy or sunny days, is converted into synthetic natural gas (SNG) and fed to the local gas grid. In times of adverse climatic conditions, SNG is withdrawn from the gas grid and re-transformed into electricity, e.g. by combustion in gas turbines. As shown in figure 1.3, the PtG technology provides a link between

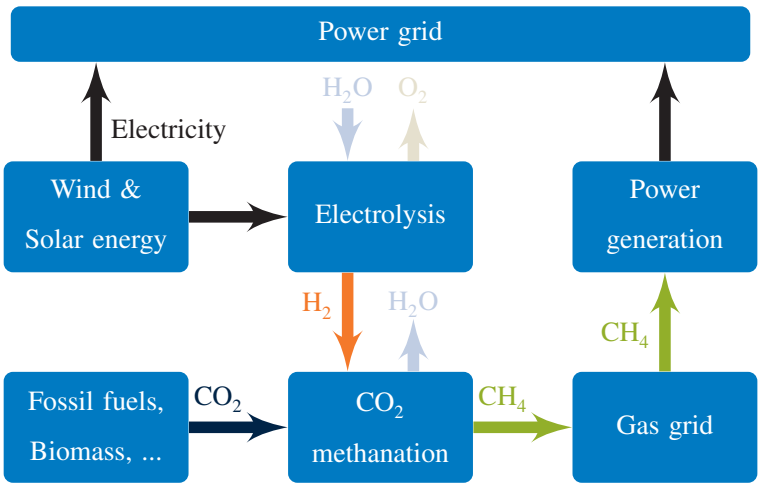


**Figure 1.3:** Implementation of the Power-to-Gas technology in the existing infrastructure. Adapted from [10].

the power grid and the gas grid via a two-step process. First, hydrogen ($H_2$) is produced by means of electrolysis, i.e. the splitting of water into the elements. Second, the resulting $H_2$ is converted with an external carbon dioxide ($CO_2$) source to methane ($CH_4$). As natural gas is composed of up to 99 % $CH_4$, the dried product of the $CO_2$ methanation reaction may be fed directly to the local gas grid. Also, it is possible to store almost indefinite amounts of $CH_4$, as the global storage capacity of natural gas is around 3600 TW h [11] and thus greatly exceeds electricity generation from wind and solar power (1530 TW h [12]). If gas storage capacities are fully exploited, the world energy demand (25 PW h [12]) could be covered exclusively by the gas grid for almost two months. Local scenarios may of course vary. In Germany, for example, a time scale of up to five months could be covered [13]. An additional benefit of the PtG concept is the transmission losses in the gas grid as compared to the electricity grid [14].

Today, several Power-to-Gas projects have been realized across Europe and the USA, mainly funded by the governments of Germany, Denmark and Switzerland [15]. The source of $CO_2$ has hereby not finally been agreed on. Hence, the following concepts can be distinguished [10]:

- Bioenergy: biogas from fermentation or biomass gasification is either fed directly to the methanation reactor or $CO_2$ is separated and subsequently converted to $CH_4$.

- Fossil fuels: $CO_2$ emissions of fossil fired power stations are used as feedstock. $CO_2$ needs to be separated after the combustion process (post-combustion), in the gasification process (pre-combustion) or in the combustion with oxygen (oxyfuel process).

- Waste management: biogas from sewage plants or landfill sites and $CO_2$ separated from $CO_2$-intensive industries are used.

- Stand alone: $CO_2$ is captured directly from the atmosphere. This concept is the most costly and unlikely to be realized on an industrial scale as long as more concentrated $CO_2$ sources are available.

The PtG technology is not commercialized yet because the ease in handling and storing methane comes with the price of a lower overall efficiency as compared to other storage technologies such as pumped hydro storage [8]. Thus, only 30–40 % of the overall required electrical energy is eventually recovered [8]. Pumped hydro on the other hand shows a power storage efficiency of up to 83 % [16]. The overall PtG efficiency is combined from several contributions. First, the electrolysis of water accounts for an efficiency of 60–80 % for the alkaline technology [17]. Second, the $CO_2$ methanation process is limited to an efficiency of 75–80 % [18]. Further withdrawals from efficiency originate from carbon dioxide separation and compression. Thus, the PtG process can only be operated economically, if there is enough potential for cheap surplus energy in the grid, which is otherwise wasted or hard to dispose of.

In summary, long-term storage of electricity by means of PtG seems to be a relevant building block of future electricity grids. At the moment, however, the PtG process cannot be operated economically since the share of renewable energy in the supply mix is still too low. Countless research projects and several pilot plants have been initiated throughout Europe to further develop the promising technology and prepare its future commercialization.

## 1.2 Objectives

This doctoral thesis is part of a series of research projects, which have been carried out at the Chair I of Technical Chemistry with a view to extend the prevailing knowledge of the $CO_2$ methanation reaction. Up to this date, aspects of reactor engineering [19–22], micro kinetic modeling [22–24], promoter metals [25–29] and hydro-thermal deactivation [30, 31] have been treated. The current thesis aims primarily at developing a deeper understanding of sulfur poisoning. This is essential for the long-term operation of catalysts under industrial conditions, as designated $CO_2$ streams contain sulfur as a main impurity [32]. The applied

methodology comprises systematic sulfur poisoning of various co-precipitated Ni-Al catalysts, thorough catalyst characterization and the derivation of structure-activity relationships.

Apart from studying sulfur poisoning, a novel analytical technique for quantitative analysis of technical catalysts by X-ray photoelectron spectroscopy was developed in close cooperation with the group of Prof. Sebastian Günther (Associate Professorship of Physical Chemistry with Focus on Catalysis).

The content is divided into the following chapters:

- **Chapter 1** gives an introduction and presents the key objectives of this work.
- **Chapter 2** introduces the theoretical background of $CO_2$ methanation and catalyst deactivation.
- **Chapter 3** introduces the experimental background of the employed analytical methods.
- **Chapter 4** contains detailed information about the preparation and characterization of Ni-Al catalysts.
- **Chapter 5** provides insights into the gradual poisoning of a fixed-bed microreactor. Thermography is identified as a powerful tool for studying *in situ* sulfur poisoning. The chapter has been published in a peer-reviewed journal under the title: *"Contactless temperature measurements under static and dynamic reaction conditions in a single-pass fixed bed reactor for $CO_2$ methanation"* [33].
- **Chapter 6** compares the poisoning behavior of Ni-Al catalysts with different Ni loadings. Fundamental conclusions about the mechanism and kinetics of sulfur poisoning are presented. The chapter has been published in a peer-reviewed journal under the title: *"Sulfur poisoning of co-precipitated Ni-Al catalysts for the methanation of $CO_2$"* [34].
- **Chapter 7** investigates the poisoning and activity behavior of Ni-Al catalysts promoted by Mn, Fe, Co, Cu and Zn. Important conclusions about catalyst activity, sulfur resistance and adsorption behavior are drawn. The chapter has been published in a peer-reviewed journal under the title: *"$CO_2$ methanation on transition-metal-promoted Ni-Al catalysts: Sulfur poisoning and the role of $CO_2$ adsorption capacity for catalyst activity*" [35].
- **Chapter 8** derives some basic principles for the introduction of internal standards to powder samples. The obtained results offer a new and promising approach for the quantitative analysis of technical catalysts by X-ray photoelectron spectroscopy. The chapter will be

submitted for publication in a peer-reviewed journal under the title: *"Novel synthesis routes towards internal intensity standards for quantitative analysis of technical catalysts by X-ray photoelectron spectroscopy"*.

- **Chapter 9** summarizes the obtained results and outlines further research impulses.

# 2 Theoretical background

## 2.1 Thermodynamic aspects

The $CO_2$ methanation reaction proceeds according to equation (2.1). It is also referred to as Sabatier reaction, named after Paul Sabatier, who discovered the reaction together with his co-worker Senderens at the beginning of the 20$^{th}$ century [36]. At standard conditions, the reaction is exothermic, exergonic and contracts in volume. Hence, according to the principle of Le Chatelier, product formation is favored at low temperatures and high pressures.

$$CO_2 + 4H_2 \rightleftharpoons CH_4 + 2H_2O \qquad \Delta H_R^0 = -165\,\frac{\text{kJ}}{\text{mol}} \qquad \Delta G_R^0 = -114\,\frac{\text{kJ}}{\text{mol}} \tag{2.1}$$

Possible side reactions are listed in equations (2.2)-(2.4), comprising the CO methanation, the reverse water-gas shift reaction and the Boudouard reaction. In experimental studies, higher hydrocarbons such as ethane and propane have been reported [23, 37]. As their concentration was however very low ($< 0.3\,\%$), they are not considered here.

$$CO + 3H_2 \rightleftharpoons CH_4 + H_2O \qquad \Delta H_R^0 = -204\,\frac{\text{kJ}}{\text{mol}} \qquad \Delta G_R^0 = -142\,\frac{\text{kJ}}{\text{mol}} \tag{2.2}$$

$$CO_2 + H_2 \rightleftharpoons CO + H_2O \qquad \Delta H_R^0 = 41\,\frac{\text{kJ}}{\text{mol}} \qquad \Delta G_R^0 = 29\,\frac{\text{kJ}}{\text{mol}} \tag{2.3}$$

$$2CO \rightleftharpoons C + CO_2 \qquad \Delta H_R^0 = -172\,\frac{\text{kJ}}{\text{mol}} \qquad \Delta G_R^0 = -120\,\frac{\text{kJ}}{\text{mol}} \tag{2.4}$$

Detailed thermodynamic data was obtained via minimization of the total Gibb's free energy [38]. Therefore, all species from equations (2.1)-(2.4) were considered and treated as ideal gases. Thermodynamic data is discussed in terms of $CO_2$ conversion, $CH_4$ and CO yield, defined according to section 6.3.2. From figure 2.1, it becomes clear, that the conversion of $CO_2$ and the yield in $CH_4$ gradually decrease with temperature up to a value of ca. 500 °C, caused by the great exothermal character of the $CO_2$ methanation reaction. For temperatures exceeding

500 °C, however, the $CO_2$ conversion increases, whereas the $CH_4$ yield further decreases. Simultaneously, the CO yield increases. This behavior reflects the consumption of $CO_2$ and formation of CO via the endothermal reverse water-gas shift reaction. At elevated pressures, $CO_2$ conversion as well as $CH_4$ yield increase at the expense of CO yield, which is due to volume contraction. From equilibrium calculations, it is also possible to estimate the carbon

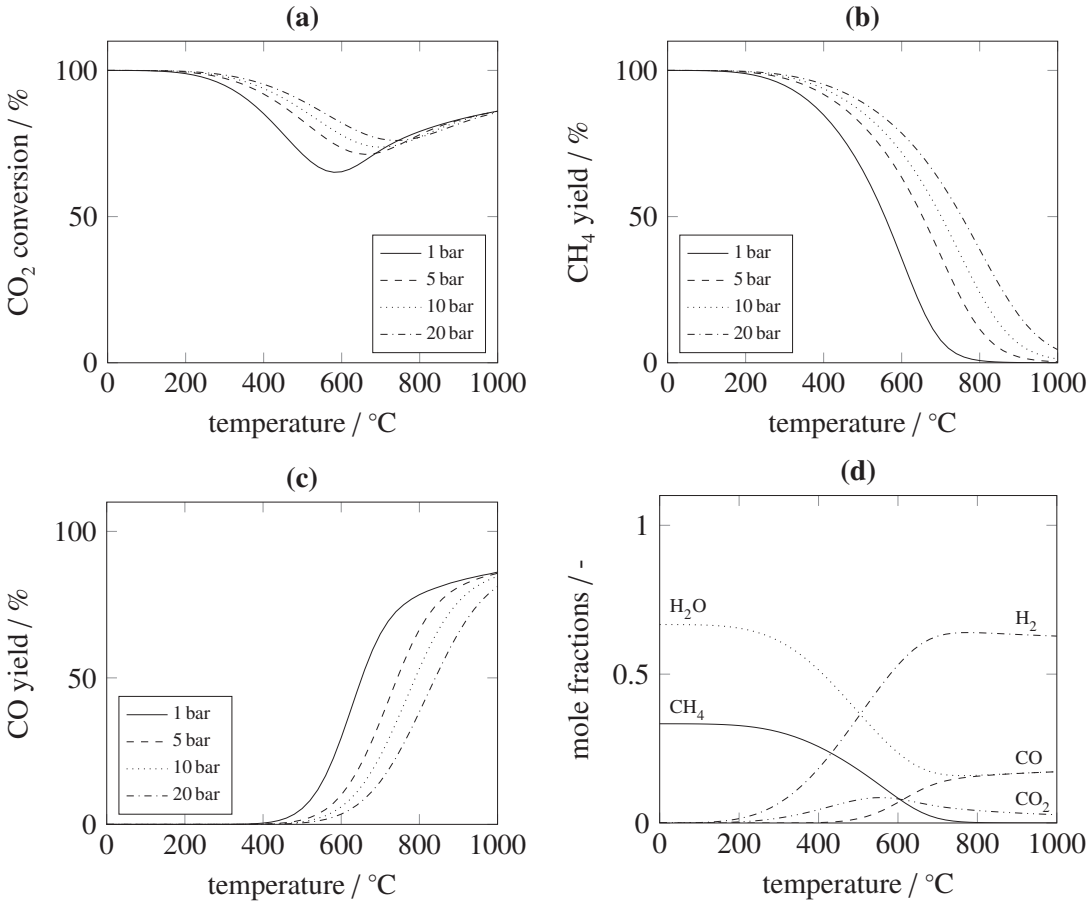


**Figure 2.1:** Thermodynamic equilibrium data for $CO_2$ conversion (a), $CH_4$ yield (b), CO yield (c) and species' mole fractions (d) for a feed gas composition of $H_2/CO_2 = 4/1$. For (d), the pressure is 1 bar.

forming potential for different feed gas compositions. This is illustrated in two ternary C-H-O diagrams in figure 2.2. The curved lines represent the boundary lines for carbon formation at different temperatures (a) or pressures (b). The black straight line indicates possible $H_2/CO_2$ feed gas ratios between pure $H_2$ and pure $CO_2$. Points A, B and C correspond to $H_2/CO_2$ ratios of 4.0, 2.0 and 1.0, respectively. At 1 bar and relevant temperatures ($\leq$ 500 °C), carbon formation greatly depends on the $H_2/CO_2$ ratio. Point A, which represents the conditions used in this thesis, is located below the boundary line, indicating carbon-free operation conditions. Conversely, Point C is located clearly above the boundary line, which indicates carbon-forming conditions. Point B is located close to the boundary line and represents the boundary $H_2/CO_2$ ratio at which carbon formation is still expected. Between points A and B, carbon formation depends on temperature. Once temperatures exceed 600 °C, carbon-free operation is achieved

at any $H_2/CO_2$ ratio. These conditions are however less relevant for the methanation of $CO_2$, as they favor the reverse water-gas shift reaction. The effect of pressure is less interesting for industrial operation but possibly relevant for material characterization. Hence, at ambient or above-ambient conditions, carbon formation is virtually not pressure dependent. Below ambient conditions, however, there exists a unique operation window, where carbon formation occurs despite using stoichiometric feed gas mixtures (point A). This operation window is located between 1 and 10 mbar. Pressures exceeding 10 mbar show similar conditions as those discussed for 1 bar and $T \leq 500\,°C$: carbon formation for points B and C, no carbon formation for point A. Pressures below 1 mbar show carbon-free operation for any $H_2/CO_2$ ratio. The transition regime between 1 and 10 mbar is particularly relevant for *in vacuo* studies of methanation catalysts under working conditions. This may for example be the case for surface sensitive techniques such as (near-ambient) X-ray photoelectron spectroscopy.

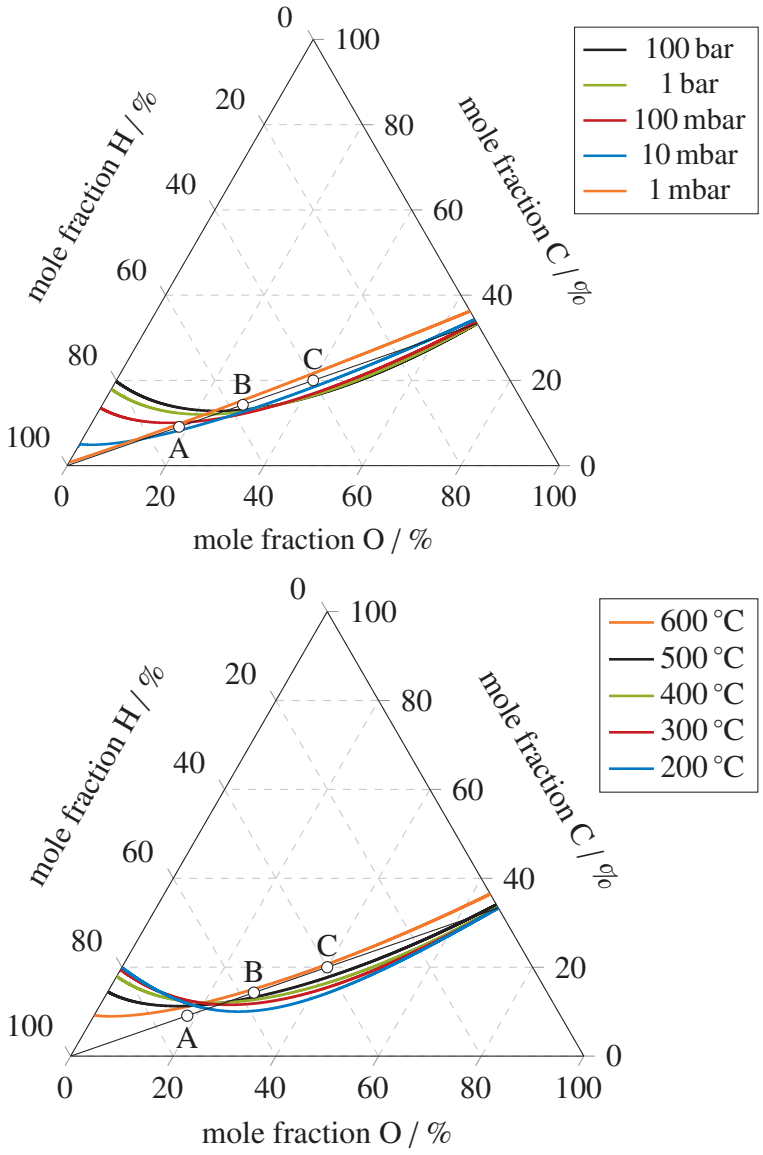


**Figure 2.2:** Ternary C-H-O diagrams for various temperatures at 1 bar (top) and various pressures at 400 °C (bottom).

Thermodynamic calculations set the framework for the achievable product quality of commercial $CO_2$ methanation reactors. For obvious reasons, plant operators are interested in meeting the specification for feeding synthetic natural gas (SNG) to the local gas grid. In Europe, the following requirements need to be fulfilled [39]:

(a) $CO_2$ mole fraction $\leq 2.5\,\%$

(b) $H_2$ content (volume) $\leq 1\,\%$ (gas turbines) or $\leq 2\,\%$ (gas motors, steel tanks)

(c) water content (volume) $\leq 250\,\text{ppm}$ (according to [39, 40] for $p \leq 12\,\text{bar}$)

(d) absolute pressures between 8 and 12 bar (varies with pipeline)

In order to meet (a), reactors need to be operated at $CO_2$ conversions above 97 % and the product gas needs to be dried. The latter is usually not a problem, as water is easily separated by condensation. A dried methane-rich gas may however still contain up to 10 % $H_2$ (volume), which is not allowed with current regulations, especially with applications listed under (b). In some parts of the grid, however, the $H_2$ limit might be increased to 10 % in the future [39, 41]. In order to meet (d), a pressure stage is needed. As high pressures favor product formation, it is beneficial to pressurize gases prior to the reactor and run the reaction at elevated pressures. According to equilibrium calculations, the required temperature to reach 97 % conversion corresponds to 260 °C at 1 bar and 320 °C at 10 bar. As the $CO_2$ methanation is a kinetically hindered process [38], highly active catalysts are needed to achieve equilibrium conditions at low temperatures. In a recent material study, it was shown, that state-of-the-art Ni catalysts allow equilibrium operation at industrial mass flow velocities, 320 °C and 8 bar [26]. Despite this success, the industrial operation of the $CO_2$ methanation reaction still provides other challenges. A reactor modeling study has for example pointed out, that fixed-bed reactors of technical dimensions, which are operated with pure stoichiometric feed gas and high $CO_2$ conversions, inevitably suffer from runaway behavior [19]. Hence, product recycle or dilution by water/methane need to be considered [19].

## 2.2 Catalyst systems

In view of the kinetic hindrance of the $CO_2$ methanation, a catalyst is needed to speed up the reaction and achieve equilibrium conditions. Ideal catalysts are highly active, i.e. achieve equilibrium conditions at low temperatures, but also highly selective, i.e. exclude side reactions. Also, for industrial operation, long-term stability is important. Among the most promising materials, mainly group VIII metals are listed in several reviews, e.g. Ni, Pt, Co, Fe and Ru

[42–47]. General consensus seems to be, that Ru exhibits the highest activity and selectivity [48, 49]. In terms of cost-effectiveness, however, Ni is the material of choice [43, 50]. Pt has been reported to catalyze primarily the reverse water-gas shift reaction [49]. Co and Fe were found to catalyze chain growth reactions [51]. Apart from the kind of active metal, performance is also greatly dependent on the exposed active metal surface area. Unsupported metallic nickel for example shows a low specific surface area of less than $2\,m^2\,g$ and poor stability due to sintering [52]. Active phases are therefore commonly dispersed on various support materials. Ni, which seems to be the most frequently studied metal, has been supported on $SiO_2$ [53], $Al_2O_3$ [54], $TiO_2$ [55], $ZrO_2$ [56], $CeO_2$ [57], MgO [58], zeolites [59], MOFs [60] and others [61–63]. The purpose of support materials is hereby not limited to metal dispersion. Instead, synergistic effects may also occur. The activity of Ni, for example, was found to increase in the order $SiO_2 < Al_2O_3 < TiO_2$ due to higher $CO_2/H_2$ adsorption ratios and stronger metal-support interactions [64]. Similar results have been reported by Pandey et al. [65], who found an increase in activity in the order $SiO_2 < TiO_2 < ZrO_2 < Al_2O_3$, which was ascribed to higher $CO_2$ adsorption capacities of the support material.

Next to supported catalysts, the preparation of bulk catalysts has been mentioned. Raney nickel, which is a classical hydration catalyst, also shows high activity for the $CO_2$ methanation reaction [66]. Furthermore, metal foams have been applied [67]. Abelló et al. [37, 68] have prepared takovite-derived nickel-alumina catalysts by co-precipitation. These materials were found to exhibit extremely high Ni loadings of up to 70 % but also high stability under reaction conditions. This phenomenon was traced back to the formation of small $Ni^0$ crystallites (3 to 6 nm) upon reduction, which are stabilized within a Ni-Al mixed oxide matrix [37, 68]. He et al. reported a superior performance of co-precipitated Ni-Al catalysts over supported $Ni/Al_2O_3$ systems, which he ascribed to an increased Ni dispersion and a strong basicity [69]. Variation of the Ni/Al molar ratio has resulted in an optimum at 2 [68]. It is however important to emphasize that the co-precipitation route is greatly influenced by the exact reaction conditions. For example, variation of the precipitation agent, aging time and calcination temperature has provoked marked differences [24]. Similar effects are expected for the variation of pH.

Independent of the type of Ni catalyst, different promoter metals were found to improve catalytic properties. Among the most prominent ones are Fe and Mn. Fe has shown to enhance the activity [25, 70–72] and stability [25] of co-precipitated Ni-Al catalysts. It has been argued that Fe increases the reducibility of the active Ni phase, leading to smaller Ni crystallites [71, 72]. Others have stated that a Ni-Fe surface alloy with improved catalytic properties is formed upon reduction [25, 70]. The latter is also backed by computational screening [73, 74]. In the case of Mn, enhanced activity has been reported for $Ni/Al_2O_3$ [75, 76] and co-precipitated Ni-Al catalysts [25]. It was argued, that Mn had a stabilizing effect on Ni crystallites and increases the overall $CO_2$ adsorption capacity as well as the number of medium basic sites. The beneficial effects of Fe and Mn on activity and stability were systematically exploited by Burger et al. [25,

26]. In a first study, Ni/promoter ratios were varied in single-doped systems [25] and optimal Ni/Mn and Ni/Fe molar ratios were obtained at 5. In a second study, both promoters were added simultaneously to find the optimum in activity and stability [26]. The best performance was obtained for Ni/Fe and Ni/Mn molar ratios of 7 and 9.5, respectively. Besides Fe and Mn, also Co [38, 77], Ce [78] and La [79] have been identified as potential rate-enhancers.

## 2.3 Mechanistic aspects

Although several experimental and theoretical studies have been conducted to clarify the exact mechanism of the $CO_2$ methanation, it is still a subject of ongoing debate. In summary, two different pathways, which are both depicted in table 2.1, have been identified. In both cases, the dissociative adsorption of reactants into H*, CO* and O* is assumed as a first (and second) step. Afterwards, C-O bond cleavage either proceeds via the direct route, i.e. CO* dissociates further into C* and O*, or via hydrogen assistance. For the latter, adsorbed hydrogen is attached to CO* and the resulting formyl species CHO* dissociates into O* and CH*. After C-O bond cleavage, both mechanisms comprise the complete hydrogenation of carbonaceous and oxygen-containing ad-species to $CH_4$ and $H_2O$. Note, that several variations of the hydrogen-assisted mechanism exist, e.g. comprising formates instead of formyl [80] and $CO_2$ adsorption on the support or metal-support interface instead of the active metal [81].

**Table 2.1:** Proposed elementary steps of direct and hydrogen-assisted CO dissociation mechanisms for $CO_2$ methanation.

| direct CO dissociation [82, 83] | hydrogen-assisted CO dissociation [84, 85] |
|---|---|
| 1: $CO_2 + 2^* \rightleftharpoons CO^* + O^*$ | 1: $CO_2 + 2^* \rightleftharpoons CO^* + O^*$ |
| 2: $H_2 + 2^* \rightleftharpoons 2H^*$ | 2: $H_2 + 2^* \rightleftharpoons 2H^*$ |
| 3: $CO^* + ^* \rightleftharpoons C^* + O^*$ | 3: $CO^* + H^* \rightleftharpoons CHO^* + ^*$ |
| 4: $C^* + H^* \rightleftharpoons CH^* + ^*$ | 4: $CHO^* + ^* \rightleftharpoons CH^* + O^*$ |
| 5: $CH^* + 3H^* \rightleftharpoons {CH_4}^* + 3^*$ | 5: $CH^* + 3H^* \rightleftharpoons {CH_4}^* + 3^*$ |
| 6: ${CH_4}^* \rightleftharpoons CH_4 + ^*$ | 6: ${CH_4}^* \rightleftharpoons CH_4 + ^*$ |
| 7: $O^* + H^* \rightleftharpoons OH^* + ^*$ | 7: $O^* + H^* \rightleftharpoons OH^* + ^*$ |
| 8: $OH^* + H^* \rightleftharpoons H_2O^* + ^*$ | 8: $OH^* + H^* \rightleftharpoons H_2O^* + ^*$ |
| 9: $H_2O^* \rightleftharpoons H_2O + ^*$ | 9: $H_2O^* \rightleftharpoons H_2O + ^*$ |

Direct CO dissociation was originally proposed for CO methanation based on a $^{13}C$ isotope-labeling study [83]. Later, similar activation energies of CO and $CO_2$ methanation on Ni(100) were reported [86]. Consequently, direct CO dissociation was also suggested to underlie $CO_2$ methanation. Further evidence for identical mechanisms of CO and $CO_2$ methanation was provided by means of temperature-programmed desorption (TPD) and temperature-programmed

reaction on $Ni/SiO_2$ [87]. Also, transient measurements of Fujita et al. [88] were interpreted in favor of direct CO dissociation.

Density functional theory (DFT) calculations on the other hand indicate the preferential formation of HC–O* or HO–C* intermediates over isolated carbon species C* [84]. In addition, activation barriers for direct CO dissociation on Ni (even for favorable steps or defect sites [89, 90]) were reported to exceed CO adsorption enthalpies [84, 91]. Apart from DFT calculations, experimental evidence of formyl, carbon-hydroxyl and formate species has been provided by infrared [81, 92], isotope-labeling [93], transient [52] and surface science studies [94]. Whether the detected compounds are mere spectator species [94] or decisive intermediates [95] seems to depend on the studied material.

The great variety of valid conclusions suggests that the reaction pathway greatly depends on the chosen catalyst and the applied experimental conditions. Some researchers even draw the conclusion that both mechanisms may operate in parallel [52, 96].

## 2.4 Catalyst deactivation

### 2.4.1 Thermal Degradation

In heterogeneous catalysis, sintering describes the growth of supported metal particles, also called crystallites, under reaction conditions. The involved mechanisms are mainly temperature-driven and resemble that of crystallization, i.e. large particles grow at the expense of small ones. In general, the following two growth mechanisms have been proposed: particle migration (coalescence) and atom migration (Ostwald ripening) [97]. Particle migration describes the movement of small clusters or entire crystallites and subsequent collision with others, resulting in larger crystallites. Ostwald ripening on the other hand describes the exchange of single atoms between crystallites. Atom transport thereby occurs either via surface diffusion or the gas phase. It has been argued, that Ostwald ripening is unfavorable at low temperatures, as the activation barrier for completely detaching single metal atoms from metal bulk phases is excessively high ($\approx$ heat of Ni sublimation) [97]. Conversely, metal-support interactions are often rather weak ($\approx$ van der Waals forces). Hence, the migration of entire particles/crystallites often occurs at lower temperatures than Ostwald ripening. Experimental proof of this concept can be found, for example, in steam reforming [97] and ammonia synthesis conditions [98]. A different concept, which has also been recommended to access sintering phenomena [99], is based on the so-called Hüttig and Tammann temperatures, $T_{\text{Hüttig}}$ and $T_{\text{Tammann}}$. Both temperatures relate to

the melting temperature of the considered bulk metal, $T_{melt}$, according to equations (2.5) and (2.6).

$$T_{Hüttig}[K] = 0.3 \cdot T_{melt}[K] \tag{2.5}$$

Above the Hüttig temperature, loosely bonded surface atoms, e.g. at edges and corners, start to dissociate. Above the Tammann temperature, atoms from the bulk phase and small clusters become mobile [99]. For metallic Ni, which exhibits a melting temperature of 1725 K (1452 °C), the Hüttig and Tamman temperatures are 518 K (245 °C) and 863 K (590 °C), respectively. Hence, at temperatures of the $CO_2$ methanation reaction, which typically range from 200 to 450 °C, mobility of surface Ni atoms is expected.

$$T_{Tamman}[K] = 0.5 \cdot T_{melt}[K] \tag{2.6}$$

Note, that strictly speaking, the limits set by the Hüttig and Tammann temperature relate to diffusion processes within the metal or on top of the metal surface (not the support surface) [100]. Nevertheless, sintering phenomena seem to be strongly related to these processes. One possible explanation was given by Sehested, who proposed that directed movements of surface metal atoms on top of a crystallite may induce a translational motion of said crystallite [97].

Sintering, apart from temperature, also depends on the degree of metal-support interaction. In the case of co-precipitated Ni-Al catalysts but also for impregnated $Ni/Al_2O_3$ systems, surprisingly strong metal-support interactions have been reported [101, 102]. Electron microscopy revealed that next to $Al_2O_3$, NiO or $Ni^0$, also nickel-aluminate structures are formed upon calcination and/or reduction [103]. These may attach to metallic Ni crystallites and encapsulate them partially or even completely [103]. It was suggested that this mechanism slows down sintering and contributes to the high thermal stability of nickel-alumina catalysts [101].

Another important factor for particle sintering was found to be the reaction atmosphere. Co-precipitated Ni-Al catalysts, for example, have shown to deactivate more rapidly if steam is introduced to the feed gas [23]. Also $Ni/Al_2O_3$ catalysts used for steam-reforming are subject to more severe sintering with an increase in $H_2O$ partial pressure [104]. The latter was ascribed to the formation of $Ni_2$–OH complexes, which show lower energies of formation and diffusion than Ni surface atoms [104]. An acceleration of particle growth was also monitored for $Ni/Al_2O_3$ catalysts operated under high CO partial pressures (> 2 bar) and temperatures below 425 °C [105]. This effect was traced back to the formation of volatile $Ni(CO)_4$.

### 2.4.2 Carbon formation

Carbon formation in methanation reactions is primarily a product of the Boudouard reaction and can usually be predicted well from thermodynamic calculations [106]. As shown in section 2.1, the current work was carried out in a regime well below the carbon deposition line. Experimental proof thereof has been reported recently [107]. Carbon formation is therefore not elaborated in greater detail here. Instead, the interested reader is referred to several reviews [106, 108, 109], where the operation of Ni catalysts in carbon forming regions is well described.

### 2.4.3 Sulfur Poisoning

Poisoning describes the deactivation of catalysts due to the formation of strong covalent bonds between a poisoning compound and the active site(s) of a catalyst's surface. The poisoning compound may thereby originate from reactants, products or impurities. Deactivation is often due to physical blockage of active centers but may also involve changes in electronic properties of neighboring sites, restructuring of the surface and hindrance or blockage of surface diffusion paths. The strong and dissociative adsorption of sulfur on Ni has been primarily validated by investigation of $H_2S$ adsorption on various $Ni^0$ surfaces: single crystals, foils, sponges, polycrystalline and supported $Ni^0$ [110]. These studies are difficult to carry out, because extremely low $H_2S$ partial pressures are needed. Hence, either vacuum conditions or highly diluted $H_2S$ streams, primarily in $H_2$, have been applied. Once the adsorption equilibrium is established, the heat and free energy of adsorption can be calculated according to

$$\Delta G = RT \cdot \ln(p_{H_2S}/p_{H_2}) = \Delta H - T\Delta S \tag{2.7}$$

where $p_i$ is the partial pressure of component i, $R$ is the universal gas constant and $T$ is the temperature. $\Delta H$ and $\Delta S$ are the enthalpie and entropy of the adsorption, respectively. $\Delta G$ is the difference in Gibb's free energy. In a linearized form, one obtains

$$\ln(p_{H_2S}/p_{H_2}) = \frac{\Delta H}{R} \cdot \frac{1}{T} - \frac{\Delta S}{R} \tag{2.8}$$

In figure 2.3, $\ln(p_{H_2S}/p_{H_2})$ is plotted versus reciprocal temperature and sample spaces of several important adsorption studies are highlighted. The solid line represents equilibrium data for the formation of bulk $Ni_3S_2$ and corresponds to a formation enthalpy of –75 kJ (per mole $H_2S$) [111]. The dashed lines represent equilibrium lines for chemisorbed sulfur with heats of adsorption of –100 kJ and –200 kJ under the assumption of $Ni_3S_2$ formation, i.e. the dashed lines have the same intercept as the solid line [112]. Now, it becomes obvious, that most of the reported results lie between the dashed lines, thus indicating a higher stability of sulfur adsorption as compared to $Ni_3S_2$ formation. Concerning sulfur coverage, different definitions

have been used. In this work, coverages are compared on the basis of equation (2.9), where $N_{S,ads}$ is the amount of adsorbed sulfur and $N_{Ni*}$ is the amount of available nickel surface site prior to sulfur adsorption. The latter may be determined by $H_2$ or CO chemisorption under the assumption of H/Ni* or CO/Ni* surface ratios [113, 114]. In this study, $H_2$ chemisorption is used under the assumption of H/Ni*=1/1 [115]. Hence, coverages reported in [114] need to be multiplied with a factor of 0.718 to account for CO chemisorption. This results in coverages between 0.45 and 1.0, which is in good agreement with other adsorption studies [112, 113, 116, 117].

$$\theta_S = \frac{N_{ads}}{N_{Ni*}} \tag{2.9}$$

Heats of adsorption were found to increase with decreasing coverage [114]. Upon increasing the temperature, coverages were found to decrease, causing also a decrease in equilibrium $H_2S$ partial pressure [114]. At 450 °C, for example, sulfur coverages of $\theta_S \approx 0.5$ are obtained at $H_2S$ partial pressures as low as 0.1-1 ppb [114]. This concentration is at the lower end of our present detection limit [118]. It is therefore no surprise, that no studies have been carried out below 0.1 ppb so far. At the same temperature (450 °C), almost complete coverage ($\theta_S > 0.7$) is obtained at $H_2S$ partial pressures between 0.1 and 1 ppm [114]. This concentrations are encountered in many catalytic processes after gas cleaning [118]. In most processes involving Ni catalysts, $H_2S$ (and other sulfur impurities) is therefore expected to adsorb irreversibly and cover high fractions of the $Ni^0$ surface.

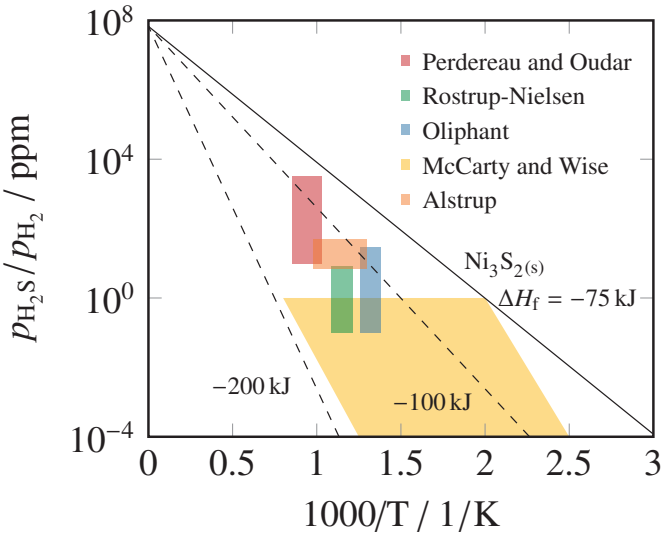


**Figure 2.3:** Sample spaces from previous equilibrium adsorption studies for $H_2S$ adsorption on $Ni^0$ [112–114, 116, 117]. Values of $\Delta H_f$ are based on 1 mol of $H_2S$.

In order to gain a deeper understanding of sulfur poisoning, surface structures of adsorbed sulfur on nickel surfaces need to be considered. These are preferably studied by sulfur adsorption

on single crystals under ultra high vacuum (UHV) conditions, which has a variety of benefits (despite the pressure gap):

- Selected crystal faces can be investigated. This is not possible with polycrystalline samples, as several facets are simultaneously exposed to the reaction atmosphere. Accordingly, sulfur coverages obtained for polycrystalline samples need to be considered as an average value of various crystal faces.

- It is possible to apply surface science methods, such as low-energy electron diffraction (LEED) and scanning tunneling microscopy (STM). These techniques directly probe the outer surface of a sample at an extremely high level of detail (up to atomic resolution). Hence, definite conclusions about surface geometries and adsorption patterns are possible.

- $H_2S$ concentrations below 0.1 ppb are more easily adjusted and thus, it is possible to achieve sulfur coverages below those obtained for diluted $H_2S$ streams.

The conducted UHV studies [116, 119–122] reveal, that adsorption structures vary in dependence of coverage and crystal face. On Ni(100), for example, an ordered p(2 x 2) overlayer is observed at low coverages ($\theta_S < 0.25$), i.e. each sulfur atom is bound to four Ni atoms. At higher coverages ($0.25 < \theta_S < 0.50$), sulfur atoms adsorb in an ordered c(2 x 2) overlayer, i.e. each sulfur atom is bound to two Ni atoms. In figure 2.4, both structures are visualized with Ni and S atoms having approximately the correct size ratio (cross sections: 0.06 and 0.12 $nm^2$). According to size, the reported saturation coverage of $\theta_S = 0.50$ on Ni(100) [116], seems logical. On higher index planes, such as Ni(110) and Ni(111), the same adsorption structure is observed for $\theta_S < 0.25$ but more complicated ones occur at higher coverages [121, 122]. Furthermore, saturation coverages increase in more open surface structures, such as Ni(110) ($\theta_S = 0.74$ ) and Ni(210) ($\theta_S = 1.09$) [116]. Hence, there seems to be a trend of increasing saturation coverage with decreasing planar density and increasing surface roughness [118]. The number of sulfur atoms per square centimeter remains however constant: $0.82 \pm 0.04 \cdot 10^{15}$ for Ni(111), Ni(100), Ni(110), Ni(210) and polycrystalline Ni [116].

The apparent discrepancies between sulfur coverages obtained from single crystal studies (primarily $\theta_S \leq 0.5$) and polycrystalline or supported nickel (primarily $0.5 < \theta_S < 1.0$), can be resolved as follows:

- Compared to low-index single crystals, supported and polycrystalline Ni show a higher fraction of edges and corners (i.e. high-index planes), which exhibit higher saturation coverages.

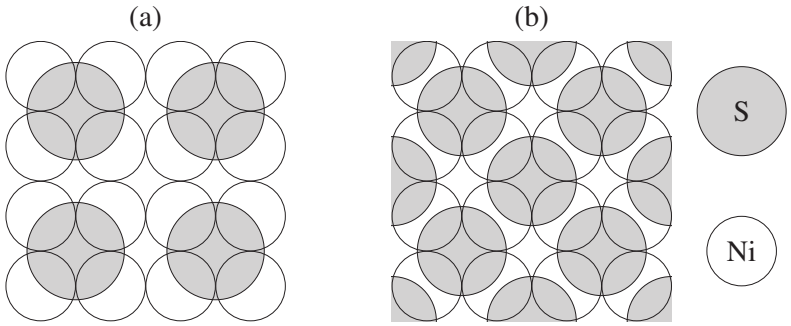


**Figure 2.4:** Schematic view of adsorbed sulfur on a Ni(100) surface at $S/Ni_S$=0.25 in a p(2x2) structure (a) and at $S/Ni_S$=0.50 in a c(2x2) structure (b). Adapted from [123].

- Sulfur adsorption on supported and polycrystalline nickel samples is primarily carried out with diluted $H_2S$ steams, where $H_2S$ (partial) pressures are markedly higher as compared to UHV conditions. According to $H_2S$ adsorption studies, sulfur coverages increase with the equilibrium $H_2S$ partial pressure [114].

- Sulfur adsorption at high $H_2S$ partial pressures leads to surface reconstruction, i.e. the roughness of surfaces increase upon adsorption. This effect has been observed in a variety of UHV studies [121, 122, 124, 125].

- Sulfur adsorption can be influenced by sample pretreatment [126] or the presence of reactant and products during reaction [127].

Apart from the investigation of surface structures of adsorbed sulfur, the effect of adsorbed sulfur on the adsorption of other molecules is crucial to understand poisoning processes. Previous studies on single crystal [128–135] and supported nickel surfaces [136–138] have primarily considered $H_2$ and CO adsorption. Both processes seem to be significantly hindered on presulfided nickel surfaces. Only results from CO adsorption at low temperatures ($< 30\,^{\circ}C$) show an increase in CO adsorption after $H_2S$ treatment, which is however due to nickel (sub)carbonyl formation [110, 138]. Conversely, on Ni(111) for example, CO adsorption has been reported to be completely inhibited at $\theta_S > 0.3$ and the sticking coefficient of $H_2$ was close to zero as sulfur coverages increase to saturation [128]. Furthermore, a temperature programmed desorption study on Ni(100) revealed a rapid and nonlinear decline of bridged CO with increasing sulfur coverage [130]. Hence, at low coverages ($\theta_S < 0.2$), one sulfur atom deactivated approximately ten nickel atom sites [130]. This behavior closely mirrored kinetic data obtained for CO methanation on presulfided Ni(100) [130]. $H_2$ adsorption was also subject to a nonlinear decrease, which was however slightly retarded towards higher $\theta_S$ values as compared to bridged CO. The coverage of linear CO stayed approximately constant with sulfur coverage. Results were interpreted in terms of long-range electronic effects of adsorbed sulfur atoms on neighboring nickel sites [130]. Unfortunately, studies of the latter kind, which combine (a) adsorption of reactants on presulfided surfaces and (b) kinetic measurements on the same system, are very

scarce in literature. To the best of our knowledge, no such investigations are currently available for the $CO_2$ methanation.

Due to the strong and irreversible adsorption of sulfur on nickel and the accompanied inhibition of reactant adsorption, sulfur often results in a substantial or complete loss of activity in many important reactions. In the case of nickel catalysts, kinetic data is available for the CO methanation [130, 137, 139–143], the Boudouard reaction [141] and steam reforming [144]. For the CO methanation reaction, probably the most detailed study considers $H_2S$ poisoning of a $Ni/Al_2O_3$ plate catalyst [143]. It shows that at 390 °C, the presence of only 13 ppb $H_2S$ causes a loss of relative methanation activity of over two orders of magnitude. Further increasing the $H_2S$ partial pressure to 62 ppb results in an additional decrease of an order of magnitude. Afterwards, activity stabilizes between 3-4 orders of magnitudes lower as compared to the initial value. Similar results have been obtained for CO methanation over presulfided $Ni/MgAl_2O_4$ [141]. The reported data is in good agreement with $H_2S$ adsorption on $Ni/Al_2O_3$, suggesting high sulfur coverages ($\theta_S \geq 0.7$ [114]) at the applied conditions (390 °C, 13-92 ppb $H_2S$ [143]).

Activity measurements under poisoning conditions also provide information about the kind of active sites present on the catalyst's surface. A classical approach to access this information has been provided by Maxted [145], using an expression of the following kind

$$a_{rel} = a_{rel}^0 \cdot (1 - c \cdot \theta_i) \tag{2.10}$$

to correlate the activity under poisoning conditions $a_{rel}$ with the surface coverage of the poisonous species $\theta_i$. $a_{rel}^0$ is the activity of the unpoisoned catalyst and $c$ is a constant, which describes the specific poisoning effect per unit poison. If equation 2.10 is slightly adjusted, the following form is obtained

$$a_{rel} = a_{rel}^0 \cdot (1 - \theta_i)^n \tag{2.11}$$

which relates to simple Langmuir kinetics. Hereby, $(1 - \theta_i)$ relates to the number of unoccupied sites and $(1 - \theta_i)^n$ describes the probability for $n$ unoccupied sites in close proximity to each other. Hence, $n$ can be interpreted as the number of active sites required for the reaction [146]. Although this concept does not consider long-range effects of the poisoning species, the shape of the ensemble and the structure of the chemisorbed molecule [147], it allows a comparison between poisoning studies and serves as an indicator to which degree the considered reaction is structure-sensitive. An advanced version of equation 2.11 has been suggested by Andersen et al. [148]. In figure 2.5, both of the discussed CO methanation studies [141, 143] are compared on the basis of equation 2.11. Both curves show an exponential decrease of activity with sulfur coverage, which indicates the preferential blockage of highly active sites, e.g. edges and corners. This result is in good agreement with the supposed structure-sensitivity of CO adsorption on nickel [84]. The reported discrepancy in the exponent $n$, which was found to be 2 in the case of

Fitzharris [143] and 4.3 in the case of Rostrup-Nielsen [141], was almost resolved completely, by using a common definition of sulfur coverage, according to equation (2.9). In contrast to

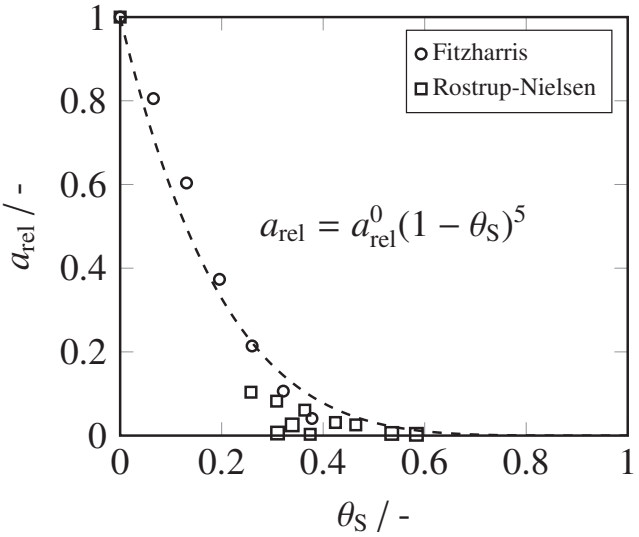


**Figure 2.5:** Relative CO methanation activities in dependence of sulfur coverage, reported by Fitzharris et al. [143] and Rostrup-Nielsen et al. [141].

equation (2.9), Fitzharris uses the amount of sulfur related to the maximum amount of sulfur adsorbed at 13 ppb, which corresponds to a sulfur to nickel surface atom ratio of S/Ni* = 1/2 (assuming H/Ni* = 1/1) [143]. Rostrup-Nielsen on the other hand uses the amount of adsorbed sulfur related to a saturation coverage obtained from $H_2S$ chemisorption at ppm levels and high temperature [117, 141]. Although the denoted sulfur to nickel surface atom ratio of S/Ni* = 0.53 seems similar to that used by Fitzharris, Rostrup-Nielsen uses a different stoichiometry for $H_2$ chemisorption on nickel (H/Ni* = 0.73) [113]. Hence, the saturation coverage actually corresponds to a value of S/Ni* = 0.72 (assuming H/Ni* = 1/1). This value is well in line with $H_2S$ equilibrium adsorption under similar conditions [112, 113]. Once sulfur coverages are adjusted according to equation (2.9), a similar exponent of approximately $n = 5$ is obtained for both studies (figure 2.5). This result is well in line with CO adsorption on $Ni^0$, which has been reported to require 4-5 Ni surface atoms (cite).

Despite the fairly good agreement between a variety of poisoning studies, it was observed that sulfur poisoning is also a function of catalyst composition [140] and reaction conditions [127]. Hence, it was found that the stability of a catalyst against sulfur poisoning, also called its sulfur resistance, can be increased by adding certain promoter materials such as Cr, Mn or Mo oxides [110]. $MoO_3$ even showed an increasing activity for the CO methanation with increasing $H_2S$ partial pressure, because molybdenum sulfides are able to dissociate $H_2$ [149]. Also, noble metals have been applied as sulfur tolerant materials, as higher $H_2S$ partial pressures as compared to Ni or Co are needed to form nobel metal surface sulfides [150]. Further materials with beneficial effects against sulfur poisoning have been summarized in [32].

In order to gain control over sulfur poisoning in an industrial environment, it was found crucial to provide gas cleaning prior to the catalytic reactor. Technologies for sulfur cleaning primarily comprise Rectisol® washes [151] or scavenger processes employing for example ZnO as an adsorber material, which selectively removes trace amounts of sulfur [152]. Typically, a hydrogenation unit is attached to the front end of the sulfur removal unit to convert hard-to-separate sulfur components into $H_2S$ [32, 152].

Although the data presented in this section comprise a fairly thorough picture of sulfur poisoning for the CO methanation reaction, similar studies for the $CO_2$ methanation are scarce [153–156]. Of the available studies, only Neubert et al. [155] provide a coherent study for thiophene poisoning of a commercial Ni catalyst. However, the applied catalyst is not sufficiently characterized and thus the obtained results cannot be put in a more general perspective or transferred to other catalysts. Thorough catalyst characterization is also missing in the study of Müller et al. [153], who has reported poisoning of a 60 wt% $Ni/SiO_2$ catalyst by 516 ppm of $SO_2$. Despite the very high concentration of the poisoning compound, which would be subject to gas cleaning prior to an industrial reactor, it is concluded that $SO_2$ poisoning is more severe than $H_2S$ poisoning. This conclusion is highly doubtful as it is based on a comparison with $H_2S$ poisoning studies from literature instead of repeating the poisoning experiment under identical conditions with $H_2S$. Bakar et al. [154] have studied $H_2S$ poisoning of an impregnated $Ru/Mn/Ni(5:35:60)/Al_2O_3$ catalyst. Despite the obviously detrimental effect of $H_2S$ on the catalyst performance, no general conclusions were presented which is partly due to the absence of catalyst characterization results and partly due to the lack of systematic data. On top, 1 % of $H_2S$ was chosen as a poisoning concentration, which is too high for an industrial feed entering a methanation reactor. Guilera et al. [156] have investigated promoted $Ni/Al_2O_3$ poisoned by 50 ppb of $H_2S$. Although the concentration of the poison was chosen reasonably low, lifetime tests were conducted in a fixed-bed reactor under equilibrium conditions ($H_2/CO_2 = 4/1$, 300 °C, 5 bar) and aborted after 146 h. Over the course of the lifetime tests, a constant $CO_2$ conversion was monitored. Based on this observation it was concluded, that sulfur poisoning does not affect the employed catalysts. However, it is well-known that monitoring the integral conversion of a fixed-bed under equilibrium conditions is not a sound procedure to study catalyst deactivation [157]. It seems highly likely that after 146 h, only a fraction of the fixed-bed was poisoned and the remaining fraction was able to achieve equilibrium conversion nonetheless.

# 3 Experimental background

## 3.1 Elemental analysis

Elemental analysis is an umbrella term for multiple qualitative and quantitative techniques, which give access to a sample's elemental composition. Prior to analysis, samples often need to be transferred into an easy-to-analyze state. In the case of solids, this involves chemical decomposition, e.g. dissolving or combustion, and in some cases, the addition of reagents, e.g. to form a colored complex, which then provides the basis for analysis. In order to quantify the obtained results, calibration is essential. Hereby, at least one reference compound, containing a known amount of the element(s) of interest, needs to be analyzed. In the following, only those techniques, which are relevant for the current thesis are briefly described.

**CHNS analysis**

CHNS analysis gives access to the elemental composition of solid samples with respect to carbon (C), hydrogen (H), nitrogen (N) and sulfur (S). Therefore solid samples are decomposed by combustion at temperatures up to 1800 °C. The resulting oxidation products are contacted with a copper catalyst (600-900 °C), which converts noxious oxides ($NO_x$) to molecular $N_2$. The product matrix then consists of the following well-defined compounds: $CO_2$, $H_2O$, $SO_2$ and $N_2$. These are directed through a separation column. After separation, gases are typically analyzed by means of a thermal conductivity detector (TCD). Depending on the applied separation column, gases pass the TCD in a prescribed order, giving rise to four subsequent signals (i.e. peaks). The amount of C, H, N and S is obtained by peak integration and conversion by means of a calibration curve. Results are given in relation to the total sample mass (i.e. mass fractions). Typical reference materials for calibration are *inter alia*: stearic acid (C, H), urea (N) and sulfanilamide (S).

**Inductively coupled plasma optical emission spectroscopy (ICP-OES)**

ICP-OES is a versatile tool to analyze almost any element in liquid samples by means of spectroscopy. In modern instruments, it is possible to analyze up to 70 compounds at the same time. For analysis, samples are dispersed within a nebulizer into a stream of argon and carried through an inductively coupled plasma. At temperatures between 6000 and 9000 K, the sample

is decomposed into free atoms and ions, which are subsequently transferred into excited states. Upon returning to the ground state, light of element specific wavelengths is emitted. The emitted intensities correlate to the concentration of elements. The exact dependence is obtained by calibration. However, care needs to be taken, as spectral interference and matrix effects may cause quantification errors [158].

**Photometry**

Photometry comprises the absorption of visible light in liquid samples. The amount of light absorbed at a specific wavelength, $E(\lambda)$, is hereby described by the Lambert-Beer law, depicted in equation (3.1). $I_0$ is the intensity of the incident beam of light, $I$ is the transmitted intensity, $\varepsilon(\lambda)$ is the absorptivity, $c$ is the concentration of the attenuating species and $d$ is the path length within the sample. In practice, $d$ typically describes the thickness of a cuvette, which contains the sample.

$$E(\lambda) = \log_{10}(I_0/I) = \varepsilon(\lambda) \cdot c \cdot d \tag{3.1}$$

If the transmitted intensity of several samples of known concentration is measured, a plot of $\log_{10}(I)$ over $c$ results in a straight line with intercept $a = \log_{10}(I_0)$ and slope $b = -\varepsilon(\lambda) \cdot d$. Upon measuring the transmitted intensity of an unknown sample, its concentration can be determined according to the obtained linear correlation. Typically, equation (3.1) only applies at low concentrations ($< 0.01$ mol/l), which is why samples need to be diluted.

If several compounds within a sample absorb visible light, the wavelength of the incident beam needs to be narrowed such that it is only adsorbed by the relevant compound. This may comprise using a monochromator or lasers. Colorless samples, which do not absorb light, can be transferred into colored samples using specific reactants to induce a color reaction.

## 3.2 X-ray diffraction

X-ray diffraction is a standard technique in scientific laboratories for the structural characterization of materials. The underlying measurement principle is the elastic scattering of light on a grating, leading to a characteristic diffraction pattern, which depends on the incident wavelength and the geometry of the grating. Laue and his coworkers [159] were the first to realize, that crystals can be used as grating and X-rays, which have wavelengths on the scale of covalent chemical bonds, can be used to characterize them. In their experiments, single crystals were placed in the beam path of a polychromatic X-ray source. Photo plates behind and to the sides of the crystal showed an ordered pattern, consisting of several bright spots arranged in circles. They concluded that X-rays have wave character and were scattered on the crystal lattice, leading

to constructive (bright spots) and destructive (dark areas) interference of the radiation. W. H. Bragg and W. L. Bragg [160] observed very similar patterns as compared to Laue when using monochromatic X-rays, striking a single crystal in a grazing angle. W. L. Bragg [161] explained this observation by the reflection of the incident X-rays on a set of parallel crystal planes. This situation is displayed in figure 3.1. As X-rays penetrate deep into the sample, they strike the

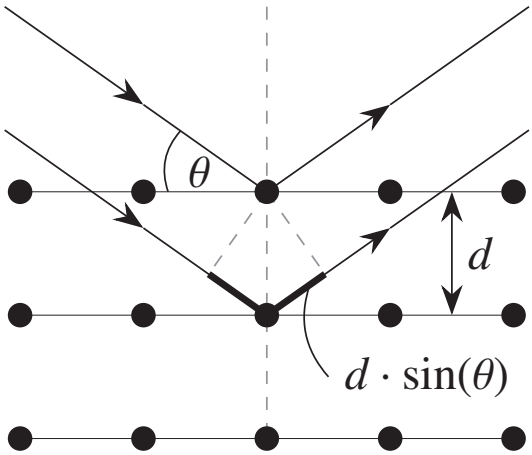


**Figure 3.1:** X-rays impinging on adjacent crystal planes of interplanar distance $d$ at a grazing angle $\theta$ (adapted from [162]).

crystal lattice at different sample depths, which results in different path lengths. For adjacent planes, as depicted in figure 3.1, the difference in path length is $2d \cdot \sin(\theta)$, where $d$ is the interplanar distance and $\theta$ is the grazing angle. Reflected waves only remain in phase and thus undergo constructive interference, if the difference in path length is equal to the wavelength of the radiation, $\lambda$, or a multiple thereof. This leads to a rather simple correlation between the interplanar distance and the grazing angle, displayed in equation (3.2), which is also known as Bragg's law.

$$2d \cdot \sin(\theta) = n \cdot \lambda \tag{3.2}$$

Based on the interplanar distance, it is possible to determine the dimensions of a crystal's unit cell: $a$, $b$ and $c$. Therefore, the crystal system (e.g. cubic, tetragonal, hexagonal) and the Miller indices ($h$, $k$, $l$) of the recorded reflection need to be known. In the case of cubic or hexagonal lattices, equations (3.3) (cubic) and (3.4) (hexagonal) can be applied.

$$\frac{1}{d^2} = \frac{h^2 + k^2 + l^2}{a^2} \tag{3.3}$$

$$\frac{1}{d^2} = \frac{4}{3} \cdot \left(\frac{h^2 + hk + k^2}{a^2}\right) + \frac{l^2}{c^2} \tag{3.4}$$

The first application of X-ray diffraction to powder samples was reported by Debye and Scherrer [163]. They used monochromatic X-rays which were run through a cylinder filled with micro crystalline powder. Due to the large number of small crystals and their random orientation within the cylinder, it was possible to determine all grazing angles for which the Bragg condition was fulfilled at once. Hence, the crystal system and the lattice parameters of the sample material could be determined without *a priori* knowledge of the crystal system.

In the early days, photo plates or cameras were used to record diffraction patterns. Also, the X-ray source was stationary. Nowadays, so-called goniometers are used to move the sample, the detector and/or the X-ray source relative to each other. Thus, increased angle resolutions and reduced analysis times are achieved [162]. The most common type of XRD instruments is build in Bragg-Brentano geometry. In theta-theta motion, both the detector and the X-ray source rotate around the sample. In 2-theta motion, the source is stationary, whereas the sample holder and the detector are moving. Spinning the sample increases the number of crystallite orientations exposed to the X-ray beam.

If Bragg's condition (equation (3.2)) is fulfilled, reflection on that specific set of crystal planes is maximized. The maximum in intensity hereby depends on the density of the lattice and also on the atoms present in the lattice. Hence, diffraction patterns differ in a) the angle of the intensity maxima and b) the relative intensities among the recorded reflections. Each material shows its very own characteristic pattern. If multiple materials are present in the same sample, the diffraction pattern results from superposition of the constituent's patterns. For qualitative analysis, measured diffraction patterns are compared to standard compounds or reference patterns collected in databases. The latter is provided, for example, by the International Centre for Diffraction Data (ICDD) or the Joint Committee for Powder Diffraction Studies (JCPDD).

Next to qualitative analysis, a variety of quantitative approaches exist. For the current thesis, the most important one is the quantification of crystal sizes. It was first observed by Scherrer [164], that the broadness of a reflection correlates with the size of crystals. This correlation is depicted in equation (3.5), which is also known as Scherrer equation.

$$d_\mathrm{i} = \frac{K \cdot \lambda}{\beta \cdot \cos(\theta)} \tag{3.5}$$

$d_\mathrm{i}$ is the mean size of the ordered (crystalline) domains of species i, $K$ is a dimensionless shape factor, $\beta$ is the line broadening at full width at half-maximum (FWHM), after subtracting the instrumental line broadening, in radians. $\lambda$ and $\theta$ are defined according to Bragg's law. However, care must be taken because equation (3.5) only applies to sub-micrometer particles or crystallites [165]. Also, other factors than crystallite size can contribute to the width of a diffraction peak. These are for example inhomogeneous strain or crystal lattice imperfections [166, 167].

## 3.3 Gas adsorption

Quantitative gas adsorption by the volumetric method is an important technique for the determination of surface areas. The underlying measurement principle is the pressure-dependent adsorption/desorption equilibrium between gases and solid surfaces at a constant temperature. In a typical adsorption experiment, a defined amount of gas is locked within a storage chamber and subsequently expanded into an evacuated adsorption chamber. After the adsorption equilibrium between gas and sample is reached, the pressure is recorded and dosing is continued stepwise. This procedure is repeated multiple times to obtain several data points of equilibrium pressure versus amount of adsorbed gas molecules. Upon plotting this data adequately, an isotherm is obtained, which provides characteristic information about the sample, in particular the overall surface area and the porosity. As gas adsorption is very sensitive towards surface impurities, gases already adsorbed on the sample need to be removed prior to analysis. This is usually done by heating and/or evacuating the sample. Depending on the applied apparatus and technique, several other steps may be necessary, e.g. measuring the blank volume(s) of storage and/or adsorption chamber. In the following, two methods, which are especially relevant for the current thesis are explained in greater detail.

**$N_2$ physisorption**

Physisorption (physical adsorption) is due to van-der-Waals interactions and unspecific to the surface composition of a sample. Hence, it is suitable to determine the overall surface area of a wide range of materials. In the case of a porous material, physisorption may also be applied to characterize the prevailing pore structure, e.g. the pore volume and the distribution of pore radii. $N_2$ physisorption is carried out by stepwise dosing gaseous $N_2$ to an evacuated sample cell, which is cooled to 77 K by liquid $N_2$. Next to the equilibrium pressure within the sample cell, $p$, which stepwise increases with added $N_2$, a reference pressure $p_0$ is measured within a non-evacuated cell at the same temperature. The adsorption is finished, once a relative pressure $p/p_0 = 1$ is reached. In order to gain information about the pore structure, a subsequent desorption experiment needs to be carried out. This is done by stepwise decreasing the pressure within the sample cell to its initial vacuum value. Plotting the total volume of adsorbed $N_2$ versus relative pressure, leads to an adsorption/desorption isotherm. Depending on the pore structure of the sample material, various types of isotherms are distinguished. According to IUPAC nomenclature [168], there are six types of isotherms, which are displayed and described in figure 3.2 and table 3.1. For determining surface areas, the monolayer coverage of the adsorptive needs to be known. Physisorption, however, is typically occuring in multilayers, even at low pressures. Brunauer, Emmet and Teller found a way to describe this process

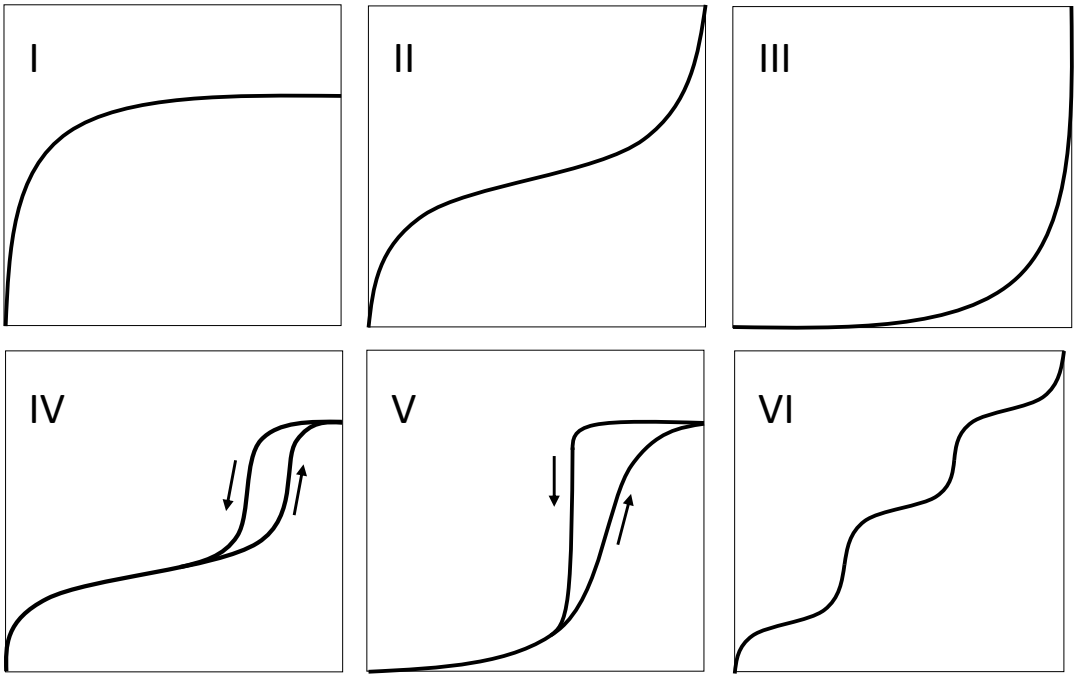


**Figure 3.2:** Classification of isotherms according to IUPAC [168].

**Table 3.1:** Classification of isotherms according to IUPAC [168].

| | |
|---|---|
| Type I | Microporous substances (pore diameter $d_p < 2\,nm$) with a small outer surface area, e.g. active charcoal, zeolites and porous oxides. Upon increasing the pressure, micropores are filled, so that the outer surface is only covered by one monolayer of $N_2$, even at saturation vapor pressure. |
| Type II | Non-porous or macroporous materials ($d_p > 50\,nm$). After the first monolayer is completed, multilayer adsorption is observed. The transition between monolayer and multilayer adsorption is typically not well pronounced. |
| Type III | Rarely observed, e.g. water adsorbed on hydrophobic surfaces. Weak adsorption at small pressures due to weak interactions between adsorptive and surface. The presence of increasing amounts of adsorbate on the surface promotes further adsorption. |
| Type IV | Mesoporous substances ($2 < d_p < 50\,nm$). The characteristic feature of the isotherm is its hysteresis loop, which indicates capillary condensation. The first part of the isotherm resembles type II, afterwards a second 'plateau' is reached at saturation vapor pressure. |
| Type V | Rarely observed, e.g. polar components on hydrophobic and porous materials. Resembles type III but comprises a hysteresis loop. |
| Type VI | Rarely observed, e.g. graphited carbon black. Multilayer adsorption on a uniform non-porous surfaces. |

mathematically [169]. According to their model, the low pressure region of type II and IV isotherms are described by the following equation:

$$\frac{p}{V_{N_2}(p-p_0)} = \frac{1}{V_m C} + \frac{C-1}{V_m C}\frac{p}{p_0} \tag{3.6}$$

$V_m$ is the volume at monolayer coverage, $V_{N_2}$ is the volume of adsorbed $N_2$ and $C$ is the BET constant. If the left side of equation (3.6) is plotted against $p/p_0$, a linear regression curve with intercept $a = 1/(V_m C)$ and slope $b = (C-1)/(V_m C)$ is obtained for $0.05 < p/p_0 < 0.30$ [170]. Resolving both equations leads to the following expressions to calculate $V_m$ and $C$.

$$V_m = \frac{1}{a+b} \tag{3.7}$$

$$C = \frac{b}{a} + 1 \tag{3.8}$$

Once $V_m$ is known, specific BET surface area, $S_{BET}$, can be calculated according to equation (3.9). For the required cross-section area of one physisorbed $N_2$ molecule, a value of $A_{N_2} = 0.162\,nm^2$ has been recommended [170]. $N_A$ is Avogadro's number and $m$ is the sample mass.

$$S_{BET} = \frac{V_m \cdot N_A \cdot A_{N_2}}{V_M \cdot m} \tag{3.9}$$

**$H_2$ and $CO_2$ chemisorption**

In contrast to physisorption, chemisorption (chemical adsorption) is due to the formation of covalent chemical bonds between the adsorptive and the surface. It is highly specific with regards to surface composition and can be used to count the strongest adsorption sites of a surface. These are specifically relevant in heterogeneous catalysis, as they enable bond rearrangements and thus the conversion of reactants to products. The process of breaking intermolecular bonds of the adsorptive compound upon adsorption is called dissociative chemisorption. The most prominent example is $H_2$ chemisorption. Volumetric chemisorption measurements comprise a similar dosing mechanism as described previously ($N_2$ physisorption). After the adsorption part is finished, a 'combined' isotherm is obtained, which consists of chemisorption and physisorption phenomena. In order to separate both processes, the sample needs to be evacuated and a second adsorption is carried out. As chemisorbed species are strongly bound to the surface, they are not removed upon evacuation and the resulting 'weak' isotherm comprises only physisorption. The 'strong' isotherm, i.e. pure chemisorption, can be calculated by subtracting 'weak' from 'combined'. In figure 3.3, the correlation between the discussed curves is visualized. In order to evaluate the recorded isotherms with regards to monolayer coverage $V_m$, several approaches exist. In this work, the extrapolation method was used. Therefore, the linear part

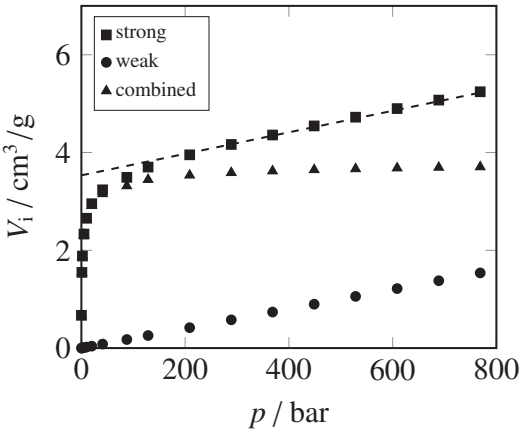


**Figure 3.3:** Exemplary isotherms obtained from a chemisorption experiment with species i. The dashed line represents the linear regression required for the extrapolation method.

of the combined curve, which comprises pure physisorption, is fitted by a straight line and extrapolated to a pressure of $p = 0$ (dashed line in figure 3.3). Under the assumption that all physisorbed species are removed at $p = 0$, the intersect gives the amount of adsorbate required for monolayer coverage. Hence, the number of adsorbed molecules within a monolayer (per mass unit of sample), $N_m$, can be calculated according to equation (3.10).

$$N_m = \frac{V_m \cdot N_A}{V_M \cdot m} \tag{3.10}$$

$H_2$ adsorption on nickel powder [171] and nickel supported on alumina or silica [115] has been reported to be dissociative with each hydrogen atom being bound to one nickel atom. The same stoichiometry ($\nu = 2$) is recommended by a German chemisorption standard [172]. As $H_2$ chemisorption is selective towards nickel, it is a powerful tool to determine several characteristic values of supported nickel catalysts. The specific nickel surface area is given by

$$S_{Ni} = N_m \cdot \nu \cdot A_{Ni} \tag{3.11}$$

where $0.0649\,nm^2$ is the cross-section of a nickel atom [172] and $\nu$ is a stoichiometry factor, which strongly depends on the regarded adsorbent-adsorbate interaction. The nickel dispersion, which describes the fraction of surface nickel atoms compared to the total amount of nickel atoms, can be calculated according to

$$D_{Ni} = \frac{N_m \cdot \nu \cdot M_{Ni}}{N_A \cdot w_{Ni}} \tag{3.12}$$

where $M_{Ni}$ is the molar mass of nickel and $w_{Ni}$ is the weight fraction of nickel. The average size of nickel crystallites is given by

$$d_{Ni} = \frac{w_{Ni} \cdot f}{S_{Ni} \cdot \rho_{Ni}} \tag{3.13}$$

where $f = 6$ is a shape factor for spherical particles and $\rho = 8.9\,\mathrm{kg/m^3}$ is the density of metallic nickel. Note, that using the latter suggests that all Ni atoms within the sample are present as $Ni^0$. In practice, this is only the case if nickel catalysts are subject to complete reduction under activation and/or reaction conditions.

Compared to $H_2$ adsorption, $CO_2$ adsorption is significantly more complex. According to several review articles [173, 174], $CO_2$ chemisorption species may adsorb in various stoichiometries, depending on surface structure. On nickel surfaces, linear ($\nu = 1$), bridged ($\nu = 2$) or multiple adsorption modes ($\nu \geq 3$) have been reported [115, 175]. If $CO_2$ does not dissociate upon adsorption, it is probably converted into a bent $CO_2^-$ surface species [174, 176]. The coordination of the $CO_2^-$ anion to the surface is however still not clear. Hence, a bent symmetry of the $C_{2v}$ or $C_S$ point group has been suggested [176], while the exact coordination, i.e. oxygen-nickel or carbon-nickel coordination, is also not yet clarified [174]. Due to the described complexity, there exists no general applicable stoichiometry factor for $CO_2$ adsorption. It is therefore not possible to apply equations (3.11)-(3.13). Nevertheless, different catalysts can be compared on the basis of their $CO_2$ adsorption capacity, calculated according to equation (3.10). The results are however not necessarily selective towards nickel. Instead, $CO_2$ adsorption on oxides, such as catalyst support materials, is a well-known phenomenon [177–180].

## 3.4 Thermogravimetric analysis and temperature programmed reduction

Thermogravimetric analysis (TGA) is a standard technique in scientific laboratories to investigate mass changes of samples caused by temperature. It provides a variety of information about physical and chemical phenomena, such as phase transitions, thermal decomposition or gas-solid reactions [181]. In this work, specific focus is laid on sample reduction in a $H_2$/Ar atmosphere, which was used to follow activation procedures of studied catalysts. As the employed TGA apparatus is connected to a mass spectrometer, it was also used for temperature programmed reduction (TPR) experiments. Combined TGA and TPR measurements were used to access the degree of reduction, the temperature of reduction and possible stages of the reduction process.

Typically, a thermogravimetric analyzer consists of a precision balance connected to a temperature stable sample holder, which is located inside a furnace. In general, the furnace temperature is raised at a constant rate to activate a temperature dependent reaction. The reaction may hereby occur under various atmospheres, such as air, inert gas, diluted $H_2$ or $O_2$ and others. In certain systems, gas phase analytics, e.g. a thermal conductivity detector or a mass spectrometer, are

connected to the exhaust line of the reaction chamber. Hence, the consumption of reactants and/or the formation of products can be followed simultaneously to mass changes. In the case of TPR, either the consumption of $H_2$ or the formation of $H_2O$ has to be followed.

In the practical application of TGA measurements, care needs to be taken because mass readings are not only influenced by weight changes of the sample but also by buoyancy effects. These are, for example, induced by the temperature dependence of the gas density within the reaction chamber. Hence, according to equation (3.14) (assumption $p = p_0$), gas densities, $\rho$, decrease with increasing temperature, $T$, as compared to the initial state $\rho_0$ at the starting temperature $T_0$. This means that buoyancy forces, $F_B$, which scale linearly with density ($F_B = \rho g V$), decrease with increasing temperature. As a result, the sample mass appears to increase with temperature.

$$\rho = \rho_0 \frac{T_0}{T} \tag{3.14}$$

In order to compensate buoyancy effects, a blank measurement (without a sample) has to be carried out at the same conditions than the actual measurement, i.e. same sample holder, same temperature program and same gas atmosphere. The resulting blank file needs to be subtracted from the actual measurement.

Like TGA experiments, TPR measurements need to be carried out carefully. This is due to the high sensitivity of the obtained TPR patterns towards experimental conditions. Monti and Baiker [182] have studied the reduction of NiO, depicted in equation (3.15), and identified the following relevant parameters: sample mass (i.e. the amount of reducible species), carrier flow rate, hydrogen concentration and heating rate.

$$NiO + H_2 \rightleftharpoons Ni + H_2O \tag{3.15}$$

In order to facilitate the selection of an appropriate set of operating variables, a characteristic number, $K$, was defined according to equation (3.16). Hereby, $n_0$ is the total amount of reducible species (in µmol), $V_{feed}$ is the total flow rate of the reducing gas (in $cm^3/s$) and $c_0$ is the $H_2$ concentration at the reactor inlet (in $\mu mol/cm^3$). For heating rates, $\beta$, between 0.1 and 0.3 K/s, it was recommended to keep $K$ values between 55 and 140 s.

$$K = \frac{n_0}{V_{feed} \cdot c_0} \tag{3.16}$$

Malet and Caballero [183] have defined a similar parameter, $P$, which also includes the heating rate. It was found, that increasing the ratio $\beta/c_0$ shifts the TPR curve towards higher temperatures, while the peak shape is not affected. Furthermore, $P$ values exceeding $P = 60$ K led to a severe distortion of the TPR curve. This phenomenon is due to mass transport limitations, which occur once the sample consumes a large fraction of the available $H_2$. Hence, as a rule of

thumb, the maximum $H_2$ uptake in a TPR experiment should always be kept below 2/3 of the hydrogen fed to the reactor [182, 183]. Malet and Caballero have further recommended to keep $P$ values in any case below 20 K [183].

$$P = \frac{\beta \cdot n_0}{V_{\text{feed}} \cdot c_0} \tag{3.17}$$

## 3.5 Infrared thermography

Infrared thermography is a very powerful tool for measuring temperatures contactless at high special and temporal resolution. The underlying measuring principle is thermal radiation, i.e. the emission of electromagnetic waves by objects due to temperature. This phenomenon is thoroughly described by Planck's law, which is depicted in equation (3.18) and plotted for selected temperatures in figure 3.4.

$$B_\lambda(\lambda, T) = \frac{2hc^2}{\lambda^5} \cdot \frac{1}{e^{\frac{hc}{\lambda k_B T}} - 1} \tag{3.18}$$

$T$ is the temperature, $h$ is Planck's constant, $c$ is the speed of light, $B$ is the spectral radiance, $k_B$ is Boltzmann's constant and $\lambda$ is the wavelength of the emitted radiation. In general, thermal radiation is polychromatic, i.e. the emitted light consists of a broad range of wavelengths. Planck's law applies to black bodies and describes their emitted thermal energy as a function of wavelength and temperature. As displayed in figure 3.4, the emitted radiation is in the infrared

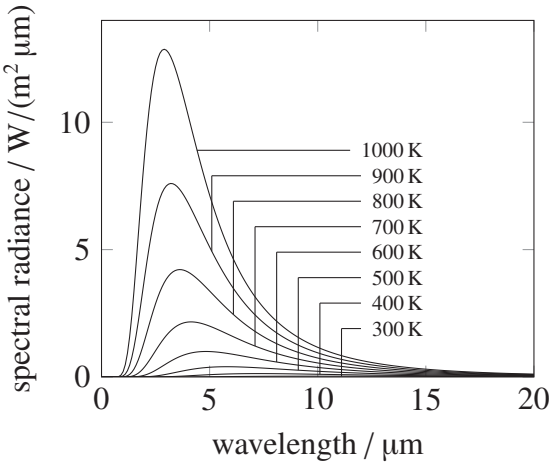


**Figure 3.4:** Planck's law plotted for selected temperatures. Curves were calculated according to equation (3.18).

(IR) and typically shows wavelengths between 0.2 and 20 µm. Hereby, each temperature displays a maximum intensity at a certain wavelength, $\lambda_{max}$, which is shifted towards lower values with increasing temperature. The curve comprising all wavelength maxima is determined by

zeroing the first derivative of (3.18) with respect to $\lambda$. The numerical solution of this problem leads to Wien's displacement law, which is depicted in equation (3.19).

$$\lambda_{max} = \frac{2897.8\,\mu m}{T} \tag{3.19}$$

The total energy radiated per unit surface area across all wavelengths is obtained by integrating Planck's law over $\lambda \in [0, \infty[$. The resulting correlation is the Stefan-Boltzmann law, which is depicted in equation (3.20). It shows that total energy of thermal radiation is proportional to the forth power of temperature.

$$P = \sigma \cdot A \cdot T^4 \tag{3.20}$$

$\sigma$ is the Stefan-Boltzmann constant and $A$ is the surface area of the black body. In practical applications, objects however rarely behave as black bodies, i.e. they do not absorb all incident radiation but only a fraction of it. These materials are often called 'grey bodies'. They are characterized by an emissivity, $\varepsilon < 1$. The Stefan-Boltzmann thus transforms to equation (3.21).

$$P = \varepsilon \cdot \sigma \cdot A \cdot T^4 \tag{3.21}$$

Thermographic cameras detect the emitted infrared radiation in a way similar to the way ordinary cameras detect visible light. Depending on radiation intensity and wavelength, conclusions about temperature are possible. However, for accurate readings, the emissivity of objects needs to be known or needs to be determined experimentally. The latter may be achieved for example by determining reference temperatures by means of a thermocouple. The emissivity value is then adjusted iteratively until the camera shows the same temperature than the reference device. Since emissivities are temperature dependent, a variety of measurements distributed over the desired temperature range is typically needed.

In practical analysis, environmental conditions must be chosen such that they do not interfere with the measurement. As thermography is a contactless technique, care has to be taken, that the emitted IR radiation does not interact with the atmosphere or materials located in the beam path. Under ambient conditions, hetero nuclear molecules from the surrounding air, e.g. water or carbon dioxide adsorb IR radiation. It is therefore advantageous to operate in so-called 'atmospheric windows' where the interaction between IR radiation and the atmosphere is minimized. Hence, conventional cameras operate in the range of 8 to 14 µm, where the transmission of the atmophere is ca. 90 %. In order to monitor non-ambient conditions by means of thermography, e.g. for catalytic reactions, additional materials such as reactor envelopes need to be introduced in the beam path. The applied material ideally has a high transmission value. However, common reactor materials such as quartz glass only permeate IR radiation between 0.8 and 2.5 µm. This effect is observed when filming persons wearing glasses with conventional infrared cameras.

Although glasses are transparent to visible light, they appear black in the infrared because the radiation emitted from the human body is completely adsorbed in the corresponding range of wavelengths (8 to 14 µm). More specialized materials such as sapphire glass exhibit broader transmission optima (sapphire glass: 0.15 to 5.0 µm) but also need to be operated at lower wavelengths as compared to conventional IR cameras. To resolve this problem, one often switches to near infrared cameras which operate in the range of 0.78 and 2.5 µm. The operation of near infrared cameras is however often restricted to elevated temperatures of at least 350 °C, since the maximum in radiation intensity is shifted to higher wavelength with decreasing temperature according to Wien's displacement law (equation (3.19)).

## 3.6 X-ray photoelectron spectroscopy

X-ray photoelectron spectroscopy (XPS) is typically performed under ultrahigh vacuum (UHV) conditions and provides information on the outermost surface of solids. The underlying measurement principle is the photoelectric effect, i.e. the emission of surface or near-surface electrons upon interaction with incident photons. A scheme of this process is presented in figure 3.5. The required energy to emit photoelectrons from a sample material is provided by an X-ray

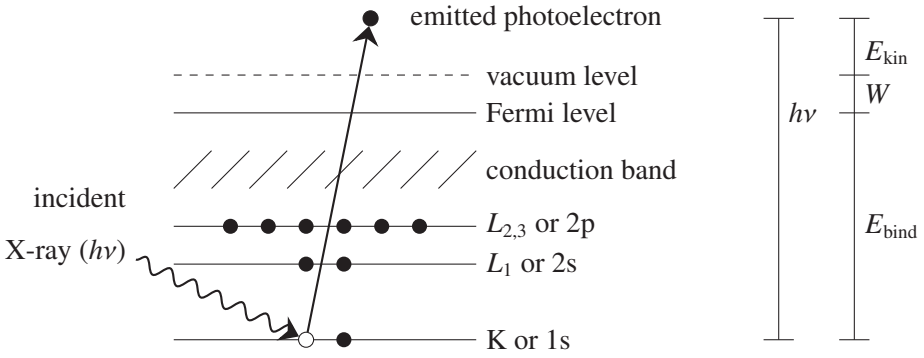


**Figure 3.5:** Emission of a photoelectron from the K shell of an atom induced by incidental X-rays. Filled circles indicate electrons, open circles indicate core holes in the final state (adapted from [184, 185]).

source, which emits photons of an energy $h\nu$ (Planck's constant $\times$ frequency of emitted light). For laboratory applications, one mostly uses Mg-K$_\alpha$ and Al-K$_\alpha$ radiation of $h\nu = 1253.6\,\text{eV}$ and $h\nu = 1486.6\,\text{eV}$. When working with synchrotron light, any photon energy $h\nu$, typically within the soft X-ray range (100-1000 eV), may be chosen. Soft X-ray photons impinging upon the sample travel some few micrometers into the solid before they are adsorbed. On their way, the photons interact with lattice atoms and transfer their energy to core level electrons, which are then emitted as photoelectrons. The energy difference of the atom before adsorption (initial state) and after emission (final state), is defined as the binding energy of the electron, $E_{\text{bind}}$.

The kinetic energy of the emitted photoelectron, $E_{kin}$, depends on $h\nu$ and $E_{bind}$ according to equation (3.22).

$$E_{bind} = h\nu - E_{kin} - W \tag{3.22}$$

$W$ is the work function of the spectrometer and describes the energy needed to move an electron from the Fermi to the vacuum level. The correlation described by equation (3.22) is also depicted in figure 3.5. In the displayed example, the indexing of the energy levels follows the notation of Bohr's shell model or the notation of the included atomic orbitals, where the photoelectron emission takes place from a K shell or 1s level. Of course electrons may be released from other core levels, such as $L_1$, $L_2$ and others, as long as the energy of the incident photon is sufficiently large. Next to signals from photoelectron core levels, a variety of other features, which can be tracked back to different physical or chemical effects, occur in an XPS spectrum. As these are of subordinate importance for the current thesis, the interested reader is referred to relevant standard literature on this subject [186, 187].

Qualitative XPS analysis allows definite conclusions about the chemical environment of surface elements. Therefore, binding energies of emitted photoelectrons are compared to reference materials listed in comprehensive data bases (NIST, [188]). The conversion of the measured variable, i.e. the kinetic energy of an emitted photoelectron, into a tabulated binding energy, is however not always straightforward. Often and especially in technical samples, common problems like sample charging or even differential charging are encountered, causing a systematic bias to the energy scale. In such cases, it is generally accepted to correct the energy scale on the basis of the known chemical environment of a surface atom and its emission of photoelectrons from a core level with known binding energy [189]. For example, this may be the adventitious carbon signal (C 1s, 284.5 eV [188]), which typically originates from photoemission of surface contaminations, or a known oxide component such as O 1s in $\gamma$-$Al_2O_3$ (530.9 eV [188]). If no intrinsic reference compound is available, it was found advantageous to add one. This may for example be a thin film of gold (84.0 eV, Au $4f_{7/2}$ [188]) evaporated *in vacuo* on top of the sample.

Measuring the amount of photoelectrons at a given kinetic energy allows to draw conclusions about surface composition. The complexity associated with a quantitative approach can however be significantly higher as compared to a qualitative analysis. This is mainly due to a more complex correlation between the measured variable, i.e. the signal intensity of a certain core level of species A, $I_A$, and the target value, i.e. the number of surface atoms of A, $N_A$, as $I_A$ does not only depend on several sample-specific but also on several device-specific parameters. In the case of a homogeneous sample, equation (3.23) can be applied for quantification.

$$I_A = \sigma_A(h\nu) \cdot D(E_A) \cdot L_A(\gamma) \cdot J_0 \cdot T(E_A) \cdot N_A \cdot \lambda_M(E_A) \tag{3.23}$$

$\sigma_A(h\nu)$ is the ionization cross section of the acquired core level, $D(E_A)$ is the detection efficiency of the electron detector, $L_A(\gamma)$ is the angular asymmetry of the emitted intensity with respect to the angle $\gamma$ between incident photons and ejected and detected photoelectrons, $J_0$ is the photon flux of the X-rays impinging upon the sample, $T(E_A)$ is the transfer function of the electron analyzer, $N_A$ is the number of surface atoms of A and $\lambda_M(E_A)$ is the so-called attenuation length of photoelectrons with kinetic energy $E_A$ in the sample matrix M.

As indicated by the definition of $\lambda_M(E_A)$, the surface sensitivity of an XPS measurement does not rely on the attenuation of the incident photons (several µm) but rather on the escape probability of the emitted photoelectrons from the solid, which rapidly drops to zero when reaching a depths of a few nm. The drastic limitation of the traveling distance of electrons through a solid is caused by elastic and inelastic scattering events of electrons with lattice atoms. As elastic scattering is often insignificant and difficult to describe, $\lambda_M(E_A)$ is in many cases assumed as the inelastic mean free path (IMFP). The kinetic energy of the traveling electron is hereby in first approximation accounted for by the empirically derived 'universal curve' by Seah and Dench [190]. A mathematical expression of the curve is depicted in equation (3.24).

$$\lambda_M(E_A) = \frac{143}{E_A^2} + 0.054 \cdot \sqrt{E_A} \tag{3.24}$$

The intensity of photoelectrons which are capable of leaving the solid, $I_A$, exponentially decays with the distance $z$ from the sample surface mainly due to inelastic electron scattering. Hence, only the intensity originating from the outermost surface atom layer, $I_A^0$, is not affected by attenuation effects. For homogeneous materials, equation (3.25) can be derived.

$$I_A(z) = I_A^0 \cdot e^{-z/\lambda_M(E_A)} \tag{3.25}$$

Obviously, the measured intensity consists of all photoelectrons emitted at any depth inside the bulk of the sample multiplied by the electron escape probability. Hence, equation (3.25) needs to be integrated over $z \in [0, \infty[$. The resulting dependence on $\lambda_M(E_A)$ is consistent with equation (3.23).

$$I_A(z) = I_A^0 \cdot \int_0^\infty e^{-z/\lambda_M(E_A)}\, dz = I_A^0 \cdot \lambda_M(E_A) \tag{3.26}$$

It is interesting to note, that in homogeneous materials, equation (3.26) also applies for other sample elements, because all compounds are randomly distributed in the same matrix. The situation becomes more complicated, however, if the elements are inhomogeneously distributed in a sample such as in layered materials.

One example for an inhomogeneous material is a thin film of material A on a substrate B. Now, the absolute intensity of A depends on the finite film thickness, $d$. Thus, the integral over $z \in [0, d[$ results in

$$I_A(z) = I_A^0 \cdot \int_0^d e^{-z/\lambda_A}\, dz = I_A^0 \cdot \lambda_A \cdot (1 - e^{-d/\lambda_A}) \tag{3.27}$$

where $\lambda_A$ is the electron attenuation length within the thin film. For simplicity, the dependence of $\lambda_A$ on kinetic energy is not depicted in equation (3.27). In contrast to equation (3.26), the finiteness of the thin film has to be accounted for and eventually results in a non-linear dependency of absolute intensity on $\lambda_A$. If the absolute intensity of B is considered, a different function is obtained:

$$I_B(z) = I_B^0 \cdot e^{-d/\lambda_A} \cdot \int_0^\infty e^{-z/\lambda_B}\, dz = I_B^0 \cdot e^{-d/\lambda_A} \cdot \lambda_B \tag{3.28}$$

$\lambda_B$ is approximately the IMFP at the kinetic energy of photoelectron B. The example of a thin film shows that for inhomogeneous samples, the correlation between absolute signal intensities and IMFPs cannot be described in a straightforward manner. Instead, the geometrical arrangement of relevant surface elements needs to be known *a priori* and the integral over $z$ needs to be resolved for each element separately. As a result, additional effort has to be raised (a) to clarify the surface geometry of a sample prior to quantitative XPS analysis and (b) to derive the correct dependence of signal intensity on IMFP (in the following referred to as $f(\lambda_i)$). Both (a) and (b) can be complicated, especially with regards to technical samples. As an example, supported catalysts shall be briefly considered. In the most basic case, those systems consist of a support material and a supported phase on top, which may be present in every conceivable form: layers, spheres, hemispheres and others. Although general dependencies of those geometries have been derived [191], additional characterization effort is required, e.g. when determining coverages of surface areas, until a reliable quantitative model of a supported catalyst is derived. The situation becomes even more complicated if ternary or quaternary phases like promoters, poisoning compounds or carbon depositions are present or if the catalyst undergoes structural changes during operation.

Apart from the complexity associated with signal attenuation lengths, there is an additional problem when applying equation (3.23) in practice. Due to the instrument-related parameters, most of which are not known entirely, absolute values of $I_A$ are only reproducible if the experimental conditions, i.e. the photon flux, the detection efficiency and the sample position with respect to the instrument are precisely controlled. This actually means that neither the instrument itself nor parts of the instrument nor the exact operation conditions are allowed to be changed over time. In practice, however, even a simple standard procedure, for example a sample change, may lead to different operation conditions. This is especially true if it involves one of the following actions:

(a) switching off or changing the operation conditions of the X-ray source

(b) switching off or changing the operation conditions of the electron multiplier

(c) changing the sample area viewed by the detector

If (a)-(c) is avoided and care is taken XPS instruments may as well be operated under the exact same conditions for elongated time periods. In many cases however, the attached ultra-high vacuum (UHV) chamber also serves other (analytical) purposes (e.g. sample sputtering) which may prohibit the simultaneous operation of XPS related devices. In those cases, steps (a)-(c) are necessary precautions to protect the XPS equipment. In addition to likely variations on a daily or weekly basis, the intensity scale inevitably changes over longer time periods, which is due to equipment aging, maintenance and the replacement of individual components [192]. Finally, equation (3.23) is also completely inconvenient, if measurements from different instruments need to be compared.

It has therefore proven practical to use a relative measure of intensity, which is composed of a ratio of two photelectron core levels (A and B) of the same sample. Thus, the varying instrument parameters, i.e. photon flux and the detector efficiency, cancel each other out. For homogeneous samples, equation (3.29) is obtained.

$$\frac{I_\mathrm{A}}{I_\mathrm{B}} = \frac{\sigma_\mathrm{A}(h\nu)}{\sigma_\mathrm{B}(h\nu)} \cdot \frac{L_\mathrm{A}(\gamma)}{L_\mathrm{B}(\gamma)} \cdot \frac{T(E_\mathrm{A})}{T(E_\mathrm{B})} \cdot \frac{N_\mathrm{A}}{N_\mathrm{B}} \cdot \frac{\lambda_\mathrm{M}(E_\mathrm{A})}{\lambda_\mathrm{M}(E_\mathrm{B})} \tag{3.29}$$

At this point, general applicability is granted, because the remaining terms are intrinsic functions of the instrument, the sample or the acquired core level. Reliable results for $N_\mathrm{A}/N_\mathrm{B}$ ratios of reference compounds have been obtained by using ionization cross sections tabulated by Scofield [193] or Yeh and Lindau [194], angular asymmetries considered according to Reilman [195] and IMFPs which either are tabulated (NIST) or calculated according to the TPP-2M model of Tanuma, Powell and Penn [196]. The dependence of the electron analyzer transfer function on photoelectron energy is either provided by the supplier or separately measured for the respective instrument.

Based on equation (3.29), Wagner et al. [197] has established so-called sensitivity factors, $S_\mathrm{i}$, which summarize instrument and sample parameters for constant instrument, sample and core level parameters, according to equation (3.30).

$$S_\mathrm{i} = \sigma_i(h\nu) \cdot L_\mathrm{i}(\gamma) \cdot T(E_\mathrm{i}) \cdot \lambda_\mathrm{M}(E_\mathrm{i}) \tag{3.30}$$

Sensitivity factors are tabulated relative to the 1s signal in elemental Fluor ($I_{\mathrm{F\ 1s}} = 1.0$, measured on the same instrument) for a broad range of reference materials [198] and have allowed a straightforward comparison between results obtained from different instruments. Eventually,

sensitivity factors have contributed to establish definite clarity, which parameters need to be taken into consideration for the general formalism for quantitative XPS analysis (equation (3.23)).

Although equation (3.29) is of great importance in XPS analysis, there is also a drawback, in particular for inhomogeneous samples. As was shown in equations (3.27) and (3.28), the dependency of intensity on $\lambda_i$ strongly depends on the considered system and is also different for each element $i$. Thus, the relative intensity of two elements (A and B) is described by

$$\frac{I_\mathrm{A}}{I_\mathrm{B}} = \frac{\sigma_\mathrm{A}(h\nu)}{\sigma_\mathrm{B}(h\nu)} \cdot \frac{L_\mathrm{A}(\gamma)}{L_\mathrm{B}(\gamma)} \cdot \frac{T(E_\mathrm{A})}{T(E_\mathrm{B})} \cdot \frac{N_\mathrm{A}}{N_\mathrm{B}} \cdot \frac{f(\lambda_\mathrm{A})}{f(\lambda_\mathrm{B})} \tag{3.31}$$

where $f(\lambda_\mathrm{A})$ and $f(\lambda_\mathrm{A})$ are two unknown functions, which do not cancel each other out. In comparison with equation (3.23), an additional unknown function occurs, which makes it difficult to solve equation (3.31). The severe drawbacks of equation (3.23) still prevail of course. A solution to this problem is the usage of an internal standard, which is presented in detail in chapter 8 of this thesis.

## 3.7 Light Scattering

Light scattering is a well-established technique to measure particle size distributions of powder samples. The measuring principle is based on the interaction of electromagnetic waves (i.e. light) with spherical particles. Hereby, dipoles are created within the particle, which in turn send out electromagnetic waves, the so-called scattered light. A thorough theoretical description of this process has been provided by Gustav Mie at the beginning of the 20$^{\mathrm{th}}$ century [199]. He deduced the following correlation for the intensity of the scattered light

$$I = I_0 \cdot \frac{F(\Theta, \Phi)}{k^2 r^2}, \tag{3.32}$$

where $I_0$ is the intensity of the incident light, $r$ is the radial direction of propagation of the scattered spherical wave, $k$ is the wavenumber and $F(\Theta, \Phi)$ is a function of the scattering angle, $\Theta$, and the polarization of the incident light, $\Phi$. $F(\Theta, \Phi)$ is however not easily resolved, as it comprises primarily spherical Bessel functions and Legendre polynomials. In praxis, equation (3.32) only strictly applies to particle sizes which are of the size of the wavelength of the incident light. This range of particle diameters is called the 'Mie range' and is limited to $\lambda/10 < d < \lambda$, where $\lambda$ is the wavelength and $d$ is the particle diameter. Smaller particle diameters ($d \leq \lambda/10$) are located in the so-called 'Rayleigh range', which is characterized by a constant phase of the

incident light throughout the entire particle. Since in the Rayleigh range, no interference of light occurs within the particle, the following simplified correlation applies

$$I = I_0 \frac{\lambda^2}{4\pi^2} \left( \frac{\pi d}{\lambda} \right)^6 \left| \frac{m^2 - 1}{m^2 + 2} \right|^2 (1 + \cos^2\theta), \tag{3.33}$$

where $m$ is the relative refraction index between the spherical particle and its surrounding. Particle diameters which are 40 times larger than the incident wavelength ($d \geq 40\lambda$) are located in the 'Fraunhofer range' [200]. In this range, equation (3.34) may be applied.

$$I = I_0 \frac{\sin^2 \left( \frac{\pi d}{\lambda} \sin\Theta \right)}{\left( \frac{\pi d}{\lambda} \sin\Theta \right)^2} \tag{3.34}$$

Note that the presented equations (3.32) to (3.34) apply for light scattering on a single particle. In a real sample, which comprises a collective of particles, the resulting scattering pattern is a superposition of the single particle contributions.

Today, light scattering experiments are primarily conducted with lasers as a monochromatic light source. The scattered light is focused on detectors by means of Fourier lenses. The resulting intensity distribution is (at small scattering angles) concentric to the incident beam. The location of spatial intensity maxima is determined by particle size. The absolute intensity of the scattered light depends on the amount of particles which contribute to the scattering pattern. Hence, the distribution of intensity is characteristic for the particle size distribution of the sample.

In practice, the presented 'classical' approach towards light scattering, suffers from a severe drawback. This is due to the angle dependence of scattering intensity. For large particles, small scattering angles and high scattering intensities are observed. For small particles, however, the scattering angle significantly increases, leading to a rapid decrease in scattering intensity. This effect is most significant for particles which are smaller than the wavelength of the incident light. One possible solution to this problem is the so-called Polarization Intensity Differential Scattering (PIDS) technique [201]. As was shown in equation (3.32), the intensity of scattered light depends on the polarization of the incident light beam. This dependence is much stronger for small particles than for large particles and allows measuring small particle sizes at an improved resolution. It has been demonstrated, that the scattering intensities obtained from a combination of horizontally and vertically polarized incident light show significant differences for particle sizes between 0.1 and 0.4 µm [202]. The PIDS technique therefore uses the so-called PIDS signal, *PIDS*, which is calculated according to

$$PIDS = I_\mathrm{v} - I_\mathrm{h}, \tag{3.35}$$

where $I_v$ and $I_h$ are the scattered intensities obtained for vertically and horizontally polarized incident light. In order to increase the reliability of the measured values, the scattering experiment is typically repeated at three different wavelengths (450, 600 and 900 nm) [202].

# 4 Co-precipitated Ni-Al catalysts

Part of this chapter is published in:

M. Wolf, C. Schüler, O. Hinrichsen, Sulfur poisoning of co-precipitated Ni-Al catalysts for the methanation of $CO_2$, *Journal of $CO_2$ Utilization* **2019**, *32*, 80-91. [34]

S. Ewald, M. Kolbeck, T. Kratky, M. Wolf, O. Hinrichsen, On the deactivation of Ni-Al catalysts in $CO_2$ methanation, *Applied Catalysis A: General* **2019**, *570*, 376-386. [30]

## 4.1 Introduction

Co-precipitated nickel-alumina catalysts, which are abbreviated Ni-Al catalysts, have recently gained considerable attention as a catalyst material for the $CO_2$ methanation [37, 68, 69, 72]. This is due to their superior activity as compared to impregnated $Ni/Al_2O_3$ systems [69] and their high stability under reaction conditions [37, 68]. General material properties are: high Ni loadings (30-70 wt%), low nickel crystallite sizes (2-15 nm) and negligible Ni particle sintering [37, 68]. Apart from material studies, researchers have developed a micro kinetic model [23], monitored catalytic properties under fluctuating reaction conditions [203] and investigated the beneficial effects of Mn and Fe promoters [25, 26]. Despite the available literature, it is indispensable to characterize the specific Ni-Al catalysts used for this study, as synthesis conditions were found to have a marked effect on material properties [24]. Apart from thoroughly characterizing the synthesized samples by standard techniques such as XRD, $N_2$ physisorption, $H_2$ and $CO_2$ chemisorption, TPR and elemental analysis, advanced spectroscopic characterization of the sample surface was provided by means of XPS.

## 4.2 Experimental

Only deionized water purified in a filter unit (Millipore) was used for the synthesis steps. All chemicals were of analytical grade and used as received. Gases were supplied by Westfalen AG and were of 5.0 purity.

### 4.2.1 Synthesis

Ni-Al catalysts were synthesized by co-precipitation of 1 M solutions of $Ni(NO_3)_2 \cdot 6H_2O$ (Merck) and $Al(NO_3)_3 \cdot 9H_2O$ (Merck). Hereby, an equimolar mixture of 1 M NaOH (Merck) and 1 M $Na_2CO_3$ (Sigma) was used as precipitation agent. In a typical synthesis, 1 l of water was maintained at 30 °C and pH 9±0.1 in a double-walled glass reactor containing two glass baffles. The liquid was thoroughly mixed by a KPG stirrer at 150 rpm. 180 ml of total nitrate solution, containing a varying $Ni^{2+}/Al^{3+}$ molar ratio (0/1, 1/5, 1/3, 1/2, 1/1, 3/1, 5/1 and 1/0), were added at a rate of 2.4 ml/min using a peristaltic pump. The pH was kept constant using a TitroLine alpha plus titrator (SI Analytics), loaded with the precipitation agent. The product slurry was aged for about 18 h at constant pH and temperature. After aging, the product was vacuum filtered and washed several times with water until the pH of the filtrate remained constant. The filter cake was then dried at 80 °C for 18 h and calcined in synthetic air at 450 °C for 5 h subsequent to heating at a linear rate of 5 K/min.

Co-precipitated Ni-Al catalysts are abbreviated with reference to their Ni/Al molar ratio, i.e. NiAl15, NiAl13, NiAl11, NiAl31 and NiAl51. The products obtained after co-precipitation and calcination are referred to as '(dried) precipitate' and 'calcined (catalyst) precursor'. The calcined reference samples with $Ni^{2+}/Al^{3+}$ molar ratios of 1/0, 1/2 and 0/1 are named according to their crystal structures, as observed by XRD [30, 34]: NiO, $NiAl_2O_4$ and $\gamma$-$Al_2O_3$.

### 4.2.2 Characterization

The elemental composition (Na, Al and Ni) was determined by ICP-OES (Agilent Technologies, Model 725). In a typical experiment, 50 ml of 1 M $H_3PO_4$ (Alfa Aesar) were added to 25 to 50 mg of catalyst and sonicated at elevated temperatures for several hours. After the solution was cooled down to room temperature, it was filtered and diluted with water by a factor of 10. Metal standards of 1, 10 and 50 mg/l were prepared from a 1000 mg/l ICP multi-element standard (IV, Merck). Wavelengths used for data evaluation were 568.263 nm (Na), 230.299 nm (Ni) and 396.152 nm (Al). Metal superposition and matrix effects were excluded.

The crystal structure of co-precipitated, calcined and activated samples was analyzed by X-ray diffraction (XRD) using a PANanalytical Empyrean diffractometer operated with Cu-$K_\alpha$ radiation ($\lambda$ = 1.540 56 Å) at 45 kV and 40 mA. Diffractograms were obtained by scanning the range between $2\theta = 5-90°$. Co-precipitated, calcined and poisoned samples were pressed on a Si wafer and measured at an angular velocity of 1.432 38°/min and a stepsize of 0.005 65°. Activated samples were sealed in glass capillaries (Ø 0.5 mm) and measured at an angular velocity of 0.401 94°/min and a stepsize of 0.013 13°. For the sake of comparison, reference diffractograms indexed by the Joint Committee on Powder Diffraction Standard (JCPDS) were used. Interplanar distances were determined by applying Bragg's law, Ni crystallite sizes, $d_{Ni}$, were determined from line broadening of the Ni (200) reflection according to the Scherrer equation.

Temperature programmed reduction (TPR) was conducted on a Netsch STA 409 thermobalance, connected to an Omnistar GSD 301 quadrupole mass spectrometer (Pfeiffer Vacuum). Prior to analysis, samples were dried for 1 h in a stream of 60 sccm Ar at 300 °C. After cooling down to room temperature, a mixture of 10 % $H_2$/Ar was introduced and the temperature was linearly raised to 900 °C at a heating rate of 3 K/min. In order to guarantee a low enough $H_2$ consumption during TPR, catalyst masses were chosen to obtain constant $P$ values of about 2 K [183]. TPR profiles were tracked via the $H_2O$ signal, which was corrected by the amount of desorbed $H_2O$ per square meter BET surface area.

Static chemisorption of $H_2$ and $CO_2$ was carried out on an Autosorb 1C (Quantachrome) at 35 °C. Hereby, sorption equilibration times of 2 and 10 min were chosen for $H_2$ and $CO_2$, respectively. Calcined precursors were activated for 4 h in 10 % $H_2$/Ar (heating rate of 5 K/min). Aged samples were kept under methanation conditions ($H_2/CO_2$/Ar = 4/1/5, 1bar, 400°C) for 24 h and transferred to the chemisorption instrument under Ar atmosphere, reactivated in 5 % $H_2/N_2$ at 450 °C for 30 min (heating rate of 2 K/min), evacuated and held for 2 h. Chemisorption of $CO_2$ on activated and aged samples was carried out consecutive to $H_2$. In between, samples were heated under vacuum to 300 °C at a heating rate of 2 K/min and held for 2 h.

BET surface areas, $S_{BET}$, of calcined precursors were determined by $N_2$ physisorption on a Nova 4000e surface area analyzer (Quantachrome). Prior to analysis, samples were heated to 120 °C in vacuum and held for 3 h. Isotherms were evaluated in the $p/p_0$ range between 0.05 and 0.3 of the adsorption branch. Repeated measurements for all sorption techniques were found to scatter within the error range of the instruments (±4 %, data provided by Quantachrome).

XPS studies of the calcined catalysts were conducted with a Leybold-Heraeus LHS 10 spectrometer using a non-monochromatized Al-$K_\alpha$ source (1486.7 eV). The powder samples were pressed into cavities and measured as pellets. In order to remove adsorbates and impurities originating from handling in air, all samples were degassed in vacuum at 400 °C for 2 h before

the XPS measurements. In addition, NiO was annealed at 1000 °C for 30 min in $O_2$ at a pressure of $1 \cdot 10^{-6}$mbar following a literature-known preparation technique [204]. The analyzer was operated at a constant pass energy of 100 eV, leading to an energy resolution with a full width at half-maximum (FWHM) of about 1.1 eV. The energy scale of the spectra was corrected for sample charging by using the O 1s signal (531 eV, $Al_2O_3$). All spectra were recorded in an ultra-high vacuum (UHV) chamber at a pressure below $5 \cdot 10^{-8}$mbar. Core level spectra were fitted by using Voigt functions and linear background subtraction. The Ni 3s/Al 2s region was deconvoluted using five components. For Ni 3s, two components account for the main peak as well as a known satellite [205]. Al 2s signals generated by Al-$K_{\alpha 3}$ (1486.5 eV) and Al-$K_{\alpha 4}$ (1486.5 eV) radiation overlap with the Ni 3s main peak and were, hence, considered in two further components [188]. The parameters for each secondary component (FWHM, relative intensities and differences in binding energies with respect to the main peak) were obtained from reference samples measured under the same conditions. The calculated Ni/Al atomic ratio obtained from the peak areas of Ni 3s and Al 2s were verified by using the peak areas of Ni 2p and Al 2s. The difference in escape depths of the Ni 2p and Al 2s photoelectrons was accounted for by a factor of 1.8 determined with the TPP-2M model [196].

## 4.3 Results and discussion

### 4.3.1 Elemental analysis

ICP-OES results obtained from the calcined precursors are listed in table 4.1. The investigated samples show the expected trends of increasing Ni and decreasing Al content from NiAl15 to NiAl51. The measured Ni/Al molar ratios are consistently close to the nominal values, with a maximum deviation of 14 % for NiAl13. No $Ni^{2+}$ ions were found in the $\gamma$-$Al_2O_3$ reference sample and vice versa. The Na content was below the detection limit for all samples (< 10 ppm).

**Table 4.1:** Elemental composition of the calcined precursors, determined by ICP-OES.

| | $\gamma$-$Al_2O_3$ | NiAl15 | NiAl13 | NiAl11 | NiAl31 | NiAl51 | NiO |
|---|---|---|---|---|---|---|---|
| $w_{Ni}$ (wt%) | 0.0 | 15.3 | 21.5 | 35.2 | 57.0 | 66.3 | 81.2 |
| $w_{Al}$ (wt%) | 44.3 | 34.4 | 27.9 | 16.2 | 8.4 | 5.8 | 0.0 |
| $n_{Ni}/n_{Al}$ (-) | 0.00 | 0.20 | 0.35 | 1.00 | 3.11 | 5.30 | n.d.[a] |

[a] Not determined.

### 4.3.2 XRD analysis

XRD patterns obtained for the dried precipitates, calcined precursors and activated catalysts are shown in figures 4.1, 4.2 and 4.3. Calculated lattice constants and crystallite sizes are given in table 4.2.

The NiAl31 precipitate, depicted in figure 4.1, shows characteristic reflections at 11.3°, 22.8°, 34.9°, 39.1°, 46.5°, 60.8° and 62.0°. Similar reflections were also found for the mineral takovite, having the stoichiometric formula $Ni_6Al_2(OH)_{16}CO_3 \cdot 4H_2O$ (JCPDS 15-0087). The takovite reflections represent basal (003), (006) and non-basal (012), (015), (018), (110), (113) planes, respectively. The takovite lattice features a double layer structure, composed of positively charged brucite-like hydroxide layers $[Ni^{2+}_{0.75}Al^{3+}_{0.25}(OH)_2]^{0.25+}$ and anionic interlayers, hosting $CO_3^{2-}$ and water [206]. The double layer can be indexed by a hexagonal unit cell with rhombohedral symmetry and R-3m space group. Thus, the distances between neighbouring OH groups within the brucite-like layer and OH groups of adjacent layers are given by the lattice parameters $a_{prec}$ and $c_{prec}$, which have been specified as 3.03 and 22.60 Å (JCPDS 15-0087). It was found that co-precipitation of Ni and Al nitrates with $Na_2CO_3$ is one way to obtain a synthetic material structured like the takovite mineral [207]. Since our synthesis is based on such a co-precipitation route and the Ni/Al molar ratio of the NiAl31 sample is almost identical as in the mineral, the NiAl31 sample is ascribed to a synthetic takovite, closely resembling its structure and stoichiometry. The structural and stoichiometric proximity arises from almost identical lattice parameters, as indicated in table 4.2, and an actual Ni/Al molar ratio of 3.11, as determined by ICP-OES (table 4.1).

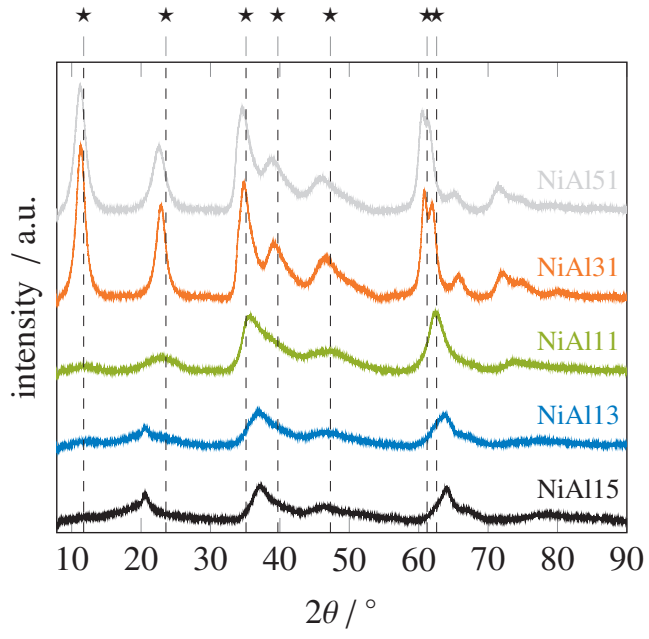


**Figure 4.1:** XRD patterns of dried precipitates and a takovite reference (⋆) (JCPDS 15-0087).

At first sight, the XRD pattern of the NiAl51 precipitate is very similar to the one of NiAl31, although the Ni/Al stoichiometry is markedly higher. A more careful look at the diffractogram reveals a slightly lower overall intensity and a weak shift of the entire pattern towards lower diffraction angles. Nevertheless, all characteristic takovite planes are visible and neither line broadening, nor asymmetric line shapes are observed. In addition, there is no evidence of a segregated $Ni(OH)_2$ phase. The NiAl51 sample therefore probably consists of a takovite-like structure with increased Ni/Al stoichiometry. The additional $Ni^{2+}$ cations seem to be incorporated into the brucite-like layer at the expense of $Al^{3+}$. This would justify the observed increase of the unit cell in $a_{prec}$ and $c_{prec}$ direction (table 4.2), as the ionic radius of $Ni^{2+}$ is larger than $Al^{3+}$ (0.69 vs 0.53 Å) [208]. Some uncertainty remains however, whether or not additional low crystalline or amorphous phases, especially $Ni(OH)_2$, co-exist with the takovite-type material. The XRD patterns of NiAl11, NiAl13 and NiAl15 precipitates differ from the

**Table 4.2:** Calculated lattice constants and Ni crystallite sizes in Å.

| | reference | NiAl51 | NiAl31 | NiAl11 | NiAl13 | NiAl15 |
|---|---|---|---|---|---|---|
| $a_{prec}$[a] | 3.03 | 3.06 | 3.04 | 2.97 | 2.93 | 2.91 |
| $c_{prec}$[b] | 22.60 | 23.08 | 22.60 | 23.95 | 17.10 | 18.02 |
| $a_{calc}$[c] | 4.18 | 4.17 | 4.17 | 4.12 | 4.03 | 3.99 |
| $a_{act}$[d] | 3.94 | 4.12 | 4.13 | 4.11 | 4.03 | 3.99 |
| $d_{Ni}$[d] | n.d.[e] | 47.88 | 34.81 | 29.90 | n.d.[e] | n.d.[e] |

[a] Dried precipitate, (110) plane, reference: JCPDS 15-0087.
[b] Dried precipitate, (012) plane, reference: JCPDS 15-0087.
[c] Calcined precursor, (220) plane, reference: JCPDS 78-0429.
[d] Activated catalyst, (440) plane, reference: JCPDS 10-0425.
[e] Not determined.

ideal takovite pattern. This especially concerns the decreased intensity, which continues with declining Ni/Al molar ratio. Hereby, reflections of the basal planes decrease more dramatically than non-basal ones. For example, the (003) and (006) planes are barely visible in case of the NiAl11 sample and completely disappear for NiAl13 and NiAl15. Conversely, the (012) and (110) lines are observed for all samples but decrease in intensity. They also turn increasingly asymmetric, which is ascribed to signal broadening and merging of the (012)/(015)/(018) and (110)/(113) reflections. A careful examination of the (012) and (110) lines shows a gradual shift towards higher diffraction angles, i.e. lower plane distances. As can be seen in table 4.2, $a_{prec}$ and $c_{prec}$ decrease from 3.04 and 22.93 Å for NiAl31 to 2.89 and 17.90 Å for NiAl15, suggesting the substitution of $Ni^{2+}$ by smaller $Al^{3+}$ ions. However, it has to be noted that the NiAl13 and NiAl15 samples are composed by at least two crystalline phases, as an additional reflections occurs at 20.7°. Based on the high $Al^{3+}$ content, a segregated $Al^{3+}$ phase would be expected. Though, neither the diffractograms of Boehmite (JCPDS 21-1307), Gibbsite (JCPDS 33-0018) nor Bayerite (JCPDS 20-0011) show a conclusive match.

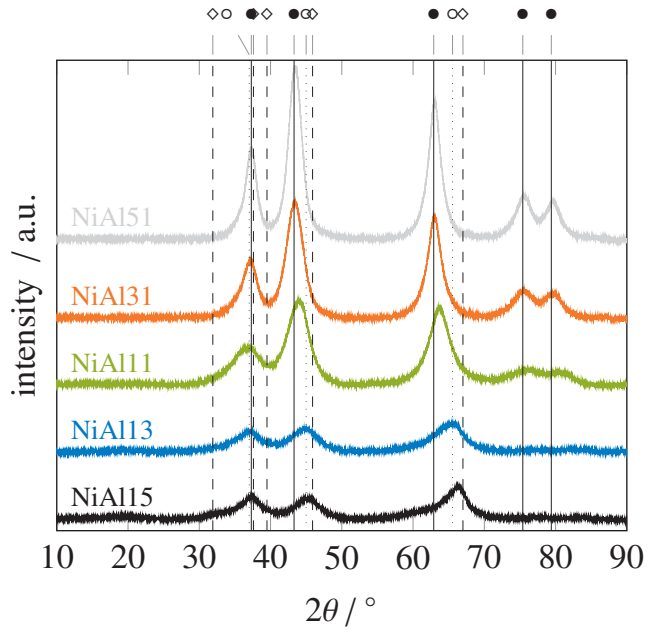


**Figure 4.2:** XRD patterns of the calcined precursors. Reference patterns are for NiO (●), $\gamma$-$Al_2O_3$ (○) and $NiAl_2O_4$ (◇) (JCPDS 78-0429, 10-0425, 10-0339).

The diffraction patterns of the calcined NiAl51 and NiAl31 catalyst precursors, depicted in figure 4.2, show characteristic reflections of a bunsenite structure (JCPDS 78-0429), which crystallizes in fcc conformation and Fm-3m symmetry. With increasing $Al^{3+}$ content, the intensity decreases and the reflections at 43.3° and 62.9° are steadily shifted to higher diffraction angles. The calculated lattice constant, $a_{calc}$, which decreases from 4.13 to 3.98 Å as shown in table 4.2 confirms this trend. The new signal positions are located between NiO and $NiAl_2O_4$ spinel (JCPDS 10-0339) for NiAl11 and between $\gamma$-$Al_2O_3$ (JCPDS 10-0425) and $NiAl_2O_4$ spinel for NiAl13 and NiAl15. According to the continously variable phase model of Puxley et al. [207], these gradual changes and the absence of additional crystalline phases, indicate a continuous change in crystal structure. Hereby, small amounts of $Al^{3+}$ ions possibly substitute octahedrally coordinated $Ni^{2+}$, resulting in a small amount of cation vacancies and a so-called 'substitute nickel oxide'. Larger amounts of $Al^{3+}$ cause an additional occupation of tetrahedral sites, resulting in a low ordered spinel structure ('disordered oxide-spinel intermediate'). As $Al^{3+}$ further increases, more tetrahedral positions are filled and the stoichiometry approaches a $NiAl_2O_4$ spinel. The corresponding structure may be called a 'spinel-like material'. Further replacement of $Ni^{2+}$ leads to an expansion of $Al^{3+}$ in octahedral sites and an increased number of vacancies. This structure then resembles $\gamma$-$Al_2O_3$. Puxley et al. [207] also argue, that a gradual enrichment of $Al^{3+}$ within a poorly ordered bunsenite- or spinel-like structure is more likely than the formation of a solid solution, as a calcination temperature as low as 450 °C does not provide enough energy for a re-arrangement of numerous cations.

The continuous signal shifts in our samples and the absence of crystalline $NiAl_2O_4$ and $\gamma$-$Al_2O_3$ phases suggest a homogeneous mixed oxide over a wide range of Ni/Al molar ratios. In

the following, the mixed oxide phase of varying composition is referred to as $NiAlO_x$. Besides $NiAlO_x$, additional low crystalline or amorphous phases may exist, resulting for example from a segregation process of excess $Ni^{2+}$ or $Al^{3+}$ ions in the form of NiO (especially NiAl51 and NiAl31), $NiAl_2O_4$ or $\gamma$-$Al_2O_3$ (especially NiAl13 and NiAl15).

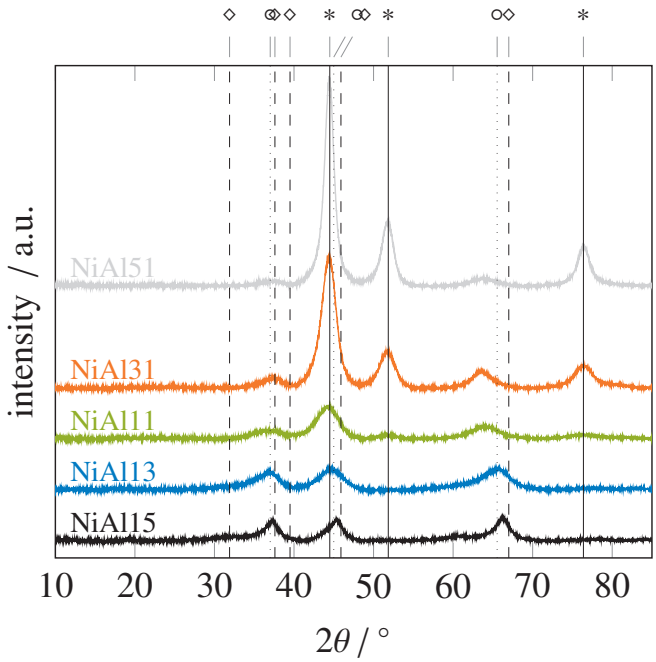


**Figure 4.3:** XRD patterns of activated catalysts. Reference patterns are for $Ni^0$ (∗), $\gamma$-$Al_2O_3$ (○) and $NiAl_2O_4$ (◇) (JCPDS 87-0712, 10-0425, 10-0339).

The diffraction patterns of activated NiAl51 and NiAl31, as depicted in figure 4.3, are similar to the calcined precursors but show a decreased intensity for the bunsenite reflections at 37.2°, 62.9°, 75.4° and 79.4°. Instead, the most intense reflections, located at 44.5°, 51.8° and 76.4°, show the characteristic pattern of metallic nickel $Ni^0$ (JCPDS 87-0712), which crystallizes in fcc conformation and Fm-3m symmetry. Also, the reflection of the mixed oxide phase at 62.9° is shifted to higher diffraction angles, i.e. higher $Al^{3+}$ contents, indicating the depletion of $Ni^{2+}$ from the mixed oxide. This is also reflected in the decreasing lattice constant, $a_{act}$, from 4.16 to 4.12 Å (table 4.2). Apparently, the activation process induces a reduction of $Ni^{2+}$ cations, located in the mixed oxide lattice, leading to an accumulation of Ni in the form of segregated $Ni^0$. The observed depletion of $Ni^{2+}$ ions from the mixed oxide seems to be a logical consequence of the accumulation mechanism. However, the reduction seems to be incomplete, as the mixed oxide lattice constant is still greater than the value obtained for pure $\gamma$-$Al_2O_3$ (3.94 Å, table 4.2), which indicates the presence of residual $Ni^{2+}$. Similar effects as discussed for NiAl51 and NiAl31 are also observed for NiAl11. They are less obvious, however, due to the low overall intensity of the diffractogram and the lower Ni content. On the other hand, $Ni^0$ formation is not readily observable for NiAl13 and NiAl15, as XRD patterns of activated and calcined samples are identical. Nevertheless, there is evidence of $Ni^0$ formation in those samples as well. First of all, the powder within the capillaries was magnetic. Second, the $H_2$

uptake of those materials was greater than zero, as displayed in table 4.3. Both effects were not observed in samples prior to activation. The determined $Ni^0$ crystallite sizes range from 4.8 nm for NiAl51 over 3.5 nm for NiAl31 to 3.0 nm for NiAl11. These values are close to the detection limit but in good agreement with literature [30, 37, 102].

### 4.3.3 Reduction behaviour

TPR profiles obtained for calcined catalyst precursors are shown in figure 4.4. Upon reduction, NiO shows $H_2O$ formation between 250 and 400 °C with a maximum at 310 °C. This is by far a lower reduction temperature as compared to $NiAlO_x$ mixed oxides, indicating that the amount of NiO is negligible in those samples. In fact, the next lowest reduction temperature is recorded for NiAl51 with a maximum at 480 °C. A further steady increase is monitored with decreasing Ni/Al molar ratio: NiAl31 (510 °C) < NiAl11 (570 °C) < NiAl13 (630 °C) < NiAl15 (670 °C). Very similar results have been reported by Zielinski [102] for co-precipitated Ni-Al catalysts with Ni/Al ratios between 2.7 and 26.3. Despite the - in some cases - higher $Ni^{2+}$ content in those samples, they were still more difficult to be reduced than pure NiO. The shift of the TPR profiles to higher temperatures with decreasing Ni/Al molar ratio is also consistent with our study. Noteworthy, the TPR curve of Zielinski's catalyst with a 2.7 Ni/Al molar ratio shows a maximum at around 450 °C, which is 60 °C lower than the comparable NiAl31 sample. His pure NiO reference shows a maximum at 250 °C, thus being also shifted by 60 °C. The somewhat constant offset is probably due to the higher ratio of heating rate to $H_2$ inlet concentration, which is known to shift the TPR profile towards lower temperatures [183]. The degree of reduction after TPR was found to be consistently close to 100 % for all samples. This was under the assumption of irreducible $Al^{3+}$ compounds and $Ni^{2+}$ being completely reduced to $Ni^0$.

The great difficulty to reduce co-precipitated Ni-Al systems is ascribed to a good dispersion of $Ni^{2+}$ ions in the prepared mixed oxides [102]. Apparently, strong interactions with the $Al^{3+}$ phase exist, which make it increasingly difficult to remove $Ni^{2+}$ ions from the oxidic lattice and accumulate it in the form of $Ni^0$.

### 4.3.4 Gas adsorption

Characterization results from $H_2$ and $CO_2$ chemisorption as well as $N_2$ physisorption are listed in table 4.3. BET surface areas of NiAl15 and NiAl13 are between 230 and 260 $m^2/g_{cat}$ and slightly higher than the value obtained for pure $\gamma$-$Al_2O_3$ and NiAl11. For NiAl31 and NiAl51, the surface area significantly decreases but still remains well above 100 $m^2/g_{cat}$. NiO on the other hand exhibits a small surface area of < 30 $m^2/g_{cat}$, which emphasizes the importance

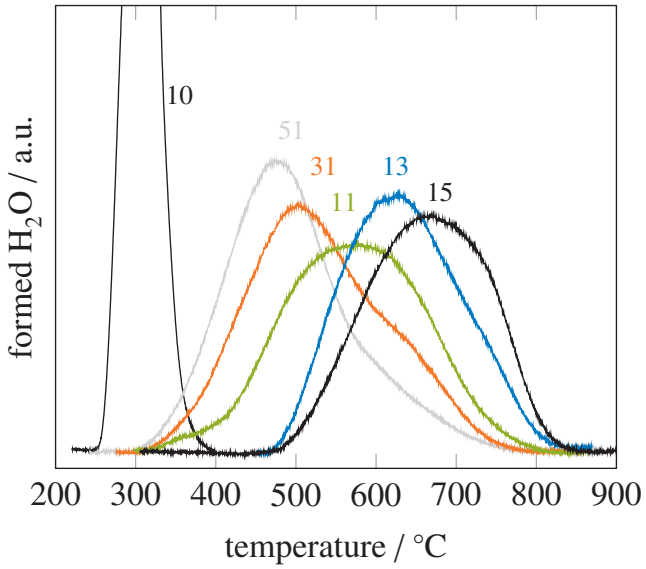


**Figure 4.4:** $H_2O$ formation during TPR of calcined precursors. Depicted numbers are based on Ni/Al molar ratios.

of adding $Al^{3+}$ ions during the synthesis. The $H_2$ uptake of activated catalysts, as determined by static $H_2$ chemisorption, increases with the Ni content from 41 $\mu mol_{H_2}/g_{cat}$ for NiAl15 to approximately 513 $\mu mol_{H_2}/g_{cat}$ for NiAl31. Further raising the Ni content was found to be disadvantageous, as the $H_2$ uptake slightly decreases to 452 $\mu mol_{H_2}/g_{cat}$ for NiAl51. The $CO_2$ uptake of activated samples shows the same trend as the BET surface area of calcined samples, which may suggest, that $CO_2$ adsorbs primarily on the mixed oxide phase. However, small amounts of $CO_2$ were also adsorbed on reduced NiO, which rather indicates the adsorption of $CO_2$ on both phases.

Subsequent to aging catalysts at reaction conditions for 24 h, the adsorption capacities for $H_2$ and $CO_2$ were found to change significantly. Regarding the $CO_2$ uptake of all catalysts and the $H_2$ uptake of NiAl31 and NiAl51, a marked decrease was observed. This behavior is in line with a recent deactivation study carried out on very similar Ni-Al catalysts, which were treated under severe hydrothermal conditions [30]. Hereby, the decrease in $H_2$ adsorption capacity was ascribed to sintering of the Ni phase, whereas the decrease in $CO_2$ uptake was mainly attributed to structural changes of the supporting mixed oxide phase [30]. The $H_2$ uptake of NiAl11 does not change during aging while NiAl13 and NiAl15 show an increase. In these cases, sintering seems to be less severe, which may be due to the lower Ni content. At the same time, the decrease in $CO_2$ uptake is most pronounced for these samples. Accompanying structural changes of the mixed oxide support may therefore trigger an additional reduction of $Ni^{2+}$ during aging, which eventually causes the $H_2$ uptake to increase. Also, it may be possible, that the increase of the $H_2$ inlet concentration from 10 % during activation to 40 % during aging facilitates the further reduction of the catalyst. TPR profiles from this study (figure 4.4) indicate a low reducibility of NiAl13 and NiAl15 during the activation procedure prior to aging, as no $H_2O$ is formed at 450 °C. This does not necessarily mean that those catalysts are not reduced at

all, as $H_2O$ formation begins at a slightly higher temperature and the residence time at 450 °C is only 20 s during the TPR experiment. However, an increase of the $H_2$ inlet concentration during TPR would cause a shift of the TPR profile towards lower temperatures [183] and thus facilitate the reduction. Note that $H_2$ consumption of the reaction causes the $H_2$ inlet concentration to decrease. However, $CO_2$ conversions greater 83 % are needed to reduce the $H_2$ concentration below 10 %. Initial $CO_2$ conversions monitored for NiAl13 and NiAl15 were 74 and 65 %.

**Table 4.3:** Adsorption properties of co-precipitated Ni-Al catalysts.

| | $S_{BET}$[a] $m^2/g_{cat}$ | $U_{0h}(H_2)$[b] $\mu mol_{H_2}/g_{cat}$ | $U_{24h}(H_2)$[c] $\mu mol_{H_2}/g_{cat}$ | $U_{0h}(CO_2)$[b] $\mu mol_{CO_2}/g_{cat}$ | $U_{24h}(CO_2)$[c] $\mu mol_{CO_2}/g_{cat}$ |
|---|---|---|---|---|---|
| $\gamma$-$Al_2O_3$ | 209 | 0 | n.d.[d] | 386 | n.d.[d] |
| NiAl15 | 258 | 41 | 123 | 311 | 237 |
| NiAl13 | 230 | 100 | 184 | 274 | 200 |
| NiAl11 | 205 | 383 | 398 | 230 | 181 |
| NiAl31 | 149 | 513 | 447 | 144 | 119 |
| NiAl51 | 128 | 452 | 348 | 136 | 111 |
| NiO | 26 | 28 | n.d.[d] | 7 | n.d.[d] |

[a] Calcined precursor.
[b] Activated catalyst.
[c] Activated and aged catalyst.
[d] Not determined.

### 4.3.5 XPS analysis

Prior to the presentation of XPS analysis data, it should be noted that co-precipitated Ni-Al catalysts presented in this section stem from a different synthesis batch than the ones referred to throughout the rest of this thesis. Since the characterization results of the 'other' batch [30, 31] are very similar to the ones reported in sections 4.3.1-4.3.4 of this thesis, it seems justified to transfer the general statements of the XPS analysis from one batch to the other. The synthesis and characterization of reference materials referred to in this section, namely NiO, $NiAl_2O_4$ and IC17, which is an impregnated $Ni/Al_2O_3$ catalysts (17 wt% Ni), has also been reported elsewhere [30]. XPS results for co-precipitated and impregnated samples are shown and compared in figure 4.5. For sample NiAl13, NiAl11 and NiAl31, the recorded binding energies (BE) of the Ni $2p_{3/2}$ main signal (figure 4.5a) and its satellite are independent from the Ni loading and centered around 856.0 eV and 862.5 eV, respectively. Also the peak shapes are identical. The differences in signal intensity originate from the increase of the Ni loading in the order NiAl13 < NiAl11 < NiAl31 [30]. In contrast, the impregnated catalyst exhibits peak broadening of the main signal and a decrease in binding energy to about 855.5 eV. This might indicate that $Ni^{2+}$ components are situated in a different chemical environment as compared

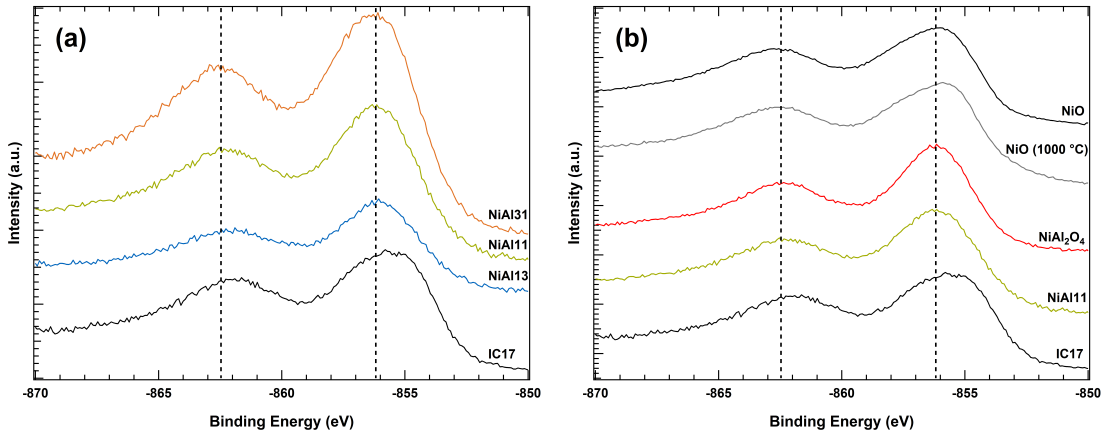


**Figure 4.5:** (a) Comparison of the Ni $2p_{3/2}$ region of co-precipitated and impregnated samples. (b) XPS results of the Ni $2p_{3/2}$ region in relation to reference materials.

to the co-precipitated samples. In figure 4.5b, the Ni $2p_{3/2}$ regions of NiAl11 and IC17 are compared with corresponding patterns of NiO and $NiAl_2O_4$. Next to the standard degassing at 400 °C, NiO was also pre-treated in $O_2$ at 1000 °C (sample NiO (1000 °C) in the following) since this procedure is known to produce clean NiO surfaces [204]. Both pre-treatments lead to identical spectra, as the Ni $2p_{3/2}$ main feature around 856.0 eV and its satellite at 862.5 eV do not differ in energy position and peak shape. This strongly suggests, that the chemical state of the NiO surface is the same in both cases and that already degassing at 400 °C results in a clean surface. Comparing the spectra of NiO and NiAl11, a slight shift of the peak maxima to lower binding energies as well as peak broadening is observed for NiO. The pattern of IC17, on the other hand, corresponds well to the one of NiO which implies that the chemical state of the $Ni^{2+}$ surface species in the impregnated sample is very similar to the one of pure NiO. The signals of NiAl11 reveal identical binding energies and peak shapes as $NiAl_2O_4$ within measurement accuracy. This implies that $NiAl_2O_4$ is present on the surface of the mixed oxide samples investigated. However, essentially the same spectrum is obtained independent of the Ni loading (figure 4.5a) which contradicts the assumption of $NiAl_2O_4$ on the surface, as spinel requires a Ni/Al ratio of 1/2. It is more likely that the differences in the chemical state of the surface species in $NiAl_2O_4$ and mixed oxides of different Ni/Al ratios are very small and cannot be revealed by means of XPS analysis. In figure 4.6, the Al 2s/Ni 3s region of the catalysts and reference materials is shown. The spectra obtained for $Al_2O_3$ and NiO, reveal the intrinsic shape and position of the Al 2s and Ni 3s signal, respectively. NiO typically exhibits a satellite structure [205] leading to a broad signal in the same region where also the Al 2s signal is observed. Determining the intrinsic peak parameters (relative binding energies, number of components and peak widths) for Al 2s and Ni 3s in pure $\gamma$-$Al_2O_3$ and NiO, respectively, allows for the deconvolution of the overlapping signals in Ni-Al mixed oxides. On this basis, a comparison of the binding energies, peak shapes and peak areas was conducted. No significant differences in the peak shape are observed. Concerning the binding energies, similar trends were obtained as for the Ni $2p_{3/2}$ region. All co-precipitated samples reveal a constant binding

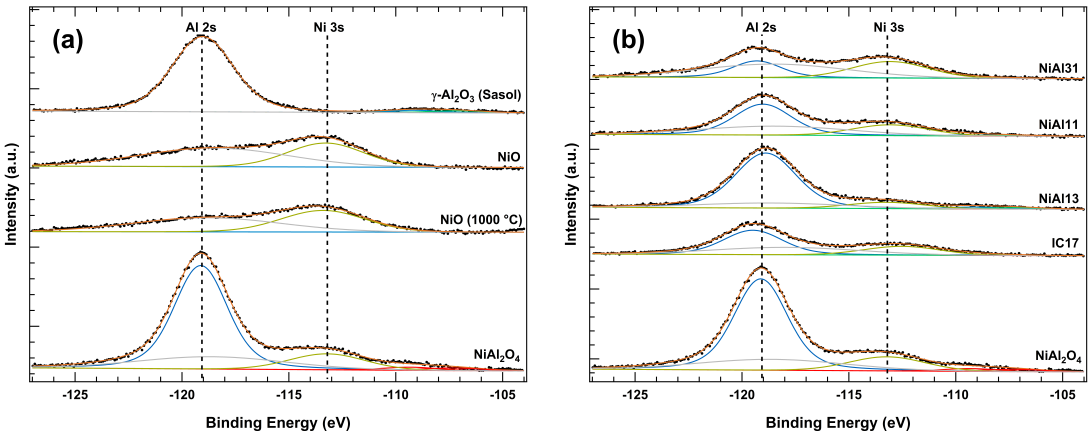


**Figure 4.6:** (a) XPS results for the Al 2s and the Ni 3s region of reference materials. (b) Comparison of Al 2s and Ni 3s signals of co-precipitated and impregnated catalyst samples.

energy of approx. 119.0 eV for the Al 2s signal. A comparison with the pattern obtained for $\gamma$-$Al_2O_3$ and $NiAl_2O_4$ demonstrates that the chemical state of the surface $Al^{3+}$ species is very similar in the precipitated samples, $\gamma$-$Al_2O_3$ and $NiAl_2O_4$. In addition, the calculation of the difference in binding energy ($\Delta$ BE) of the Ni $2p_{3/2}$ and Al 2s signal results in a similar value of $737.1 \pm 0.1$ eV (table 4.4), which is within the spectral resolution limit of the instrument ($\pm 0.1$ eV). This additionally proves that a decisive elucidation of the exact surface composition in precipitated samples is not possible by means of XPS. The pattern of IC17, however, reveals a different trend. The binding energy of the Al 2s signal is shifted to a higher value by 0.5 eV as compared to the other samples. The difference might arise from the inhomogeneous character of the surface in the impregnated sample.

Our results seem contradictory to a comparable study by Shalvoy et al. [209]. There, substantial differences were reported for the binding energy of the Ni $2p_{3/2}$ in NiO (854.6 eV), $NiAl_2O_4$ (856.1 eV) and co-precipitated Ni-Al samples ($856.8 \pm 0.4$ eV). However, the calculated values for $\Delta$ BE of the Ni $2p_{3/2}$ and Al 2s signal, on average $737.1 \pm 0.45$ eV, are in good agreement with corresponding results in this work. We assume that the discrepancy in binding energies arises from an inaccurate correction for sample charging in [209], as the C 1s signal originating from adventitious carbon was used. In the study presented here, only insignificant amounts of carbon species were observed after pre-treatment and the O 1s peak as an intrinsic signal was used for correction.

**Table 4.4:** XPS results.

| | NiAl31 | NiAl11 | NiAl13 | $Ni/Al_2O_3$ | $NiAl_2O_4$ |
|---|---|---|---|---|---|
| $\Delta$BE (eV)[a] | 737.07 | 737.06 | 737.17 | 736.40 | 737.05 |
| Ni/Al (-)[b] | $2.98 \pm 0.60$ | $0.93 \pm 0.19$ | $0.28 \pm 0.06$ | $0.93 \pm 0.19$ | $0.41 \pm 0.08$ 8.4 |

[a] difference in binding energy of Ni $2p_{3/2}$ and Al 2s
[b] on the catalyst surface calculated from XPS results

Calculated values for the Ni/Al ratio on the catalyst surface are summarized in table 4.4. For co-precipitated systems, the surface composition in the calcined samples agrees well with the bulk Ni/Al ratio obtained in the corresponding precursors after precipitation. The rather high experimental error of 20 % is induced by the broad Ni 3s signals.

## 4.4 Conclusion

A wide range of co-precipitated Ni-Al catalysts with Ni loadings between 15 and 70 wt% was synthesized and characterized. After co-precipitation, XRD reveals a layered structure resembling the natural mineral takovite. Depending on the Ni content, XRD reflections of calcined samples shift between the reflections of NiO and $\gamma$-$Al_2O_3$, indicating the formation of a Ni-Al mixed oxide. Phase segregation of NiO or $\gamma$-$Al_2O_3$ was not observed. $N_2$ physisorption of mixed oxides reveals high BET surface areas of 100–260 $m^2/g_{cat}$. Surface sensitive XPS measurements show that $Ni^{2+}$ surface species of the mixed oxides are coordinated similar to $NiAl_2O_4$ and significantly different to NiO. Furthermore, the surface stoichiometry was observed to be similar to the bulk stoichiometry obtained by elemental analysis. Activation of the mixed oxides in $H_2$ was found to be more difficult than activating NiO and complete reduction was becoming increasingly difficult with increasing Al content. $Ni^{2+}$ was (partly) removed from the bulk and enriched on the surface as $Ni^0$, which led to Ni crystallite sizes of 2-5 nm. The ability to adsorb $H_2$ was between 40 and 520 $\mu mol_{H_2}/g_{cat}$. $CO_2$ adsorption capacities range between 100 and 400 $\mu mol_{CO_2}/g_{cat}$. After 24 h under methanation conditions, catalysts were found to change their gas adsorption properties, suggesting sintering and other thermal deactivation phenomena. A detailed description of the latter is provided in [30].

# 5 Contactless temperature measurements under dynamic reaction conditions in a single-pass fixed bed reactor for $CO_2$ methanation

Part of this chapter is published in:

C. Schüler, M. Wolf, O. Hinrichsen, Contactless temperature measurements under static and dynamic reaction conditions in a single-pass fixed bed reactor for $CO_2$ methanation, *Journal of $CO_2$ Utilization* **2018**, *25*, 158-169.

## 5.1 Abstract

Resolving the temperature profile in catalytic fixed bed reactors is essential for the investigation of reactions. However, this is not readily possible at laboratory scale without affecting the flow regime. Thermography tracks temperature profiles contactless with a high spatial resolution and without influencing the flow regime in the reactor. This study applies thermography for a powder fixed bed reactor to study a dynamic phenomenon, namely the *in situ* poisoning of a nickel-alumina catalyst. The temperature of the fixed bed was thereby spatially resolved at any point in time during the reaction. It was found that poisoning causes the reactive zone to move through the catalytic bed at a constant velocity. A simple poisoning model was applied to correlate the observed moving velocity to the catalyst's specific active surface area as determined by static $H_2$ chemisorption at room temperature.

## 5.2 Introduction

The increasing climate change forces society to rethink how the required energy is obtained. By focusing on the expansion of renewable energy sources such as wind power, hydropower and solar energy, the dependence of the industry on fossil fuels is to be reduced in order to limit global warming to 1.5 °C above pre-industrial levels by 2050. This, among other aims in Germany, is to be achieved by the Energiewende [210, 211]. A problem caused by the transition of energy production to renewable sources is that these sources are subjected to temporal as well as quantitative fluctuations. Furthermore, there is a spatial problem between power generation and consumption. Large off-shore wind parks, for example, generate the electricity which is mainly required in urban conurbations and industrial sites. In order to solve this problems, concepts, which feature suitable storage and transport media have to be developed. One of these concepts is the so-called power-to-gas (PtG) concept [10]. This demonstrates the possibility of converting $CO_2$ from anthropogenic sources or from the atmosphere to $CH_4$ by means of $H_2$ derived from water electrolysis [212]. The basis for this process was laid by Paul Sabatier and Jean Baptiste Senderens in 1902 [36]. Nowadays, the $CO_2$ methanation has come to the forefront of science [44, 47], especially since the passing of the Energiewende. For the catalytic conversion of $CO_2$ with $H_2$ to $CH_4$, many metals were tested. Among them are Ru [48, 213–221], Rh [222–226], and Pd [227–230]. Their high methanation rate, however, is offset by the very high price, which prohibited them from being used industrially. In addition to the noble metals, transition metals such as Co [216, 231], Fe [216, 232–234], Cu [232], Ir [232] and Ni [235–240] were also applied. Here, Ni predominantly prevails, which, in addition to a very high activity, also shows a high selectivity towards $CH_4$. Moreover, Ni has a very favorable price in comparison with other metals, which made it the catalyst of choice for industry [42]. In order to further increase the activity of $Ni/Al_2O_3$ catalysts for $CO_2$ methanation, different promoter metals have been added. Zhao et al. [75] reported an enhanced activity for Mn promoted systems and the group of Grunwaldt [70] found an increased activity for NiFe alloys. The overall reaction equation of the methanation is summarized in (5.1):

$$CO_2 + 4H_2 \rightleftharpoons CH_4 + 2H_2O \tag{5.1}$$

As the reaction is highly exothermic, there is a risk of creating a hot spot in the reactor, which was also observed for other exothermic reactions [241–245]. In addition, sintering processes which significantly impair the life-time of the catalyst may occur due to local temperature maxima. This can be observed not only in industrial applications but also in laboratory scale. Single-pass fixed bed reactors are often assumed to be isothermal, although hardly enough thermocouples can be placed in small fixed beds. If reactors are built large enough, several thermocouples can be placed at selected points [246, 247]. Horn et al. developed a reactor design using a movable sampling capillary to measure the spatial reactor profile in terms of mass and temperature within the reactor [248–250]. The sampling capillary was connected to a

mass spectrometer and was also equipped with a thermocouple or a pyrometer fiber. However, all these methods potentially disturb the flow within the reactor [251]. Another promising way of dealing with this problem is thermography. Despite the potential of this method, this technique has only begun to prevail in recent years. Above all, fixed beds of active moldings [252, 253], foams [254], monoliths [255, 256] or overflowed catalyst particles [257], and plate catalysts [258, 259] were investigated for determining the kinetics of $CO/CO_2$ methanation and the partial oxidation of $CH_4$. In this work, the applicability of the contactless temperature measurement technique under dynamic reaction conditions to permeated, powder fixed beds is shown, using the $CO_2$ methanation as an example for a strongly exothermic reaction. Time dependency is achieved by poisoning a co-precipitated $NiAlO_x$ catalyst (Ni/Al=1/1) in the presence of a feed gas containing 5 vppm $H_2S$.

## 5.3 Experimental

### 5.3.1 Catalyst synthesis

For the synthesis of the nickel-alumina precursor, the reverse co-precipitation method at constant pH was used following the synthesis route described in [23, 37]. The water was purified by a Millipore water clearing rig. Nickel nitrate, aluminum nitrate, sodium hydroxide and sodium carbonate (Merck KGaA) with the purity of p.a. were used as purchased. Co-precipitation was performed in a 3 l double-walled glass reactor (Büchi) preloaded with 1 l of water, stirred at 150 rpm by a KPG stirrer and heated to 30 °C. For an improved mixing, two flow breakers were additionally inserted in the vessel. 120 ml of the metal nitrate salt solution (1 M $Ni(NO_3)_2 \cdot 6H_2O$ and 1 M $Al(NO_3)_3 \cdot 9H_2O$, both Merck KGaA, p.A) were added by a peristaltic pump (Medorex e.K.) with 2.3 ml/min. The precipitating agent was a mixture of 0.5 mol NaOH and 0.5 mol $Na_2CO_3$. A Titrino Autotitrator 716DMS by Methrom dosed the solution into the vessel to keep the pH value constant during precipitation. The molar ratio of Ni/Al was set to 1/5 and 1/1 (NiAl15 and NiAl11). After precipitation, the product slurry was aged for 18 h under stirring in the mother liquor. Subsequently, the precipitate was washed with purified water until the pH value of the filtrate reached the original one of water. The retentate was first dried overnight at 80 °C and then calcined at 450 °C for 6 h under synthetic air flow (heating rate 5 K/min).

### 5.3.2 Characterization

For powder X-ray diffraction analysis (XRD), a PANanalytic Empyrean with Cu-$K_\alpha$ radiation and a monochromator was used. The diffractogram resulted from scanning in the range between $2\theta = 5-90$ and with an angular velocity of 0.057 08 °/s. The specific surface area of the calcined catalyst was determined by $N_2$ physisorption. Therefore, a Nova 4000e surface area analyzer from Quantachrome was used. The isotherm was measured in the $p/p_0$ range between 0.05 and 1 and the BET surface area was calculated by using the $p/p_0$ range between 0.05 and 0.3. As a pretreatment, the sample was heated up to 120 °C under vacuum and kept for 3 h to remove physisorbed water. The specific metal surface area of the catalyst was measured by means of $H_2$ chemisorption. For this purpose, a Quantachrome Autosorb-1 was used. Prior to the measurement, the catalyst was reduced in 5 vol% $H_2$ $N_2$ at 450 °C for 5 h (heating rate of 2 K/min). Chemisorption was conducted at 35 °C and the $H_2$ uptake was calculated by the extrapolation method.

### 5.3.3 Experimental setup

For the temperature measurement, an optical accessible reactor setup was employed. The main parts consisted of a gas dosing and mixing section, the reactor section and the analysis section. All gases were purchased from Westfalen AG and had a purity of 5.0. The gases were dosed by mass flow controllers (Bronkhorst). To prevent condensation of produced water, the exhaust line was heated. The reaction section consisted of a massive heating block equipped with two heating cartridges, allowing a maximum temperature of 700 °C. Further, the heating block also had an opening for the contactless temperature measurements. The optical accessible tube reactor was a 30 cm long quartz glass tube with an inner diameter of 4 mm and a wall thickness of 1 mm and was placed in the heating block. The fixed bed was held in place by silica wool plugs in the isothermal zone of the quartz glass tube reactor. For an additional temperature measurement, a thermocouple was placed at the beginning of the fixed bed. The product composition was analyzed every 20 min by a Shimadzu GC-14B equipped with a flame ionization and thermal conductivity detector. The GC was regularly calibrated with gas mixtures of known composition and tested with a bench mark catalyst of known $CO_2$ conversion. A sketch of the overall testing rig is presented in figure 5.1. It is worth mentioning, that the sampling rate of a GC, which is slow as compared to other gas analyzers, e.g. IR cells, might be a limiting factor for tracking fast dynamic processes. In the current case however, the complete deactivation of 50 mg of a highly active material by a few vppm of $H_2S$, can be expected to occur on the scale of several days. A response time of 20 min was therefore considered adequate.

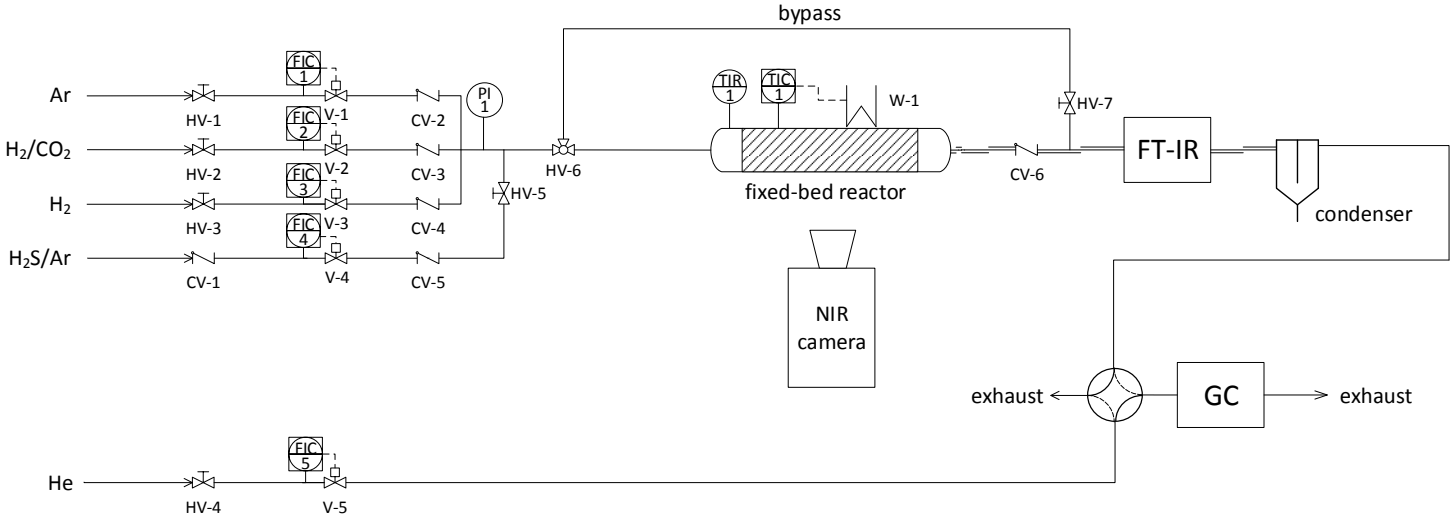


**Figure 5.1:** Schematic illustration of the testing rig.

For the contactless temperature measurements, a SC-2500 near-infrared camera (FLIR) equipped with an indium gallium arsenide (InGaAs) detector working with a wavelength range of 0.9 to 1.7 µm and a standard frame rate of 50 Hz was used. The nominal accuracy of the camera is ±1 °C, which is for example higher than a Type K thermocouple (±2.2 °C). The choice of the working range allows using the so-called atmospheric windows where no interaction of the emitted IR radiation with the atmosphere occurs. Therefore, the interaction of the emitted IR radiation with heteronuclear molecules of the surrounding atmosphere can be neglected. The working range of the camera also meets perfectly with the optical permeability of quartz glass, whereby only a small attenuation of the emitted infrared radiation is observed. Another important factor is the emissivity of the investigated material. This emissivity is temperature dependent and decreases with increasing temperature. Therefore, it is very important to consider this change in the temperature calibration of the camera. The following calibration method was chosen to take the emissivity into account: a mixture of SiC and $NiAlO_x$ with the same ratio as used in the experiments was placed in the reactor together with a thermocouple. The calibration was conducted under argon flow in the temperature range of 380 to 550 °C. A detailed description of the calibration method is given in [257]. During the dynamic measurement, the camera recorded 1 s long videos of the reactor, consisting of 50 individual pictures at a resolution of 320 × 265 pixels. For evaluating the temperature along the reactor axis over the course of the reaction, line profiles of 30 pixels were placed in the center of the reactor, parallel to the wall. Since the poisoning reaction was expected to run several days, it was not considered necessary to record temperature changes on the scale of seconds. Instead, videos were recorded at an interval of 5 min. This is still four times faster than GC sampling and avoids the accumulation of several terabytes of data. As described earlier [257], the SC-2500, even operated at 50 Hz, is also capable of resolving fast dynamic processes on the scale of a few seconds, e.g. the startup of the $CO_2$ methanation reaction.

### 5.3.4 Dynamic temperature measurement

For the dynamic measurements under poisoning conditions, 50 mg of NiAl11 (particle diameter of 150 to 200 µm) diluted with 450 mg SiC (particle diameter of 150 to 250 µm) were used. In addition, a cold bed of 100 mg SiC was placed upstream of the catalyst bed. The experiment was then divided into three parts, namely activation, aging and poisoning. The catalyst was first activated with 10 % $H_2$ in Ar for 4 h at 450 °C (heating rate of 5 K/min). Afterwards, an aging treatment was carried out to ensure that the catalyst was not subjected to thermal deactivation during the poisoning reaction. Therefore, the catalyst was held for 24 h at 400 °C with a feed gas composition of $Ar/H_2/CO_2$ = 5/4/1 and a total volume flow of 62.5 sccm. Subsequent to the aging treatment, the poisoning treatment was initiated by adding 5 vppm $H_2S$ to the feed gas at otherwise unchanged conditions. The experiment was run until the catalyst was completely deactivated.

# 5.4 Results and discussion

## 5.4.1 Catalyst characterization

The NiAl11 catalyst shows a BET isotherm with a hysteresis at about $p/p_0$=0.5–0.95. According to IUPAC classification, the BET isotherms are ascribed to mesoporosity and can be categorized as a type IV, with an H3 hysteresis loop [260]. The evaluation of the specific surface area $S_{BET}$ shows a value of 225 $m^2/g_{cat}$. The specific metal surface area $S_{AM}$ is 26.7 $m^2/g_{cat}$. Figure 5.2 presents the XRD pattern of the NiAl11 catalyst. It can be assigned to NiO (JCPDS-78-0429). An exception to this are the reflexes at 43.6° and 63.3° which are shifted towards higher angles. This is probably caused by the formation of a mixed oxide phase during the calcination process.

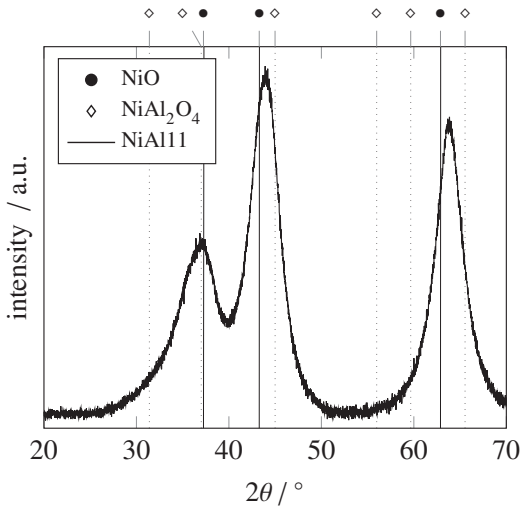


**Figure 5.2:** XRD pattern of the calcined $NiAlO_x$ catalyst, having a Ni to Al ratio of 1/1.

## 5.4.2 Dynamic temperature measurement

A promising application of thermography is the temperature measurement under dynamic reaction conditions. Special focus in this study is laid on deactivation of catalysts due to poisoning. The $H_2S$ poisoning of a NiAl11 catalyst was chosen as a proof of concept. Subsequent to the reduction of the catalyst, the sample was aged at an oven temperature of 400 °C for 24 h with a feed gas composition of $Ar/H_2/CO_2$=5/4/1 using 62.5 sccm. After the aging treatment, the poisoning was started by adding 5 vppm $H_2S$ to the used feed gas. The poisoning reaction lasted 2340 min until the catalyst was completely deactivated. The results of the poisoning experiment are summarized in figure 5.3a and b. In figure 5.3a, the results of the GC analysis, i.e. $CO_2$

conversion and $CH_4$, resp. CO yield, are plotted against time on stream (TOS). In figure 5.3b, the movement of the reactive zone (indicated by temperature) is illustrated by plotting the time course of the reaction against the relative reactor length. Hereby, the catalyst bed is located between 0.2 and 1.0 relative length units and a cold bed for improved heat transfer is located from 0 to 0.2. During the aging treatment of the catalyst, a constant $CO_2$ conversion of 78 % was monitored and no movement of the reactive zone was observable, which indicates that no thermal deactivation occurred during this treatment. At this point, the reactive zone is located at the front end of the reactor, just behind the cold bed. This shows the high activity of the NiAl11 catalyst and suggests, that full conversion, which is thermodynamically limited to 78 % at the chosen conditions, is reached within the first 10 to 15 % of the catalyst bed. At a TOS of 1500 min, $H_2S$ was added to the feed and the actual poisoning reaction was started. As can be observed in figure 5.3b, the reactive zone immediately begins to migrate towards the rear end of the reactor. Although this effect is clearly visible by means of the NIR camera, it does not seem to have an impact on the catalytic performance of the catalyst, which stays constant until a TOS of 3000 min. Only when the reactive zone reaches the end of the catalyst bed, the conversion notably decreases. At the same time, CO yield starts to increase at further expense of $CH_4$. At this point, the reactive zone cannot migrate further but sulfur is continuously supplied, which causes the catalyst to rapidly deactivate. Eventually, it deactivates completely at a TOS of 3800 min. Afterwards, only the gas phase equilibrium of the reverse water-gas shift reaction can be measured. Interestingly, the formation of CO reaches a maximum before decreasing to its equilibrium value, whereas $CH_4$ is steadily decreasing. It is safe to conclude that sulfur is primarily reducing the hydrogenation ability of the catalyst but not necessarily the ability for $CO_2$ dissociation. In order to better understand the time dependence of the poisoning behavior, a simple model was applied. Therefore, the sulfur balance of the reactor was calculated according to eq. (5.2):

$$n_S(t) = \int_0^{\infty} (\dot{n}_{S,in} - \dot{n}_{S,out})\, dt \tag{5.2}$$

Hereby, $\dot{n}_{S,in}$,in and $\dot{n}_{S,out}$ are the molar flow of sulfur into and out of the reactor and $n_S(t)$ is the amount of sulfur accumulated on the catalyst. As there was no sulfur sensitive GC detector available for this study, we were not able to determine the inlet and outlet concentrations of sulfur of such low content experimentally. However, we used stainless steel tubing coated with SilkoNert2000 (formerly known as Sulfinert) and a quartz glass tube reactor, in order to prevent adsorption of $H_2S$ in our lines. Assuming that the nominal $H_2S$ concentration of 5 vppm was fed to the reactor and the $H_2S$ concentration leaving the reactor was several magnitudes lower than the inlet, as $H_2S$ readily reacts with the catalyst's Ni surface atoms, even at $H_2S$ levels as low as 1 vppb [114], eq. (5.2) can be simplified to:

$$n_S(t) = \dot{n}_{S,in} \cdot t \tag{5.3}$$

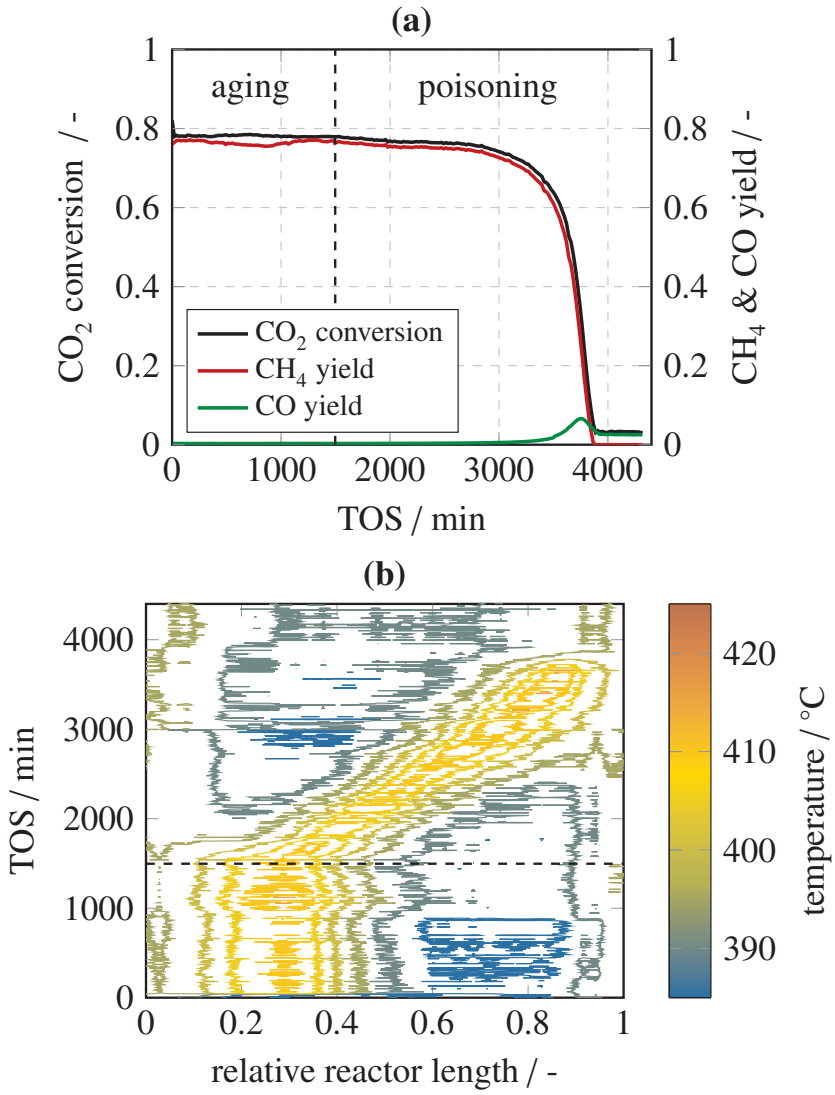


**Figure 5.3:** Course of the hot spot under dynamic conditions. Conversion and yield (a). Temperature course under dynamic conditions (b).

linear time dependency of $n_S(t)$ is in good accordance to the constant moving velocity of the reactive zone, which may be derived from figure 5.3b. For obtaining quantitative information about the moving velocity calculated from the model, additional assumptions were made. These are in line with the common understanding of sulfur poisoning of $Ni/Al_2O_3$ catalysts [110]:

(a) The poisoning mechanism can be described by the irreversible adsorption of sulfur on Ni surface atoms, leading primarily to a geometrical blockage of $H_2$ adsorption sites [110].

(b) The poisoning reaction is limited to surface sulfide formation, as 5 vppm of $H_2S$ is well below the threshold for bulk sulfide formation of a Ni catalyst [111].

(c) Adsorption of sulfur on alumina is negligible [112].

If the above mentioned assumptions are valid, the $H_2$ adsorption capacity of NiAl11, as determined by static $H_2$ chemisorption at room temperature, may be correlated with the maximum sulfur uptake of the catalyst. This approach has been demonstrated for conditions very similar to ours, whereby the stoichiometry of S/H uptake was reported in the range between 0.75 and 1.0 [112]. For our catalyst, this results in a maximum sulfur uptake capacity of the entire bed between 25.6 and 34.1 µmol sulfur. Normalized by the length of the catalyst bed (x=0.8 in figure 5.3b) and correlated with the molar inlet flow of sulfur ($2.32 \cdot 10^{-10}$mol/s), the moving velocity of the reaction zone through the catalyst bed can be calculated to 0.33 and 0.44 relative length units per 1000 min. This again suggests a deactivation time of the catalyst of 1800 to 2400 min, which agrees well with the recorded deactivation time of the GC measurement of 2340 min.

## 5.5 Conclusion

The applicability of thermography for the investigation of exothermic reactions using $CO_2$ methanation under dynamic reaction conditions has been shown. As a proof of concept , sulfur poisoning of a Ni catalyst was monitored. Thermography can provide full information about the temperature distribution within the catalyst bed over the complete time course of the poisoning reaction. In fact, the movement of the reactive zone through the catalytic bed was entirely monitored and the moving velocity was found to be constant. This allowed us to use a simple poisoning model, whereby the sulfur uptake capacity of the catalyst was described sufficiently accurate by its hydrogen uptake capacity at room temperature. Further studies have to be carried out in order to test this correlation for a broader range of nickel-alumina catalysts with various Ni loadings and maybe also dopants.

# 6 Sulfur poisoning of co-precipitated Ni-Al catalysts for the methanation of $CO_2$

Part of this chapter is published in:

M. Wolf, C. Schüler, O. Hinrichsen, Sulfur poisoning of co-precipitated Ni-Al catalysts for the methanation of $CO_2$, *Journal of $CO_2$ Utilization* **2019**, *32*, 80-91.

## 6.1 Abstract

This study provides deep insights into the mechanism and kinetics of sulfur poisoning of co-precipitated Ni catalysts for the methanation of $CO_2$. A large number of catalysts with different Ni loadings were poisoned with 5 ppm of $H_2S$ and $SO_2$ at equilibrium conditions ($H_2/CO_2/Ar = 4/1/5$, 400 °C, 1 bar). Prior to the complete loss of activity, thermography reveals a moving reaction front through the fixed-bed microreactor. The stability of catalysts depends on available Ni surface atoms. $H_2$ chemisorption and post-mortem CHNS analysis show an average S/Ni* surface atom ratio of $0.73 \pm 0.02$. Based on this stoichiometry, a model for predicting catalyst lifetimes is derived and extrapolated to different $H_2S$ partial pressures. In an *ex situ* poisoning approach, liquid $(NH_4)_2S$ was used to adjust sulfur coverages between 0 and 0.73. Activity measurements under differential conditions reveal an activity loss of more than 80 % at coverages as low as $\theta_S = 0.2$. A kinetic description based on a Maxted-type correlation is derived. The strong dependence of activity on sulfur coverage is explained by the space requirements of $CO_2$ adsorption on $Ni^0$. Activation energies of non-poisoned and poisoned samples are similar and in the range of 80 to 87 kJ/mol. Sulfur poisoning is therefore ascribed to site blockage rather than electronic effects.

## 6.2 Introduction

The generation of synthetic natural gas (SNG) via the methanation of $CO_2$ has recently gained widespread interest in academia and industry, because it offers a potential route to greenhouse gas reduction and chemical energy storage on an industrial scale [42, 43, 50]. Based on the idea of the so-called 'Power-to-Gas' (PtG) concept formulated by Sterner in 2010 [10], surplus energy from renewable sources allows the generation of low-cost $H_2$ via water electrolysis, which is further reacted to $CH_4$ for ease of transportation. The second reactant, $CO_2$, is separated from industrial large scale emitters, e.g. from biogas plants or fossil fired power stations.

The methanation reaction of $CO_2$, depicted in equation (6.1), is a highly exothermic gas phase reaction, which is commonly catalyzed by a nickel catalyst. It has been known as the Sabatier reaction since the beginning of the 20$^{th}$ century [36].

$$4H_2 + CO_2 \rightleftharpoons 2H_2O + CH_4 \qquad \Delta H_R^0 = -165\,\frac{\text{kJ}}{\text{mol}} \tag{6.1}$$

Thermodynamic calculations, which have been presented in detail elsewhere [38], show, that the Sabatier reaction is well described following Le Chatelier's principle. Thus, $CH_4$ yields greater 90 % and selectivities close to 100 % are achieved at temperatures below 350 °C and pressures exceeding 1 bar. These conditions are the key to meet strict regulations (in Germany: < 10 % $H_2$ [39]) for feeding SNG to the local gas grid and avoid intensive gas purification. For operating reactors under industrial relevant conditions, highly active and selective catalysts are required. Of specific interest have been supported metals such as Ru [216, 261–263], Pd [264] or Ni [37, 53, 55, 57, 265], with Ni being the most cost-effective. As support materials, $SiO_2$ [53, 216, 264], $Al_2O_3$ [70, 75, 76], $CeO_2$ [57, 263] and others [55, 261, 265] have been applied. Moreover, adding small amounts of Fe or Mn [25, 26, 70, 75, 76] was found to further improve catalytic activity and stability. An overview of recent developments can be found in current reviews [42, 44, 45].

In the last years, our group has focused on understanding co-precipitated Ni-Al catalysts, which have proven to be highly active but also stable under $CO_2$ methanation conditions [37]. Besides a thorough description of the micro kinetics under industrial reaction conditions [23], we have contributed extensive characterization and reactor studies, specifically on Mn- and Fe-promoted systems [25, 26], and recently published detailed knowledge about long-term deactivation [30]. In an industrial environment, catalysts are however not only stressed by long-term operation but also by impurities in the feed. Hereby, a specific problem arises from the usage of $CO_2$ separated from industrial exhaust gases, as they often contain sulfur. The quick and irreversible poisoning of Ni catalysts in the presence of sulfur is well-known and has been addressed by several thorough reviews on catalyst deactivation [118, 123, 266]. With regards to $CO_2$ methanation, however, detailed studies about sulfur poisoning are scarce. Guilera et

al. [156] conducted lifetime testing with 50 ppb $H_2S$ at 300 °C for 146 h, using 0.3 g of Ni/$\gamma$-$Al_2O_3$ doped with $CeO_2$ and $La_2O_3$. All tested catalysts have maintained their initial $CO_2$ conversion (77 to 95 %) during poisoning and sulfur was not detected in spent samples. It is however well-known from thermodynamic measurements, that significant amounts of $H_2S$ adsorb on Ni/$\gamma$-$Al_2O_3$ at the chosen conditions [114]. It is therefore necessary to compare catalyst activities at low conversions to exclude equilibrium effects [157]. In the case of sulfur poisoning, additional care has to be taken because a sulfur gradient is readily formed along the reactor axis [143]. To investigate sulfur poisoning and compare catalyst stability, fixed beds have to be poisoned homogeneously. This is either achieved by performing elongated lifetime tests or by increasing the sulfur partial pressure. The authors of this study have conducted a lifetime test with 5 ppm $H_2S$ on co-precipitated Ni-Al catalyst at 400 °C [33]. The catalyst maintained its performance over 24 h but completely deactivated afterwards. This behavior was ascribed to a moving reaction front caused by progressive $H_2S$ adsorption. Only once the fixed bed was completely saturated, the catalyst's performance started to decline. Severe loss of $CO_2$ methanation activity due to sulfur poisoning has also been reported by Müller [153], Wan Abu Bakar [154] and Neubert [155].

Unfortunately, most of the published studies do not couple activity measurements with catalyst characterization. Therefore, general statements about the poisoning mechanism and structure-activity relations are impeded. The current study is meant to bridge this gap and verify the concept of a site-blocking mechanism, which has been postulated for other reactions and reaction conditions [143, 144]. Based on this concept, an existing approach for predicting catalyst lifetimes [33] is refined, validated and extrapolated to different $H_2S$ partial pressures. Furthermore, a kinetic description of sulfur poisoning along with detailed catalyst characterization is presented.

## 6.3 Experimental

Only deionized water purified in a filter unit (Millipore) was used for the synthesis steps. All chemicals were of analytical grade and used as received. Gases were supplied by Westfalen AG and were of 5.0 purity, except for the $SO_2$/Ar and $H_2S$/Ar mixtures, which were composed of Ar 6.0, $SO_2$ 3.0 and $H_2S$ 1.8.

### 6.3.1 Catalyst synthesis

All catalysts tested in this study were synthesized by co-precipitation of 1 M solutions of $Ni(NO_3)_2 \cdot 6H_2O$ (Merck) and $Al(NO_3)_3 \cdot 9H_2O$ (Merck). Hereby, an equimolar mixture of 1 M NaOH (Merck) and 1 M $Na_2CO_3$ (Sigma) was used as precipitation agent. In a typical synthesis, 1 l of water was maintained at 30 °C and pH 9±0.1 in a double-walled glass reactor containing two glass baffles. The liquid was thoroughly mixed by a KPG stirrer at 150 rpm. 180 ml of total nitrate solution, containing a varying $Ni^{2+}/Al^{3+}$ molar ratio (0/1, 1/5, 1/3, 1/1, 3/1, 5/1 and 1/0), were added at a rate of 2.4 ml/min using a peristaltic pump. The pH was kept constant using a TitroLine alpha plus titrator (SI Analytics), loaded with the precipitation agent. The product slurry was aged for about 18 h at constant pH and temperature. After aging, the product was vacuum filtered and washed several times with water until the pH of the filtrate remained constant. The filter cake was then dried at 80 °C for 18 h and calcined in synthetic air at 450 °C for 5 h subsequent to heating at a linear rate of 5 K/min.

In the following sections, the binary Ni-Al samples are named after their Ni/Al molar ratio, i.e. NiAl15, NiAl13, NiAl11, NiAl31 and NiAl51. The products obtained after co-precipitation and calcination are referred to as '(dried) precipitate' and 'calcined (catalyst) precursor'. The calcined reference samples with $Ni^{2+}/Al^{3+}$ molar ratios of 1/0 and 0/1 are named according to their crystal structures, as observed by XRD (section 6.6.1): NiO and $\gamma$-$Al_2O_3$.

### 6.3.2 Sulfur Poisoning

Sulfur poisoning experiments were conducted in an optically accessible quartz glass reactor setup, equipped with inert tubings (SilcoNert) to avoid sulfur cross-contaminations between the measurements. The reactor was operated at atmospheric pressure, a volume flow of 62.5 sccm and a stoichiometric feed gas mixture, containing Ar as a carrier gas ($H_2/CO_2/Ar$ = 4/1/5). The catalytic fixed bed, which was typically composed of 50 mg of catalyst (150 to 200 µm) and 450 mg of SiC (ESK, 250 to 355 µm), was placed between two cold beds of SiC (each 50 mg) and two plugs of glass wool. Different particle sizes of catalyst and SiC were chosen on purpose to simplify the separation of both fractions by sieving. Each poisoning experiment was based on a sequence of three distinct treatments. First, catalysts were activated in 10 % $H_2$/Ar over a period of 4 h at 450 °C (heating rate of 2 K/min). Second, an aging period of 24 h was conducted at 400 °C. Aging was meant to decouple activity losses caused by the poisoning reaction from activity losses due to changes of the Ni-Al catalyst. These are typically observed within the first hours of hydrothermal conditions [23, 30]. Finally, the third treatment was specific with regards to the *in situ* or *ex situ* experiment. Details are given in sections 6.3.2.1 and 6.3.2.2.

In order to monitor changes during the reaction, two analytical techniques were combined: online gas chromatography (GC) and thermography. GC analysis was carried out on a Shimadzu GC-14B, equipped with a thermal conductivity detector (TCD) and a micropacked ShinCarbon ST column. Hereby, the column was kept at a constant temperature of 40 °C, allowing the detection of $H_2$, Ar, CO, $CH_4$ and $CO_2$ during a measuring interval of 20 min. Based on this data and equations (6.2)-(6.6), $CO_2$ conversions, $CH_4$ and CO yields, as well as weight time yields (WTY) of $CH_4$ and CO were calculated. $[i]_{in}$ denotes the fraction of species i in the feed gas and $[i]_{out}$ the fraction of species i in the product gas. $\dot{V}_{feed}$ is the feed gas volume flow, $V_M$ the molar volume and $m_{cat}$ the mass of calcined catalyst precursor placed in the reactor. In order to account for the volume contraction of the reaction, Ar was used as an internal standard. The consistency of each data set was checked via the carbon balance, depicted in equation (6.7), which was typically closed with an accuracy of $\pm$ 3 %.

$$X(CO_2) = \frac{[CO_2]_{in} - [CO_2]_{out}}{[CO_2]_{in}} \tag{6.2}$$

$$Y(CH_4) = \frac{[CH_4]_{out}}{[CO_2]_{in}} \tag{6.3}$$

$$Y(CO) = \frac{[CO]_{out}}{[CO_2]_{in}} \tag{6.4}$$

$$WTY(CH_4) = \frac{\dot{V}_{feed} \cdot [CH_4]_{out}}{V_M \cdot m_{cat}} \tag{6.5}$$

$$WTY(CO) = \frac{\dot{V}_{feed} \cdot [CO]_{out}}{V_M \cdot m_{cat}} \tag{6.6}$$

$$[CO_2]_{in} = [CH_4]_{out} + [CO]_{out} + [CO_2]_{out} \tag{6.7}$$

For thermographical measurements, a SC-2500 near-infrared (NIR) camera (FLIR), equipped with an indium gallium arsenide detector (InGaAs), was operated at wavelengths between 0.9 and 1.7 µm and a standard frame rate of 50 Hz. During aging and poisoning periods, 1 s long videos of the reactor, each consisting of 50 individual pictures (320 × 265 pixels), were

recorded at an interval of 10 min. In the course of data evaluation, the temperature along the reactor axis was extracted from the video files by placing a line profile of 30 pixels in the center of the reactor and parallel to the wall. This essentially resulted in one temperature profile for every 10 min, each consisting of 30 data points, equally distributed along the reactor axis. An in-depth description of the reactor setup and the applied methodology, including detailed information about calibration procedures of the utilized equipment, can be found in section 5.3.3 and reference [257].

#### 6.3.2.1 In situ poisoning

*In situ* poisoning was achieved by co-feeding 5 ppm of either $H_2S$ or $SO_2$ at reaction conditions. Therefore, the Ar stream used for reduction and aging treatments was replaced by an equivalent stream of 10 ppm $H_2S$/Ar or 10 ppm $SO_2$/Ar. This changeover was conducted right after the aging period. Sulfur was fed to the reactor at 1 bar, 400 °C, 62.5 sccm and $H_2/CO_2/Ar$ = 4/1/5. As soon as no more $CH_4$ was detected by the TCD, the reactants were switched off and the fixed bed was purged with Ar and cooled down to room temperature. In the case of a subsequent CHNS measurement, the SiC/catalyst mixture was removed from the reactor and separated by sieving. In the case of a subsequent chemisorption measurment, the entire reactor content was transferred to the analysis cell under inert conditions.

#### 6.3.2.2 Ex situ poisoning

*Ex situ* poisoning was achieved by incipient-wetness impregnation of the calcined catalyst precursors of NiAl11 and NiAl31 with aqueous solutions of diluted ammonium sulfide (40 to 44 wt%, abcr). The poisoned samples were dried at 80 °C for 18 h. Nominal quantities of adsorbed sulfur obtained by this method ranged from 0.1 to 3.0 wt%. In order to exclude influences of the preparation method on the catalysts' activity, sulfur free reference samples were obtained by impregnation with water.

Activation and aging conditions for the *ex situ* experiment were chosen identically to the *in situ* experiment. After aging, the reactor was purged with Ar and cooled down to 160 °C. The steady-state activity was then monitored under differential reaction conditions ($CO_2$ conversion < 10 %) in 10 °C steps between 160 and 330 °C for 2 h each (heating rate of 2 °C between steps). As the operation of the applied NIR camera is limited to temperatures $\geq$ 380 °C, lower temperatures were measured with a type K thermocouple placed inside the reactor. At the end of the experiment, the reactor was purged with Ar and cooled down to room temperature. Samples were removed from the setup and transferred to the chemisorption instrument under

inert conditions. After $H_2$ and $CO_2$ uptakes were measured, samples were sieved and prepared for CHNS analysis.

In order to compare the activity and adsorption properties of samples containing various amounts of sulfur, the sulfur coverage, $\theta_S$, the relative activity, $a_{rel}$, and the relative adsorption of species i, $U_{rel}(i)$, were defined according to equations (6.8)-(6.10). $N_{S,ads}$ is the amount of adsorbed S atoms, which was calculated from the sulfur weight fraction $w_S$ determined by CHNS analysis and the molar mass of sulfur $M_S$. $N_{Ni*}$ is the maximum possible amount of adsorbed S atoms, which was treated as equivalent to the amount of Ni surface sites in the non-poisoned state, which was calculated from $H_2$ chemisorption results of the non-poisoned samples: $2 \cdot U(H_2)(\theta_S = 0)$. $U(i)(\theta_S)$ is the uptake of species i in the poisoned samples and $U(i)(\theta_S = 0)$ is the uptake of species i in the non-poisoned samples. Activity data is compared on the basis of WTY ($CH_4$) of poisoned and non-poisoned samples, denoted as WTY ($\theta_S$) and WTY ($\theta_S = 0$).

$$\theta_S = \frac{N_{S,ads}}{N_{Ni*}} = \frac{w_S}{M_S \cdot 2 \cdot U(H_2)(\theta_S = 0)} \tag{6.8}$$

$$U_{rel}(i)(\theta_S) = \frac{U_{rel}(i)(\theta_S)}{U_{rel}(i)(\theta_S = 0)} \tag{6.9}$$

$$a_{rel}(\theta_S) = \frac{WTY(\theta_S)}{WTY(\theta_S = 0)} \tag{6.10}$$

### 6.3.3 Characterization

The elemental composition (Na, Al and Ni) of the non-poisoned samples was determined by ICP-OES (Agilent Technologies, Model 725). In a typical experiment, 50 ml of 1 M $H_3PO_4$ (Alfa Aesar) were added to 25 to 50 mg of catalyst and sonicated at elevated temperatures for several hours. After the solution was cooled down to room temperature, it was filtered and diluted with water by a factor of 10. Metal standards of 1, 10 and 50 mg/l were prepared from a 1000 mg/l ICP multi-element standard (IV, Merck). Wavelengths used for data evaluation were 568.263 nm (Na), 230.299 nm (Ni) and 396.152 nm (Al). Metal superposition and matrix effects were excluded.

The sulfur content of poisoned samples was determined by CHNS analysis using a Euro EA elemental analyzer (HEKAtech). A sample mass of 10 to 15 mg was weighed out into a tin boat and burned at a local temperature of 1800 °C in a $O_2$/He atmosphere over a Cu catalyst.

The resulting products ($CO_2$, $N_2$, $H_2O$ and $SO_2$) were separated in a GC column and analyzed by means of a TCD. Calibration of the instrument was carried out via a four-point calibration. Therefore, 1 and 3 mg of a low NS standard (elementar, 0.86 wt% sulfur) and sulfanilamide (HEKAtech, 18.62 wt% sulfur) were used. For the purpose of consistency, the calibration was verified over the course of one measured series by including the low NS standard several times as a sample.

The crystal structure of co-precipitated, calcined and activated samples was analyzed by X-ray diffraction (XRD) using a PANanalytical Empyrean diffractometer operated with Cu-$K_\alpha$ radiation ($\lambda$ = 1.540 56 Å) at 45 kV and 40 mA. Diffractograms were obtained by scanning the range between $2\theta = 5 - 90°$. Co-precipitated, calcined and poisoned samples were pressed on a Si wafer and measured at an angular velocity of 1.432 38°/min and a stepsize of 0.005 65°. Activated samples were sealed in glass capillaries (ø 0.5 mm) and measured at an angular velocity of 0.401 94°/min and a stepsize of 0.013 13°. For the sake of comparison, reference diffractograms indexed by the Joint Committee on Powder Diffraction Standard (JCPDS) were used. Interplanar distances were determined by applying Bragg's law, Ni crystallite sizes, $d_{Ni}$, were determined from line broadening of the Ni (200) reflection according to the Scherrer equation.

Temperature programmed reduction (TPR) was conducted on a Netsch STA 409 thermobalance, connected to an Omnistar GSD 301 quadrupole mass spectrometer (Pfeiffer Vacuum). Prior to analysis, samples were dried for 1 h in a stream of 60 sccm Ar at 300 °C. After cooling down to room temperature, a mixture of 10 % $H_2$/Ar was introduced and the temperature was linearly raised to 900 °C at a heating rate of 3 K/min. In order to guarantee a low enough $H_2$ consumption during TPR, catalyst masses were chosen to obtain constant $P$ values of about 2 K [183]. TPR profiles were tracked via the $H_2O$ signal, which was corrected by the amount of desorbed $H_2O$ per square meter BET surface area.

Static chemisorption of $H_2$ and $CO_2$ was carried out on an Autosorb 1C (Quantachrome) at 35 °C. Hereby, sorption equilibration times of 2 and 10 min were chosen for $H_2$ and $CO_2$, respectively. Calcined precursors were activated according to the procedure applied in the methanation reactor. Aged and poisoned samples were removed from the methanation reactor and transferred to the reaction cell under Ar atmosphere, reactivated in 5 % $H_2/N_2$ at 450 °C for 30 min (heating rate of 2 K/min), evacuated and held for 2 h. Chemisorption of $CO_2$ on activated and aged samples was carried out consecutive to $H_2$. In between, samples were heated under vacuum to 300 °C at a heating rate of 2 K/min and held for 2 h.

BET surface areas, $S_{BET}$, of calcined precursors were determined by $N_2$ physisorption on a Nova 4000e surface area analyzer (Quantachrome). Prior to analysis, samples were heated to 120 °C in vacuum and held for 3 h. Isotherms were evaluated in the $p/p_0$ range between 0.05 and

0.3 of the adsorption branch. Repeated measurements for all sorption techniques were found to scatter within the error range of the instruments (±4 %, data provided by Quantachrome).

## 6.4 Results and discussion

### 6.4.1 Catalyst characterization

As we will see in later sections, sulfur poisoning is a surface rather than a bulk phenomenon. Changes in the bulk phase of the synthesized materials during calcination, activation and poisoning are therefore only briefly addressed by using the NiAl31 system as an example. In-depth discussion of elemental analysis (section 4.3.1), XRD analysis (section 4.3.2) and TPR analysis (section 4.3.3) is presented elsewhere in this thesis. As the adsorption of $H_2$ and $CO_2$ was found to be of great importance to describe sulfur poisoning, those results are discussed in greater detail here. An overview of the most relevant characterization results is given in table 6.1.

#### 6.4.1.1 XRD analysis

XRD patterns obtained from co-precipitated NiAl31 in the dried, calcined, activated and poisoned state are shown in figure 6.1. The dried precipitate is ascribed to a synthetic takovite. The material obtained after calcination is ascribed to a homogeneous Ni-Al mixed oxide, as described by Puxley et al. [207]. For high Ni contents as in NiAl31, reflections resemble those of NiO. With increasing Al content, a gradual shift towards Al-rich phases like $NiAl_2O_4$ or $\gamma$-$Al_2O_3$ was monitored (section 4.3.2). Phase segregation was however not observed. Upon activation, $Ni^0$ crystallites of an estimated size of 3 to 5 nm are formed. As the former mixed oxide phase is not shifted as far as $\gamma$-$Al_2O_3$ or $NiAl_2O_4$ upon reduction, small amounts of $Ni^{2+}$ are expected to remain in the Al-rich lattice. TPR measurements confirm the difficulties encountered in reducing $Ni^{2+}$ within a mixed oxide as compared to pure NiO (section 4.3.3). XRD patterns recorded after *in situ* and *ex situ* poisoning resemble those obtained after activation. Peak broadening of the 62.9° reflection is probably caused by oxidation, as samples were stored in air. Most importantly, though, additional bulk phases such as $Ni_3S_2$ were not observed, indicating that sulfur is well distributed over the catalyst's surface.

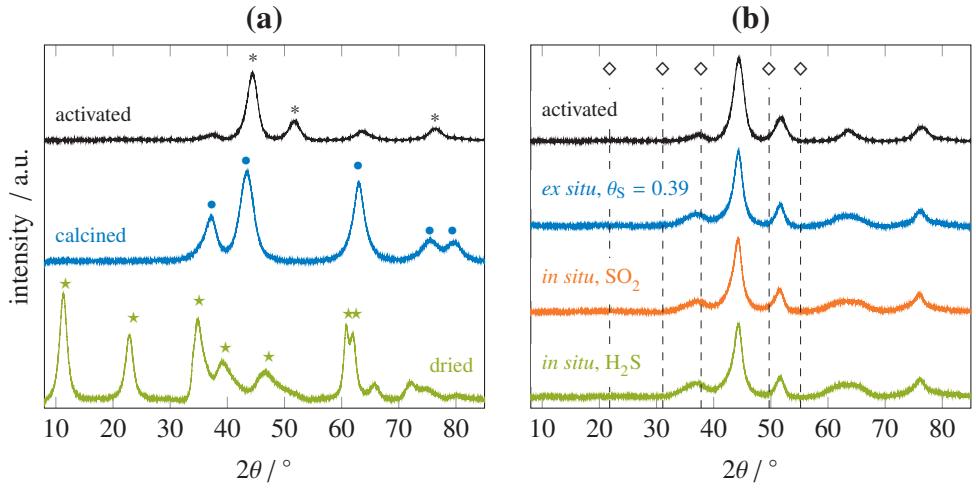


**Figure 6.1:** XRD pattern of co-precipitated NiAl31 after drying, calcination and activation (a). XRD patterns of activated, *in situ* and *ex situ* poisoned NiAl31 (b). Reference patterns are for takovite (⋆), NiO (●), $Ni^0$ (∗) and $Ni_3S_2$ (◇) (JCPDS 15-0087, 78-0429, 87-0712, 44-1418).

### 6.4.1.2 Adsorption properties

Characterization results from $H_2$ and $CO_2$ chemisorption as well as $N_2$ physisorption are listed in table 6.1. BET surface areas of NiAl15 and NiAl13 are between 230 and 260 $m^2/g_{cat}$ and slightly higher than the value obtained for pure $\gamma$-$Al_2O_3$ and NiAl11. For NiAl31 and NiAl51, the surface area significantly decreases but still remains well above 100 $m^2/g_{cat}$. NiO on the other hand exhibits a small surface area of < 30 $m^2/g_{cat}$, which emphasizes the importance of adding $Al^{3+}$ ions during the synthesis. The $H_2$ uptake of activated catalysts, as determined by static $H_2$ chemisorption, increases with the Ni content from 41 $\mu mol_{H_2}/g_{cat}$ for NiAl15 to approximately 513 $\mu mol_{H_2}/g_{cat}$ for NiAl31. Further raising the Ni content was found to be disadvantageous, as the $H_2$ uptake slightly decreases to 452 $\mu mol_{H_2}/g_{cat}$ for NiAl51. The $CO_2$ uptake of activated samples shows the same trend as the BET surface area of calcined samples, which may suggest, that $CO_2$ adsorbs primarily on the mixed oxide phase. However, small amounts of $CO_2$ were also adsorbed on reduced NiO, which rather indicates the adsorption of $CO_2$ on both phases.

Subsequent to aging catalysts at reaction conditions for 24 h, the adsorption capacities for $H_2$ and $CO_2$ were found to change significantly. Regarding the $CO_2$ uptake of all catalysts and the $H_2$ uptake of NiAl31 and NiAl51, a marked decrease was observed. This behavior is in line with a recent deactivation study carried out on very similar Ni-Al catalysts, which were treated under severe hydrothermal conditions [30]. Hereby, the decrease in $H_2$ adsorption capacity was ascribed to sintering of the Ni phase, whereas the decrease in $CO_2$ uptake was mainly attributed to structural changes of the supporting mixed oxide phase [30]. The $H_2$ uptake of

NiAl11 does not change during aging while NiAl13 and NiAl15 show an increase. In these cases, sintering seems to be less severe, which may be due to the lower Ni content. At the same time, the decrease in $CO_2$ uptake is most pronounced for these samples. Accompanying structural changes of the mixed oxide support may therefore trigger an additional reduction of $Ni^{2+}$ during aging, which eventually causes the $H_2$ uptake to increase. Also, it may be possible, that the increase of the $H_2$ inlet concentration from 10 % during activation to 40 % during aging facilitates the further reduction of the catalyst. TPR profiles of catalysts from this study (figure 4.4) indicate a low reducibility of NiAl13 and NiAl15 during the activation procedure prior to aging, as no $H_2O$ is formed at 450 °C. This does not necessarily mean that those catalysts are not reduced at all, as $H_2O$ formation begins at a slightly higher temperature and the residence time at 450 °C is only 20 s during the TPR experiment. However, an increase of the $H_2$ inlet concentration during TPR would cause a shift of the TPR profile towards lower temperatures [183] and thus facilitate the reduction. Note that $H_2$ consumption of the reaction causes the $H_2$ inlet concentration to decrease. However, $CO_2$ conversions greater 83 % are needed to reduce the $H_2$ concentration below 10 %. Initial $CO_2$ conversions monitored for NiAl13 and NiAl15 were 74 and 65 %.

**Table 6.1:** Adsorption properties of co-precipitated Ni-Al catalysts.

| | $w_{Ni}$[a] wt% | $S_{BET}$[a] $m^2/g_{cat}$ | $U_{0h}(H_2)$[b] $\mu mol_{H_2}/g_{cat}$ | $U_{24h}(H_2)$[c] $\mu mol_{H_2}/g_{cat}$ | $U_{0h}(CO_2)$[b] $\mu mol_{CO_2}/g_{cat}$ | $U_{24h}(CO_2)$[c] $\mu mol_{CO_2}/g_{cat}$ | $D_{Ni,0h}$[b] (%) | $D_{Ni,24h}$[c] (%) | $d_{Ni}$[b] nm |
|---|---|---|---|---|---|---|---|---|---|
| $\gamma$-$Al_2O_3$ | 0.0 | 209 | 0 | n.d.[d] | 386 | n.d.[d] | n.d.[d] | n.d.[d] | n.d.[d] |
| NiAl15 | 15.3 | 258 | 41 | 123 | 311 | 237 | 3.1 | 9.4 | n.d.[d] |
| NiAl13 | 21.5 | 230 | 100 | 184 | 274 | 200 | 5.5 | 10.0 | n.d.[d] |
| NiAl11 | 35.2 | 205 | 383 | 398 | 230 | 181 | 12.8 | 13.3 | 3.0 |
| NiAl31 | 57.0 | 149 | 513 | 447 | 144 | 119 | 10.6 | 9.2 | 3.5 |
| NiAl51 | 66.3 | 128 | 452 | 348 | 136 | 111 | 8.0 | 6.2 | 4.8 |
| NiO | 81.2 | 26 | 28 | n.d.[d] | 7 | n.d.[d] | n.d.[d] | n.d.[d] | n.d.[d] |

[a] Calcined precursor.
[b] Activated catalyst.
[c] Activated and aged catalyst.
[d] Not determined.

## 6.4.2 In situ poisoning

Interesting questions arising from the sulfur poisoning reaction are related to predicting the lifetime of catalysts and understanding of the prevailing mechanism. For sulfur poisoning of Ni-Al catalysts, systematic *in situ* poisoning data for $H_2S$ and $SO_2$ was collected over a wide range of Ni/Al molar ratios. In a first step, the results obtained from product gas analysis and thermography are discussed exemplarily for the NiAl11 system. Afterwards, a comparison of all Ni-Al systems is given with regards to catalyst lifetimes, sulfur and hydrogen adsorption capacities.

### 6.4.2.1 Co-precipitated NiAl11

Figure 6.2 shows the full set of data obtained for the NiAl11 catalyst upon $H_2S$ (left column) and $SO_2$ poisoning (right column). As there are no major differences between both columns, the following discussion is only carried out for $H_2S$ but also applies to $SO_2$.

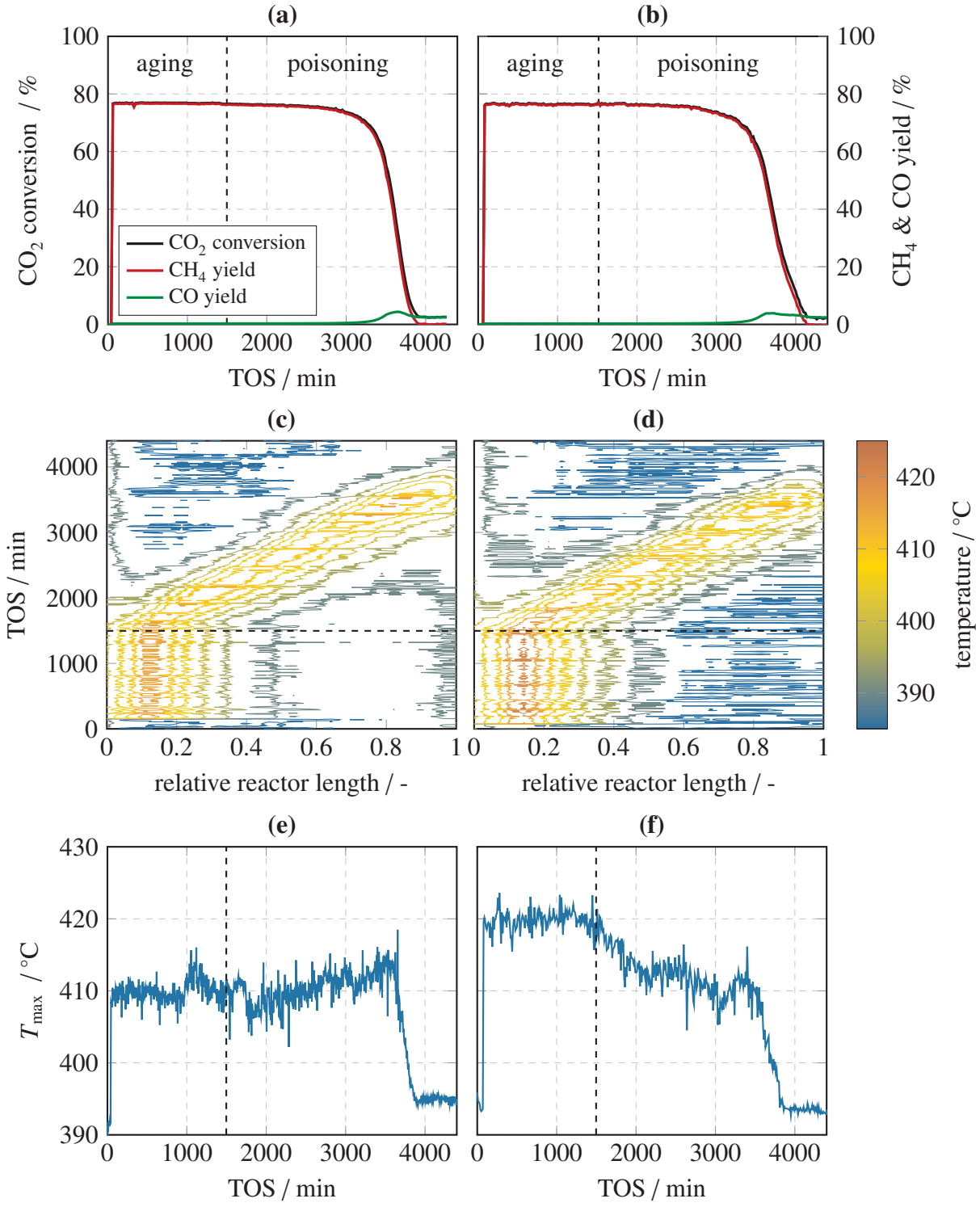


**Figure 6.2:** Results obtained from product gas analysis (a,b) and thermography (c-f) during *in situ* poisoning of NiAl11 by 5 ppm of $H_2S$ (a,c,e) and $SO_2$ (b,d,f), respectively.

Figures 6.2a and 6.2b show the results from product gas analysis depicted as $CO_2$ conversion, $CH_4$ and CO yield. Prior to the reaction, the reactor was purged with Ar for about 60 min. Afterwards, the reactants were introduced and the $CO_2$ conversion increases to an initial value of 77 %. This conversion value remains constant up to a time on stream (TOS) of 3300 min,

which includes the entire aging period (60 to 1500 min TOS) and a great part of the poisoning period. Afterwards, the conversion rapidly decreases to 3 % within a rather short time span of 3300 to 3800 min. The exact same trend is observed for the $CH_4$ yield, which however decreases to 0.0 % in the end. Conversely, the CO yield increases from 0.1 to 6.6 % over the time period of 3300 to 3800 min. Afterwards, a maximum and a decline to 2.5 % is monitored.

Additional insights into the poisoning process is provided by thermography. In figures 6.2c and 6.2d, the temperature profile within the fixed bed is depicted in the form of a contour plot as a function of reactor length and TOS. Hereby, the reactor length is defined between 0 and 1, whereas 0 describes the inlet and 1 the outlet of the catalytic fixed bed (excluding glass wool and SiC cold beds). During the aging treatment, a region of elevated temperatures, including a maximum of ca. 410 °C, was detected at the entrance of the reactor. This is ascribed to the exothermicity of the reaction. Downstream this zone, the temperature drops to 390 °C, which indicates a surplus of catalyst particles, being not actively involved in the reaction. Over the course of the aging treatment, the observed temperature profile does not change significantly. This indicates a steady-state condition of the bed and the absence of severe deactivation processes. Once sulfur is introduced, however, the situation changes drastically. Starting right after the aging period at 1500 min, the reactive zone is shifted steadily towards the reactor outlet. The position of the temperature maximum in the fixed bed is hereby changing linearly with TOS, indicating a constant moving velocity. When the end of the fixed bed is reached, the reactive zone vanishes and the entire bed shows a constant temperature of around 390 °C. Interestingly, the maximum temperature of the bed, $T_{max}$, depicted in figures 6.2e and 6.2f, does not change over the course of poisoning. An observation, which suggests that the adsorption of sulfur is (a) quantitative and (b) fast as compared to the diffusion into the bed. Note, the decrease in $T_{max}$, which is observed in figure 6.2f after changing to a sulfur containing feed, is ascribed to a variation in the overall volume flow.

In order to put the individual results from product gas analysis and thermography into a greater perspective, figures 6.2a and 6.2c need to be compared. Thereby it turns out, that the drop in activity chronologically matches the arrival of the reactive zone at the reactor outlet (3300 to 3800 min). Once the temperature of the bed has dropped to 390 °C, the catalyst's ability to form $CH_4$ is lost.

The interpretation of the *in situ* experiment is based on the idea of a poisoning front, moving through the reactor. Hereby, sulfur is continuously supplied to the front end of the reactive zone, where it adsorbs quickly and quantitatively. As a result, catalyst particles located in that area are completely deactivated and the reactive zone moves downstream the reactor, where sufficient fresh catalyst particles are available. During this process, the $CO_2$ conversion, which is an integral parameter of the entire bed, stays constant. As soon as the reservoir of fresh catalyst particles is depleted, i.e. the reactive zone reaches the end of the fixed bed, the conversion begins

to decrease. The integral activity eventually reaches its minimum, once the last particle of the bed is poisoned.

#### 6.4.2.2 Co-precipitated Ni-Al catalysts in general

In figure 6.3, an overview of all tested Ni-Al catalysts, poisoned by $H_2S$ (left column) and $SO_2$ (right column), is given. For reasons of clarity, results from product gas analysis are solely compared on the basis of $CO_2$ conversion (figures 6.3a and 6.3b) and results from thermography are solely compared on the basis of $T_{max}$ and its position within the reactor over time (figures 6.3c and 6.3d). The full set of data, as discussed for NiAl11 in figure 6.2, is shown for all samples in the supporting information (section 6.6.2). As the type of poisoning compound did not influence the results significantly, $H_2S$ poisoning is again discussed exemplarily.

Conversion data of all Ni-Al catalysts is shown in figures 6.3a and 6.3b. During the aging period, NiAl15 and NiAl13 exhibit an increase before reaching a steady-state value of 70 and 73 %, respectively. This increase in activity reflects the observed increase in $H_2$ uptake during the aging period (table 6.1) and indicates that the catalyst's surface changes within the first few hours on stream. All the other catalysts (NiAl11, NiAl31 and NiAl51) do not show any variation in conversion and the same absolute conversion of about 77 %, indicating a limitation of the reaction by thermodynamics. Following the aging period, all catalysts show a more or less extended period of constant product gas composition. Afterwards, a rapid decline to very low conversion values, as already discussed for NiAl11, was detected. Catalyst lifetimes, which are defined as the time span between introducing sulfur to the reactor and a decrease of $CH_4$ yield to half its initial value (discussed in section 4.3.1), were found to decrease in the following order: NiAl31 > NiAl11 > NiAl51 > NiAl13 > NiAl15. Interestingly, the same order was observed for $H_2$ adsorption capacities, determined after catalysts had been aged (table 6.1). A quantitative evaluation of this finding will be presented in the following section.

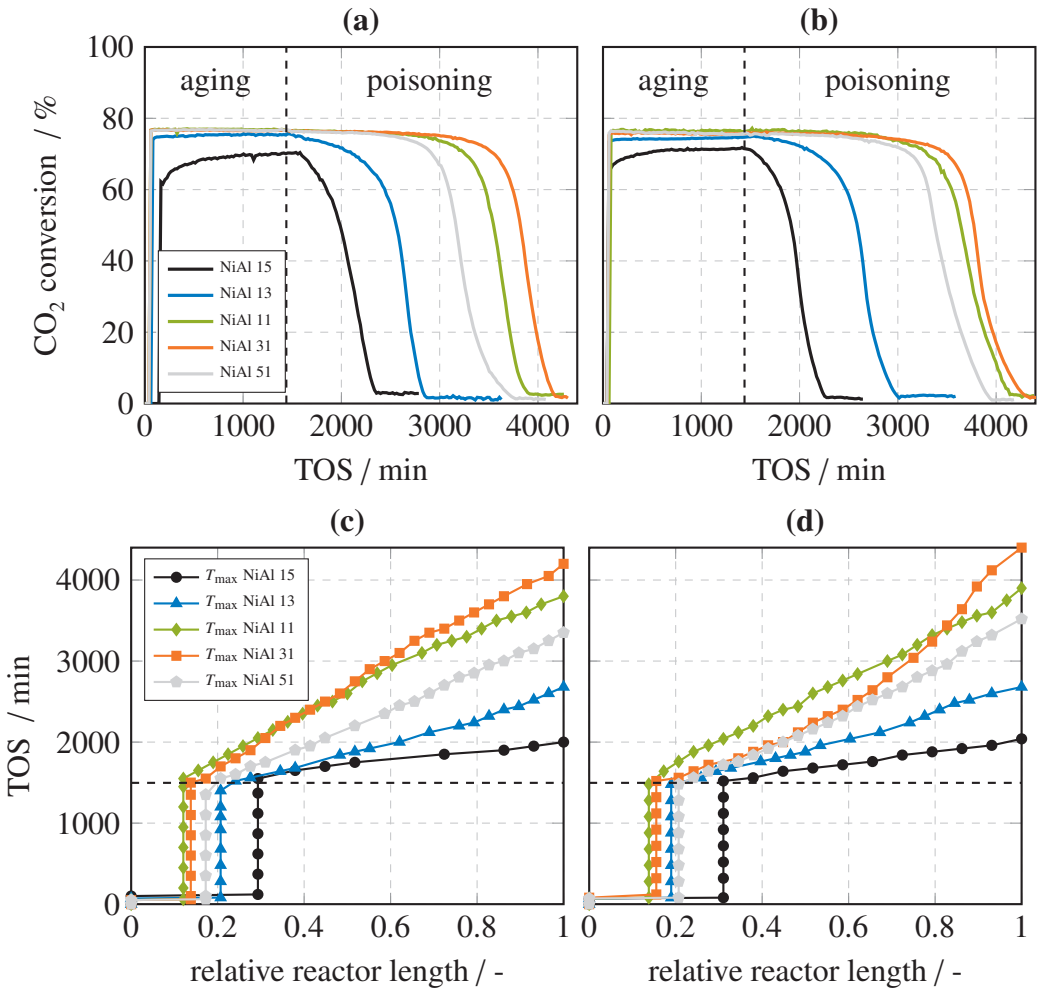


**Figure 6.3:** Results obtained from product gas analysis (a,b) and thermography (c,d) during *in situ* poisoning of different Ni-Al catalysts by 5 ppm of $H_2S$ (a,c) and $SO_2$ (b,d), respectively. Experimental errors of $T_{max}$ obtained from thermography measurements are $\pm 10$ min for TOS and $\pm 0.017$ for relative reactor length (not shown).

The results obtained from thermography are summarized in figures 6.3c and 6.3d. As observed for NiAl11, all catalysts show a constant position of $T_{max}$ over the course of the aging treatment. Once sulfur is introduced to the reactor, $T_{max}$ begins to migrate at a constant velocity towards the outlet of the reactor. The moving velocity hereby increases in the following order: NiAl15 > NiAl13 > NiAl51 > NiAl11 > NiAl31. Note, the reverse order was observed for catalyst lifetimes, which confirms the consistency of GC and thermography analysis. Further differences between the catalysts, as for example the position of $T_{max}$ during aging, are attributed to different intrinsic activities. Changes in the expansion of the reactive zone and changes in the absolute value of $T_{max}$, as observed in figures 6.12-6.15, are explained likewise.

#### 6.4.2.3 Comparison of sulfur and hydrogen adsorption capacities

In order to find a general descriptor for the lifetime of Ni-Al catalysts under *in situ* poisoning conditions, the adsorption properties of the tested catalysts were studied. Hereby, the S adsorption capacity, which is defined in this work as the amount of S determined by CHNS after completion of the *in situ* experiment, is compared to

(a) catalyst lifetimes and the cumulative amount of gaseous S fed to the reactor (figure 6.4a)

(b) $H_2$ uptakes determined by $H_2$ chemisorption after aging (figure 6.4b).

In figure 6.4a, the S adsorption capacity is plotted over catalyst lifetime. Hereby, the experimental values show an approximately linear trend, which proves the principal coherence of the CHNS data and confirms that sulfur is the reason for deactivation. Furthermore, the amount of S detected on $H_2S$ and $SO_2$ poisoned catalysts is found to be comparable, which again reflects the similar poisoning behavior of both components under the applied conditions. The dashed line in figure 6.4a describes the cumulative amount of gaseous S fed to the reactor. The close proximity of this model curve with the experimental values confirms the quantitative nature of S adsorption and provides a tool for closing the S balance of the reactor without knowing the exact breakthrough curves of $H_2S$ and $SO_2$. A detailed discussion of the model curve is given at the end of this section.

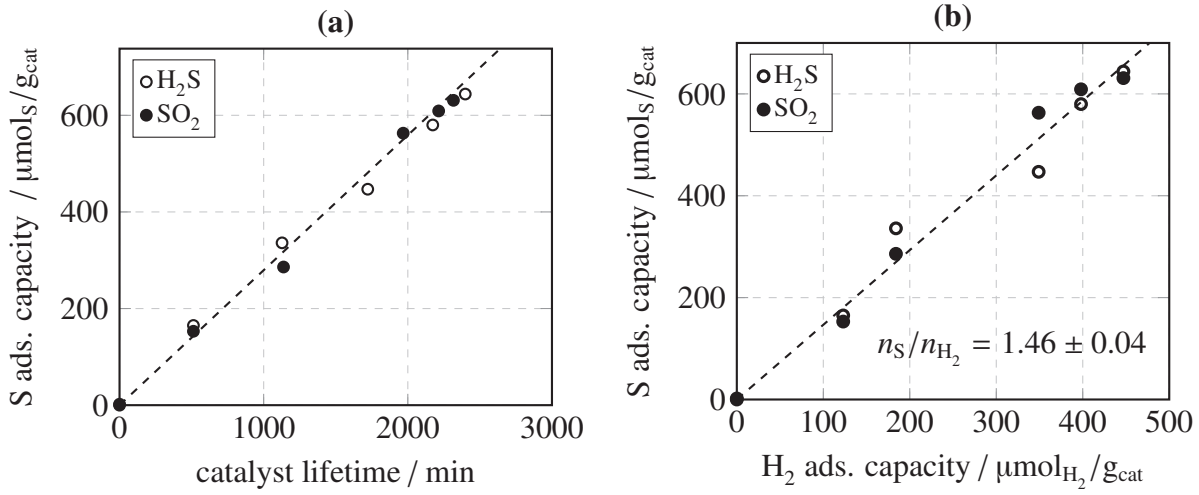


**Figure 6.4:** Dependence of S adsorption capacity on (a) catalyst lifetime and (b) $H_2$ adsorption capacity. The dashed line in (a) represents the cumulative amount of S fed to the reactor, calculated according to equation (6.17). The dashed line in (b) represents a linear regression of data obtained from $H_2S$ and $SO_2$ poisoning.

In figure 6.4b, the S adsorption capacity is plotted over the $H_2$ uptake of aged samples. Hereby, another linear correlation is obtained, suggesting, that S adsorbs on the same adsorption sites

than $H_2$. By means of a linear regression curve, the average stoichiometry of S adsorption was found to be $1.46 \pm 0.04$ per $H_2$ molecule. As the regression curve passes the origin, which represents adsorption on pure $\gamma$-$Al_2O_3$, it is suggested that neither S nor $H_2$ adsorb in considerable amounts on the support. As a consequence, the adsorption of S and $H_2$ takes place exclusively on the $Ni^0$ phase. It is well-known from chemisorption studies of $H_2$ on $Ni^0$, that each $H_2$ molecule occupies two Ni surface atoms upon chemisorption [115]. We therefore conclude that one S atom occupies on average $0.73 \pm 0.02$ Ni surface atoms. This stoichiometry lies somewhere in between the S/Ni bulk stoichiometry of $Ni_3S_2$ and NiS, being 0.67 and 1.00, respectively. However, as $H_2$ adsorption only considers Ni surface atoms, the S/Ni* surface atom ratio should be far greater than unity for bulk sulfides. Let's for example consider the NiAl11 system and assume that the degree of reduction is somewhere around 57 % [30]. The amount of $Ni^0$ then results in $0.20\,g/g_{cat}$ or $3418\,\mu mol/g_{cat}$. This is approximately one order of magnitude higher than the amount of adsorbed $H_2$ after aging ($398\,\mu mol_{H_2}/g_{cat}$, table 6.1). Thus, we should have measured a S/Ni* surface atom ratio of 4.3 in the case of bulk NiS and 6.4 in the case of bulk $Ni_3S_2$. As the measured ratio of $0.73 \pm 0.02$ is drastically smaller, we conclude that sulfur is only adsorbed on the surface. Note also, that in the case of bulk sulfide formation, the S capacity of catalysts would not correlate to the amount of Ni surface atoms but rather Ni bulk atoms.

Besides these basic estimations, our results compare quite well with literature results obtained on similar systems and the general understanding of sulfur poisoning in literature. In 1968, Rostrup-Nielsen et al. [113] have reported the adsorption of 0.03 to 30 ppm $H_2S$ in $H_2$ at 550 and 645 °C over 10 wt% Ni supported on $MgAl_2O_4$. They found an increase in the amount of adsorbed sulfur for increasing $H_2S$ partial pressures between 0.03 and 2 ppm and the development of a saturation layer above 2 ppm. The amount of sulfur in the saturation layer was found to correlate with the $H_2$ adsorption capacity of different catalysts, resulting in a S/H stoichiometry of 0.74. This value matches our result of $0.73 \pm 0.02$ very well. The formation of bulk $Ni_3S_2$ on the other hand was only observed at a significantly higher $H_2S$ partial pressure of 1000 ppm [113]. 10 years later, Oliphant et al. [112] have confirmed Rostrup-Nielsen's results by reporting S/H stoichiometries of 0.83 and 0.73 for $H_2S$ partial pressures of 8 and 12 ppm over 3 wt% Ni supported on alumina at 450 °C. Another two years later, McCarty and Wise [114] published a thorough thermodynamic study carried out on 5 wt% Ni/$\alpha$-$Al_2O_3$, showing that the chemisorption of ppb amounts of $H_2S$ is energetically highly favored over the formation of bulk $Ni_3S_2$. The obtained isosteres were obtained at $H_2S$ partial pressures between 0.01 and 1000 ppb and 140 and 700 °C. An overview of these results is given in figure 6.5. If isosteres are extrapolated, an estimated S/Ni* surface atom ratio between 0.80 and 0.86 is obtained for 5 ppm and 400 °C. This is slightly higher than observed in our study, but clearly within the same order of magnitude and far away from bulk $Ni_3S_2$ formation, which would be expected at significantly higher $H_2S$ partial pressures of about 100 ppm. Since $\xi$ values from the original publication are based on CO rather than $H_2$ uptake, they were converted to S coverages ($\theta_S$,

definition identical to S/Ni*) by multiplication with a factor of 0.714. The conversion factor results from the assumption that $11.0 \cdot 10^{14}$ molecules of CO adsorb per $cm^2$ Ni surface area, corresponding to $15.4 \cdot 10^{14}$ Ni atoms [114].

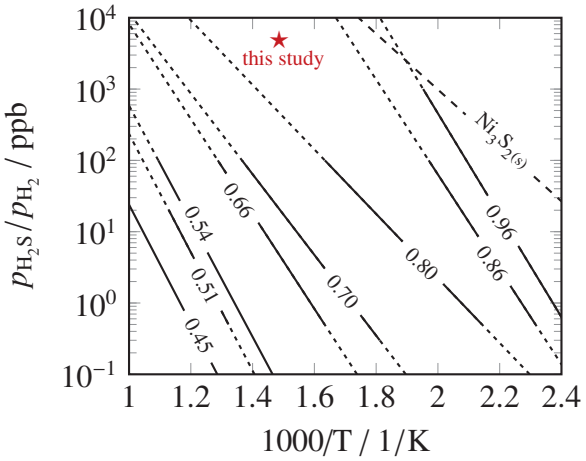


**Figure 6.5:** Sulfur chemisorption isosteres on 5 wt% Ni/$\alpha$-$Al_2O_3$ according to [114]. S coverages ($\theta_S$), based on $H_2$ adsorption, were derived from $\xi$ values, based on CO adsorption, by multiplication with a factor of 0.714. Straight lines represent the parameter space covered by [114], dotted lines represent extrapolations.

Based on our own results and the good match with literature data, we ascribe the observed poisoning effect in this study to a site-blocking mechanism of S on the catalytically active $Ni^0$ surface. As our *in situ* experiments eventually result in the complete loss of methanation activity, the adsorption/desorption equilibria for $H_2S$ and $SO_2$, depicted in equations (6.11) and (6.12), need to be greatly shifted to the adsorption side.

$$H_2S + Ni^* \rightleftharpoons Ni\text{-}S + H_2 \tag{6.11}$$

$$SO_2 + Ni^* + 2H_2 \rightleftharpoons Ni\text{-}S + 2H_2O \tag{6.12}$$

In terms of a three-dimensional $Ni^0$ crystallite, which exposes a two-dimensional $Ni^0$ surface to the reaction atmosphere, this situation corresponds to a one monolayer thick, two-dimensional Ni-S surface sulfide on top of the crystallite. The poisoning effect now obviously results form the assumption that free adsorption sites, Ni*, are able to participate in the catalytic cycle, whereas blocked sites, Ni-S, are catalytically inactive.

#### 6.4.2.4 Prediction of catalyst lifetimes

The observed linear dependency between S adsorption capacity, catalyst lifetime and $H_2$ adsorption capacity, allows for the accurate prediction of catalyst lifetimes under poisoning conditions. Hereby, the amount of S adsorbed on the catalyst's surface after saturation of the fixed bed, $n_S^\infty$, needs to be balanced by the cumulative amount of S fed to the reactor over time, as depicted in equation (6.13).

$$n_S^\infty = \int_0^t \dot{n}_S \, dt = \int_0^t (\dot{n}_{S,in} - \dot{n}_{S,out}) \, dt \tag{6.13}$$

$\dot{n}_{S,in}$ is the inlet and $\dot{n}_{S,out}$ the outlet mole stream of sulfur. $n_S^\infty$ depends on the sulfur adsorption capacity of the catalyst, which correlates with $H_2$ adsorption capacity according to figure 6.4b. If the catalytic mass within the reactor is taken into account and the S/Ni* ratio is replaced by $\theta_S$, equation (6.14) applies.

$$n_S^\infty = 2 \cdot \theta_S \cdot U_{24h}(H_2) \cdot m_{cat} \tag{6.14}$$

The right side of equation (6.14) can also be expressed as

$$\int_0^t (\dot{n}_{S,in} - \dot{n}_{S,out}) \, dt = \frac{\dot{V}_{feed}}{V_M} \cdot \int_0^t (y_{S,in} - y_{S,out}) \, dt \tag{6.15}$$

where $y_{S,in}$ and $y_{S,out}$ are the sulfur volume fractions in the inlet and outlet. The results from this study suggest that sulfur is adsorbed quantitatively until the adsorption front reaches the end of the fixed bed. From this point onwards, deactivation occurs gradually and not abruptly, suggesting that sulfur breakthrough shows the same behavior. Once no more $CH_4$ is formed, the bed is saturated. Due to these boundary conditions, it seems reasonable to assume a breakthrough curve, which is symmetric towards the $Y(CH_4)$ curve. This situation is depicted in figure 6.6. The cumulative amount of sulfur fed to the reactor then results in

$$\frac{\dot{V}_{feed}}{V_M} \cdot \int_0^t (y_{S,in} - y_{S,out}) \, dt = \frac{\dot{V}_{feed}}{V_M} \cdot y_{S,in} \cdot t_{life} \tag{6.16}$$

where $t_{life}$ is defined as the 'catalyst lifetime' and corresponds to the time when half of the initial methane yield, $1/2 \cdot Y_0(CH_4)$, is reached. It is noted, that this approach overestimates the amount of adsorbed sulfur between the time of breakthrough, $t_{bt}$, and $t_{life}$ ($A_1$ in figure 6.6) but underestimates the amount of adsorbed sulfur between $t_{life}$ and the time of complete deactivation, $t_{deac}$ ($A_2$ in figure 6.6). As the breakthrough curve is assumed to be symmetrical, both contributions cancel each other out. Summarizing equations (6.13) - (6.16) results in

$$t_{life} = \frac{2 \cdot \theta_S \cdot U_{24h}(H_2) \cdot m_{cat} \cdot V_M}{y_{S,in} \cdot \dot{V}_{feed}} \tag{6.17}$$

The suggested approach was validated for our conditions by correlating measured S adsorption capacities after *in situ* poisoning to catalyst lifetimes. The model curve in figure 6.4a shows, that equation (6.17) accurately describes the conducted measurements.

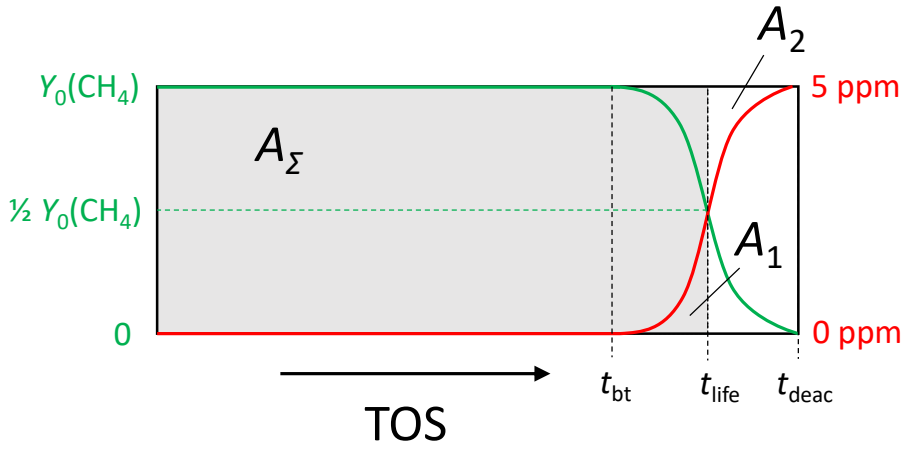


**Figure 6.6:** Correlation between sulfur breakthrough and methane yield during *in situ* poisoning experiments.

If the derived model is extrapolated to lower $H_2S$ partial pressures by means of the data provided in figure 6.5, it becomes clear that these conditions are quite unfavorable for the investigation of sulfur poisoning. On the one hand, saturation of the fixed bed requires severe amounts of time. On the other hand, sulfur coverage is only weakly dependent on sulfur partial pressure. At our conditions for instance, a decrease in sulfur coverage by only 16 % (from $\theta_S = 0.83$ to $\theta_S = 0.70$) would require a drastically reduced partial pressure of 20 ppb, resulting in an excessive saturation time of 350 days for NiAl11. Besides time aspects, there is a lower limit for adjusting sulfur partial pressures. As the detection limit of sophisticated sulfur analyzers is typically a few ppb, reproducible partial pressures below 0.1 ppb seem out of reach [114, 143, 267]. The maximum achievable sulfur coverage for the $CO_2$ methanation reaction, operated at maximum temperatures of around 450 °C due to thermodynamic reasons [38], is therefore in the region of 0.54 (figure 6.5).

Due to the described uncertainties, we backed away from *in situ* poisoning for adjusting sulfur coverages below $\theta_S = 0.73$. Instead, we turned to an *ex situ* method which we found highly suitable for studying activities of partly sulfided Ni-Al catalysts. We will see that this was a reasonable decision, because methanation rates decrease exceptionally fast with sulfur coverage. For considerable $CH_4$ formation, coverages below $\theta_S = 0.2$ are required (compare figure 6.7). We therefore firmly believe, that $H_2S$ partial pressures significantly below those adjusted by McCarty and Wise [114] are required to avoid the complete poisoning of the reaction.

As sulfur feed gas concentrations below 0.1 ppb are out of reach for current gas cleaning technologies [151, 268], the complete deactivation of catalyst particles at the inlet needs to be

accepted for industrial applications. These ‘losses’ however prevent the poisoning of catalyst particles downstream and make sure, that fixed bed lifetimes scale approximately linear (if $\theta_S$ is considered as constant) with sulfur inlet concentration. Long enough catalyst lifetimes are achievable if inlet concentrations are kept at adequate values. The exact numbers for a given catalyst and a given space velocity, are calculated according to equation (6.17). On this basis, it is also possible to compare the cost effectiveness of different gas cleaning technologies.

### 6.4.3 Ex situ poisoning

In the following sections, the effects of S coverage, $\theta_S$, on the catalytic activity, adsorption properties and apparent activation energy are discussed exemplarily for NiAl11 and NiAl31. An overview of the most relevant results is given in table 6.2. Activity data is hereby compared at 220 °C, because at this temperature all samples meet the strict criterion for differential conditions ($X(CO_2) < 10\,\%$). More flexible criteria ($< 15\,\%$, $< 20\,\%$, $< 30\,\%$) allow for the comparison of activity data at higher temperatures, which results in higher absolute activities but very similar relative activities (section 6.6.3). The dependence of activity over the entire temperature range is displayed in figures 6.17 and 6.18.

**Table 6.2:** Activities, adsorption properties and apparent activation energies of *ex situ* and *in situ* poisoned NiAl11 and NiAl31.

| | $w_S$[a] (wt%) | $\theta_S$[b] (-) | $U(H_2)$[c] ($\mu mol_{H_2}/g_{cat}$) | $U^{\Sigma}(CO_2)$[d] ($\mu mol_{CO_2}/g_{cat}$) | $U^{Ni}(CO_2)$[e] ($\mu mol_{CO_2}/g_{cat}$) | WTY ($CH_4$)[f] ($\mu mol_{CH_4}/g_{cat}$) | WTY (CO)[f] ($\mu mol_{CO}/g_{cat}$) | $E_A$ (kJ/mol) |
|---|---|---|---|---|---|---|---|---|
| NiAl11 | 0.00 | 0.00 | 397 | 173 | 66 | 5.0 | 0.0 | 80.6 |
| | 0.05 | 0.02 | 351 | 164 | 57 | 4.3 | 0.0 | 84.5 |
| | 0.24 | 0.10 | 249 | 153 | 48 | 1.7 | 0.0 | 84.8 |
| | 0.37 | 0.15 | 213 | 137 | 30 | 1.1 | 0.0 | 83.7 |
| | 0.77 | 0.30 | 119 | 116 | 9 | 0.5 | 0.1 | 81.1 |
| | 1.86* | 0.73* | 0* | 107* | 0* | n.d.* | n.d.* | n.d.* |
| NiAl31 | 0.00 | 0.00 | 575 | 130 | 75 | 8.1 | 0.0 | 81.5 |
| | 0.23 | 0.06 | 444 | 114 | 59 | 3.7 | 0.0 | 86.2 |
| | 0.40 | 0.11 | 356 | 94 | 39 | 2.1 | 0.0 | 87.0 |
| | 0.77 | 0.19 | 235 | 71 | 16 | 1.2 | 0.0 | 81.9 |
| | 1.31 | 0.36 | 101 | 63 | 8 | 0.3 | 0.1 | 81.5 |
| | 1.45 | 0.39 | 84 | 66 | 11 | 0.2 | 0.1 | 81.1 |
| | 2.60* | 0.71* | 0* | 55* | 0* | n.d.* | n.d.* | n.d.* |

[a] Determined by CHNS analysis after the *ex situ* reactor experiment and $H_2$ and $CO_2$ chemisorption.
[b] Calculated according to equation (6.8).
[c] Determined from chemisorption after *ex situ* poisoning.
[d] Determined from chemisorption after *ex situ* poisoning and $H_2$ chemisorption.
[e] Calculated according to equation (6.18).
[f] Measured at 220 °C.
[*] Determined from *in situ* poisoned samples.

#### 6.4.3.1 Activity and adsorption properties

In figure 6.7, the relative activity of NiAl11 and NiAl31 is plotted over $\theta_S$. Hereby, the activity is found to decrease exponentially with increasing coverage. This trend was found to be independent of the catalyst and of temperature (figure 6.16). Until $\theta_S = 0.2$, a drastic loss of more than 80 % of the initial activity was recorded. For $\theta_S$ between 0.2 and 0.4, activity approaches zero with the decline being less severe as compared to $\theta_S < 0.2$. Coverages exceeding 0.4 were not obtained for *ex situ* poisoned samples, although the amount of sulfur after impregnation and drying was in some cases higher. We ascribe this to the desorption of sulfur during activation and/or aging. In fact, studies conducted under low $H_2S$ partial pressures (< 0.1 ppm) [143] or UHV conditions [130] have reported saturation coverages of $\theta_S \approx 0.5$. Higher values were only obtained for specific Ni crystal planes [110] and $H_2S$ partial pressures > 0.1 ppm [112, 113]. Regarding the cross-section of a sulfur atom (0.12 nm) and a Ni atom (0.06 nm), one may speculate whether surface coverages exceeding 0.5 – 0.6 are due to surface reconstruction of the $Ni^0$ phase [110].

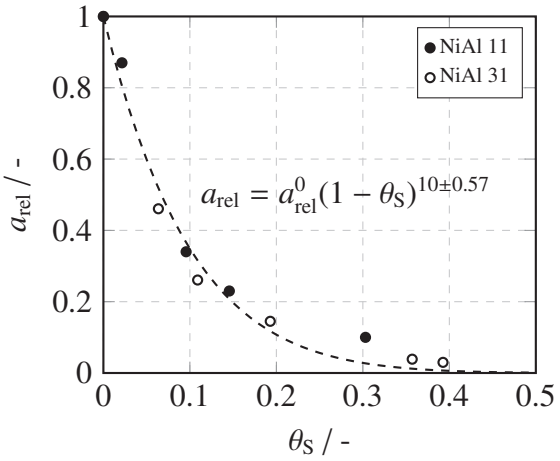


**Figure 6.7:** Relative activity over S coverage for *ex situ* poisoned NiAl11 and NiAl31 compared at 220 °C and X($CO_2$) < 10 %. The dashed line displays the best fit to a Maxted-type correlation [145] of the following kind: $a_{rel} = a^0_{rel} \cdot (1 - \theta_S)^n$.

In order to understand the drastic decrease in activity at low S coverages, $H_2$ and $CO_2$ adsorption data of poisoned catalysts need to be compared. In figure 6.8, the relative amounts of $H_2$ and $CO_2$, calculated according to equation (6.9), are plotted over $\theta_S$. In the case of $CO_2$ uptake, it was necessary to separate $CO_2$ adsorbed on $Ni^0$, $U^{Ni}_{rel}(CO_2)$, from the amount adsorbed on the Al-rich mixed oxide phase $U^{Al}_{rel}(CO_2)$. This was accomplished via the following correlation:

$$U^{Ni}_{rel}(CO_2) = U^{\Sigma}_{rel}(CO_2) - U^{Al}_{rel}(CO_2). \tag{6.18}$$

$U^{\Sigma}_{rel}(CO_2)$ is the total amount of $CO_2$ adsorbed on the catalyst, as determined by $CO_2$ chemisorption. $U^{Al}_{rel}(CO_2)$ is the amount of $CO_2$ adsorbed after *in situ* poisoning. As it was observed that *in*

*situ* poisoned samples did not adsorb any $H_2$ (table 6.2), it was assumed that the residual amount of $CO_2$ is solely adsorbed on the remaining mixed oxide phase. If now the relative amounts of $H_2$ and $CO_2$ associated to $Ni^0$ are plotted against $\theta_S$ in figure 6.8, a drastic decrease of both adsorbates is observed for $\theta_S < 0.2$. This behavior mirrors the decline in activity (figure 6.7) and can therefore be regarded as the reason for deactivation. A closer look at figure 6.8 reveals, that the decrease in $H_2$ adsorption is less pronounced as compared to $CO_2$. For $\theta_S = 0.2$, the amount of $H_2$ adsorption is 40 % of its initial value, whereas $CO_2$ adsorption is only 20 %. The decrease in $CO_2$ adsorption thus resembles the activity curve more closely, which indicates that methanation activity is limited by $CO_2$ rather than $H_2$ adsorption. From the recorded adsorption data (table 6.2), it is possible to calculate the amount of Ni* adsorption sites needed for the adsorption of S and $CO_2$. In the first case, one S atom is found to occupy on average 3 Ni* adsorption sites for $\theta_S < 0.2$ (exact value: $3.04 \pm 0.13$). This is in good agreement with studies on Ni single crystals [130], where 4 Ni* sites per S atom have been reported for $\theta_S < 0.2$. In the case of $CO_2$ adsorption, we find an average of 10 occupied Ni* surface atoms per molecule for $\theta_S < 0.2$ (exact value: $10.44 \pm 0.78$). This amount of Ni* surface sites seems rather high if the cross-section of a $CO_2$ molecule is compared to Ni atom (0.17 nm and 0.06 nm). The adsorption of $CO_2$ therefore seems to be limited to specific $Ni^0$ sites, which have a unique geometric and/or electronic configuration. This may be the interface between $Ni^0$ crystallites and the surrounding mixed oxide phase, as suggested in literature [81, 269], or simply defects, kinks, edges or corners. Unfortunately, gas adsorption is not conclusive in this respect because apparently the arrangement of Ni* sites needed for $CO_2$ adsorption cannot be distinguished from other Ni* surface sites titrated by $H_2$ chemisorption.

As it was shown in early experimental [145] and theoretical [146] approaches, the space requirements for poisoning as well as adsorbate compounds are crucial parameters for the apparent rate of deactivation. In general, deactivation was found to occur even faster, the more space was needed for reactant and poisoning species [146]. This behavior can be described by a so-called 'Maxted-type' expression [145] of the following kind: $a = a_0 \cdot (1 - \theta_i)^n$. Hereby, the exponent $n$, describes the curvature of the activity curve and $\theta_i$ the surface coverage of a poisonous species i. In a more descriptive way, $n$ can be referred to as the amount of active sites needed for the reaction [148]. Although, various other parameters, e.g. reaction order [146] and electronic effects [130, 148], have been found to influence $n$, there seems to be general consensus that it is a measure for the structure sensitivity of a reaction. In the current case, an exponent $n$ of about 10 (exact value: $10 \pm 0.57$) was found to fit the activity data best (figures 6.7 and 6.16). This result is in coherence with the amount of Ni* surface sites needed for $CO_2$ adsorption. In comparison to CO methanation studies, the $CO_2$ methanation reaction seems to be more sensitive to poisoning. Fitzharris et al. [143], for example, obtained an exponent of $n = 2$ for $H_2S$ poisoning of Ni/$\alpha$-$Al_2O_3$. Rostrup-Nielsen et al. [141] have obtained a value of $n \approx 4$ for 25 wt% Ni on stabilized alumina, also poisoned by $H_2S$. This is in line with the reported requirement of 4 Ni* sites for CO adsorption on a Ni surface [175].

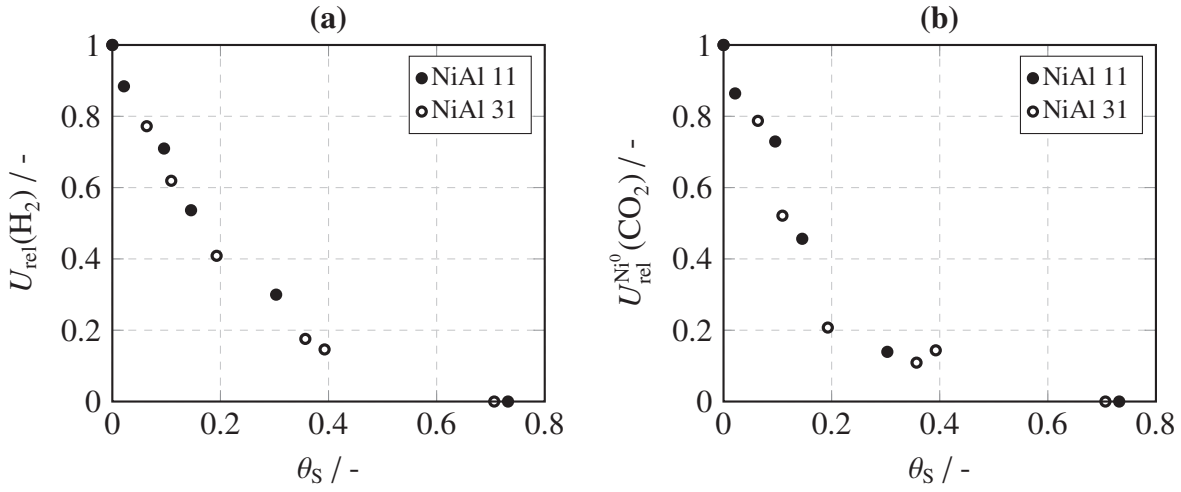


**Figure 6.8:** Relative amount of adsorbed $H_2$ (a) and $CO_2$ (b) over S coverage of *ex situ* poisoned NiAl31 and NiAl11.

In order to verify the strong dependence of activity and $CO_2$ adsorption, the absolute activity values obtained from the *ex situ* experiment, depicted as WTY($CH_4$) over the absolute amount of $H_2$ (a) and $CO_2$ (b) adsorption, are shown in figure 6.9. Both graphs show an approximately exponential increase in activity. The adsorption of up to 300 $\mu mol_{H_2}/g_{cat}$ describes the activity data very well. However, for $H_2$ uptakes greater 300 $\mu mol_{H_2}/g_{cat}$, NiAl11 and NiAl31 show a significant different behavior. The adsorption of $CO_2$ on $Ni^0$ on the other hand describes the full range of activity data without significant differences between both catalysts. Apparently, the sheer number of Ni* adsorption sites, as determined by $H_2$ chemisorption, is not the crucial parameter of activity. Instead, it seems that a certain configuration of several Ni* surface atoms is needed to enable $CO_2$ adsorption, which is then the limiting factor for activity.

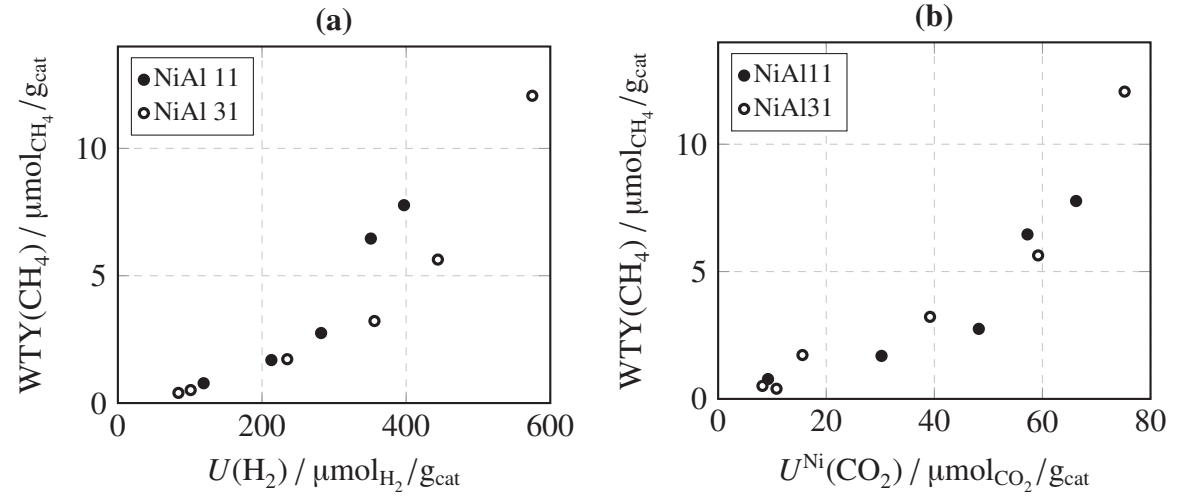


**Figure 6.9:** Absolute activities in terms of WTY($CH_4$) plotted over $H_2$ (a) and $CO_2$ (b) adsorption capacitity for *ex situ* poisoned NiAl31 and NiAl11.

#### 6.4.3.2 Determination of the apparent activation energy

From activity data recorded between 160 and 330 °C, apparent activation energies were determined before and after S poisoning. The obtained results and corresponding Arrhenius plots are shown in table 6.2 and figure 6.10. As can be seen, the determined values for different S coverages compare well to non-poisoned samples and lie in a rather narrow range of 80 to 87 kJ/mol. Furthermore, the obtained results are in good agreement with literature values of 80 and 106 kJ/mol reported for $Ni/Al_2O_3$ [86, 270, 271]. The obtained results therefore confirm the absence of mass and heat transport limitations during activity measurements and indicate, that sulfur atoms merely block the active sites of the reaction, but do not influence electronic properties of their surroundings or even change the reaction mechanism.

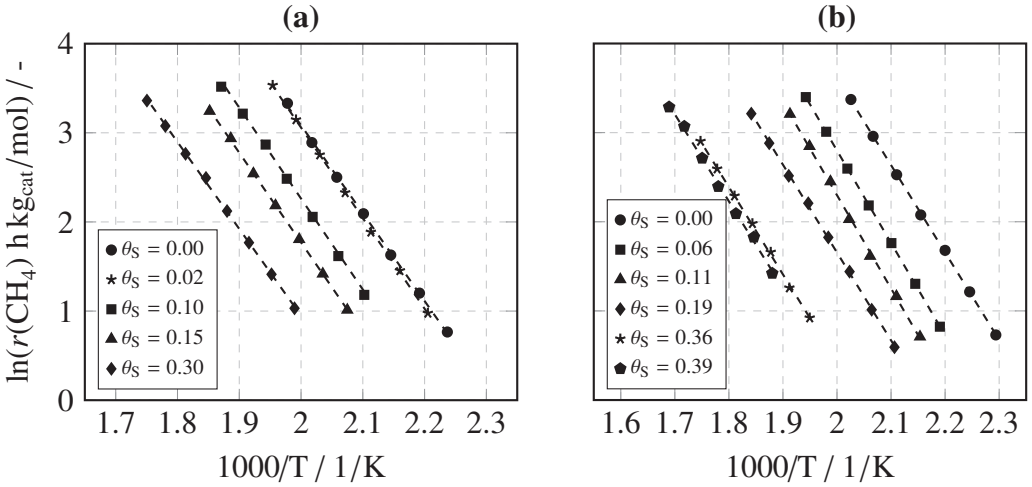


**Figure 6.10:** Arrhenius plots for different sulfur coverages of *ex situ* poisoned NiAl11 (a) and NiAl31 (b).

## 6.5 Conclusion

Sulfur poisoning of co-precipitated Ni-Al catalysts was investigated and described with regards to prevailing mechanisms and kinetics. *In situ* poisoning results in a movement of the reactive zone from the reactor inlet to the outlet. At equilibrium conditions, the activity of the bed stays constant as long as excess catalyst is available. Afterwards, activity is completely lost. The stability of catalysts against poisoning depends on available Ni surface atoms. At conditions applied here, an average sulfur adsorption capacity of $0.73 \pm 0.02$ S atoms per Ni surface atom was validated for a wide range of Ni-Al catalysts and two sulfur compounds, i.e. $H_2S$ and $SO_2$. On this basis, a generally applicable model for predicting catalyst lifetimes was derived. It was extrapolated to lower $H_2S$ partial pressures to address limitations of the *in situ* approach. For *ex situ* poisoned NiAl11 and NiAl31, a kinetic description of methanation activity as a function

of S coverage was derived. The enormous poisoning potential of a single S atom is ascribed to the space requirements for $CO_2$ adsorption. Constant activation energies of poisoned and non-poisoned samples suggest pure site blockage as the main reason for poisoning. Summarizing *in situ* and *ex situ* results, it is concluded that S poisoning of Ni catalysts cannot be avoided in industrial $CO_2$ methanation reactors. Adequate gas cleaning however extends the lifetime of fixed beds to tolerable time periods.

# 6.6 Supporting Information

## 6.6.1 XRD patterns of reference samples

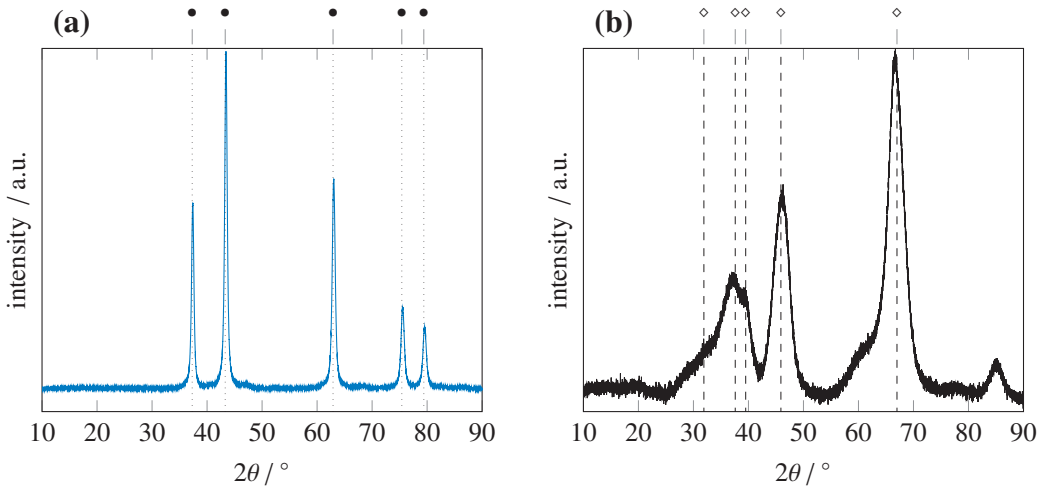


**Figure 6.11:** XRD patterns of precipitated and calcined Ni (a) and Al nitrate (b). Reference patterns are for NiO (•) and $\gamma$-$Al_2O_3$ (◇) (JCPDS 78-0429, 10-0425).

### 6.6.2 In situ poisoning of NiAl51, NiAl31, NiAl13 and NiAl15

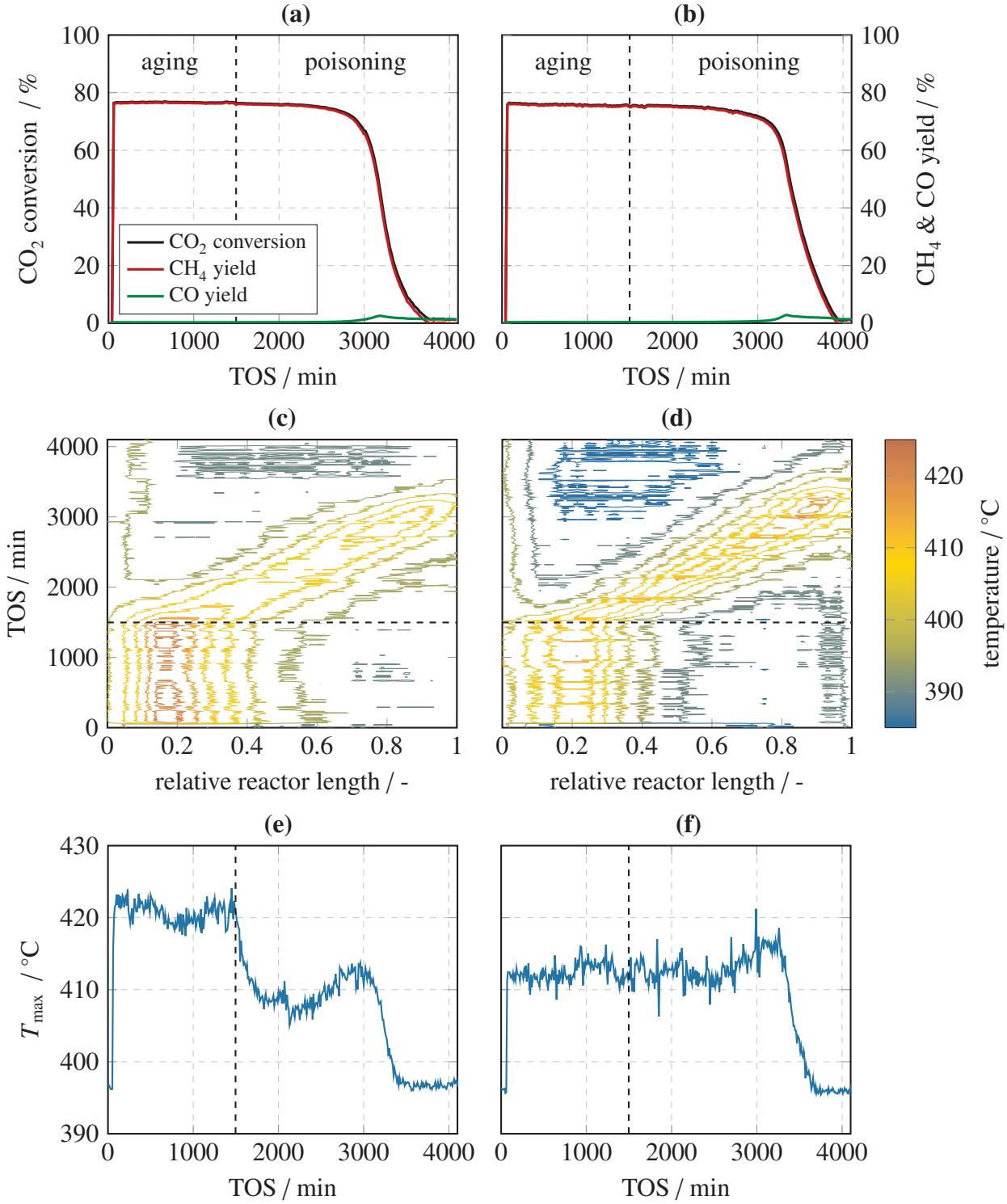


**Figure 6.12:** Results obtained from product gas analysis (a,b) and thermography (c-f) during *in situ* poisoning of NiAl51 by 5 ppm of $H_2S$ (a,c,e) and $SO_2$ (b,d,f), respectively.

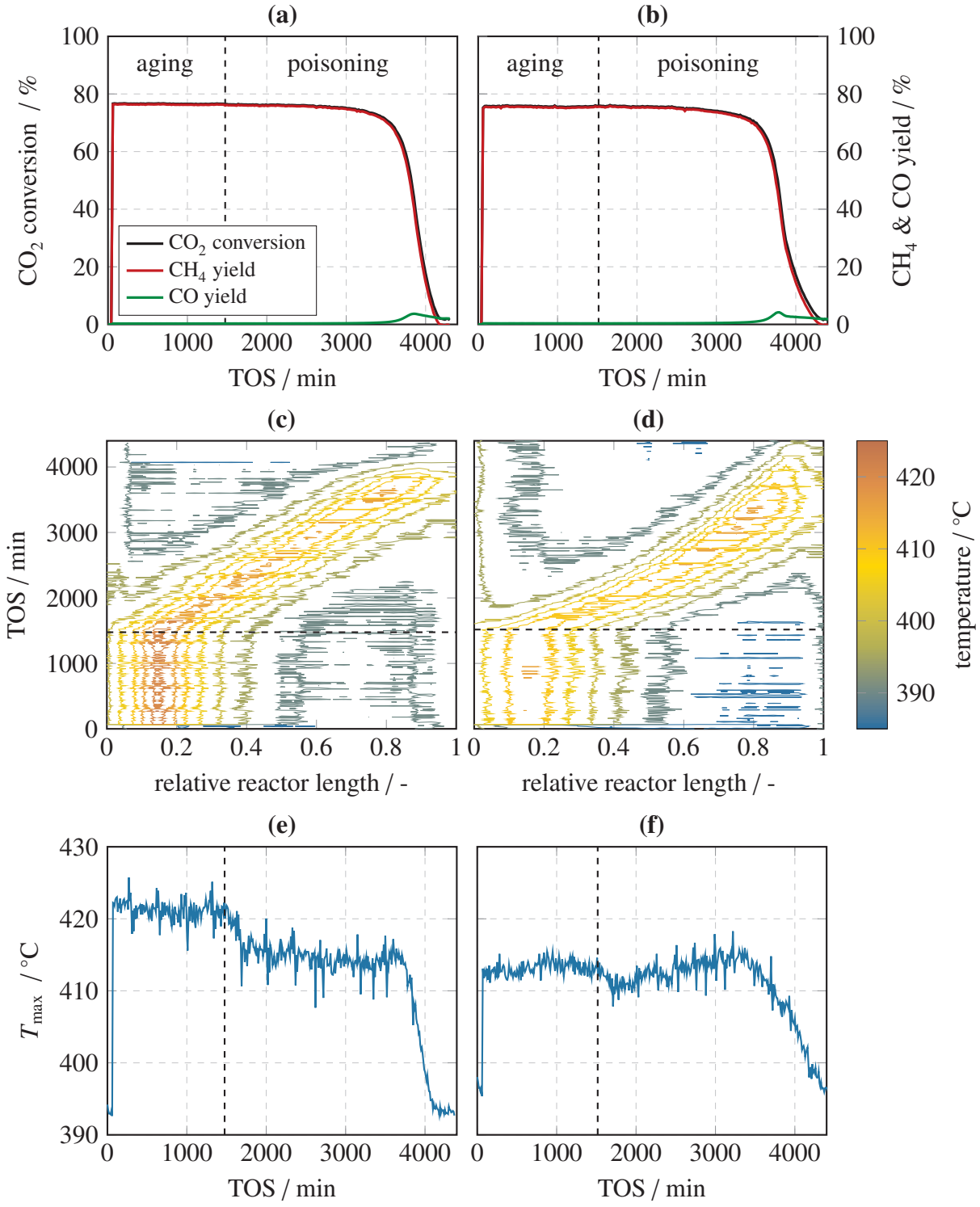


**Figure 6.13:** Results obtained from product gas analysis (a,b) and thermography (c-f) during *in situ* poisoning of NiAl31 by 5 ppm of $H_2S$ (a,c,e) and $SO_2$ (b,d,f), respectively.

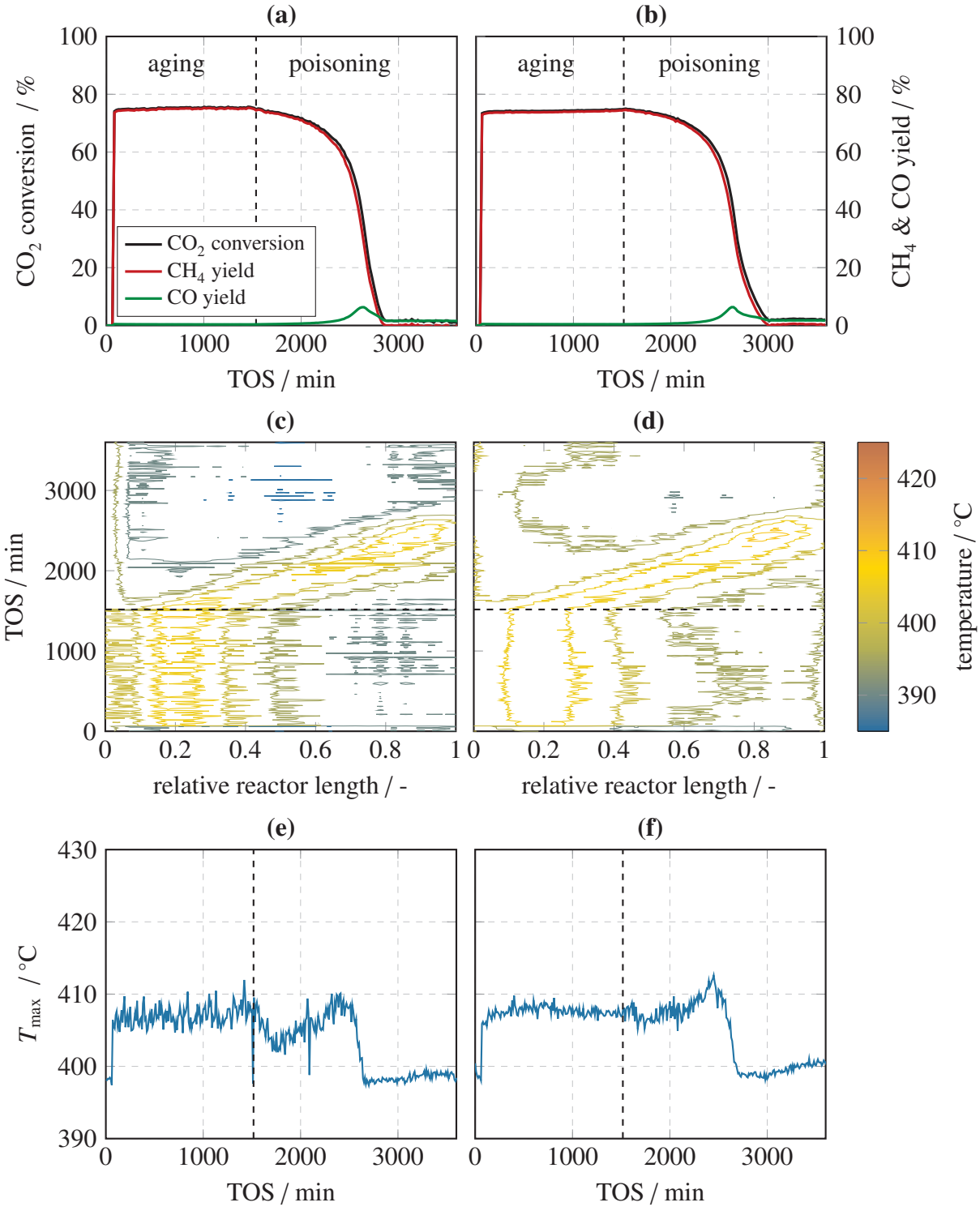


**Figure 6.14:** Results obtained from product gas analysis (a,b) and thermography (c-f) during *in situ* poisoning of NiAl13 by 5 ppm of $H_2S$ (a,c,e) and $SO_2$ (b,d,f), respectively.

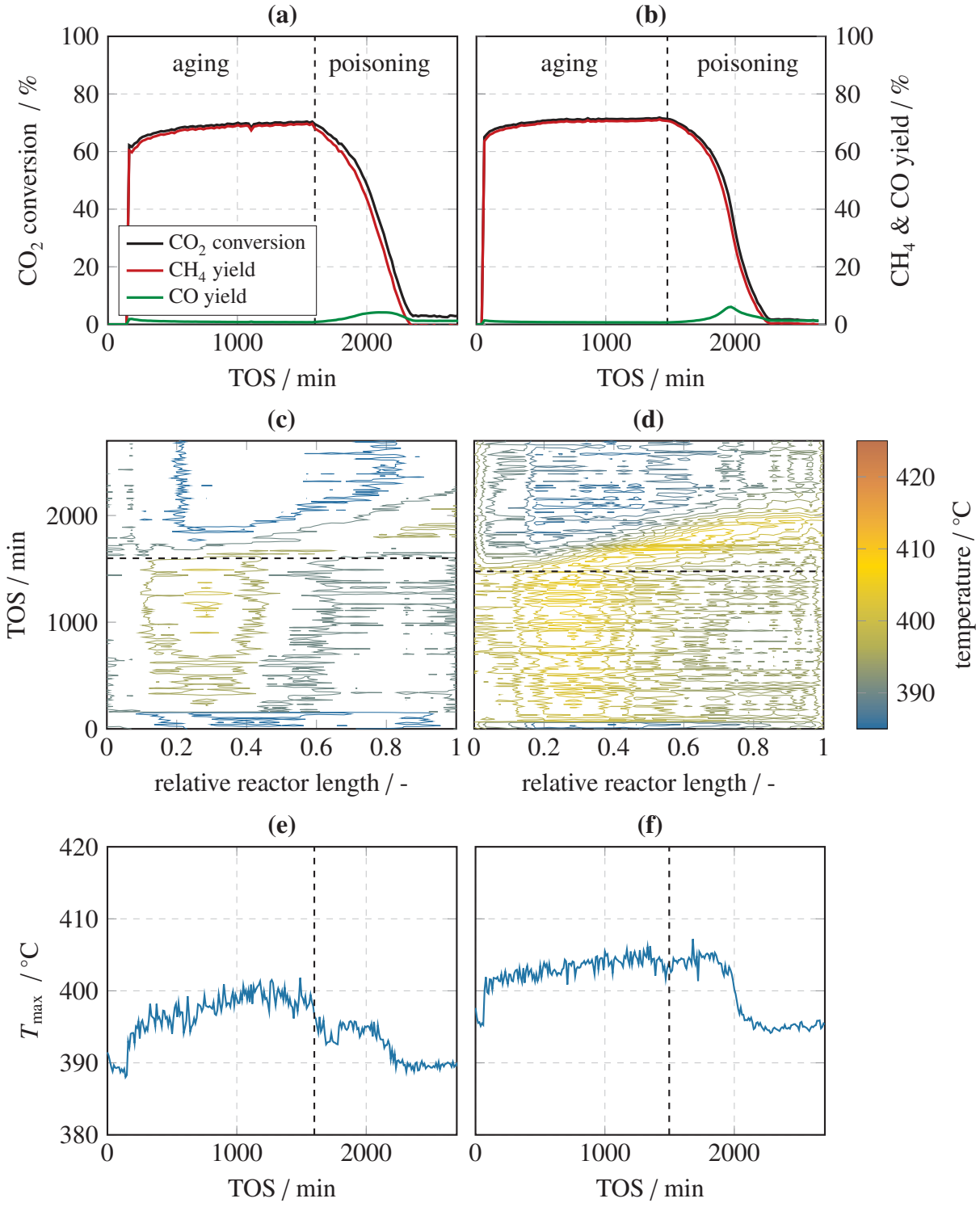


**Figure 6.15:** Results obtained from product gas analysis (a,b) and thermography (c-f) during *in situ* poisoning of NiAl15 by 5 ppm of $H_2S$ (a,c,e) and $SO_2$ (b,d,f), respectively.

### 6.6.3 Ex situ poisoning of NiAl11 and NiAl31

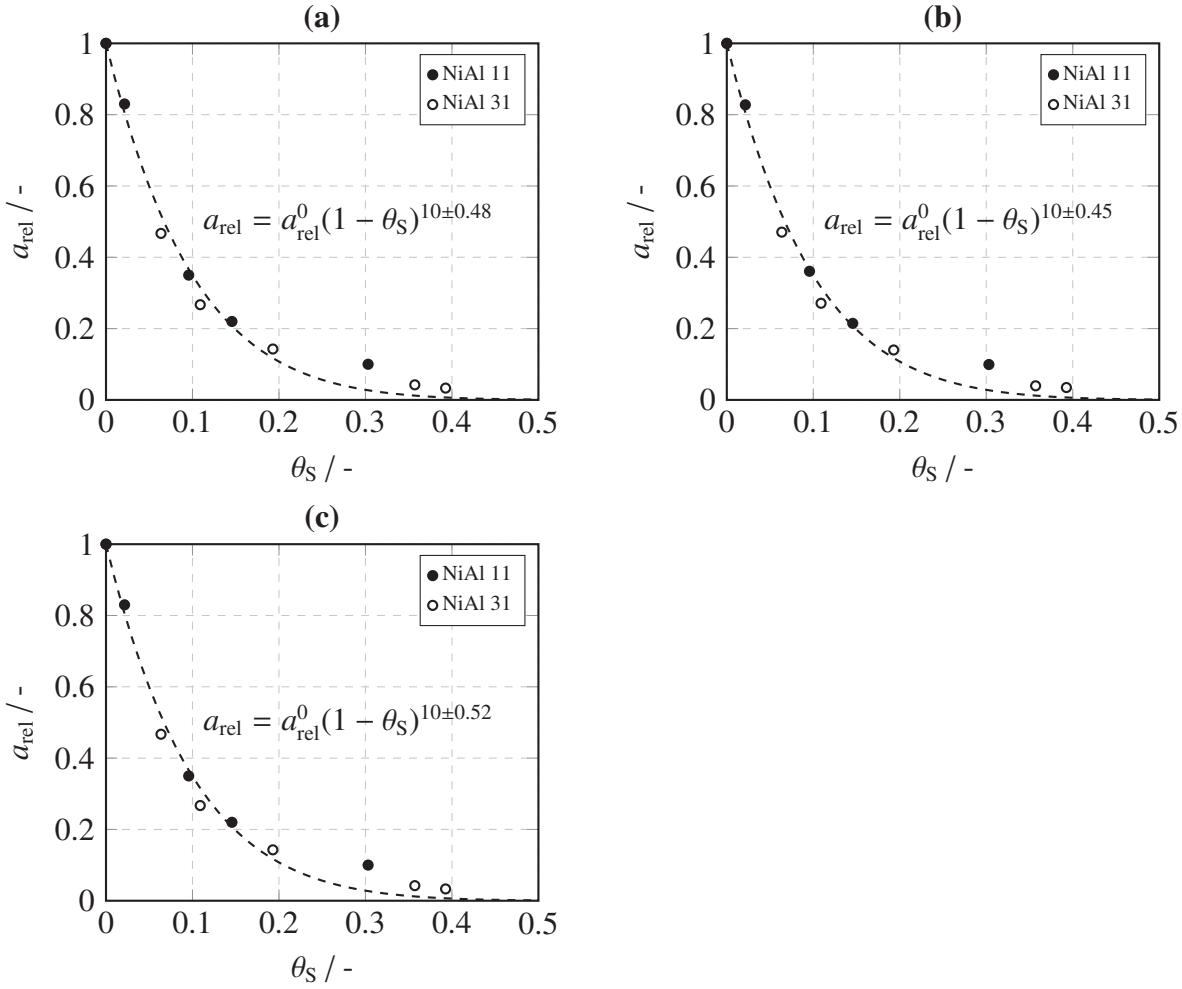


**Figure 6.16:** Relative activity over S coverage for *ex situ* poisoned NiAl11 and NiAl31 compared at 230 °C and X($CO_2$) < 15 % (a), 240 °C and X($CO_2$) < 20 % (b), and 250 °C and X($CO_2$) < 30 % (c). The dashed lines display regression curves.

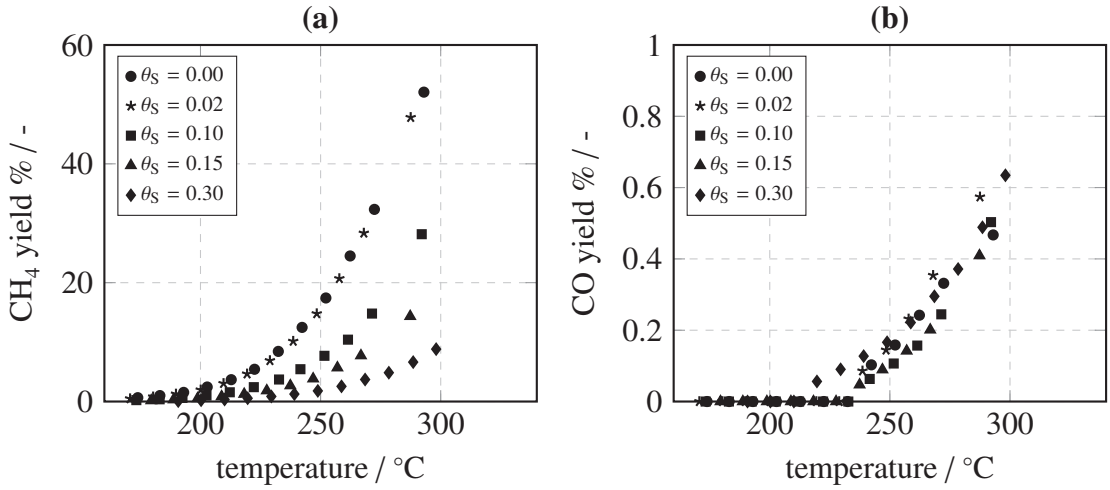


**Figure 6.17:** Activity data of *ex situ* poisoned NiAl11 obtained in the temperature range between 170 and 300 °C and displayed as $CH_4$ yield (a) and CO yield (b) over temperature.

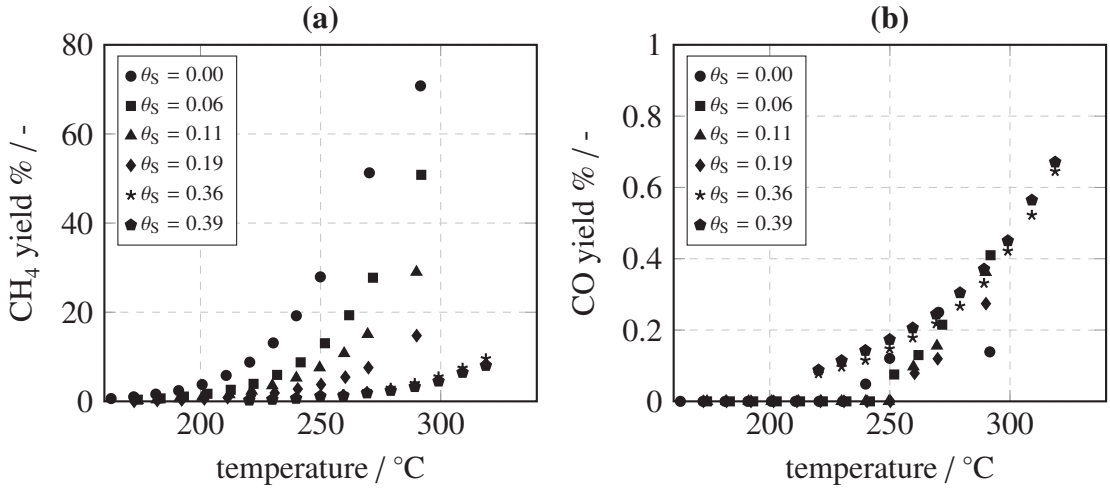


**Figure 6.18:** Activity data of *ex situ* poisoned NiAl31 obtained in the temperature range between 160 and 320 °C and displayed as $CH_4$ yield (a) and CO yield (b) over temperature.

# 7 $CO_2$ methanation on transition-metal-promoted Ni-Al catalysts: Sulfur poisoning and the role of $CO_2$ adsorption capacity for catalyst activity

Part of this chapter is published in:

M. Wolf, L. H. Wong, C. Schüler, O. Hinrichsen, $CO_2$ methanation on transition-metal-promoted Ni-Al catalysts: Sulfur poisoning and the role of $CO_2$ adsorption capacity for catalyst activity, *Journal of $CO_2$ Utilization* **2020**, *36*, 276-287.

## 7.1 Abstract

Co-precipitated and promoted Ni-Al catalysts, specifically Mn- and Fe-doped systems, rank among the most active and thermostable catalysts for the $CO_2$ methanation reaction. However, little is known about the resistance of those catalysts against sulfur poisoning and the exact reasons for activity enhancement. In order to resolve these questions, a co-precipitated Ni-Al benchmark catalyst with a Ni loading of 41 wt% was promoted by up to 5 wt% of Mn, Fe, Co, Cu and Zn. $CO_2$ methanation activity and stability against sulfur poisoning was evaluated by *in situ* poisoning with 5 ppm of $H_2S$ and *ex situ* poisoning with liquid $(NH_4)_2S$. Characterization results obtained from XRD, TPR, $N_2$ physisorption, $H_2$ and $CO_2$ chemisorption contributed to derive structure-activity relationships. All promoted samples show a superior resistance versus $H_2S$ poisoning, which is correlated to $H_2S$ adsorption on promoter phases, protecting active Ni sites. Based on the adsorption properties of spent *in situ* poisoned samples, the individual $CO_2$ uptake of the $Ni^0$ and the promoter phase were identified and correlated to $CO_2$ methanation activities of *ex situ* poisoned samples. Enhanced activities of Mn- and Fe-doped samples are

ascribed to $CO_2$ adsorption on promoter phases and subsequent conversion to $CH_4$. In contrast, $CO_2$ adsorbed on Cu is converted to CO, causing severe catalyst deactivation. Regarding activity, Co and Zn have insignificant impact. Apparent activation energies of all samples are similar and in the range of 81–92 kJ/mol. Sulfur poisoning and promoter-induced activity changes are therefore ascribed to structural rather than electronic effects for the investigated promoter loadings.

## 7.2 Introduction

Global warming has been of growing concern since decades ago. Despite numerous efforts from various countries and organizations, 2016 ranked as the warmest year since 1880, showing a higher annual global temperature than former record holders [272]. Without any declining trend in sight, it is imperative to tackle global warming. Greenhouse gases were found to contribute significantly to climate change and in particular, enormous amounts of $CO_2$ make up for more than 50 % of the key emission gases [273]. Therefore, the efficient capture and usage of $CO_2$ will provide one sustainable route to impede global warming [274, 275].

One approach to utilize $CO_2$ is catalytic hydrogenation, which can be used to produce base chemicals and fuels, e.g. methanol, dimethyl ether or synthetic natural gas (SNG). The reaction leading to the latter is also known as methanation of $CO_2$ or Sabatier reaction, named after its discoverer Paul Sabatier, who was the first to study the reaction of $CO_2$ and $H_2$ over a nickel catalyst [36]. Though known since the beginning of the 19$^{th}$ century, the Sabatier reaction has only recently gained renewed interest [42–47], because it offers a potential route towards the long term storage of large amounts of electricity from renewable sources. This idea was initially picked up by Sterner and developed to the so-called 'Power-to-Gas' concept [10]. Hereby, $H_2$ is supplied from electrolysis using surplus energy from renewable sources and is reacted with $CO_2$ separated from industrial point sources. The formed product comprises primarily $CH_4$ and $H_2O$ and can easily be stored or transported within the national gas gird after drying. At a later point in time, it can be reconverted to electricity by using gas fired power plants. This cycle is able to serve two essential needs of an energy system based on renewable energy carriers: a) providing long-term energy storage in order to absorb high fluctuations on the supplying side and b) providing fast and efficient transport between highly distributed suppliers.

The thermodynamics of the Sabatier reaction, depicted in equation (7.1), are well described and follow Le Chatelier's principle. As the reaction is exothermic and contracts in volume, low temperatures and high pressures shift the equilibrium to the product side.

$$CO_2 + 4H_2 \rightleftharpoons CH_4 + 2H_2O \qquad \Delta_r H^0_{298\,K} = -165\,\frac{kJ}{mol} \tag{7.1}$$

Thermodynamic calculations, which have been presented elsewhere [38], show that $CH_4$ yields greater 90 % and selectivities close to 100 % are achieved below 350 °C and pressures exceeding 1 bar. These conditions are the key to meet the specification for feeding SNG to the local gas grid (in Germany: < 10 % $H_2$ [39]) without costly gas purification. In this operation window, the reaction rate is however greatly limited due to slow kinetics. Hence, suitable catalysts comprising high performance but also great durability are needed. In general, several group VIII-X transition metals were found to be active for the $CO_2$ methanation [220]. Nobel metals, such as Ru [216, 276], Pd [264, 277] and Rh [224, 278] show high activities but also high costs. First row transition metals such as Fe or Co suffer from a low selectivity [85]. Ni, on the other hand, seems to be the most cost-effective metal which has been most frequently studied [30, 37, 54–58, 216]. Commonly studied support materials for Ni are $SiO_2$ [216], $Al_2O_3$ [54], $TiO_2$ [55], $ZrO_2$ [56], $CeO_2$ [57], MgO [58] and others [59–63]. Independent of the type of support, different promoter metals were found to improve catalytic properties. The most prominent ones are Fe and Mn. The latter was reported to enhance the catalytic activity of impregnated $Ni/Al_2O_3$ [75, 76] and co-precipitated Ni-Al catalysts [25, 26]. Fe was reported to enhance the catalytic activity of deposition-precipitated $Ni/Al_2O_3$ [107] and co-precipitated Ni-Al [25, 26, 62, 72] and to improve the resistance against catalyst deactivation due to hydrothermal conditions [25, 26].

In an industrial environment, catalysts are however not only stressed by long-term deactivation but also by impurities in the feed. Hereby, a specific problem arises from the usage of $CO_2$ separated from industrial exhaust gases, as these often contain sulfur. The quick and irreversible poisoning of Ni catalysts in the presence of sulfur is well-known and has been addressed by several thorough reviews on catalyst deactivation [118, 123, 266]. Systematic poisoning studies for relevant catalyst systems and operation conditions of the $CO_2$ methanation reaction are however scarce [153–156, 279].

Due to the lack of reliable data, we have recently contributed a systematic study of sulfur poisoning of co-precipitated Ni-Al catalysts [34]. In the current work, we aim at expanding our previous knowledge by the aspect of promoter metals. Therefore, we use a unique methodology, which comprises a combination of *in situ* and *ex situ* poisoning techniques, unraveling a) the impact of promoters on sulfur poisoning and b) different adsorption sites in promoted samples. The latter is particularly relevant to clarify the role of $CO_2$ adsorption capacity for $CO_2$ methanation activity. Since Mn- and Fe-promoted Ni-Al systems have shown exceptionally high catalytic performances [25], we focus on those systems in particular. For the sake of comparison, we will also discuss the impact of Co, Cu and Zn on sulfur poisoning, catalyst activity and adsorption behavior.

## 7.3 Experimental

Deionized water purified in a filter unit (Millipore) was used for the synthesis steps. All chemicals were of analytical grade and used as received. Gases were supplied by Westfalen AG and were of 5.0 purity, except for the $H_2S$/Ar gas mixture, which was composed of Ar 6.0 and $H_2S$ 1.8.

### 7.3.1 Catalyst preparation

Catalysts were prepared by co-precipitation, following a procedure described in full detail elsewhere [34]. An equimolar Ni-Al catalyst, which is serving as a benchmark sample, was synthesized from an equimolar mixture of 1 M $Ni(NO_3)_2 \cdot 6H_2O$ (Merck) and 1 M $Al(NO_3)_3 \cdot 9H_2O$ (Merck). Promoted Ni-Al catalysts were prepared by using an equimolar Ni/Al mixture and adding one promoter metal, X, at a molar ratio of Ni/X = 10/1, resulting in a promoter loading of 3-5 wt% (table 7.1), or Ni/X = 4/1, resulting in a promoter loading of 8-12 wt% (section 7.6.1). 1 M solutions of the following metal nitrates were used for promoted samples: $Mn(NO_3)_2 \cdot 4H_2O$ (Merck), $Fe(NO_3)_3 \cdot 9H_2O$ (Merck), $Co(NO_3)_2 \cdot 6H_2O$ (Merck), $Cu(NO_3)_2 \cdot 3H_2O$ (Sigma) and $Zn(NO_3)_2 \cdot 6H_2O$ (Sigma). In all experiments, the total volume of the metal nitrate solutions was kept constant at 180 ml. Calcination of the obtained precipitates was conducted in synthetic air at 450 °C for 5 h and a linear heating rate of 5 K/min. The absence of sodium ions in the calcined product was confirmed by ICP-OES. The benchmark Ni-Al catalyst is named 'Ni41', according to its Ni loading (table 7.1). Promoted catalysts are labeled 'NiX#.#', with X indicating the type of promoter metal (i.e. Mn, Fe, Co, Cu or Zn) and #.# indicating the promoter loading rounded to one decimal place (table 7.1).

### 7.3.2 Characterization

Catalyst characterization by means of ICP-OES, CHNS, XRD, TPR, $H_2$ and $CO_2$ chemisorption and $N_2$ physisorption was conducted widely in accordance with the accurate descriptions in reference [34]. Here, only diverging aspects are listed.

Apart from the content of Na, Al and Ni in non-poisoned (calcined) samples, also the content of Mn, Fe, Co, Cu and Zn was determined by ICP-OES. Therefore, the following additional wavelengths were used: 257.610 nm (Mn), 238.204 nm (Fe), 230.287 nm (Co), 324.754 nm (Cu) and 213.857 nm (Zn). In order to dissolve insoluble $MnO_2$, which was formed during

dissolution of NiMn3.3 in acidic solution, 50 mg of $Na_2SO_3$ (Merck) were added during the sonication step [34].

*In situ* XRD measurements of activated samples were carried out on a Philips X'pert instrument operated with monochromatic Cu-$K_\alpha$ radiation at 45 kV and 40 mA. Diffractograms were obtained by scanning the range between $2\theta = 5 - 90°$ with 0.013° per step and 250/min. Prior to analysis, catalysts were activated in 5 % $H_2/N_2$ at 450 °C for 8 h. Particle diameters were calculated using the Scherrer equation.

### 7.3.3 Sulfur poisoning

Sulfur poisoning experiments were conducted in an optically accessible setup described previously [33, 34]. The calcined catalyst precursor was pelletized at a pressure of ca. 9.5 kg/mm$^2$, grated and sieved to a fraction of 150 to 200 µm. 50 mg of this fraction were premixed with 450 mg of SiC (ESK, 250-355 µm), placed in the quartz glass reactor tube and sandwiched between two plugs of glass wool. Catalyst activation was carried out in 10 % $H_2$/Ar at a temperature of 450 °C for 4 h (heating rate of 2 K/min, flow rate of 62.5 sccm). Afterwards, catalysts were aged for 24 h under the following equilibrium conditions: 400 °C, $H_2/CO_2$/Ar = 4/1/5, 1 bar, 62.5 sccm. This treatment was applied to decouple catalyst deactivation due to hydrothermal conditions [23, 30] and catalyst deactivation due to sulfur poisoning [34]. The poisoning reaction was started directly after aging and comprises either *in situ* poisoning, as described in section 7.3.3.1, or *ex situ* poisoning, as described in section 7.3.3.2.

In order to monitor the reaction, gas chromatography (GC) and near-infrared thermography (NIRT) were used. GC analysis was carried out on a Shimadzu GC-14B, equipped with a thermal conductivity detector (TCD) and a micropacked ShinCarbon ST column, operated at 40 °C. NIRT was conducted by a SC-2500 near-infrared (NIR) camera (FLIR), equipped with an indium gallium arsenide detector (InGaAs), operated at wavelengths between 0.9 and 1.7 µm and a standard frame rate of 50 Hz.

By means of NIRT, the temperature profile of the fixed-bed was resolved spatially and temporally under reaction conditions. Therefore, 1 s long videos of the reactor, each consisting of 50 individual pictures (320 × 265 pixels), were shot at an interval of 10 min. The temperature along the reactor axis was extracted from the videos by placing a line profile of 30 pixels in the center of the reactor, parallel to the wall. More details on this routine are given in references [33] and [257].

Via GC analysis, the following gases were detected and quantified: $H_2$, Ar, CO, $CH_4$ and $CO_2$. Based on equations (7.2)-(7.4), the $CO_2$ conversion, the $CH_4$ yield and the CO yield were

calculated. The volume contraction of the Sabatier reaction was taken into account by using Ar as an internal standard.

$$X(CO_2) = \frac{[CO_2]_{in} - [CO_2]_{out}}{[CO_2]_{in}} \tag{7.2}$$

$$Y(CH_4) = \frac{[CH_4]_{out}}{[CO_2]_{in}} \tag{7.3}$$

$$Y(CO) = \frac{[CO]_{out}}{[CO_2]_{in}} \tag{7.4}$$

$[i]_{in}$ is the fraction of species i in the feed gas and $[i]_{out}$ is the fraction of species i in the product gas. The consistency of each data set was checked via the carbon balance, displayed in equation (7.5), which was typically closed with an accuracy of $\pm$ 3 %.

$$[CO_2]_{in} = [CH_4]_{out} + [CO]_{out} + [CO_2]_{out} \tag{7.5}$$

Furthermore, weight time yields (WTY) of $CH_4$ and CO were calculated according to equations (7.6) and (7.7), where $\dot{V}_{feed}$ is the feed gas volume flow, $V_M$ is the molar volume and $m_{cat}$ is the mass of calcined catalyst.

$$WTY(CH_4) = \frac{\dot{V}_{feed} \cdot [CH_4]_{out}}{V_M \cdot m_{cat}} \tag{7.6}$$

$$WTY(CO) = \frac{\dot{V}_{feed} \cdot [CO]_{out}}{V_M \cdot m_{cat}} \tag{7.7}$$

#### 7.3.3.1 In situ poisoning

*In situ* poisoning was carried out by co-feeding 5 ppm of $H_2S$ under thermodynamic equilibrium conditions (400 °C, $H_2/CO_2$/Ar = 4/1/5, 1 bar, 62.5 sccm). Hence, after aging, the 'clean' Ar stream was replaced by an equivalent stream of 10 ppm $H_2S$/Ar. Once the entire fixed-bed was poisoned, which was indicated by the absence of $CH_4$ in the product gas, reactants were shut off and the reactor was cooled down to room temperature upon purging with Ar. The reactor content was removed and transferred to the chemisorption instrument under inert conditions. After $H_2$ and $CO_2$ uptakes were measured, catalysts were separated from SiC and prepared for CHNS analysis.

#### 7.3.3.2 Ex situ poisoning

*Ex situ* poisoning was achieved by incipient-wetness impregnation of calcined samples with aqueous ammonium sulfide, $(NH_4)_2S_{(aq)}$. The impregnation solution was prepared by diluting the aqueous stock solution (40–44 wt% $(NH_4)_2S_{(aq)}$, abcr GmbH) by a factor of 55. 1.4 ml/$g_{cat}$ of the impregnation solution were added dropwise to the catalyst. Thus, a nominal sulfur loading of 0.50 wt% was obtained. Blank samples without sulfur were prepared with an impregnation solution containing solely water. All samples were dried at 80 °C for 18 h and subsequently treated as described in section 7.3.3, i.e. pressed, grated, sieved, mounted in the reactor, activated and aged. After aging, the reactor was purged with Ar and cooled down to 180 °C. In order to monitor the catalytic performance in dependence of temperature, the oven temperature was stepwise increased at varying step sizes of 10, 20 or 40 °C (held for 2 h each) to a final temperature of 400 °C. Afterwards, the reactor was purged with Ar and cooled down to room temperature. The reactor content was removed and transferred to the chemisorption instrument under inert conditions. After $H_2$ and $CO_2$ uptakes were measured, catalysts were separated from SiC and prepared for CHNS analysis.

## 7.4 Results and Discussion

### 7.4.1 Catalyst characterization

The goal of this chapter is to clarify the effect of promoter metals on the bulk and surface properties of an equimolar Ni-Al catalyst during calcination, activation and aging. Therefore, a variety of techniques, such as elemental analysis, XRD analysis, TPR, TGA, $N_2$ physisorption and $H_2$ and $CO_2$ chemisorption, are applied. The obtained results and discussion thereof will provide the basis for understanding activity and sulfur poisoning data.

#### 7.4.1.1 Elemental analysis

Metal loadings and molar metal ratios from ICP-OES analysis are listed in table 7.1. In general, all samples show very similar Ni/Al and Ni/promoter molar ratios of about 1/1 and 10/1, similar Ni loadings of about 40 wt% and similar promoter loadings between 3.3 and 4.6 wt%. The lowest Ni and promoter loading is obtained for NiMn3.3, which is in line with previous results for Mn-promoted systems, indicating a competitive incorporation between $Mn^{2+}$ and $Ni^{2+}$ in the precipitate [25].

**Table 7.1:** ICP-OES results of Ni41 and promoted Ni-Al catalysts.

| Sample | $w_{Ni}$ wt% | $w_{Al}$ wt% | $w_X$[a] wt% | $n_{Ni}/n_{Al}$ - | $n_{Ni}/n_X$[b] - |
|---|---|---|---|---|---|
| Ni41 | 40.6 | 18.7 | - | 1.00 | - |
| NiMn3.3 | 37.1 | 17.2 | 3.3 | 1.00 | 10.5 |
| NiFe4.4 | 43.7 | 18.3 | 4.4 | 1.00 | 9.8 |
| NiCo4.4 | 41.2 | 18.9 | 4.4 | 1.00 | 9.5 |
| NiCu4.6 | 39.4 | 18.1 | 4.6 | 1.00 | 9.3 |
| NiZn4.3 | 37.7 | 17.5 | 4.3 | 0.99 | 9.7 |

[a] Mass fraction of promoter species.
[b] Molar ratio of nickel to promoter species.

#### 7.4.1.2 X-ray powder diffraction

The XRD patterns of precipitated and calcined samples are illustrated in figures 7.1a and 7.1b. After precipitation and drying, all samples show distinct reflections at 22.8°, 34.9°, 46.5° and 62.0°, which resemble the natural mineral takovite, having a layered double hydroxide (LDH) structure and a Ni/Al molar ratio of 3. The low Ni/Al molar ratio of 1 in our samples forces the replacement of $Ni^{2+}$ by $Al^{3+}$ within the brucite-like hydroxide layers. Thus, additional positive charges are created, which need to be balanced by intercalation of anions between the layers. This typically results in a lower crystallinity when compared to Ni-Al-LDHs with high Ni/Al molar ratio [23]. Hence, the reflections at 11.3°, 22.8°, 39.1° and 60.8° are not well pronounced in our Ni41 sample. A further loss in intensity is observed for NiFe4.3, especially concerning the reflections at 11.3° and 39.1°. As $Fe^{3+}$ is added as a trivalent cation in the co-precipitation step, it might be inserted in the Ni-Al-LDH just like $Al^{3+}$, causing a similar effect on structure. In contrast, bivalent promoter ions have a neutral ($Mn^{2+}$) or positive ($Co^{2+}$, $Cu^{2+}$, $Zn^{2+}$) effect on the crystallinity of the precipitate.

After calcination, displayed in figure 7.1b, distinct reflections appear at 37.4°, 44.4°, 64.0°, 76.5° and 80.2°. This pattern resembles that of NiO but it is systematically shifted towards higher diffraction angles, which is ascribed to the formation of a $NiAlO_x$ mixed oxide. These structures are metastable and primarily observed upon low-temperature calcination of Ni-Al-LDHs [207, 280]. For high-temperature calcination between 600 and 800 °C, decomposition into $NiAl_2O_4$ spinel and NiO has been reported [23]. In our samples, which were calcined at 450 °C, we do not observe crystalline bulk $NiAl_2O_4$ spinel. Instead, the shifted NiO phase is interpreted in terms of a 'substituted nickel oxide' [207], where small amounts of $Al^{3+}$ partially have substituted octahedrally coordinated $Ni^{2+}$. Also, amorphous phases such as an Al-rich phase, containing small amounts of $Ni^{2+}$ might be present [281]. Since identical XRD patterns

are observed for all samples, promoters seem to be thoroughly incorporated and dispersed in the $NiAlO_x$ mixed oxide lattice upon calcination.

During *in situ* activation, displayed in figure 7.1c, $Ni^{2+}$ is removed from the mixed oxide phase and a crystalline $Ni^0$ phase is formed. For Ni41, this process results in a shift of the mixed oxide reflection from 64.0° to 65.0°, i.e. towards $\gamma$-$Al_2O_3$, and the formation of new signals at 44.2°, 51.8° and 76.4° due to $Ni^0$ formation. The fact that the mixed oxide reflection is not shifted as far as the $\gamma$-$Al_2O_3$ reflection at 67.0° indicates that $Ni^{2+}$ is only partially reduced and a fraction stays in the mixed oxide. For promoted samples, a very similar behavior is observed. In the case of NiMn3.3, NiCo4.4 and NiZn4.3, the mixed oxide phase is however only shifted to around 64.4°, suggesting that these promoters are not withdrawn from the Ni-depleted mixed oxide [25]. NiFe4.4 and NiCu4.6 on the other hand feature the same shift as Ni41, which indicates that these promoters behave similar to $Ni^{2+}$ and at least partially leave the $NiAlO_x$ mixed oxide. In order to confirm these trends, samples with higher promoter loadings were prepared and analyzed (section 7.6.1). XRD patterns of activated samples (figure 7.9) show identical or more pronounced trends when compared to figure 7.1c. Most noteworthy, the NiFe9.9 sample shows a clear shift of $Ni^0$ reflections towards lower diffraction angles, indicating lattice expansion due to the formation of a Ni-Fe alloy [25, 107].

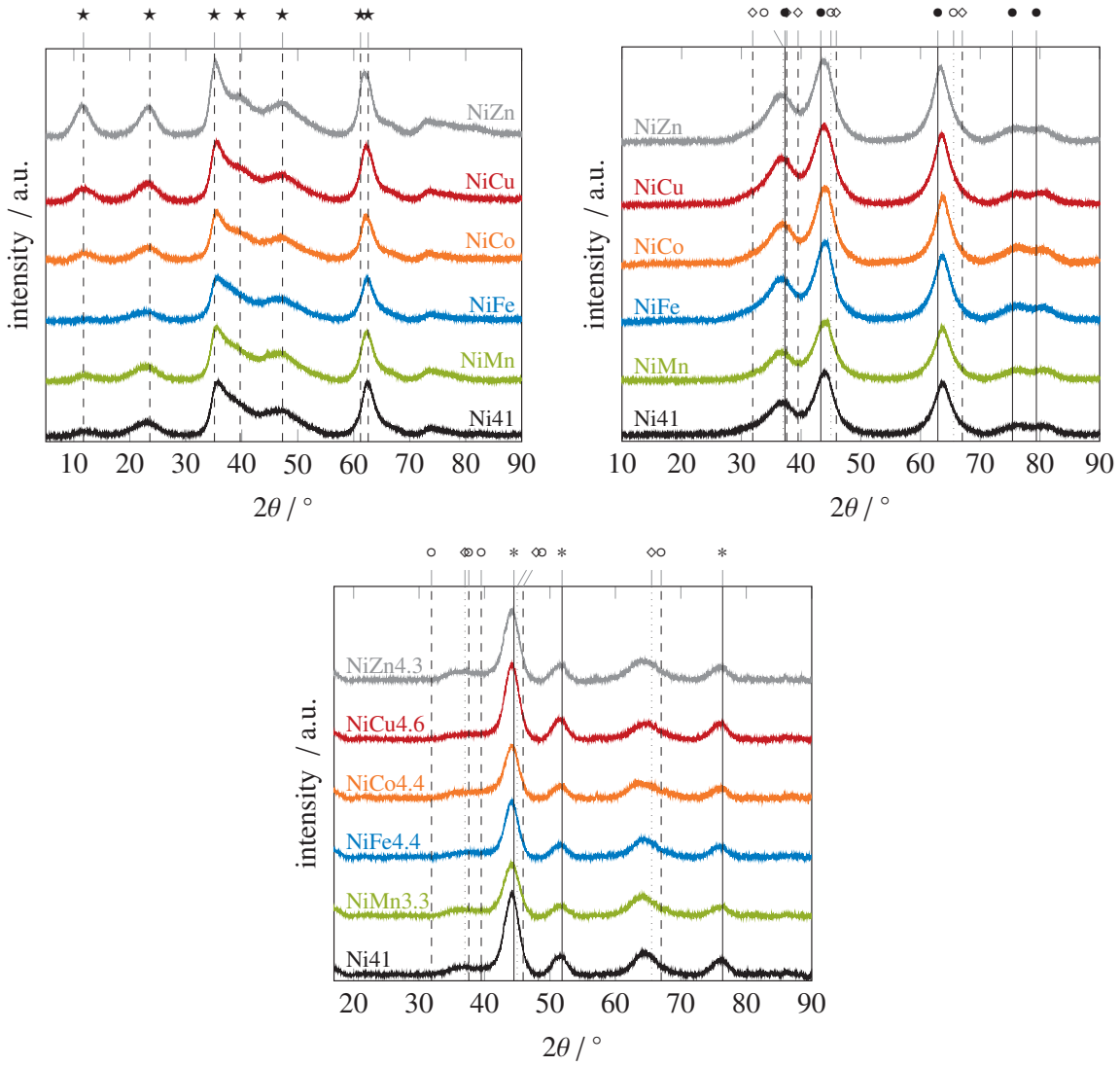


**Figure 7.1:** XRD patterns of Ni41 and promoted Ni-Al catalysts after co-precipitation and drying (a), calcination (b) and *in situ* activation (c). Reference patterns are for takovite (⋆), NiO (•), $\gamma$-$Al_2O_3$ (○), $NiAl_2O_4$ (◇) and $Ni^0$ (∗) (JCPDS 15-0087, 78-0429, 10-0425, 10-0339, 87-0712).

### 7.4.1.3 Temperature-programmed reduction

TPR profiles between 100 and 900 °C are shown in figure 7.2. Ni41 features a broad reduction signal from 350 to 850 °C, which is typical for co-precipitated Ni-Al catalysts due to the strong interactions of $Ni^{2+}$ and $Al^{3+}$ in the mixed oxide phase [101, 282]. The broad signal may be interpreted as an overlap of two reduction signals. The first one, being centered around 520 °C, may comprise the reduction of $Ni^{2+}$ from the Al-containing NiO phase. The second one, which is centered around 620 °C, might correspond to the reduction of $Ni^{2+}$ from an amorphous Ni-containing alumina phase [26].

NiCu4.6 shows a markedly different TPR curve when compared to Ni41, which features a shift of the signal maximum from 580 to 475 °C and a broad shoulder between 200 and 350 °C. The shoulder is attributed to the reduction of $Cu^{2+}$ to $Cu^{0}$, which typically occurs at lower temperatures than $Ni^{2+}$ [283]. The signal shift suggests a synergistic interaction between $Cu^{2+}$ and $Ni^{2+}$, which is known to lower the barrier for $Ni^{2+}$ reduction [283, 284]. Since the maximum of the TPR curve of NiCu4.6 is located close to 450 °C, which is the catalyst activation temperature of this study, we expect $Ni^{0}$ and $Cu^{0}$ species in the activated sample. This assumption is in line with the XRD pattern of activated NiCu4.6, indicating the removal of $Cu^{2+}$ from the mixed oxide phase (figure 7.1).

The TPR pattern of NiMn3.3 is similar to the one observed for Ni41 but features a significant low-temperature signal between 175 and 320 °C, which is ascribed to the reduction of $Mn^{2+/3+}$ to $Mn^{2+}$ [25]. Furthermore, the amount of $Ni^{2+}$ located in the Ni-rich phase seems to be lower as compared to the Ni41 reference, whereas the amount of $Ni^{2+}$ in the Al-rich phase is constant but harder to reduce, as indicated by a shift of the signal maximum towards a higher temperature of 650 °C. These results are in line with the XRD pattern of the activated NiMn3.3 sample, showing a comparably high fraction of $Ni^{2+}$ remaining in the Al-rich mixed oxide after activation (figure 7.1).

The Fe-promoted catalyst shows a similar pattern as Ni41 but a slight broadening towards lower temperatures. This behavior is assigned to the reduction of $Fe^{3+}$ to $Fe^{0}$, because XRD measurements of activated samples (figure 7.9) indicate the formation of a Ni-Fe alloy. In contrast to NiCu4.6 or NiMn3.3, the impact of promoter ions on the reduction of $Ni^{2+}$ seems to be smaller.

The Co-promoted catalyst shows a broadening towards the high-temperature side, which is attributed to the reduction of $Co^{2+/3+}$ to $Co^{2+}$ and further to $Co^{0}$. This is in concordance with XRD results presented in figure 7.1, which show that Co stays in the Al-enriched mixed oxide after activation at 450 °C.

The Zn-promoted catalysts shows an identical TPR curve as the Ni41 reference, except an additional shoulder between 750 and 900 °C. This shoulder is accompanied by a significant mass loss in the TGA curve (figure 7.10), which is explained by the reduction of $Zn^{2+}$ to $Zn^{0}$ and subsequent sublimation.

The discussed differences in TPR signals are also reflected by the simultaneously recorded TGA curves, which are presented in the supporting information (section 7.6.2).

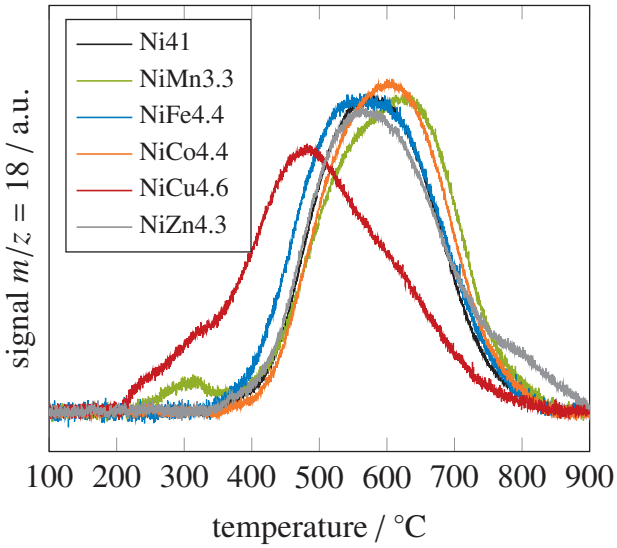


**Figure 7.2:** TPR profiles of Ni41 and promoted Ni-Al catalysts.

#### 7.4.1.4 Gas adsorption

Gas adsorption properties of all catalysts are listed in table 7.2. The BET surface area is constant between 200 and 220 $m^2/g_{cat}$ in the calcined state, confirming the thorough insertion of promoters into the $NiAlO_x$ mixed oxide. This result is in line with constant pore diameters (not shown) and XRD analysis (figure 7.1b). After activation, the Ni41 benchmark catalyst shows a $H_2$ uptake of 410 $\mu mol_{H_2}/g_{cat}$, which is comparable to the value of 416 $\mu mol_{H_2}/g_{cat}$ obtained for CoNi4.4 but higher when compared to the other samples. These differences vanish once $H_2$ uptake values are related to Ni loading. As a result, constant Ni dispersion values of 10.8 to 11.9 % are obtained. Only NiFe4.4 shows a significantly lower Ni dispersion of 8.8 %. Also, mean $Ni^0$ crystallite sizes, determined by XRD line broadening of the Ni (200) reflection, are constant within 3.6 nm $\pm$ 0.1 for all samples. As a consequence, the comparably low Ni dispersion of NiFe4.4 seems to originate from a replacement of Ni surface atoms by Fe surface atoms, which indeed show an insignificant $H_2$ uptake under the chosen conditions [285, 286].

$CO_2$ chemisorption on activated catalysts varies between 219 and 309 $\mu mol_{CO_2}/g_{cat}$. Without further information, these results are difficult to interpret, because under the chosen conditions, $CO_2$ adsorption is not selective towards $Ni^0$ or the Al-rich mixed oxide [34]. Also, an interaction between $CO_2$ and the promoter phase cannot be excluded. Hence, a detailed discussion of $CO_2$ chemisorption is conducted in section 7.4.2, where additional results of sulfur poisoned samples allow to distinguish between $CO_2$ adsorbed on different phases.

After aging, the ability for $H_2$ and $CO_2$ adsorption changes, which is a typical phenomenon observed for Ni-Al catalysts treated under hydrothermal conditions [30, 34]. The Ni41 benchmark shows a constant $H_2$ uptake, which varies only within the error of the instrument ($\pm 4\,\%$), and a severe reduction in $CO_2$ uptake. Regarding the $CO_2$ uptake, a similar behavior was observed previously and ascribed to the release (and reduction) of additional $Ni^{2+}$ from the Al-rich mixed oxide under reaction conditions, leading to pore destabilization and collapse [30, 34]. The latter directly relates to the loss of $CO_2$ adsorption sites, as those are primarily located on the structure-directing Al-rich mixed oxide [30, 34, 287]. Regarding the $H_2$ uptake, our results seem somewhat contradictory to a thorough aging study performed by Ewald et al. [30], showing that the $H_2$ uptake capacity of Ni-Al catalysts is significantly reduced within the first 24 h time on stream. It needs to be noted, however, that the reaction conditions chosen in that study are much harsher than ours (i.e. 8 bar, 15 Nml/min vs. 1 bar, 62.5 Nml/min). Hence, the constant $H_2$ uptake observed in this study can be explained by a very slow sintering rate and the release of additional $Ni^{2+}$ from the mixed oxide [34].

A similar behavior as the one described for Ni41 is observed for NiFe4.4, NiCo4.4, NiMn3.3 and NiZn4.3. In the case of NiMn3.3 and NiZn4.3, a constant $CO_2$ uptake is observed, suggesting a stabilizing effect of $Mn^{2+/3+}$ and $Zn^{2+}$ on the Al-rich mixed oxide.

In contrast to other catalysts, the $H_2$ uptake of NiCu4.6 decreases significantly upon aging, resulting in a Ni dispersion of only 8.3 %, which is comparable to NiFe4.4 (8.8 %). Based on sulfur uptake capacities, presented in section 7.4.2 (table 7.3), enhanced sintering of NiCu4.6 can be excluded. Hence, the reason for the low Ni dispersion of aged NiCu4.6 seems to be the replacement of Ni surface atoms by Cu surface atoms. An identical phenomenon is observed in Ni-Cu alloy catalysts, where Cu segregates to the surface and causes a severe decrease of $H_2$ adsorption at ambient temperatures [288].

**Table 7.2:** Characterization data including results from $N_2$ physisorption and $H_2$ and $CO_2$ chemisorption.

| Sample | $S_{BET}$ [a] $m^2/g_{cat}$ | $U_{0h}(H_2)$ [b] $\mu mol_{H_2}/g_{cat}$ | $D_{Ni,0h}$ [c] % | $d_{Ni,0h}$ [d] nm | $U_{0h}(CO_2)$ [b] $\mu mol_{CO_2}/g_{cat}$ | $U_{24h}(H_2)$ [e] $\mu mol_{H_2}/g_{cat}$ | $D_{Ni,24h}$ [c] % | $U_{24h}(CO_2)$ [e] $\mu mol_{CO_2}/g_{cat}$ |
|---|---|---|---|---|---|---|---|---|
| Ni41 | 221 | 410 | 11.9 | 3.7 | 248 | 428 | 12.4 | 196 |
| NiMn3.3 | 204 | 368 | 11.6 | 3.5 | 238 | 381 | 12.0 | 234 |
| NiFe4.4 | 209 | 326 | 8.8 | 3.6 | 252 | 328 | 8.8 | 207 |
| NiCo4.4 | 217 | 416 | 11.9 | 3.6 | 309 | 389 | 11.1 | 210 |
| NiCu4.6 | 210 | 361 | 10.8 | 3.7 | 219 | 277 | 8.3 | 156 |
| NiZn4.3 | 204 | 353 | 11.0 | 3.7 | 221 | 333 | 10.4 | 214 |

[a] Determined by $N_2$ physisorption of calcined samples.
[b] Determined by $H_2$ and $CO_2$ chemisorption of activated samples.
[c] Calculated from $U(H_2)$ and $w_{Ni}$ (table 7.2).
[d] Calculated from XRD data of activated samples, analyzing line broadening of the Ni(200) reflection.
[e] Determined by $H_2$ and $CO_2$ chemisorption of aged samples.

## 7.4.2 In situ poisoning

### 7.4.2.1 Catalytic measurements

In figure 7.3, results from catalyst deactivation and $H_2S$ poisoning at 400 °C are presented for all catalysts except NiCu4.6. The deactivation pattern of the latter differs significantly from all other samples and is therefore displayed and discussed separately based on figure 7.4.

Catalysts presented in figure 7.3 exhibit a constant $CO_2$ conversion of about 75 % during the aging period, being well in line with the thermodynamic equilibrium value under the chosen reaction conditions [33]. The corresponding thermography data, which is illustrated in figure 7.11, reveals a high-temperature region (i.e. hot spot) located at the reactor entrance (10–20 % relative reactor length). During aging, the hot spot, which is caused by fast reaction rates and the exothermal character of the $CO_2$ methanation reaction [33], neither changes its position nor its temperature, which suggests negligible catalyst deactivation. This finding is in line with $H_2$ chemisorption capacities, which are not altered upon aging (table 7.2).

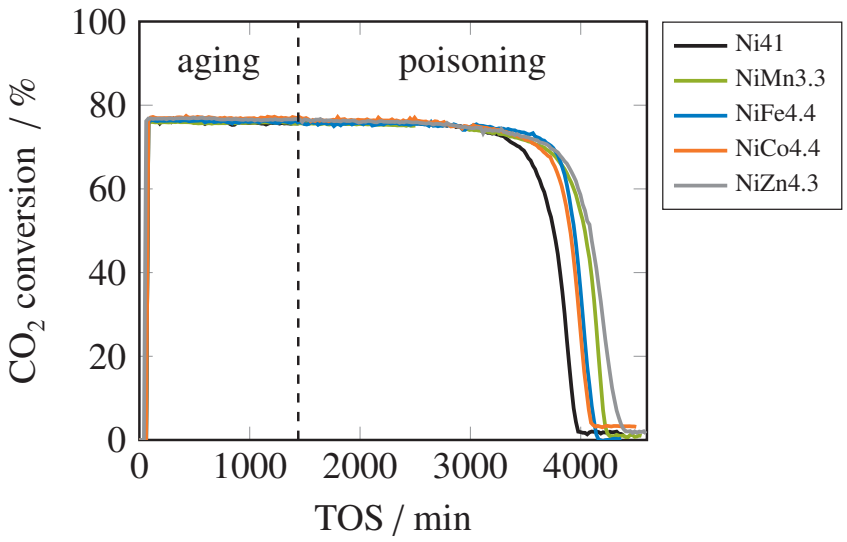


**Figure 7.3:** Results obtained from product gas analysis during *in situ* poisoning of Ni41 and promoted Ni-Al catalysts (except NiCu4.6) by 5 ppm of $H_2S$.

Subsequent to the aging period, catalysts are poisoned by 5 ppm of $H_2S$ under otherwise unchanged conditions. Hereby, the $CO_2$ conversion follows a typical pattern [34, 279], which can be divided into three distinct stages [279]: (1) constant $CO_2$ conversion, (2) rapid decrease and (3) stabilization at a very low level. In combination with thermography (figures 7.11 and 7.12), the three-staged $CO_2$ conversion curves can be explained as follows:

- In stage 1, $H_2S$ is adsorbed at the front end of the hot spot, causing the complete deactivation of catalyst particles in that region and inducing an evasive movement of the reactive zone down the reactor axis. The $CO_2$ conversion stays constant because the catalyst activity is greatly limited by thermodynamics and the non-poisoned fraction of the fixed-bed is still able to reach equilibrium conversion.

- In stage 2, $H_2S$ poisoning of the fixed-bed is far advanced and the reactive zone has moved to the rear end of the reactor. Now, the non-poisoned fraction of the fixed-bed is small and becomes a limiting factor for $CO_2$ conversion, which begins to drop very quickly.

- In stage 3, the fixed-bed is saturated and the catalyst's methanation ability is completely lost. CO is the only product formed.

At this point, it is interesting to note, that $H_2S$ concentrations in the ppb range, as they are typically observed after industrial feed gas cleaning units such as Rectisol® washes [151] or ZnO adsorbers [152], significantly elongate stage 1 of the observed $CO_2$ conversion pattern. Of course, this is the desired effect from the viewpoint of a plant operator. From a scientific standpoint, however, lifetime tests carried out under those conditions are disproportionately time consuming [34]. In order to circumvent this problem, researchers have aborted lifetime tests in stage 1 [156]. This is however not a sound procedure since the poisoning effect is obscured and results might be misinterpreted [157]. Hence, our approach to lifetime testing is the usage of a higher $H_2S$ concentration, which greatly speeds up the poisoning reaction but at the same time does not affect the poisoning mechanism [34]. In particular, the formation of bulk sulfides, which does not occur under industrial relevant $H_2S$ concentrations [114, 151, 152], needs to be avoided. By choosing $H_2S$ concentrations in the low ppm range, we are able to stay in the regime of $H_2S$ adsorption [34, 114] but increase the amount of $H_2S$ fed to the reactor (and thus the poisoning rate) by several orders of magnitude. For more details, the interested reader is referred to reference [34]. An alternative but technically more complex approach aims at completely avoiding sulfur gradients within the reactor and within the catalyst [143].

In figure 7.4, the $CO_2$ conversion of NiCu4.6 is compared to the Ni41 benchmark. Obviously, both curves differ significantly over the entire course of the experiment. During aging, the initial $CO_2$ conversion value of 75 %, staying constant for Ni41, rapidly decreases to 70 % within the first 300 min TOS and stays constant afterwards. This phenomenon is accompanied by a slight decrease in the maximum hot spot temperature (figure 7.12) and a unique drop in $H_2$ adsorption capacity during aging, being not observed for the other samples (table 7.2). We ascribe these atypical phenomena to the formation of a Ni-Cu alloy and Cu surface segregation. This mechanism is known to drastically reduce $CO_2$ methanation activities of Ni-Cu alloy catalysts [83] and also explains the drop in $H_2$ chemisorption capacity [288].

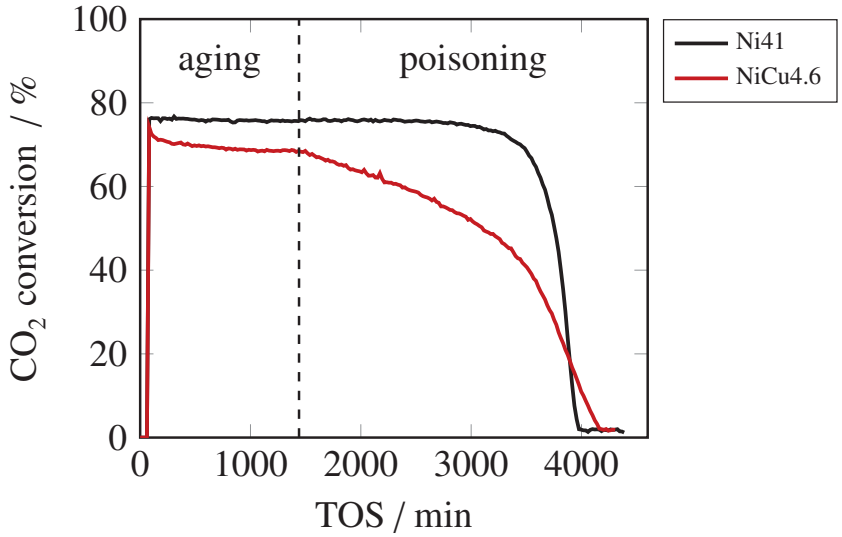


**Figure 7.4:** Results obtained from product gas analysis during *in situ* poisoning of Ni41 and NiCu4.6 by 5 ppm of $H_2S$.

Apart from catalyst aging, the NiCu4.6 sample also shows a different poisoning behavior. Instead of an initially constant $CO_2$ conversion, which is exhibited for Ni41 between about 1440 and 3400 min, a linear decrease from 70 to 50 % is observed for NiCu4.6. Afterwards, the Ni41 benchmark shows a rapid drop towards the final $CO_2$ conversion value, whereas the NiCu4.6 samples deactivates faster than before but not as drastic as Ni41. We believe that these differences are primarily a result of the activity loss of NiCu4.6 during aging. Due to the lower catalyst activity, the equilibrium value of 75 % $CO_2$ conversion is not reached at the reactor outlet. Consequently, the entire fixed-bed of NiCu4.6 contributes to $CO_2$ conversion and $H_2S$ addition immediately affects the product gas composition at the reactor outlet.

#### 7.4.2.2 Sulfur resistance

Chemisorption properties of spent catalysts, comprising CHNS analysis and $H_2$ and $CO_2$ chemisorption, are listed in table 7.3. Most noteworthy, the sulfur uptake of all promoted Ni-Al catalysts is about 10 to 20 % higher when compared to the Ni41 benchmark sample. Comparable amounts of sulfur, which significantly exceed 600 $\mu mol_S/g_{cat}$, are not reached in non-promoted Ni-Al catalysts unless the Ni/Al molar ratio is greatly increased from 1/1 to 3/1 [34]. Hence, adding a small amount of a promoter metal is an effective technique for providing additional sites for sulfur adsorption. As a consequence, promoted catalysts show elongated lifetimes when compared to Ni41. To illustrate this effect more clearly, catalyst lifetimes are plotted versus sulfur uptake in figure 7.5. The linear dashed line represents the cumulative amount of $H_2S$ fed to the reactor. All samples with the exception of NiCu4.6 are located close to the dashed

line, which means that sulfur uptake and catalyst lifetime are clearly correlated and that $H_2S$ is quantitatively adsorbed on the catalyst surface during *in situ* poisoning.

Note that the parameter 'catalyst lifetime' is defined based on a sulfur balance around the reactor, and describes the time span between the beginning of $H_2S$ poisoning and the loss of half the catalysts' initial activity. The exact details of this calculation can be found in [34]. Most importantly, the underlying assumptions are only fulfilled for the typical poisoning patterns described in section 7.4.2.1. For atypical poisoning patterns, such as the one observed for NiCu4.6 (figure 7.4), the 'catalyst lifetime' is underestimated. This is the reason why NiCu4.6 does not fit to the other samples in figure 7.5. Please note, however, that the complete loss of activity for NiCu4.6 occurs at ca. 4200 min TOS, which is significantly later than for Ni41 (ca. 4000 min, figure 7.4). Hence, the Ni surface atoms located at the very rear end of the reactor are protected more efficiently once Cu is present. This finding suggests that Cu adsorbs significant amounts of $H_2S$ and thus protects active Ni sites.

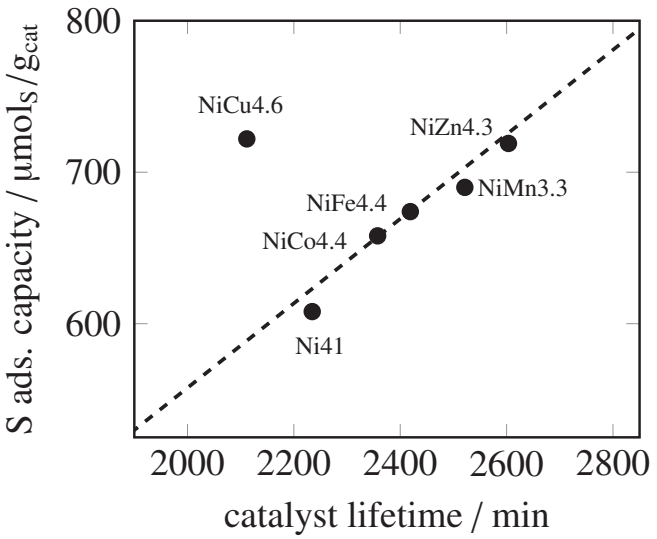


**Figure 7.5:** Dependence of S adsorption capacity on catalyst lifetime. The dashed line represents the cumulative amount of sulfur fed to the reactor, calculated according to [34].

Another result from table 7.3 is the non-existent $H_2$ uptake capacity of poisoned samples. This finding indicates the complete blockage of Ni surface atoms by sulfur atoms, assuming an insignificant $H_2$ adsorption capacity of Fe [285, 286] and Cu surface atoms [288]. In fact, for non-promoted Ni-Al catalysts, we have recently established a linear correlation between the $H_2$ uptake of aged samples and post-mortem sulfur uptake [34]. Thereby, a constant ratio of $1.46 \pm 0.04$ sulfur atoms per adsorbed $H_2$ molecule was obtained, independent of Ni loading [34]. The Ni41 benchmark of the current study shows a value of $U(S)/U_{24h}(H_2) = 1.42$ and thus confirms the previously determined ratio. In contrast, promoted samples show systematically higher values, ranging from $U(S)/U_{24h}(H_2) = 1.69$ for NiCo4.4 to $U(S)/U_{24h}(H_2) = 2.61$ for NiCu4.6. This trend indicates that $H_2S$ does not only adsorb on Ni surface atoms but also on

promoter surface atoms. In other words, the added promoter metals are able to 'protect' Ni surface atoms and consequently cause an increase in catalyst lifetime (figure 7.3).

**Table 7.3:** Chemisorption properties of *in situ* poisoned catalysts.

| Sample | $U(S)^a$ $\mu mol_S/g_{cat}$ | $U_S(H_2)^b$ $\mu mol_{H_2}/g_{cat}$ | $U(S)/U_{24h}(H_2)$ $\mu mol_S/\mu mol_{H_2}$ | $U_S(CO_2)^b$ $\mu mol_{CO_2}/g_{cat}$ |
|---|---|---|---|---|
| Ni41 | 608 | 0 | 1.42 | 125 |
| NiMn3.3 | 690 | 0 | 1.81 | 137 |
| NiFe4.4 | 674 | 0 | 2.05 | 117 |
| NiCo4.4 | 658 | 3 | 1.69 | 144 |
| NiCu4.6 | 722 | 1 | 2.61 | 80 |
| NiZn4.3 | 719 | 3 | 2.16 | 140 |

[a] Determined by CHNS analysis of *in situ* poisoned catalysts.
[b] Determined by $H_2$ and $CO_2$ chemisorption of *in situ* poisoned catalysts.

#### 7.4.2.3 $CO_2$ adsorption sites

Regarding the $CO_2$ uptake of spent samples, a marked decrease is observed for all samples when compared to the $CO_2$ uptake after aging (table 7.2). The Ni41 benchmark, for example, shows a $CO_2$ uptake of 196 $\mu mol_{CO_2}/g_{cat}$ after aging but only a value of 125 $\mu mol_{CO_2}/g_{cat}$ after poisoning. A similar decrease was observed during the aging period (table 7.2) and was ascribed to structural changes of the catalyst. During the poisoning period, however, structural changes can be neglected. Instead, the drop in $CO_2$ uptake is solely related to the blockage of Ni surface sites by sulfur. The fact that Ni surface sites do not only adsorb $H_2$ but also $CO_2$ under the chosen conditions has been demonstrated recently [34].

Despite the drop in $CO_2$ uptake upon poisoning, all samples still adsorb significant amounts of $CO_2$ in the poisoned state. This is in contrast to $H_2$ chemisorption, which is completely lost, and means that $CO_2$ adsorption is not selective towards the $Ni^0$ phase. Indeed, several recent publications have revealed a significant interaction between $CO_2$ and the Al-rich mixed oxide phase of activated Ni-Al catalysts [30, 34, 287]. Hence, the total $CO_2$ uptake of 196 $\mu mol_{CO_2}/g_{cat}$ of the Ni41 benchmark accounts for 125 $\mu mol_{CO_2}/g_{cat}$ adsorbed on the Al-rich mixed oxide (table 7.3) and 71 $\mu mol_{CO_2}/g_{cat}$ adsorbed on the $Ni^0$ phase (table 7.4). These values are in good agreement with our previous study and results of an equimolar, non-promoted Ni-Al catalyst therein [34]. Note, that the key to distinguish between $CO_2$ adsorbed on $Ni^0$ and the Al-rich mixed oxide is a $CO_2$ chemisorption measurement of an *in situ* sulfur poisoned Ni catalyst. Since this experiment is usually not carried out in conventional $CO_2$ methanation studies, only the total $CO_2$ uptake can be discussed [25, 61, 75, 289]. However, this parameter might be imprecise to establish structure-activity relationships.

For promoted Ni-Al catalysts, the situation is even more complicated, since the total $CO_2$ uptake may also contain a fraction of $CO_2$ associated to the promoter phase. However, based on our unique set of data presented in this work, we have developed a simple model to handle these kinds of ternary systems and quantify the amount of $CO_2$ adsorbed on each of the three phases, i.e. $Ni^0$, the Al-rich mixed oxide and the promoter phase. Note, that this kind of phase separation is only of imaginary nature, well-knowing that mixed phases might be present in the actual catalysts, for example the incorporation of Mn, Co and Zn into the Al-rich mixed oxide, or possible alloy formation between Fe and Ni or Cu and Ni. Nevertheless, the idea of separated phases will help to elucidate the effect of promoters on $CO_2$ uptake. Hence, we establish the following $CO_2$ balance

$$U^{\Sigma}(CO_2) = U^{Ni}(CO_2) + U^{Al}(CO_2) + U^{X}(CO_2), \tag{7.8}$$

where $U^{i}(CO_2)$ describes the $CO_2$ uptake capacity and superscripts, i, relate to the sum over the entire sample ($i = \Sigma$), the $Ni^0$ phase ($i = Ni$), the Al-rich mixed oxide phase ($i = Al$), or the promoter phase ($i = X$).

The sum of all contributions to $CO_2$ uptake, $U^{\Sigma}(CO_2)$, is equal to the $CO_2$ uptake prior to poisoning, $U_{24h}(CO_2)$, being listed in table 7.2. Also, for promoted samples, higher sulfur uptakes than Ni41 were found, which indicates that sulfur does not only adsorb on Ni surface sites but also on promoter surface sites. Under the assumption that these sites are occupied by sulfur and not available for $CO_2$ adsorption, the $CO_2$ uptake of poisoned samples, $U_S(CO_2)$, solely relates to the Al-rich mixed oxide, being therefore equal to $U^{Al}(CO_2)$. The assumption that sulfur poisons $CO_2$ chemisorption sites is justified by the fact that sulfur is a common poison for all kinds of metal and oxide catalysts [110, 290] and reactant adsorption of presulfided surfaces commonly decreases when compared to the non-poisoned state [110, 291].

In the case of the Ni41 benchmark, no promoter is present, and the last term of equation (7.8), $U^{X}(CO_2)$, can be set to zero. Consequently, the amount of $CO_2$ adsorbed by Ni surface atoms, $U^{Ni}(CO_2)$, results in $71\,\mu mol_{CO_2}/g_{cat}$. If this value is related to the corresponding $H_2$ uptake, $U_{24h}(H_2) = 428\,\mu mol_{H_2}/g_{cat}$, a stoichiometry factor of 6.0 is obtained for $H_2$ and $CO_2$ chemisorption on $Ni^0$. If it is now assumed, that $H_2$ and $CO_2$ adsorption on $Ni^0$ is not affected by the promoter, the $CO_2$ uptake of the promoter phase can be expressed as

$$U^{X}(CO_2) = U_{24h}(CO_2) - U_S(CO_2) - \frac{1}{6} \cdot U_{24h}(H_2). \tag{7.9}$$

Note, that the latter assumption is acceptable for promoters like Mn, Co and Zn, which are incorporated into the Al-rich mixed oxide, but somewhat controversial for Fe and Cu. Regarding those promoters, a deviation of the determined stoichiometry factor, induced for example by

alloy formation and electronic interaction with the $Ni^0$ phase, cannot be ruled out. This possible bias will be taken into account when discussing structure-activity relationships in section 7.4.3.3.

Based on equation (7.9), it is possible to determine each of the summands of equation (7.8) separately. Results are listed in table 7.3. Most noteworthy, the highest $CO_2$ uptake of the promoter phase is observed for NiMn3.3, NiFe4.4 and NiCu4.6, showing $CO_2$ uptakes between 30 to 35 $\mu mol_{CO_2}/g_{cat}$. A slightly lower value of 19 $\mu mol_{CO_2}/g_{cat}$ is observed for NiZn4.3. Negligible amounts of $CO_2$ were adsorbed on the promoter phase of NiCo4.4.

**Table 7.4:** Chemisorption properties of aged and *in situ* poisoned samples.

| Sample | $U^{Al}(CO_2)$[a] $\mu mol_{CO_2}/g_{cat}$ | $U^{Ni}(CO_2)$ [b] $\mu mol_{CO_2}/g_{cat}$ | $U^{X}(CO_2)$ [b] $\mu mol_{CO_2}/g_{cat}$ | $U^{Ni+X}(CO_2)$[c] $\mu mol_{CO_2}/g_{cat}$ |
|---|---|---|---|---|
| Ni41 | 125 | 71 | 0 | 71 |
| NiMn3.3 | 137 | 64 | 34 | 98 |
| NiFe4.4 | 117 | 55 | 35 | 90 |
| NiCo4.4 | 144 | 65 | 1 | 66 |
| NiCu4.6 | 80 | 46 | 30 | 76 |
| NiZn4.3 | 140 | 56 | 19 | 75 |

[a] Equal to $U_S(CO_2)$ from table 7.3.
[b] Calculated by equations (7.8) and (7.9).
[c] Sum of $U^{Ni}(CO_2)$ and $U^{X}(CO_2)$.

## 7.4.3 Ex situ poisoning

In this chapter, the effect of small amounts of sulfur, distributed homogeneously throughout each catalyst particle and the entire fixed-bed, is discussed with regards to activity, adsorption properties and apparent activation energy. Sulfur-free reference catalysts, with a nominal sulfur loading of $w_S = 0.00\,wt\%$, and sulfur-containing catalyst, with a nominal sulfur loading of $w_S = 0.50\,wt\%$, were synthesized following the procedure described in section 7.3.3.2. Sulfur loadings of spent samples are listed in table 7.5.

### 7.4.3.1 Catalytic measurements

$CO_2$ methanation activities of all catalysts were determined after aging, following the procedure described in section 7.3.3.2. Results are displayed in figure 7.6 in terms of $CH_4$ and CO yield, grouped by non-poisoned (a,b) and poisoned (c,d) samples. In order to highlight the effect of

sulfur on the individual catalyst, activity data is grouped for each catalyst separately in figures 7.13 and 7.14.

Non-poisoned samples show a slight increase in $CH_4$ yield between temperatures of 170 and 230 °C, followed by a steep growth of the reaction rate. The approach to equilibrium for $CH_4$ yields exceeding 70 % slows down as primarily $H_2O$ starts to dampen the reaction [23]. NiCu4.6 is the only sample which does not reach the equilibrium $CH_4$ yield at 400 °C. Regarding $CH_4$ formation, the following activity order can be determined in the temperature range between 230 and 310 °C: NiFe4.4 > NiMn3.3 > Ni41 ≈ NiCo4.4 ≈ NiZn4.3 ≫ NiCu4.6. The reverse order is observed for CO formation between 270 and 350 °C. However, very low CO yields between 0 and 0.5 % are monitored for all catalysts except NiCu4.6 over the entire temperature range (170–400 °C). NiCu4.6 shows an exceptionally high CO yield of up to 2.5 %.

Regarding $CH_4$ yields of poisoned samples, all monitored curves show a marked shift towards higher temperatures. Hence, the steep growth of the reaction rate is shifted by approximately 40 °C from 230 to 270 °C. Furthermore, equilibrium yields are not achieved until the temperature is increased to 400 °C, which is approximately 50 °C higher when compared to the non-poisoned state. However, a similar activity order is monitored: NiMn3.3 ≈ NiFe4.4 > Ni41 ≈ NiCo4.4 ≈ NiZn4.3 ≫ NiCu4.6. Again, the reverse trend is observed for CO yield, only this time at a slightly higher temperature range of 300–400 °C. All poisoned samples show a higher CO yield than non-poisoned samples, ranging between 0–1.5 % for all samples except NiCu4.6 and between 0–4.5 % for NiCu4.6.

Note, that most of the experimental values obtained for the CO yield in figures 7.6b and 7.6d are located above the thermodynamic equilibrium. It needs to be emphasized that this phenomenon only occurs in the presence of a catalyst, whereas an empty reactor led to negligible CO formation. Without studying the kinetics in detail, we hypothesize that the specific role of CO as an intermediate in the Sabatier reaction pathway may provide a coherent explanation. To us, it seems possible that the increase in CO yield above equilibrium values is caused by an increase of the $CO_2$ dissociation rate relative to the CO activation rate, resulting in an accumulation of adsorbed CO on the catalyst's surface and subsequent CO desorption. At higher temperatures, this situation is reversed and the CO yield runs through a local maximum before finally approaching equilibrium values. For temperatures exceeding 400 °C, the CO yield of all catalysts was in line with equilibrium values.

The presented kinetic explanation may be further expanded to cover also the drastic effect of sulfur and copper on CO yield. Both components were found to decrease the amount of accessible Ni surface atoms and at the same time increase CO formation. Thus, the blockage of Ni surface atoms seems to hinder primarily CO hydrogenation and to a lesser extent $CO_2$ dissociation. Experimental evidence for this theory is provided by the completely poisoned

catalysts of the *in situ* experiment, which still exhibit some residual activity for CO formation. The activity for $CH_4$ formation is however completely lost (section 7.6.3).

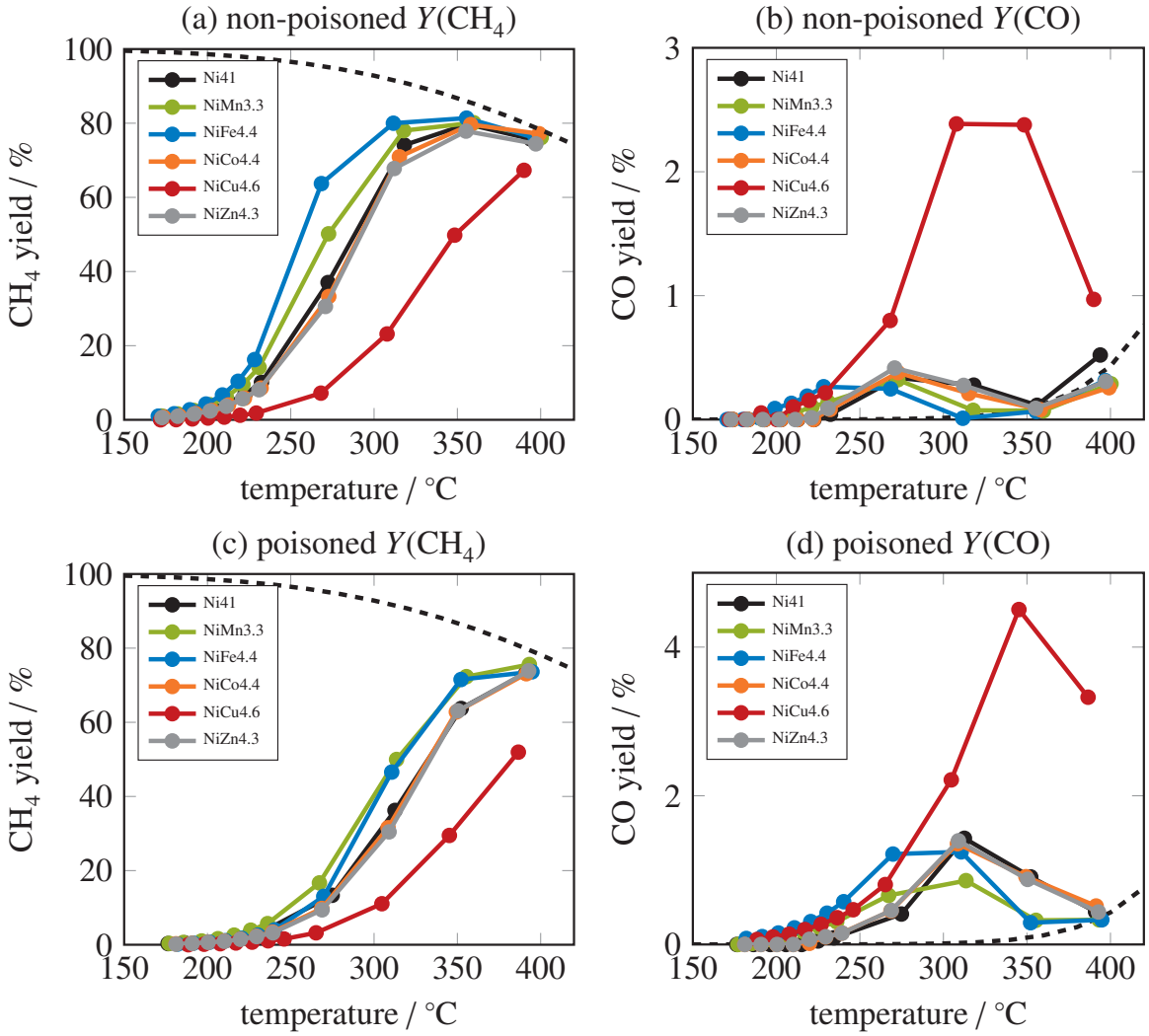


**Figure 7.6:** Temperature-dependent catalyst performance of Ni41 and promoted Ni-Al catalysts in terms of $CH_4$ yield (a,c) and CO yield (b,d). Dashed lines represent thermodynamic equilibrium. Data was recorded after aging catalysts for 24 h at 400 °C, $H_2/CO_2/Ar$ = 4/1/5, 1 bar and 62.5 sccm. Sulfur loadings of spent samples are listed in table 7.5.

### 7.4.3.2 Apparent activation energies

From activity data recorded between 160 and 330 °C, apparent activation energies were determined before and after S poisoning. The obtained results and corresponding Arrhenius plots are shown in table 7.5 and figure 7.15. The determined values for poisoned samples compare well to non-poisoned samples and lie in a rather narrow range of 81 to 92 kJ/mol. These results are in good agreement with recent values of 80 to 87 kJ/mol obtained for Ni-Al catalysts (Ni/Al molar

ratio 1 and 3) [34] and literature values of 80 to 106 kJ/mol reported for $Ni/Al_2O_3$ [86, 270, 271]. The obtained results therefore confirm the absence of mass and heat transport limitations during activity measurements and indicate, that sulfur atoms merely block the active sites of the reaction, but do not influence electronic properties of their surroundings or even change the reaction mechanism. In the case of NiFe4.4, apparent activation energies of 88-92 kJ/mol are observed, which are out of the previously determined range for Ni-Al catalysts (80-87 kJ/mol) [34]. One may therefore speculate, whether Fe influences the electronic properties of Ni surface atoms, for example due to the formation of a Ni-Fe alloy [25, 26].

#### 7.4.3.3 Characterization of spent samples

In order to understand the observed activity patterns, spent samples were analyzed by CHNS analysis and $H_2$ and $CO_2$ chemisorption. Results are listed in table 7.5, together with weight time yields (WTY) of $CH_4$ and CO determined under differential conditions (230 °C, $X(CO_2)$ < 10 %) and apparent activation energies, which are discussed in section 7.4.3.2. Note that $H_2$ and $CO_2$ data for non-poisoned samples is equal to the one obtained for aged catalysts (table 7.2). Hence, the discussion about $CO_2$ uptakes in section 7.4.2.2 and data presented in table 7.4 also apply here.

**Table 7.5:** Characterization and activity data of *ex situ* poisoned Ni41 and promoted Ni-Al catalysts.

| | $w_S$[a] (wt%) | $U(S)$[b] ($\mu mol_S/g_{cat}$) | $U_{24h}(H_2)$[c] ($\mu mol_{H_2}/g_{cat}$) | $U_{24h}(CO_2)$[d] ($\mu mol_{CO_2}/g_{cat}$) | $2 \cdot \Delta U_{24h}(H_2)/\Delta U(S)$[e] ($\mu mol_{H_2}/\mu mol_S$) | WTY ($CH_4$)[f] ($\mu mol_{CH_4}/(g_{cat}\ s)$) | WTY (CO)[f] ($\mu mol_{CO}/(g_{cat}\ s)$) | $E_A$ (kJ/mol) |
|---|---|---|---|---|---|---|---|---|
| Ni41 | 0.00 | 0 | 428 | 196 | - | 9.4 | 0.0 | 81.4 |
| | 0.37 | 115 | 230 | 156 | 3.4 | 2.5 | 0.0 | 84.4 |
| NiMn3.3 | 0.00 | 0 | 381 | 234 | - | 13.5 | 0.1 | 84.2 |
| | 0.34 | 106 | 252 | 190 | 2.4 | 3.7 | 0.2 | 87.1 |
| NiFe4.4 | 0.00 | 0 | 328 | 207 | - | 15.1 | 0.2 | 88.9 |
| | 0.43 | 134 | 171 | 168 | 2.3 | 2.5 | 0.4 | 91.1 |
| NiCo4.4 | 0.00 | 0 | 389 | 210 | - | 8.0 | 0.1 | 81.8 |
| | 0.44 | 137 | 224 | 169 | 2.4 | 2.1 | 0.1 | 85.6 |
| NiCu4.6 | 0.00 | 0 | 277 | 156 | - | 1.7 | 0.2 | 85.5 |
| | 0.43 | 134 | 142 | 119 | 2.0 | 0.7 | 0.3 | 85.0 |
| NiZn4.3 | 0.00 | 0 | 333 | 214 | - | 7.7 | 0.1 | 84.1 |
| | 0.39 | 122 | 214 | 176 | 2.0 | 2.0 | 0.1 | 84.6 |

[a] Determined by CHNS analysis of *ex situ* poisoned samples.
[b] Calculated from sulfur loadings, using a molar mass of sulfur of $M_S = 32.065$ g/mol.
[c] Determined by $H_2$ chemisorption of *ex situ* poisoned samples.
[d] Determined by $CO_2$ chemisorption of *ex situ* poisoned samples.
[e] Amount of Ni surface atoms blocked per S atom.
[f] Measured at 230 °C.

The sulfur loading of sulfur-free samples is in all cases 0.00 wt%. Sulfur-containing samples show values between 0.34 to 0.44 %, which is significantly lower than the nominal value of 0.50 wt%. We ascribe this to losses during activation and/or aging. If sulfur loadings are converted into sulfur uptakes, values between 106 and 137 $\mu mol_S/g_{cat}$ are obtained, which is significantly lower than S uptakes after *in situ* poisoning and explains the residual activity observed for *ex situ* poisoned samples. Nevertheless, a marked decrease of activity is monitored for *ex situ* poisoned samples, which is reflected in significant losses in $H_2$ and $CO_2$ uptake. If the decrease in $H_2$ uptake is related to S uptake, an average blockage of 3.4 Ni atoms per S atom is observed for Ni41 (assuming a ratio of H/Ni = 1). For promoted samples, this ratio is significantly lower, ranging from 2.4 for NiCo4.4 to 2.0 for NiZn4.3. Hence, S atoms are not only adsorb on the $Ni^0$ phase but also on the promoter phase. These results confirm the findings of *in situ* poisoning.

Most noteworthy, though, Mn- and Fe-promoted Ni-Al catalysts show higher activities for $CO_2$ methanation in the non-poisoned and poisoned state than the Ni41 benchmark catalyst. This finding is rather surprising, since the $H_2$ uptake, which is often considered to be the most relevant parameter for the $CO_2$ methanation activity of Ni-$Al_2O_3$ catalysts [23, 292], does not match the activity order of promoted Ni-Al catalysts. In the non-poisoned state, the $H_2$ uptake decreases in the following order: Ni41 (428 $\mu mol_{H_2}/g_{cat}$) > NiMn3.3 (381 $\mu mol_{H_2}/g_{cat}$) > NiFe4.4 (328 $\mu mol_{H_2}/g_{cat}$). In contrast, the observed order in activity is exactly the other way around (NiFe4.4 > NiMn3.3 > Ni41). In the poisoned state, the $H_2$ uptake decreases in the following order: NiMn3.3 (252 $\mu mol_{H_2}/g_{cat}$) > Ni41 (230 $\mu mol_{H_2}/g_{cat}$) > NiFe4.4 (174 $\mu mol_{H_2}/g_{cat}$). In contrast, the corresponding activity order is NiMn3.3 ≈ NiFe4.4 > Ni41. Based on these results, we come to the conclusion, that $H_2$ chemisorption data is not able to describe the $CO_2$ methanation activity of Mn- and Fe-promoter Ni-Al catalysts.

To illustrate this point more clearly, figure 7.7 shows a plot of $CH_4$ weight time yield (WTY), obtained at 230 °C, over $H_2$ uptake. The continuous line represents previous results of an equimolar Ni-Al catalysts [34]. In the non-poisoned state (filled circles), only Ni41 and NiCo4.4 match the continuous line or an extrapolation thereof (dashed line). NiMn3.3 on the other hand shows a methanation activity which is by a factor of 1.7 higher than NiCo4.4, although both samples show a comparable $H_2$ uptake. A similar situation is obtained for NiFe4.4, showing an increase in activity by a factor of about 2.5 when compared to the continuous line. Higher activities of Mn- and Fe-promoted samples are also exhibited in the poisoned state (open circles).

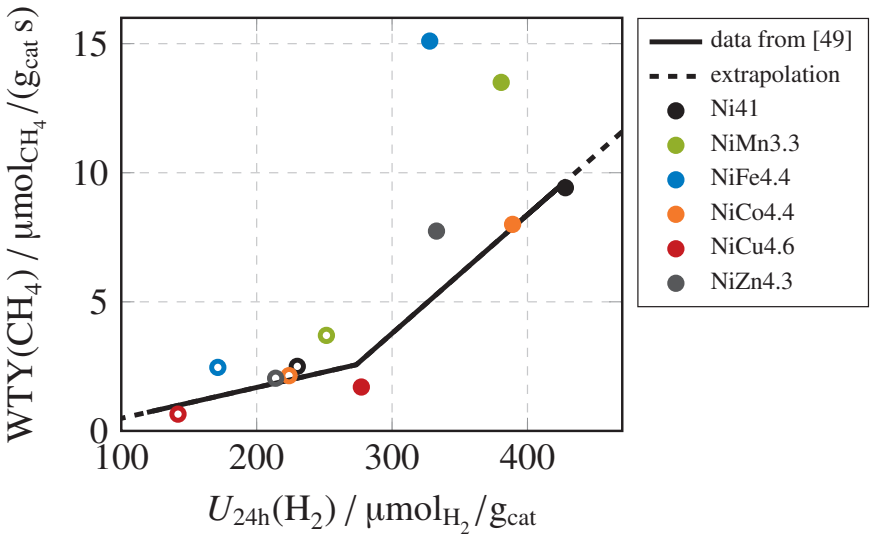


**Figure 7.7:** $CH_4$ weight time yield (WTY) plotted over $H_2$ adsorption capacity for *ex situ* poisoned Ni41 and *ex situ* poisoned promoted Ni-Al catalysts. Filled circles represent a nominal sulfur loading of 0.00 wt%, open circles represent a nominal sulfur loading of 0.50 wt%. Sulfur loadings of spent samples are listed in table 7.5.

Apart from $H_2$ chemisorption, researchers have also used the amount of adsorbed $CO_2$ to explain the activity behavior of promoted Ni catalysts [25, 26, 75, 156, 289]. Up to this point, however, it was not distinguished between different $CO_2$ adsorption sites (compare section 7.4.2.3). Instead, the total amount of adsorbed $CO_2$ was used to derive structure-activity relationships. In our study, however, this approach fails because the total amount of adsorbed $CO_2$ is enhanced not only for Mn- and Fe-promoted catalysts, which do show a higher activity when compared to Ni41, but also for Co- and Zn-promoted systems, which show the same activity than Ni41. We ascribe this discrepancy to different $CO_2$ adsorption sites, which contribute differently to catalyst activity.

In figure 7.8, a correlation between methanation activity in terms of $CH_4$ weight time yield and $CO_2$ uptake is plotted. Hereby, the amount of $CO_2$ assigned to $Ni^0$ and the promoter phase, $U(CO_2)^{Ni+X}$, was considered. Now, a better correlation is obtained for NiMn3.3 and NiFe4.4, when compared to figure 7.7, since the differences between the continuous line or an extrapolation thereof (dashed line) almost vanish. This indicates, that rate-enhancement of Mn- and Fe-promoted catalysts is in both cases due to an enhanced $CO_2$ adsorption capacity. According to our model presented in section 7.4.2.3, the additional amounts of $CO_2$ are related to Mn- and Fe-containing promoter phases. Interestingly, the Mn-containing promoter phase is associated to the Al-rich mixed oxide, whereas the Fe-containing promoter phase is associated to $Ni^0$. For the latter, it needs to be noted, that some insecurity remains about the effect of Ni-Fe alloy formation. Hence, the increase in $CO_2$ capacity may not necessarily be related (completely) to the Fe promoter phase but possibly also to a modified $Ni^0$ phase, comprising a different $H_2/CO_2$ adsorption stoichiomtery (compare section 7.4.2.3). Hence, an electronic

effect, which is also indicated by the slight change of the apparent activation energy in section 7.4.3.2 and discussed in detail elsewhere [25], cannot be ruled out. Nevertheless, our data clearly suggest that an increase in $CO_2$ adsorption capacity is the main reason for activity enhancement of Fe- and Mn-promoted Ni-Al catalysts.

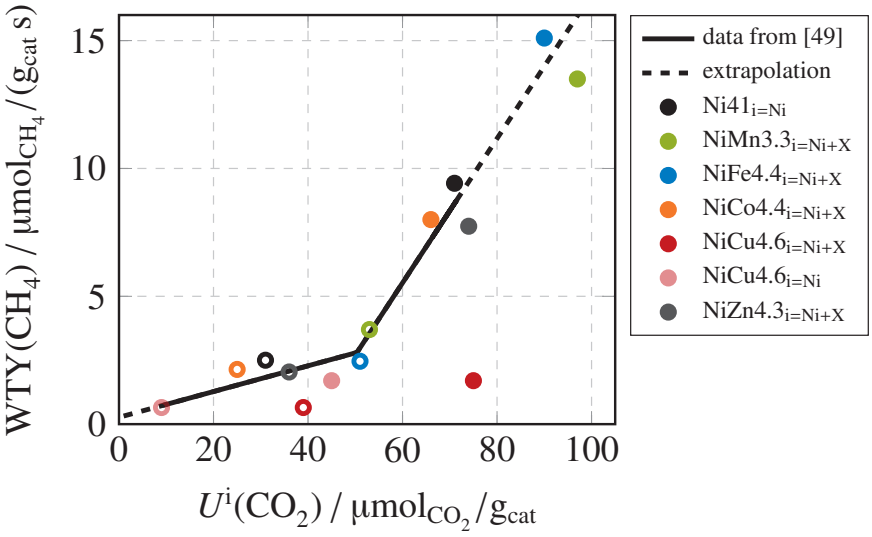


**Figure 7.8:** $CH_4$ weight time yield (WTY) plotted over $CO_2$ adsorption capacity for *ex situ* poisoned Ni41 and *ex situ* poisoned promoted Ni-Al catalysts. Filled circles represent a nominal sulfur loading of 0.00 wt%, open circles represent a nominal sulfur loading of 0.50 wt%. Sulfur loadings of spent samples are listed in table 7.5.

Regarding the other samples except NiCu4.6, a similarly good match between previous activity and $CO_2$ uptake data and the current study is obtained. Interestingly, this is also the case when correlating activity data and $H_2$ uptakes, which indicates that the catalytic activity of Co- and Zn-promoted samples is primarily dominated by the $Ni^0$ phase. In the case of NiCo4.4, this is readily understandable, because the Co-containing promoter phase does not adsorb $CO_2$ (compare table 7.4). The Co-containing promoter phase is therefore ascribed to a spectator species. In the case of NiZn4.3, the situation is less clear, since the corresponding promoter phase does adsorb $CO_2$ and, in the non-poisoned state, the sample shows a higher activity than expected from its $H_2$ uptake. Therefore, a beneficial effect of $CO_2$ adsorbed on the Zn-containing promoter phase cannot be excluded.

Most interestingly, though, the NiCu4.6 samples is not described very well by the correlation between activity and $CO_2$ uptake (figure 7.8). In contrast, the correlation between activity and $H_2$ uptake fits better. Since the amount of $CO_2$ adsorbed on the Cu-containing promoter phase is significant, we assume that this fraction does not contribute to the $CO_2$ methanation activity. Instead, the exceptionally high CO yield of NiCu4.6 indicates, that $CO_2$ is partially dissociated to CO but not hydrogenated further. We assume that this dissociation step occurs on segregated Cu surface atoms and does not contribute to $CH_4$ formation. In fact, if we correct

the relevant $CO_2$ uptake for NiCu4.6 and consider only the amount of $CO_2$ adsorbed on $Ni^0$ as relevant for the reaction, a much better fit is obtained in figure 7.8 (as indicated by the data for $NiCu4.6_{i=Ni}$).

## 7.5 Conclusion

The activity and sulfur resistance of an equimolar Ni-Al catalyst, both decisive criteria for the industrial application of the $CO_2$ methanation reaction, were altered by promotion with Mn, Fe, Co, Cu and Zn. *In situ* poisoning by 5 ppm of $H_2S$ revealed 10–20 % higher catalyst lifetimes of promoted samples when compared to the Ni-Al benchmark. This was ascribed to the adsorption of $H_2S$ on $Ni^0$ and promoter phases, with the latter acting as an additional sulfur sink and thus offering a protection mechanism for active sites located on $Ni^0$. Characterization data obtained from *in situ* poisoned samples allowed to determine the individual $CO_2$ uptakes of the Al-rich mixed oxide, the $Ni^0$ phase and the promoter phase. From that data, it was possible to correlate the beneficial effect of Mn- and Fe-doping on catalyst activity to $CO_2$ adsorbed on the corresponding promoter phases. Interestingly, the Cu-containing promoter phase also showed a significant $CO_2$ uptake but at the same time exhibited the lowest $CO_2$ methanation activity. The different behavior of Mn, Fe and Cu containing samples was ascribed to the formation of $CH_4$ from $CO_2$ adsorbed on Mn- and Fe-containing promoter phases and the formation of CO from $CO_2$ related to the Cu-containing promoter phase. The effect of Co and Zn on activity was negligible.

# 7.6 Supporting Information

## 7.6.1 Effect of promoter loading on activated catalysts

**Table 7.6:** ICP-OES results of promoted Ni-Al catalysts with nominal molar ratios of Ni/X = 4/1.

| Sample | $w_{Ni}$ wt% | $w_{Al}$ wt% | $w_X$[a] wt% | $n_{Ni}/n_{Al}$ - | $n_{Ni}/n_X$[b] - |
|---|---|---|---|---|---|
| NiMn8.3 | 31.9 | 15.2 | 8.3 | 0.96 | 3.6 |
| NiFe9.9 | 37.7 | 17.3 | 9.9 | 1.00 | 3.6 |
| NiCo10.5 | 37.3 | 17.1 | 10.5 | 1.00 | 3.6 |
| NiCu11.6 | 37.4 | 17.2 | 11.6 | 1.00 | 3.5 |
| NiZn10.9 | 38.3 | n.d. | 10.9 | n.d. | 3.9 |

[a] Mass fraction of promoter species.
[b] Molar ratio of nickel to promoter species.

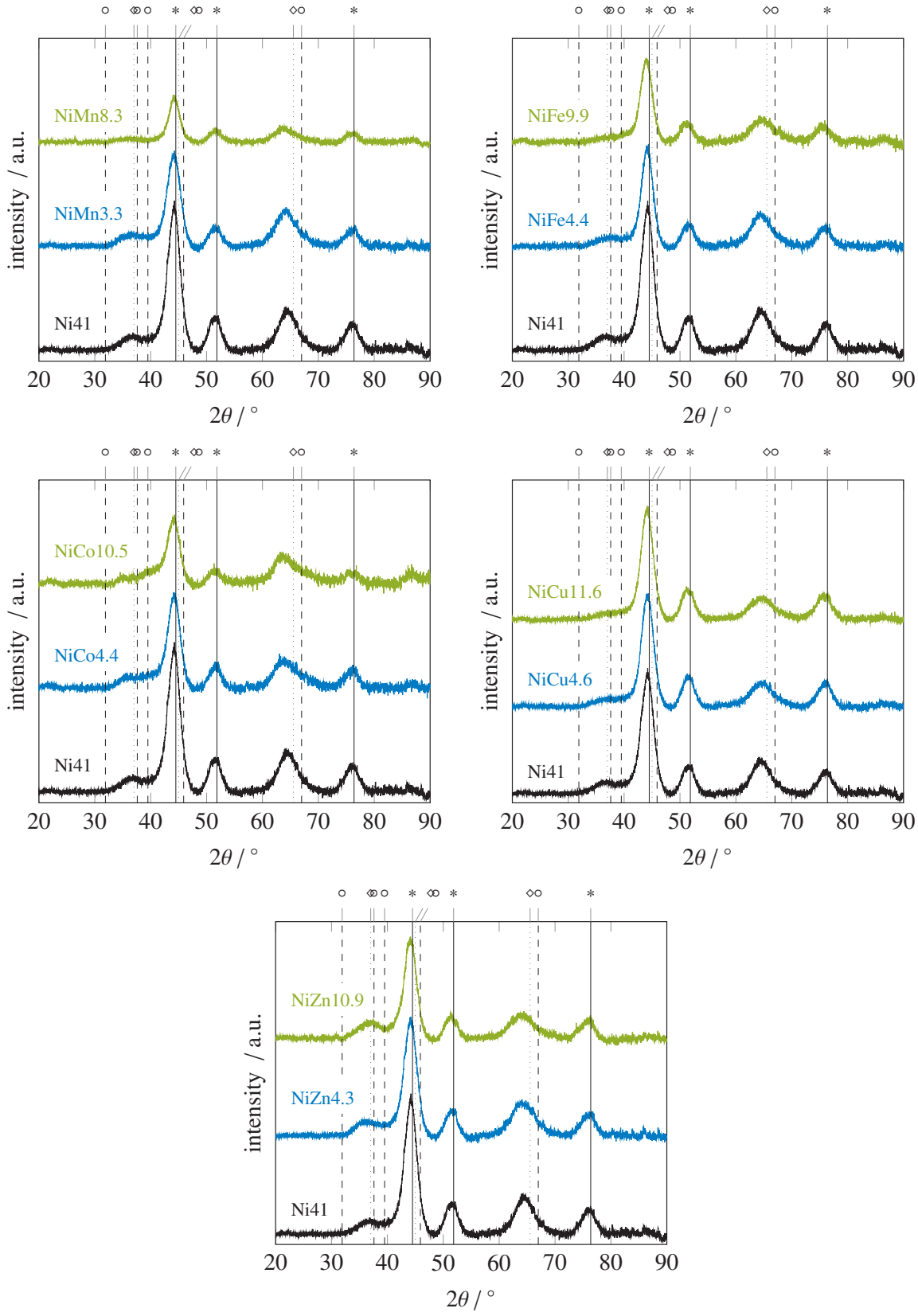


**Figure 7.9:** XRD patterns of promoted Ni-Al catalysts featuring different promoter loadings after *in situ* activation. Catalysts are named 'NiX#.#' with X indicating the promoter metal and #.# the promoter loading rounded to one decimal place. Reference patterns are for $Ni^0$ (∗), $\gamma$-$Al_2O_3$ (○) and $NiAl_2O_4$ (◇) (JCPDS 87-0712, 10-0425, 10-0339).

### 7.6.2 Thermogravimetric analysis of Ni-Al and promoted Ni-Al during temperature-programmed reduction

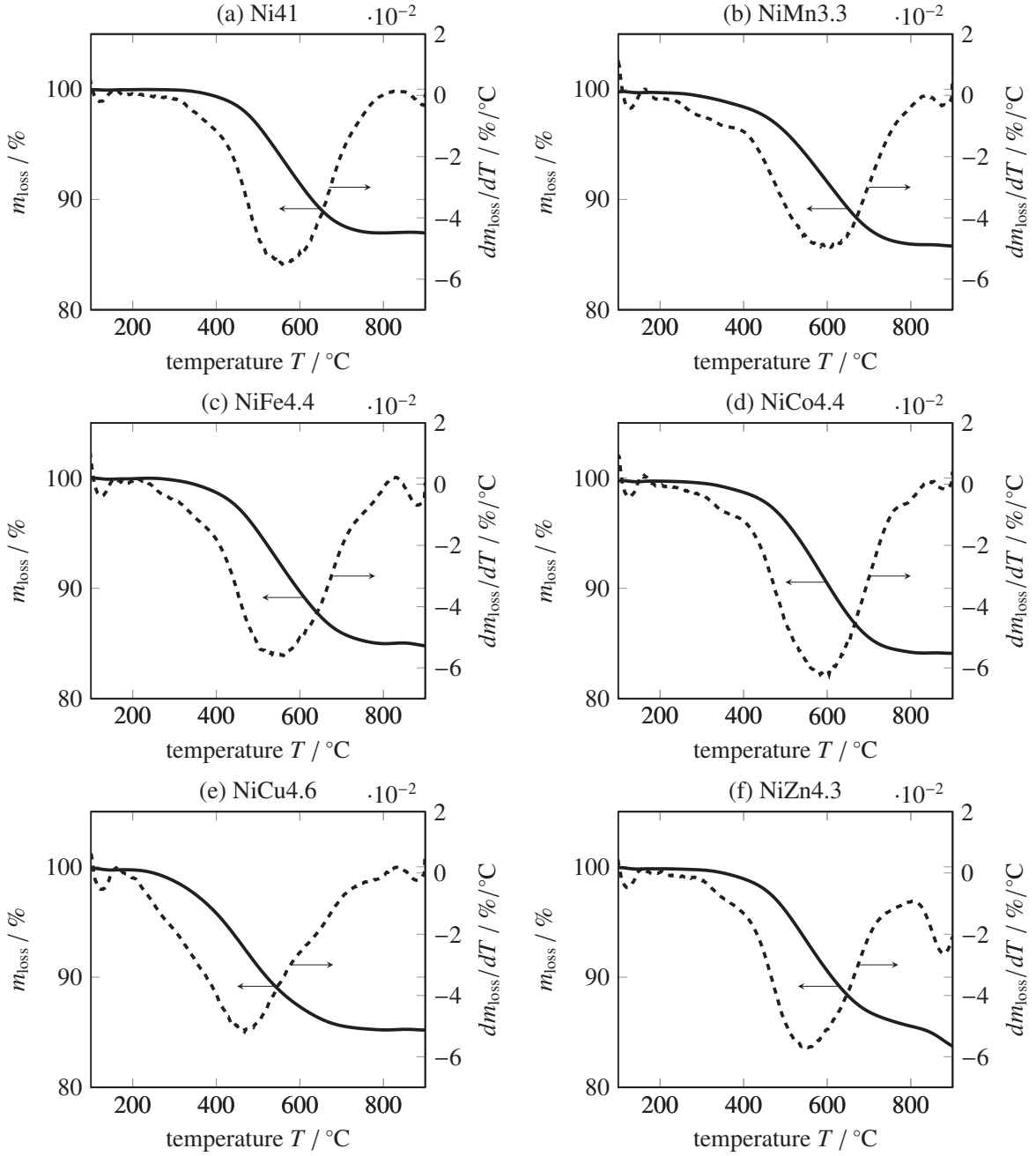


**Figure 7.10:** Integral (continuous) and differential (dashed) TGA curves of Ni41 (a) and promoted (b-f) Ni-Al catalysts.

### 7.6.3 In situ poisoning of Ni41 and promoted Ni-Al catalysts

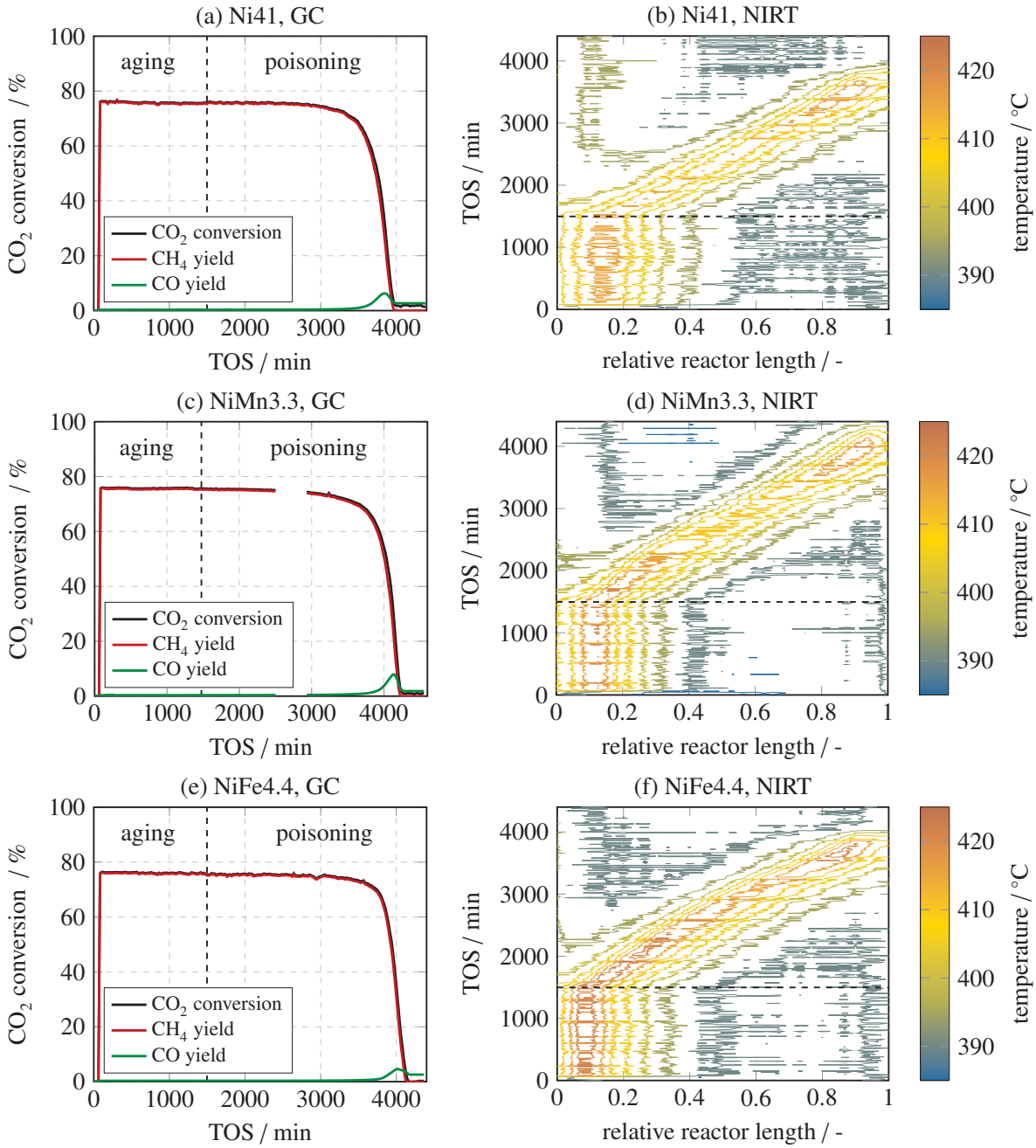


**Figure 7.11:** Results obtained from gas chromatography (GC) and near-infrared thermography (NIRT) during *in situ* poisoning of Ni41 (a,b), NiMn3.3 (c,d) and NiFe4.4 (e,f) by 5 ppm of $H_2S$.

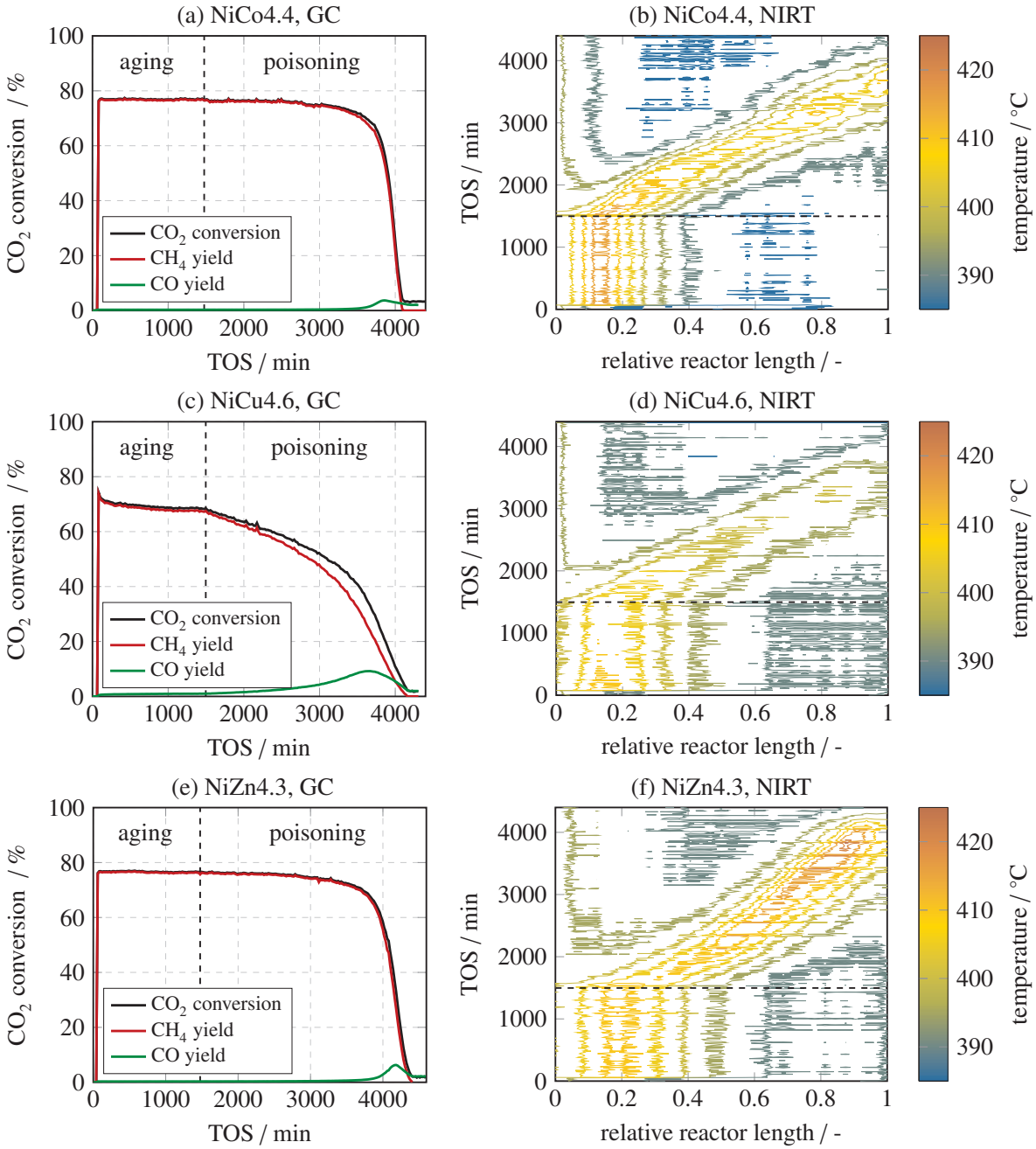


**Figure 7.12:** Results obtained from gas chromatography (GC) and near-infrared thermography (NIRT) during *in situ* poisoning of NiCo4.4 (a,b), NiCu4.6 (c,d) and NiZn4.3 (e,f) by 5 ppm of $H_2S$.

### 7.6.4 Ex situ poisoning of Ni41 and promoted Ni-Al catalysts

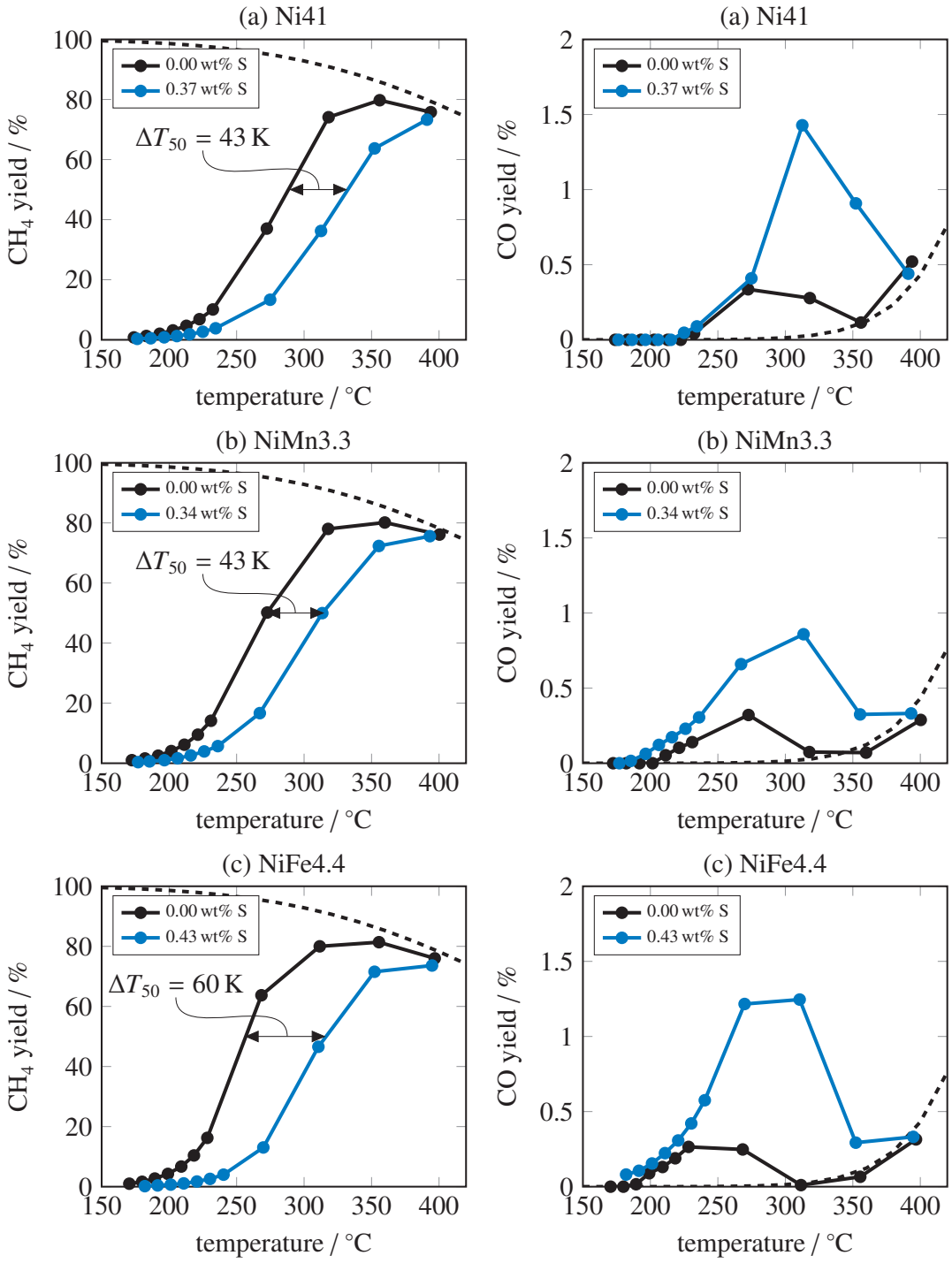


**Figure 7.13:** Temperature-dependent $CH_4$ (a,c,e) and CO yield (b,d,f) of *ex situ* poisoned Ni41 (a,b), NiMn3.3 (c,d) and NiFe4.4 (e,f). Dashed lines represent thermodynamic equilibrium. Data was recorded after aging the catalysts for 24 h at 400 °C, $H_2/CO_2$/Ar = 4/1/5, 1 bar and 62.5 sccm. Specified sulfur loadings were obtained from spent samples. Linear lines are only a guide to the eye.

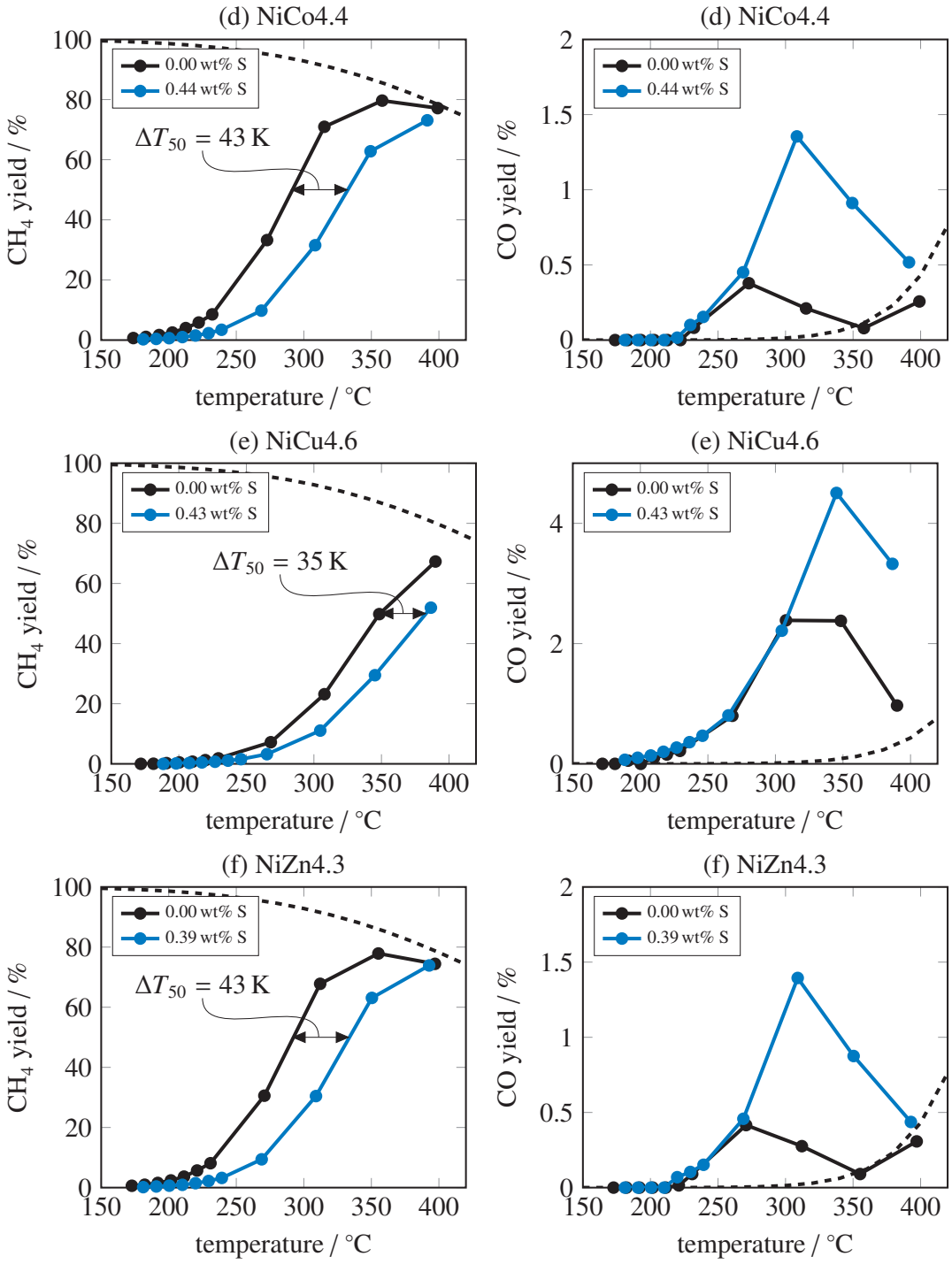


**Figure 7.14:** Temperature-dependent $CH_4$ (a,c,e) and CO yield (b,d,f) of *ex situ* poisoned NiCo4.4 (a,b), NiCu4.6 (c,d) and NiZn4.3 (e,f). Dashed lines represent thermodynamic equilibrium. Data was recorded after aging the catalysts for 24 h at 400 °C, $H_2/CO_2/Ar$ = 4/1/5, 1 bar and 62.5 sccm. Specified sulfur loadings were obtained from spent samples. Linear lines are only a guide to the eye.

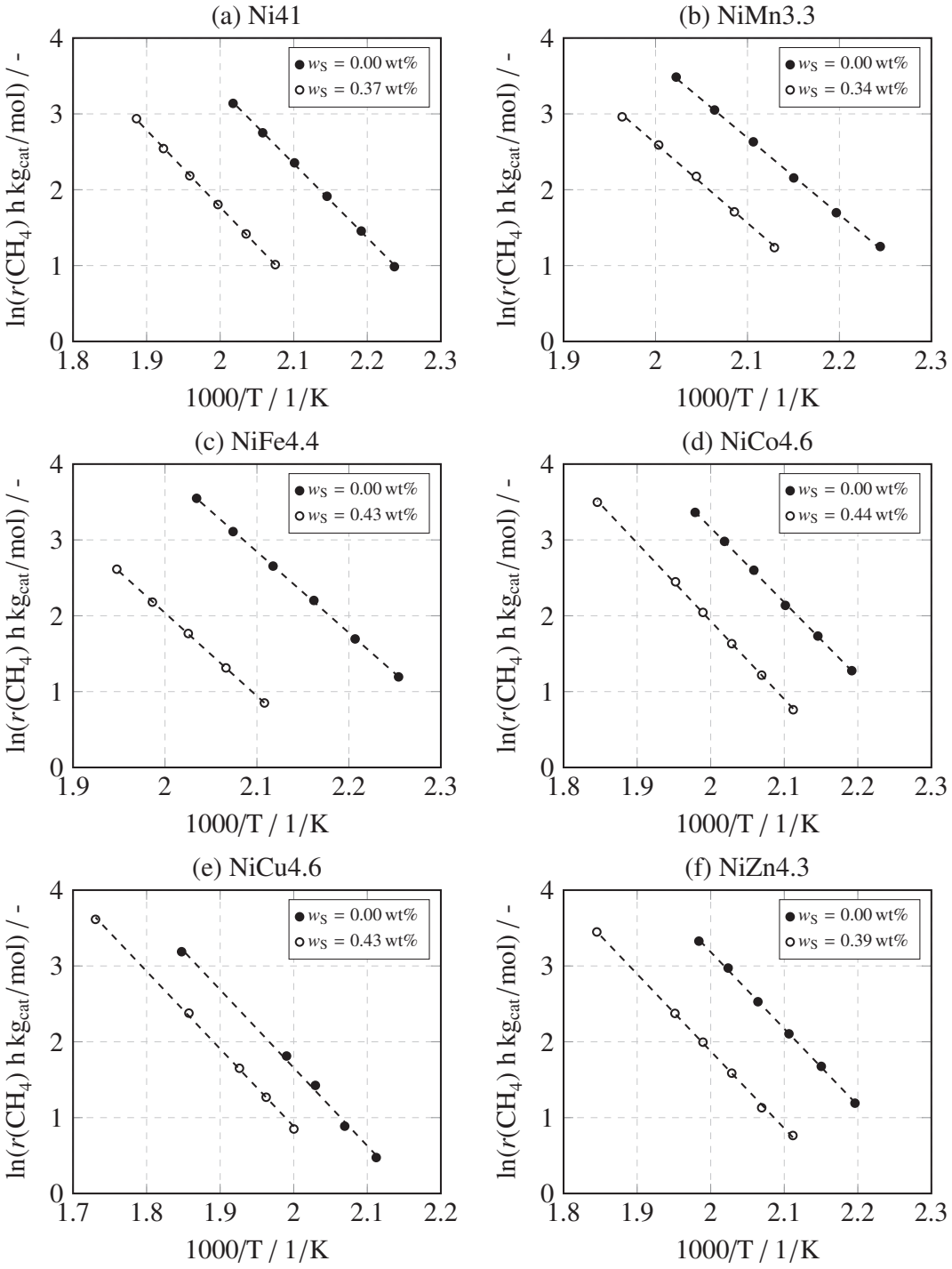


**Figure 7.15:** Arrhenius plots of *ex situ* poisoned Ni41 (a) and promoted (b-f) Ni-Al catalysts. Specified sulfur loadings were obtained from spent samples.

# 8 Novel synthesis routes towards internal intensity standards for quantitative analysis of technical catalysts by X-ray photoelectron spectroscopy

This chapter was developed in close cooperation with Prof. Sebastian Günther, Tim Kratky and Tabea Gros.

## 8.1 Abstract

This study provides detailed knowledge about the usage of internal intensity standards for the analysis of technical catalysts by quantitative X-ray photoelectron spectroscopy (XPS). It is demonstrated, that the key challenge, i.e. achieving binary solid mixtures of high quality, is a problem of mechanical process engineering and can be solved by adequate particle design. In a first test series, it is shown that cohesive powders of different particle size distributions but a maximum particle size of 10 µm give repeatable XPS readings upon grinding and dispersing powders in ethanol ($s_{rel} \leq 7\,\%$). In a second test series, it is verified, that arbitrary particle sizes can be used if both powders show identical particle size distributions. This situation is obtained by spreading volatile metal oxides, e.g. $MoO_3$ and $Cr_2O_3$, over common catalyst support materials, i.e. $\gamma$-$Al_2O_3$ and anatase $TiO_2$. Repeatable XPS readings were obtained for cohesive (anatase $TiO_2$) but also free-flowing ($\gamma$-$Al_2O_3$) powders upon shaking, grinding and dispersing powders in ethanol ($s_{rel} \leq 12\,\%$). As $MoO_3$ and $Cr_2O_3$ were found to re-disperse for the latter techniques, it is recommended to mix $MoO_3$- and $Cr_2O_3$-containing materials by shaking.

## 8.2 Introduction

X-ray photo electron spectroscopy (XPS) is a very powerful tool to probe the outermost surface of a sample in scientific laboratories on a routine basis. It has rendered extremely valuable services for fundamental research [293–295] and has become indispensable for industrial application [296–298]. Among others, heterogeneous catalysis is one of the major fields of interest, because the chemical and physical surface constitution of solid catalysts is one of the crucial parameters for catalytic activity and stability [299, 300].

In many cases and for good reasons, researchers rely on qualitative XPS analysis. It provides a well-tested and straightforward method, which allows definite conclusions about the chemical environment of almost any element present on the sample surface. Therefore, measured binding energies are compared to reference materials listed in well-tested and comprehensive data bases (NIST, [188]). Although, insulators and poorly conducting materials may induce a charging bias to the energy scale [301, 302], those who are skilled in the art, know effective techniques to circumvent these problems [189]. Hence, it is generally accepted to correct the energy scale on the basis of the known chemical environment of one photoelectron core level. This may for example be the adventitious carbon signal [303], which is typically introduced by surface contamination, or a known oxide component [304]. If no intrinsic reference compound is available, it was found advantageous to add one. This may for example be a thin film of gold evaporated *in vacuo* on top of the sample [305].

Next to the qualitative approach, quantitative XPS analysis provides another highly valuable analytic tool, which allows drawing conclusions about the surface composition of a sample. The underlying principle is the correlation of counted photoelectrons to the number of excited surface atoms. However, just like in other analytical spectroscopies, absolute intensities strongly depend on the exact experimental conditions, which are not easily controlled [306]. The usage of a reference signals is therefore indispensable, especially if samples were recorded on different instruments [307] or over elongated time periods [192]. C. D. Wagner, who has pioneered this field, introduced the concept of an intensity normal, using a reference signal recorded on the same instrument, e.g. the F 1s or K 2p signal in fluorine or potassium containing compounds [308]. For arbitrary technical samples, however, additional care needs to be taken, as relative intensities not only depend on surface composition but also surface geometry [191]. The surface geometry is however seldom *a priori* known. In these cases, an adequate intensity normal within the sample would be highly desirable [186]. In most cases, however, such a component is not readily available [186]. Nevertheless, the addition of an internal standard, as it is common practice in qualitative XPS analysis [305] or other spectroscopic analysis methods [309–311], has not received a lot of attention in quantitative XPS analysis. This is probably due to the complexities involved with mixing two powder samples homogeneously [312]. C. D. Wagner

has even come to the conclusion that the usage of binary powder systems for quantitative analysis is not possible at all [197]. Other researchers have reported promising results for specific binary mixtures [313–317], but refrained from characterizing their samples, specifically with regards to particle size. Up to now, a generalized approach to the application of internal standards is still missing.

This study aims at solving the existing problems and providing some basic criteria for the simple and routine usage of internal standards in quantitative XPS analysis. The key problem, i.e. achieving binary mixtures of high quality, is tackled by the theoretical principles of mechanical process engineering.

## 8.3 Theory

As our research approach combines two theoretical fields which are not naturally connected to each other, we provide a short theoretical description of quantitative XPS and solids mixing.

### 8.3.1 Quantitative XPS

The commonly applied formalism to correlate the signal intensity of a certain core level species A, $I_A$, and the target value, i.e. the number of surface atoms of A, $N_A$, is depicted in equation (8.1) for homogeneous samples.

$$I_A = \sigma_A(h\nu) \cdot D(E_A) \cdot L_A(\gamma) \cdot J_0 \cdot T(E_A) \cdot N_A \cdot f(\lambda_M) \tag{8.1}$$

$\sigma_A(h\nu)$ is the ionization cross section of the acquired core level, $D(E_A)$ is the detection efficiency of the electron detector, $L_A(\gamma)$ is the angular asymmetry of the emitted intensity with respect to the angle $\gamma$ between incident photons and ejected and detected photoelectrons and $J_0$ is the photon flux of X-rays impinging upon the sample. $T(E_A)$ is the transfer function of the electron analyzer and $f(\lambda_M)$ is a functional dependence with respect to the attenuation length of photoelectrons in the sample matrix M. Often, the latter is described by the inelastic mean free path (IMFP) of a photoelectron in the sample matrix M which, to a first approximation, can be described by the universal curve of Seah and Dench [190] or with more sophisticated models of Tanuma, Powell and Penn [196].

In practice, it is often convenient to use a relative measure of intensity, according to equation (8.2) where instrument parameters such as the photon flux and the detection efficiency, cancel out.

$$\frac{I_A}{I_B} = \frac{\sigma_A(h\nu)}{\sigma_B(h\nu)} \cdot \frac{L_A(\gamma)}{L_B(\gamma)} \cdot \frac{T(E_A)}{T(E_B)} \cdot \frac{N_A}{N_B} \cdot \frac{f(\lambda_A)}{f(\lambda_B)} \tag{8.2}$$

Reliable results for $N_A/N_B$ ratios have been obtained by using ionization cross sections tabulated by Scofield [193] or Yeh and Lindau [194], angular asymmetries considered according to Reilman [195] and IMFPs which are either tabulated (NIST) or calculated according to the TPP-2M model of Tanuma, Powell and Penn [196]. The dependence of the transfer function on photoelectron energy is either provided by the supplier of the used electron analyzer or has to be measured separately at the respective instrument.

Although equation (8.2) is of great importance in XPS analysis, it can be used straight-forward only when dealing with homogeneous samples. Homogeneous in this case refers to an even distribution of elements A and B within the sample matrix M. In these cases, it can be shown that

$$f(\lambda_i) = \lambda_M, \tag{8.3}$$

where *i* describes photoelectrons of a specific core level of A or B. For inhomogeneous samples, on the other hand, $f(\lambda_A)$ and $f(\lambda_B)$ are significantly more complex, as was shown for example for thin films [186] or supported catalysts [191]. In order to accurately determine $f(\lambda_i)$, a geometrical description of the sample surface is necessary. This requires additional characterization effort by other (often sophisticated) techniques.

If a known standard, comprising an element S, was added to an unknown inhomogeneous sample, comprising an element of interest A, equation (8.2) could be written in the following form

$$\frac{I_A}{I_S} = \frac{\sigma_A(h\nu)}{\sigma_S(h\nu)} \cdot \frac{L_A(\gamma)}{L_S(\gamma)} \cdot \frac{T(E_A)}{T(E_S)} \cdot \frac{N_A}{N_S} \cdot \frac{f(\lambda_A)}{f(\lambda_S)}. \tag{8.4}$$

If the standard is prepared with a suitable geometry, $f(\lambda_S)$ is known and the only remaining unknown in equation (8.4), besides $N_A$, is $f(\lambda_A)$. This situation is comparable to equation (8.1) but with the additional advantage that equation (8.4) is not dependent on intensity variations caused by setting instrument parameters that are not easily reproduced from one experiment to another. Also, $I_S$ is independent from the sample of interest and variations of $I_A$ do not affect $I_S$. This is not necessarily the case if $I_A$ and $I_S$ both stem from the same sample matrix, as is the case for $I_A$ and $I_B$ in equation (8.2). This very beneficial situation now actually allows for determining $f(\lambda_A)$ experimentally in a series of similar samples. At the same time, the functional dependency $f(\lambda_i)$ of any other sample element *i* can be obtained. The aforementioned necessity

to characterize the sample *a priori* by other techniques may thus be omitted. Of course, it is also possible to simply monitor qualitative changes in $I_A$ between different samples, e.g. a catalyst 'prior to activation', 'after activation', 'after reaction', 'after poisoning', etc. and thus to draw conclusions about changes in surface composition due to surface reconstruction, segregation or enrichment mechanisms.

### 8.3.2 Solids mixing

Solids mixing is significantly different and also significantly more difficult than fluid mixing. The main differences and difficulties can be summarized as follows [318]:

(a) There is no relative movement such as molecular diffusion without energy input to the mixture.

(b) Solids differ widely in physical properties, e.g. size, density, shape or resilience, which is why the input of mechanical force rather leads to segregation (i.e. de-mixing) than random distribution.

(c) The ultimate element of a solid mixture, i.e. a particle, is several orders of magnitude larger than the ultimate molecular element in fluids. Thus, the maximum achievable mixture quality of particulate systems is always poorer when compared to fluids.

Although a variety of mixing techniques exist, solids mixing can only be successful, if the employed technique is tailored to the specific powder system or *vice versa*. A major influence on the mechanism of mixing and segregation are the flow characteristics of a powder [318]. In general, two categories are distinguished, in which powders are primarily grouped according to particle size: 'free-flowing' and 'cohesive' [318]. Free-flowing powders show large particle sizes, which are easily separated by gravity and therefore show a high tendency to segregate in mixtures. Cohesive powders on the other hand exhibit small particle sizes and high interparticulate bonding forces, i.e. van der Waals, electrostatic or moisture [318]. These systems are less prone to segregation but show a high tendency to form agglomerates. The boundary particle size, which separates cohesive from free-flowing systems strongly depends on the smoothness and compliance of a surface [319]. As a rough guideline for dry powders, boundary values in the range of 10-100 µm have been reported [318, 320]. Although mixing is also influenced by density, shape or resilience, particle size is by far the most important parameter [318]. As a rule of thumb, mean particle sizes of free-flowing powders should not differ by more than 1.3:1 [321]. Otherwise, for example, 'top-to-bottom' segregation may occur, which is characterized by the movement of small particles through the void spaces formed by large particles [322].

If segregation is brought under control, the best quality of a mixture is that of a random mixture [323]. It is characterized by identical compositions of random portions of the mixture and the mixture as a whole. Thus, if the true composition of the mixture as a whole is not known, it may be estimated by taking $n$ samples and determining their composition, i.e. the fraction of one component in each samples $\nu_1, \nu_2, \nu_3, ...\nu_n$. The arithmetic mean of all compositions, $\bar{\nu}$, calculated in equation (8.5), is an estimated value for the true composition of the mixture.

$$\bar{\nu} = \frac{1}{n}\sum_{i=1}^{n}\nu_i \tag{8.5}$$

In order to assess the mixture quality, the standard deviation, $s$, may be used. A low standard deviation indicates a narrow spread in composition of the samples and therefore good mixing. The standard deviation of $n$ samples is given by

$$s = \sqrt{\frac{1}{n-1}\cdot\sum_{i=1}^{n}(\nu_i - \bar{\nu})^2}. \tag{8.6}$$

It is noted, that equation (8.6) is only an estimate of the true standard deviation of the mixture and different sets of samples will result in different estimated values. The true standard deviation of a random binary mixture (uniform particle size), $\sigma$, can be deduced from statistics [324]. It is given by

$$\sigma = \sqrt{\frac{P(1-P)}{N}}, \tag{8.7}$$

where $P$ and $(1-P)$ are the fractions of both components and $N$ is the number of particles in each sample. For a predefined samples size (mass, volume, ...) is now obvious, that increasing the amounts of particles by a factor of $k$, decreases the standard deviation by a factor of $1/\sqrt{k}$. Thus, mixing a multitude of very fine particles may significantly improve the statistically attainable mixture quality.

## 8.4 Experimental

All solids were of analytical grade and used as received. Synthesis steps were carried out with deionized water purified in a filter unit (Millipore). Light scattering experiments and mixing steps involving a solvent were conducted in 99 % ethanol denaturated with 1 % methyl ethyl ketone (Brenntag). $Al_2O_3$ and $TiO_2$ are used as abbreviation for $\gamma$-$Al_2O_3$ and anatase $TiO_2$.

### 8.4.1 Sample preparation

**Grinding** of selected powders was carried out in a planetary ball mill (PM100, Retsch). Therefore, a 50 ml grinding jar made from $ZrO_2$ and grinding balls made from the same material (ø 2 or 5 mm) were applied. In a typical run, the jar was filled with 17 ml of powder, 17 to 23 ml of ethanol and 190 grinding balls. The mill was operated at 650 rpm for an overall time of 20 to 60 min, which was divided in alternating grinding (60 s) and pausing (30 s) intervals. Between two subsequent grinding intervals, the rotational direction was reversed. The obtained suspensions were separated in a centrifuge (Hettich, 400 rpm, 4 min). Powders were dried at room temperature. In the following, pre-treated powders are referred to as 'milled'. Untreated powders, which were used as supplied, are named 'as is'. Particle sizes vary between 0.03–16 µm for 'milled' and 0.03–800 µm for 'as is' powders. Concise data is given and discussed in sections 8.5.1 and 8.5.2.1.

**Weighing** of binary mixtures, comprising a nominal analyte and a nominal standard compound, was conducted on a *Satorius Cubis MSE3.6P-000DM* microbalance (reading accuracy 0.001 mg). The analyte and standard component were weighed out in a certain mass ratio, $\xi$, as defined by equation (8.8). $m_A$ is the mass of the analyte component and $m_S$ is the mass of the internal standard component.

$$\xi = \frac{m_A}{m_S} \tag{8.8}$$

Unless otherwise stated, a fixed value of $\xi$ = 5/1 was used, which usually resulted in a good signal to noise ratio for the relevant photoelectron signals. Absolute masses were in the range of 10 to 170 mg. Losses during sample transfer, especially due to electrostatic charging, were minimized by using aluminum tin boats and metallic spatulas. Typical weighing errors resulted in a relative uncertainty of the $\xi$ values of $\pm$0.30 %. As this is one order of magnitude lower than the uncertainty of the obtained XPS results (section 8.4.4), weighing errors were neglected in error considerations.

Special care was taken in the case of porous powders. Prior to weighing, they were placed open next to the balance for at least several hours to reach a steady state of $CO_2$ and $H_2O$ adsorption/desorption from the surrounding lab air. In some cases, especially for porous powders removed from an oven, longer waiting times were necessary. Hence, powders were placed in the weighing lab for up to 48 h and checked regularly by means of a balance until no more mass loss or gain was observed. A typical mass gain curve of a baked out $Al_2O_3$ powder, which can be regarded as a worst case scenario, is displayed in the supporting information (section 8.7.1).

## 8.4.2 Spreading of $MoO_3$ and $Cr_2O_3$

$MoO_3$ and $Cr_2O_3$ were dispersed on 'as is' $\gamma$-$Al_2O_3$ (Sasol) and 'as is' anatase $TiO_2$ (Alfa Aesar) according to literature known recipes [325, 326]. Metal salt solutions were prepared from ammonium heptamolybdate (tetrahydrate, abcr GmbH), $(NH_4)_6Mo_7O_{24} \cdot 4H_2O$, and chromium(III) nitrate (nonahydrate, abcr GmbH), $Cr(NO_3)_3 \cdot 9H_2O$. In preliminary tests, the pore volume of the support materials was determined via the stepwise addition of water, resulting in 0.8 ml/g for $Al_2O_3$ and 0.6 ml/g for $TiO_2$.

Incipient wetness impregnation was conducted with a metal salt solution of the required pore volume, which was dropwise added to the support material and dispersed afterwards by stirring with a spatula. After removing excess solvent at 80 °C for 18 h, samples were calcined in humid synthetic air at 450 °C (Mo containing samples) or 600 °C (Cr containing samples) for 15 h at a heating rate of 5 °C/min. Reference samples were synthesized by calcining pure ammonium heptamolybdate and chromium(III) nitrate. Since $TiO_2$-supported samples were found to form large agglomerates after calcination, those powders were subject to an additional grinding and sieving step. Only the fraction < 150 µm was used for mixing.

For the sake of comparison, amounts of Mo and Cr are compared on the basis of coverages, as defined by equation (8.9). $N_i$ is the amount of added atoms of species i, $S_{BET}$ is the specific BET surface area and $m$ the mass of the support material.

$$\theta_i = \frac{N_i}{S_{BET} \cdot m} \tag{8.9}$$

With BET surface areas of 207 $m^2/g$ for $Al_2O_3$ and 52 $m^2/g$ for $TiO_2$, the following coverages were obtained: $MoO_3/Al_2O_3$ ($\theta_{Mo}$ = 2.85 at/nm$^2$), $MoO_3/TiO_2$ ($\theta_{Mo}$ = 1.46 at/nm$^2$), $Cr_2O_3/Al_2O_3$ ($\theta_{Cr}$ = 2.81 at/nm$^2$) and $Cr_2O_3/TiO_2$ ($\theta_{Cr}$ = 11.23 at/nm$^2$).

## 8.4.3 Mixing

### 8.4.3.1 General aspects

Over the course of this study, mixing was conducted via shaking, grinding and dispersing powders in a liquid. Shaking (in a glass container) and grinding (in a corundum mortar with a corundum pestle) were carried out manually. The term 'dispersing powders in a liquid' describes a novel technique, which was specifically developed for the purpose of this study and is described in section 8.4.3.2. All mixtures were composed of two powders of different color and/or texture, which allowed for an optical impression of the achieved mixture quality.

In order to quantify the obtained degree of mixing, each mixing experiment was carried out five times. The agreement between the resulting five independent mixtures is expressed by the relative standard deviation, $s_{\mathrm{rel}}$, of a set of $n = 5$ samples (one sample per mixture), according to equation (8.10). Nomenclature is according to equation (8.6).

$$s_{\mathrm{rel}} = \frac{1}{\bar{\nu}} \sqrt{\frac{1}{n-1} \cdot \sum_{i=1}^{n} (\nu_i - \bar{\nu})^2} = \frac{1}{2\bar{\nu}} \sqrt{\sum_{i=1}^{5} (\nu_i - \bar{\nu})^2} \tag{8.10}$$

#### 8.4.3.2 Dispersing powders in a liquid

Prior to dispersion, the analyte and standard were transferred into a glass container and suspended in ethanol (1 ml per 12 mg of solid). The suspension was then placed in an ultrasonic bath (Bandelin) and sonicated for at least 15 min. As shown in figure 8.12, this was enough time to disperse all powders completely. Flocculation or other re-agglomeration processes were not observed, even for elongated dispersion times.

Subsequent to sonication, mixtures were dried *in vacuo* at elevated temperatures. Therefore, a slightly modified rotary evaporator (Heidolph), as depicted in figure 8.1, was applied. During operation, the pre-installed inlet line, including a glass stopcock and two PTFE hoses, was used for feeding the suspension batchwise from the ultrasonic bath to the evaporation flask. Opening and closing was hereby not conducted via the glass stopcock to avoid the release of stopcock grease, which would contaminate the powder. Instead, a PTFE stopcock was retrofitted to the setup and used as a valve. Removal of the solvent was carried out in batches of 3 to 4 ml at 60 mbar, 80 °C and 280 rpm of the rotary evaporator. Thus, drying times of less than 30 s per batch were achieved. Once the suspension was used up, the evaporator was vented and the evaporation flask was placed in a drying closet for at least another 30 min. The dry powder was removed from the flask by means of a spatula. Cleaning tubing and flask between consecutive runs was conducted by sonication in KOH and HCl.

### 8.4.4 Characterization

**X-ray photoelectron spectroscopy** was conducted on a Leybold-Hereaus LHS 10 spectrometer using a non-monochromatized Mg $K_\alpha$ source (1253.6 eV). The powder samples were pressed into cavities and measured as pellets. The analyzer was operated at a constant pass energy of 100 eV, leading to an energy resolution with a full width at half-maximum (FWHM) of $\sim$1.1 eV.

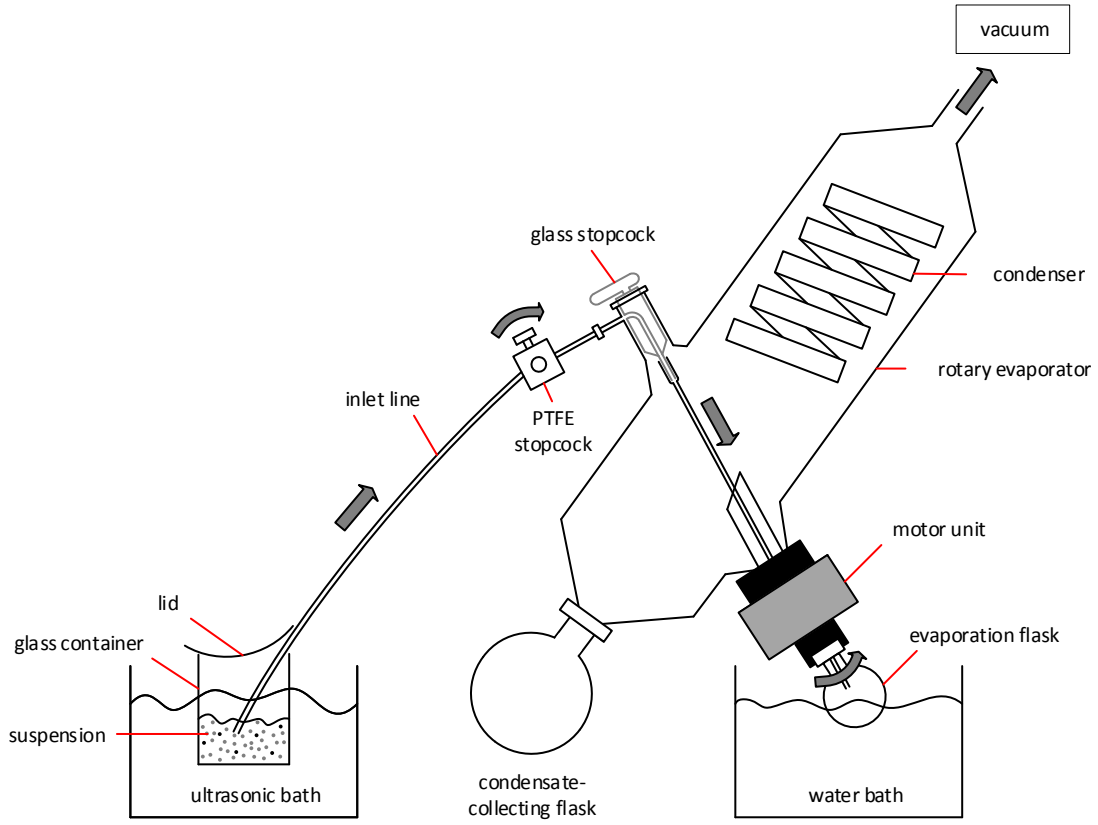


**Figure 8.1:** Modified rotary evaporator used for drying binary mixtures dispersed in ethanol [185].

The energy scale of the spectra was corrected for sample charging by using the O 1s signal (530.9 eV, $Al_2O_3$ [188] and 529.9 eV, $TiO_2$ [188]). All spectra were recorded in a UHV chamber at a pressure below $5 \cdot 10^{-8}$ mbar. In order to exclude variations of experimental conditions over time, e.g. inhomogeneous sample charging or beam damage such as electron induced reduction, the core level spectrum measured at the beginning of a measurement series was repeated at the end. Only if the first and last spectrum of a measurement series showed (a) the same binding energy within 0.2 eV of each other and (b) the same peak area within 3 % of each other, the entire data set was considered for evaluation. Core level spectra were fitted by using Voigt functions and linear background subtraction.

**Light scattering** was performed in ethanol on a Beckman Coulter LS 13220 instrument equipped with an universal liquid sample module. Prior to analysis, particles were suspended in ethanol and stirred or sonicated until agglomerates were completely dispersed (criterion as in section 8.4.3). Diffraction sizing was conducted by simultaneously using two different light sources. Particles between 40 and 1000 µm were captured via the elastic light scattering (ELS) method, using monochromatic light (780 nm) from a 5 mW laser diode. Particles between 0.17 and 0.40 µm were captured via the Polarization Intensity Differential Scattering (PIDS) method [201], using light from an incandescent tungsten-halogen lamp. In order to get wavelength dependent polarization patterns, the applied light source was filtered to 450, 600 or 900 nm and polarized either horizontally or vertically.

Particle size distributions were calculated according to the Mie theory [199], assuming spherical particles. Wavelength dependent refraction indices for the employed materials are given in table 8.1. For supported samples, the refractive index of the support material was used. The correct functionality of the instrument was verified by using a SICG35 standard (Beckman).

**Table 8.1:** Optical constants used for determining particle size distributions according to the Mie theory.

| | $Al_2O_3$ [327] | | $TiO_2$ [328] | | $WO_3$ [329] | | Ethanol [330] | |
|---|---|---|---|---|---|---|---|---|
| | real | imaginary | real | imaginary | real | imaginary | real | imaginary |
| 780 nm | 1.75 | 0.02 | 2.80 | 0.00 | 1.92 | 0.5 | 1.36 | 0.00 |
| 450 nm | 1.75 | 0.02 | 3.14 | 0.00 | 2.00 | 0.5 | 1.37 | 0.00 |
| 600 nm | 1.75 | 0.02 | 2.90 | 0.00 | 1.95 | 0.5 | 1.36 | 0.00 |
| 900 nm | 1.75 | 0.02 | 2.77 | 0.00 | 1.90 | 0.5 | 1.36 | 0.00 |

**Elemental analysis** (EA) of selected mixtures with regards to tungsten was conducted by photometry of the colored thiocyanate complex at 401 nm [331]. Prior to analysis, solids were brought into solution by an oxidation melt process [332]. In a typical experiment, 5 to 150 mg of powder were mixed with a spoon of $K_2CO_3/KNO_3$, two droplets of ethylene glycol and an excess amount of $Na_2O_2$. The mixture was heated in a micro bomb, i.e. a small pressure vessel

made from metallic nickel, over a Bunsen burner flame. After cool down, the molten mass was dissolved in 100 ml of water and heated slowly with a piece of platinum to decompose the peroxide. Photometric analysis is based on a method described by Gottschalk [331]. Calibration of the photometer (Shimadzu, UV-160) was conducted by a two-point method. Complete dissolubility of the metal component was verified in reference experiments using ammonium heptamolybdate, $Na_2WO_4$ and $Cr_2O_3$. Likewise, metal superposition and matrix effects were excluded.

**X-ray diffraction** (XRD) was carried out on a PANanalytical Empyrean diffractometer operated with Cu-$K_\alpha$ radiation ($\lambda = 1.54$ Å) at 45 kV and 40 mA. Diffractograms were obtained by scanning the range between $2\theta = 5 - 90°$. Samples were pressed on a Si wafer and measured at an angular velocity of 1.432 38°/min and a stepsize of 0.005 65°. For the sake of comparison, reference diffractograms indexed by the Joint Committee on Powder Diffraction Standard (JCPDS) were used.

## 8.5 Results and Discussion

Over the course of this study, two series of experiments were carried out. In the first series, various powders of arbitrary sizes are mixed to reveal the impact of particle size on the quality of a solid mixture with regards to volume (EA) and surface (XPS) composition. Results are discussed in terms of precision, i.e. relative standard deviation, and trueness, i.e. the agreement of obtained arithmetic means to theoretical reference values (section 8.7.3). In the second series, powders of equal size, obtained by spreading of $MoO_3$ and $Cr_2O_3$ over employed support materials, are mixed to advocate the concept of tailoring internal standards for quantitative XPS of technical catalysts.

### 8.5.1 Effect of particle size

Powders applied in this section are named and compared with regards to particle size as displayed in figure 8.2. A boundary value of 75 µm was chosen to separate the regimes of cohesive and free-flowing particulate systems [318]. It is noted, that particle size distributions were measured after complete de-agglomeration of powders in ethanol and therefore comprise 'ultimate elements' (i.e. primary particle sizes). The time-dependent process of de-agglomeration is shown in the supporting information (section 8.7.2).

Particle size distributions of 'as is' powders (i.e. used as supplied), are depicted in figure 8.2 (left). Particle size distributions of 'milled' powders are displayed in figure 8.2 (right). With regards to flow characteristics, 'as is' $Al_2O_3$ comprises the only free-flowing particulate system in this study, having a mean particle diameter of 181 µm. After ball-milling, a cohesive powder with a mean particle diameter of 2.41 µm is obtained. $TiO_2$ and $WO_3$ are already cohesive powders in the 'as is' state with a mean particle diameter of 0.58 and 3.02 µm, respectively. Upon grinding, mean particle sizes slightly decrease to 0.46 µm for $TiO_2$ and 0.78 µm for $WO_3$. The reason for the less pronounced changes (as compared to $Al_2O_3$) is the size of the utilized grinding balls. Hence, the minimum achievable particle diameter is limited to a value approximately three orders of magnitude below the ball size.

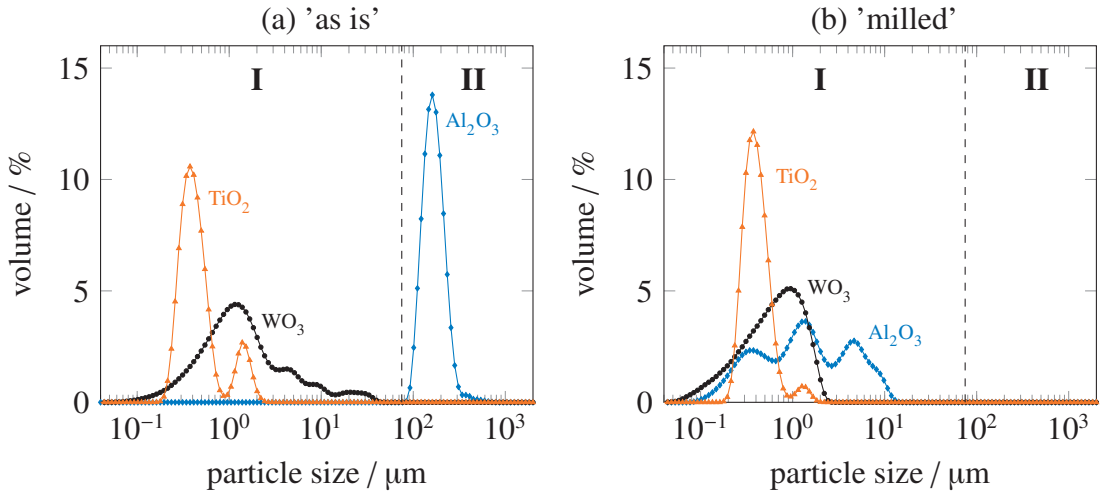


**Figure 8.2:** Particle size distributions of $Al_2O_3$, $WO_3$ and $TiO_2$ in the 'as is' (left) and 'milled' (right) state. The dashed line positioned at 75 µm denotes the boundary value between cohesive (domain I) and free-flowing (domain II) powders.

#### 8.5.1.1 Shaking

Probably the most intuitive procedure for mixing two solids is placing them in a container and shake them. Although this method is in principle very simple and straightforward, it does not produce satisfactory results for arbitrary particle sizes. To illustrate this, the 'as is' fractions of $Al_2O_3$ and $WO_3$ were weighed out in a glass container and shaken. The same was repeated for the corresponding 'milled' fractions. Results obtained from elemental and XPS analysis of both mixtures (labeled 'as is' and 'milled') are depicted in figure 8.3. Relative standard deviations for elemental analysis (left column) are greater than 10 %. Relative standard deviations for XPS analysis (right column) are even greater than 30 %. These values are far beyond the accuracy of the applied analysis techniques, which are estimated to be 3 % (EA) and 7 % (XPS), respectively (section 8.7.3). Apart from the poor precision, the presented data also show a lack of trueness. Hence, theoretical calculations (section 8.7.3) suggest a tungsten mass fraction

of $m_W = 13.22\,wt\%$ and an intensity ratio of $I_{Al\,2p}/I_{W\,4f} = 2.50$. Instead, the 'as is' experiment shows a significantly lower tungsten mass fraction of 9.90 wt% and also a lower intensity ratio of 1.57. For 'milled' samples, a higher tungsten mass fraction of 16.74 wt% and a greater intensity ratio of 12.15 were monitored.

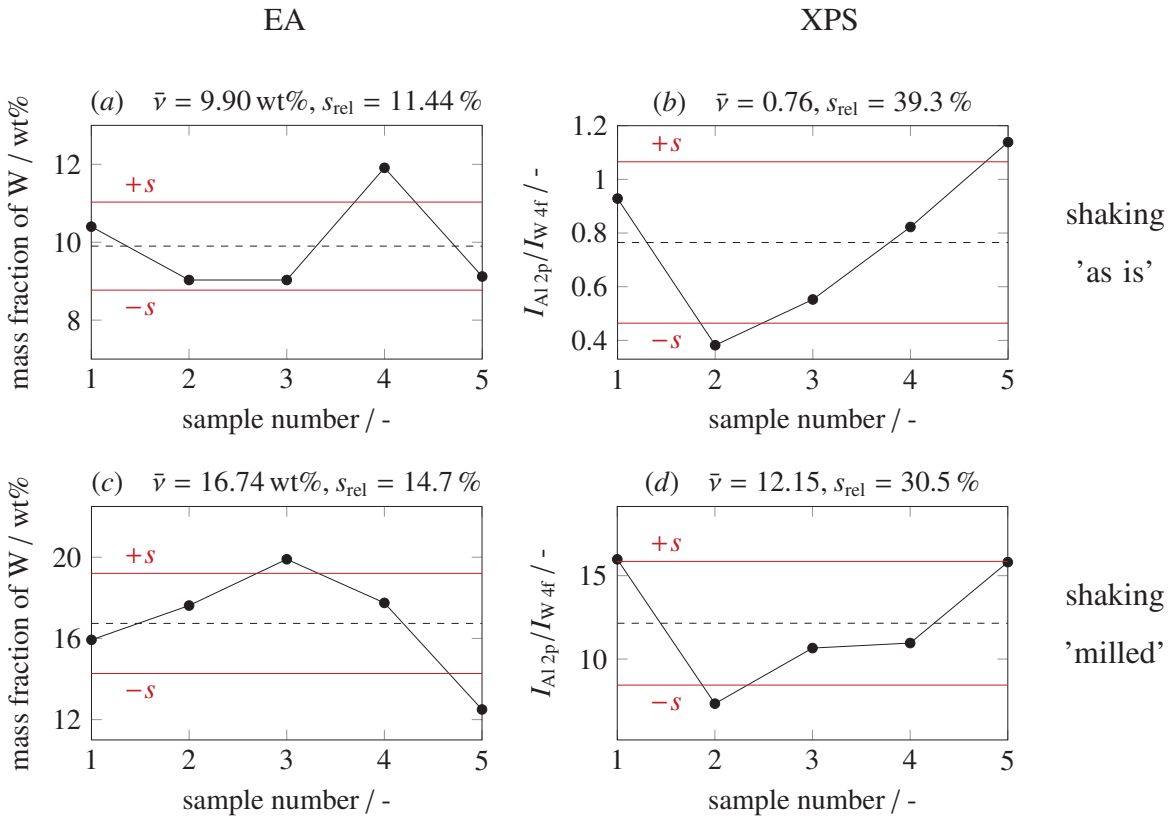


**Figure 8.3:** Results from EA (a,c) and XPS analysis (b,d) from shaking 'as is' (a,b) and 'milled' (c,d) $Al_2O_3$ and $WO_3$.

The reason why arbitrary powders are generally not easily mixed by shaking (or other mechanical treatments) is the difference in particle size. The recommended size ratio of 1.3:1 for free-flowing systems [321] is neither reached for 'as is' (60:1) nor for 'milled' samples (3:1). Thus, a strong tendency for segregation may contribute to the observed deviations. For cohesive powders, the 1.3:1 criterion does not strictly apply, as those systems readily form agglomerates, which are not described well by the primary particle size. Nevertheless, large enough agglomerates behave just like free-flowing particles and may also lead to segregation. In the current 'as is' powders, it was indeed observed, that $WO_3$ forms large agglomerates with itself but only weakly interacts with $Al_2O_3$ particles. Upon shaking, this situation did not significantly change and thus, the visible impression of bright yellow 'spots' in an otherwise white powder already indicated a low mixture quality. An even closer look revealed larger $WO_3$ agglomerates as compared to $Al_2O_3$ particles, which led to a top-to-bottom segregation of $Al_2O_3$ particles, with $WO_3$ agglomerates on top. The systematically lower mass fraction of tungsten compared to the theoretical value (9.90 vs. 13.22 wt%) may be due to a sampling bias,

as large $WO_3$ agglomerates readily rolled off the sampling device (spatula), whereas less of the $Al_2O_3$ was lost. The systematically lower $I_{Al\ 2p}/I_{W\ 4f}$ ratio (0.76) with respect to the theoretically expected value (2.50) can be explained by the flattening of $WO_3$ agglomerates upon pressing the solids mixture into the cavities of the sample holder. Thus, $Al_2O_3$ particles were systematically covered with large 'patches' of $WO_3$ particles and shielded from the surface.

The 'milled' results show the opposite trends as compared to the 'as is' samples, because the behavior of cohesive $Al_2O_3$ was much different than free-flowing $Al_2O_3$. Instead of a top-to-bottom segregation as before, the optical impression was that of a 'coverage' or 'wrapping' of $WO_3$ agglomerates by $Al_2O_3$. This situation may have caused a bias at the expense of $Al_2O_3$ when extracting a sample from the mixed powder with a spatula, i.e. the preferential loss of the $Al_2O_3$ 'shell' as compared to the $WO_3$ 'core'. This bias only affects volume compositions (EA). In the case of surface composition (XPS), the opposite situation as before, i.e. a shielding of $WO_3$ agglomerates by $Al_2O_3$, led to a severe underestimation of $WO_3$.

#### 8.5.1.2 Grinding

Grinding is a standard homogenization technique, which is easily carried out in any kind of scientific laboratory. The positive effect of grinding on the volume homogeneity of a mixture containing two arbitrary powders is confirmed by manually grinding 'as is' $Al_2O_3$ and $WO_3$. As shown in figure 8.4a, the volume composition scatters with a relative standard deviation of only 4 %, which is a significant improvement as compared to mere shaking. Also, the absolute mass fraction of tungsten (11.26 wt%) is much closer to the theoretical value of 13.2 wt%. The surface composition derived by XPS (figure 8.4b) shows a relative standard deviation of 21.4 %, which is better than shaking but still far away from the theoretically achievable value of 7 %. In addition, the absolute intensity ratio is still systematically too low (0.95 vs 2.50). A different situation is observed for 'milled' powders. The surface composition shows a very high precision of $s_{rel} = 4\,\%$, which is in the range of the theoretical achievable value. Also, the absolute value is closer to the nominal one (4.83 vs 2.50). The high accuracy of this set of data is also reflected in volume composition ($s_{rel} = 3.60\,\%$, $m_W = 12.95$ wt%).

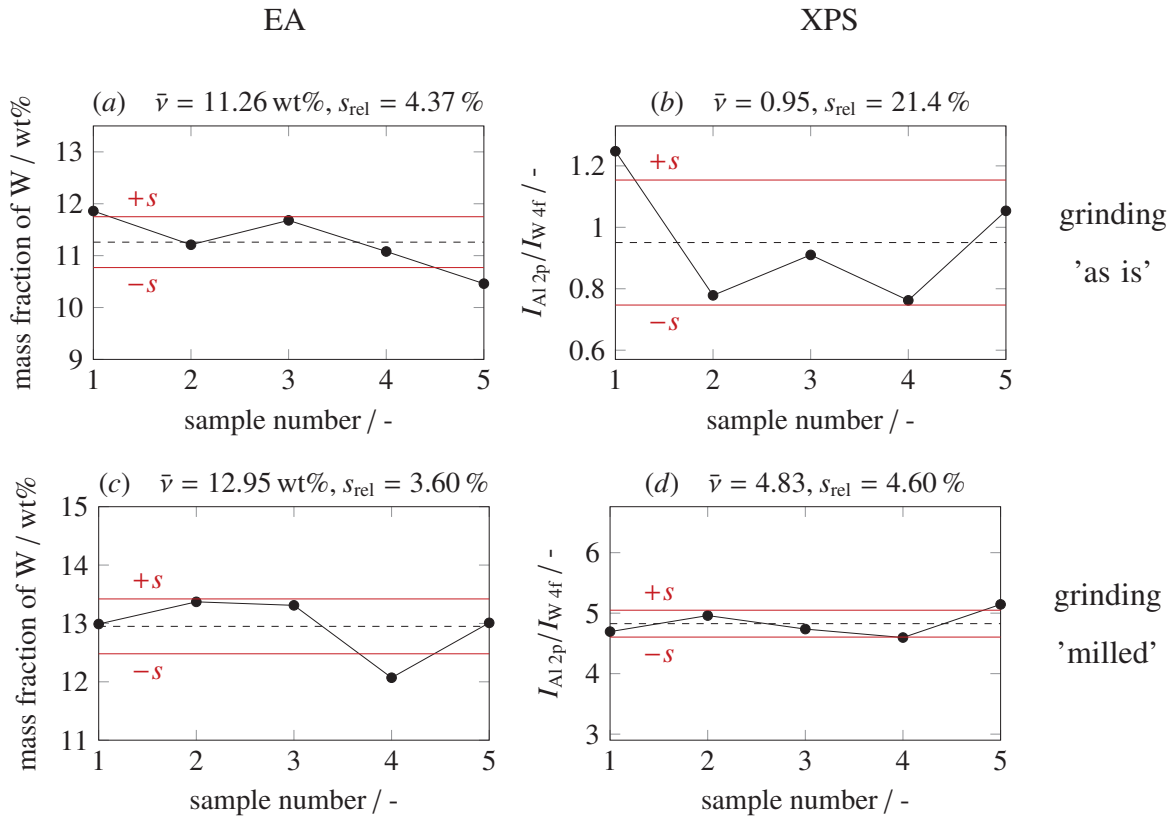


**Figure 8.4:** Results from EA (a,c) and XPS analysis (b,d) from grinding 'as is' (a,b) and 'milled' (c,d) $Al_2O_3$ and $WO_3$.

The main reason for the superior performance of grinding as compared to shaking is the input of higher shear forces, which are required for de-agglomeration of cohesive powders. Upon the steady destruction and reorganization of agglomerates, the mixture quality is greatly increased, as stable agglomerates comprising both powders are formed. This process of 'micro-mixing' also gives a statistical advantage as shown in equation (8.7). For free-flowing powders on the other hand, manual grinding is not an ideal mixing technique, as it involves the size reduction of primary particles. When decisive grinding parameters such as the contact pressure and the amount of grinding cycles are not well controlled, the obtained particle sizes are ill-defined and segregation effects cannot be ruled out.

In general, our results are in line with several other quantitative XPS studies, which have also achieved a satisfactory degree of mixing by manual grinding [313, 316, 317]. In those studies, however, no information about particle sizes was given. We can therefore only speculate whether very fine fractions were used or not.

#### 8.5.1.3 Dispersing powders in ethanol

Dispersing cohesive powders in a liquid is a valuable tool for completely separating agglomerates into primary particles because liquids enter void spaces between particles and, thus, drastically reduce interparticle forces [318]. Once complete de-agglomeration is achieved, thorough mixing is simplified because particle-particle interactions are reduced as compared to the dry state. Hence, dispersing two powders in a liquid is considered to result in a state of maximum disorder which should be preserved by quickly drying the obtained suspension in the already described manner outlined in section 8.4.3. Mixtures obtained by the described novel technique might be regarded as a benchmark with respect to the maximum achievable mixing quality. As will be shown below, superior mixing quality is achieved indeed by the applied mixing method, which justifies the increased experimental effort associated with this technique.

The prerequisite for the suggested technique is the thorough dispersion of both powders in the liquid. This is however not necessarily achieved for any particle size, which turns obvious, when mixing 'as is' $Al_2O_3$ and $WO_3$ powder samples (see figure 8.5). The relative standard deviation for elemental and XPS analysis is in both cases greater 20 %, which indicates an insufficient degree of mixing. The absolute values of tungsten mass fraction (6.6 wt%) and XPS intensity ratio (0.50) show the same trends as shaking 'as is' powders, i.e. lower than expected for elemental analysis (13.22 wt%) and also lower than the expected $I_{\mathrm{Al\ 2p}}/I_{\mathrm{W\ 4f}}$ intensity ratio of 2.50. These results can be explained by the observed formation of a sediment of $Al_2O_3$ particles during the sonication procedure. This behavior was not observed when using 'milled' powders, which show an excellent precision for elemental analysis (1.58 wt%) as well as XPS analysis (5.92 %). Also, absolute values are reasonably close to the expected ones.

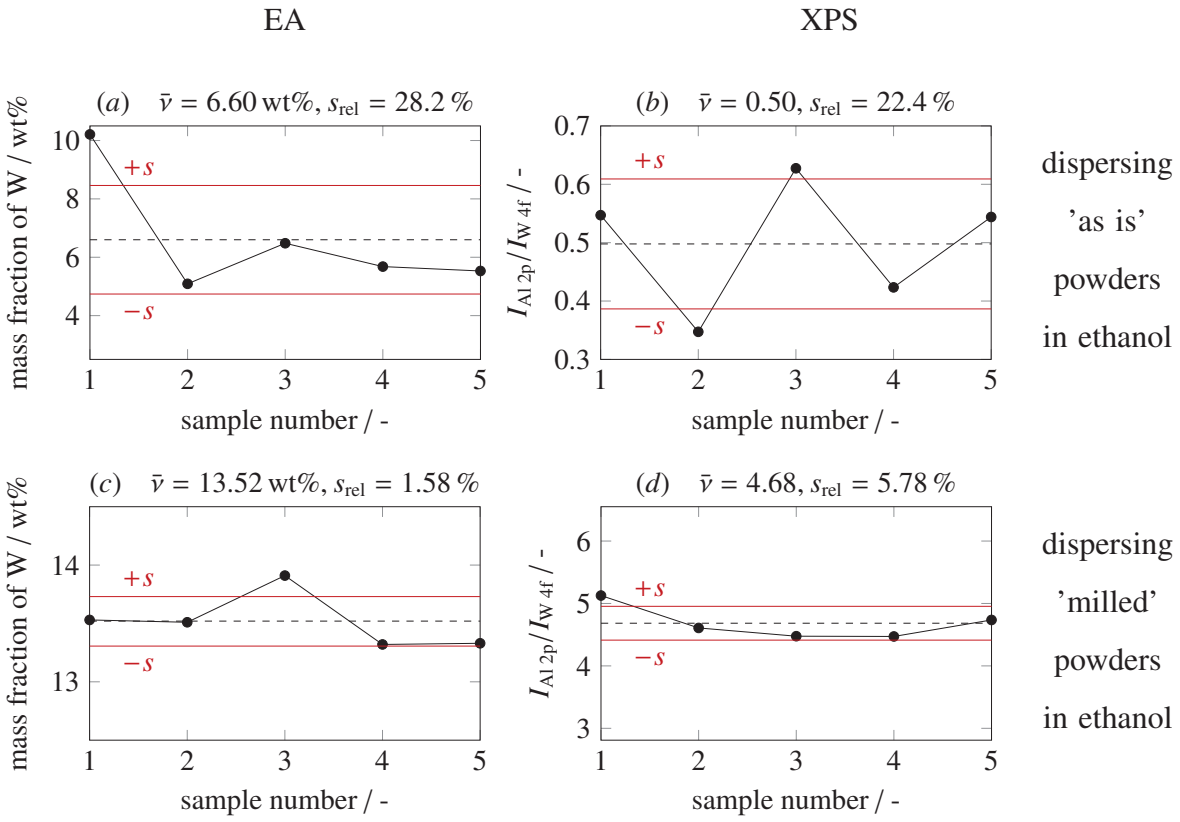


**Figure 8.5:** Results from EA (a,c) and XPS analysis (b,d) from dispersing 'as is' (a,b) and 'milled' (c,d) $Al_2O_3$ and $WO_3$ powders in ethanol.

In order to evaluate whether XPS intensities scale with the concentration of the analyte ($Al_2O_3$), the mass ratio $\xi = m_{Al_2O_3}/m_{WO_3}$ was varied in the following way: $\xi$ = 9/1, 5/1, 3/1, 2/1 and 1/1. In a simple model approach, the intensities of the mixture, $I_{Al\,2p}$ and $I_{W\,4f}$, result from the Al 2p intensity of pure alumina, $I^{\infty}_{Al\,2p}$, and the W 4f intensity of pure tungsten oxide, $I^{\infty}_{W\,4f}$, multiplied by the corresponding surface area fraction, which shall be $x$ for alumina and $1-x$ for tungsten oxide. The described correlations are depicted in equations (8.11) and (8.12).

$$I_{Al\,2p} = I^{\infty}_{Al\,2p} \cdot x \tag{8.11}$$

$$I_{W\,4f} = I^{\infty}_{W\,4f} \cdot (1-x) \tag{8.12}$$

As a consequence, equation (8.13) is obtained

$$\frac{I_{Al\,2p}}{I_{Al\,2p}+I_{W\,4f}} = \frac{I^{\infty}_{Al\,2p} \cdot x}{I^{\infty}_{Al\,2p} \cdot x + I^{\infty}_{W\,4f} \cdot (1-x)} = \frac{x}{x+(1-x) \cdot I^{\infty}_{W\,4f}/I^{\infty}_{Al\,2p}}, \tag{8.13}$$

which in its reciprocal form leads to

$$\frac{I_{\mathrm{Al\,2p}} + I_{\mathrm{W\,4f}}}{I_{\mathrm{Al\,2p}}} = 1 - \frac{I^{\infty}_{\mathrm{W\,4f}}}{I^{\infty}_{\mathrm{Al\,2p}}} + \frac{I^{\infty}_{\mathrm{W\,4f}}}{I^{\infty}_{\mathrm{Al\,2p}}} \cdot \frac{1}{x}. \tag{8.14}$$

Equation (8.14) describes the intensity ratio as a linear function of the alumina surface area fraction, comprising a constant intercept $t = 1 - I^{\infty}_{\mathrm{W\,4f}}/I^{\infty}_{\mathrm{Al\,2p}}$ and a constant slope $m = I^{\infty}_{\mathrm{W\,4f}}/I^{\infty}_{\mathrm{Al\,2p}}$. $1/x$ is the reciprocal alumina surface fraction, which is given by

$$\frac{1}{x} = \frac{A_{\mathrm{Al_2O_3}} + A_{\mathrm{WO_3}}}{A_{\mathrm{Al_2O_3}}} \approx \frac{V_{\mathrm{Al_2O_3}} + V_{\mathrm{WO_3}}}{V_{\mathrm{Al_2O_3}}} = 1 + \frac{V_{\mathrm{WO_3}}}{V_{\mathrm{Al_2O_3}}} = 1 + \frac{1}{\xi} \cdot \frac{\rho_{\mathrm{Al_2O_3}}}{\rho_{\mathrm{WO_3}}}. \tag{8.15}$$

Now, figure 8.6 is obtained by plotting the measured data according to equation (8.14). The dashed line represents the theoretical model. For error indicators, relative standard deviations of $\xi$ = 1/5 and 'milled' powders were used, i.e. $\pm$ 5.78 % for $y$ and $\pm$1.58 % for $x$ (figure 8.5).

The resulting plot validates the theoretical model and confirms the high reproducibility of the applied mixing technique. Furthermore, the absence of any systematical errors is suggested, caused for example by segregation effects, selective loss or gain of one of the powders or matrix effects. It is worth mentioning, that the observed concentration dependence is the desired one for using the $WO_3$ powder as internal standard for determining quantitatively the Al content of the $Al_2O_3$ analyte powder, because the analyte is seemingly not affected by the presence of the standard and *vice versa*. This is however not naturally the case. From analytical chemistry, plenty of examples are known, where the usage of internal standards is aggravated due to matrix effects [333]. Also, we will show further below that one has to be very careful when preparing samples by mixing analyte and standard powders.

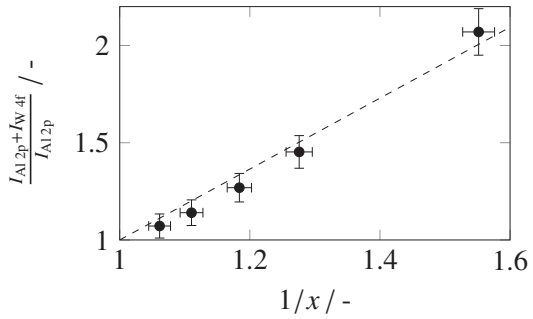


**Figure 8.6:** Results obtained from XPS analysis of 'milled' $Al_2O_3$ and $WO_3$ powders dispersed in ethanol with different mass ratios ($\xi = m_{\mathrm{Al_2O_3}}/m_{\mathrm{WO_3}}$ = 1/1, 2/1, 3/1, 5/1 and 9/1). The dashed line represents the best fit to the function described by equation (8.14). The exact result for the fitting parameter is $I^{\infty}_{\mathrm{W\,4f}}/I^{\infty}_{\mathrm{Al\,2p}} = 1.8233 \pm 0.0974$.

In order to confirm the general applicability of the used method, we also assessed mixing another analyte, namely $TiO_2$, with an internal powder standard. For this purpose, we used the milled fractions of $TiO_2$ and $Al_2O_3$. The reason why we switched to $Al_2O_3$ as an internal

standard instead of $WO_3$ was primarily because the W 4f core level possibly overlaps with Ti 3p. In addition, $Al_2O_3$ in the 'milled' state was readily available in an easy-to-disperse form. The results displayed in figure 8.7 show that high precision can also be obtained with mixtures different from $Al_2O_3/WO_3$. Regarding trueness, the theoretical intensity ratio of $I_{Ti\ 2p}/I_{Al\ 2p}$ = 23.62 is missed by a factor of 2 (section 8.3).

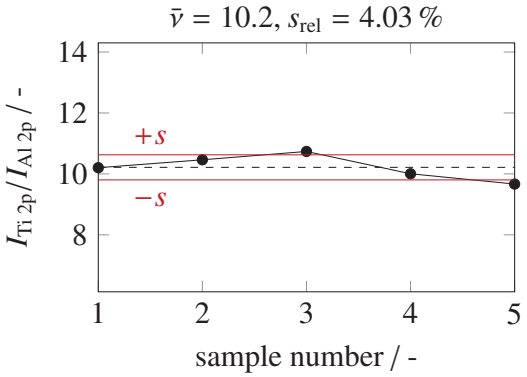


**Figure 8.7:** Results from XPS analysis from dispersing 'milled' $TiO_2$ and $Al_2O_3$ powders in ethanol. The mass ratio is $\xi = m_{TiO_2}/m_{Al_2O_3}$ = 5/1.

Despite the excellent results obtained by dispersing cohesive powders with a maximum particle size of 10 µm in ethanol, it should be noted, that the technique involves a higher experimental effort as compared to shaking or grinding. Also, the addition and removal of a liquid make the method more error-prone and labor intensive. We therefore use the technique primarily as a benchmark technology, providing a maximum degree of mixing. In comparison, grinding particles smaller 10 µm shows an equally good precision at greatly reduced complexity.

Although we believe that the effect of particle size is of rather general nature, i.e. mixing by grinding and dispersion in a liquid is generally facilitated for particle sizes below 10 µm, we explicitly note that the obtained results are not readily transferable to other powder systems, even if these show sufficiently small particle sizes. This is because grinding and dispersion in a liquid both comprise a marked energy input which might cause changes in the sample material. As we have used very simple and stable powders, which are (a) not prone to material redistribution and (b) do not show a material gradient between surface and volume (on a particle scale), we have not monitored a preparation bias. However, as we will see in the next section, care must be taken in the case of technical samples, such as supported catalysts or layered materials, as grinding and dispersion in a liquid may indeed cause significant changes to the surface composition.

## 8.5.2 The concept of coating

In the previous section it was shown, that mixing cohesive powders below 10 µm results in reproducible XPS readings, if agglomerates are broken by high enough shear forces. This section utilizes the previous findings and presents a strategy to overcome the encountered limitations, which are (a) mixing of particle sizes greater than 10 µm and (b) material stress during mixing. In order to solve theses problems, internal standards with similar physical properties as the analyte, in particular similar particle sizes of analyte and standard, are needed. Standards of this kind are not readily available [318] and thus, adequate materials need to be designed. Here, we suggest coating as a straightforward synthesis method to obtain identical particle sizes of analyte and standard with similar physical properties since a thin layer on top of a support does not significantly contribute to the volume properties of the material.

For common support materials such as $Al_2O_3$ and $TiO_2$ but also for $ZrO_2$, $SiO_2$ and others, the formation of monolayer coatings has been observed for various volatile oxides, e.g. $MoO_3$ [334], $Cr_2O_3$ [325] and others [335]. This behavior is explained by their low Tammann temperature and strong adhesive forces between the spreading material and the support [336, 337]. For the following sections, $MoO_3/Al_2O_3$ ($\theta_{Mo} = 2.85\,at/nm^2$) and $MoO_3/TiO_2$ ($\theta_{Mo} = 1.46\,at/nm^2$) will be used as the nominal analyte and $Cr_2O_3/Al_2O_3$ ($\theta_{Cr} = 2.81\,at/nm^2$) and $Cr_2O_3/TiO_2$ ($\theta_{Cr} = 11.23\,at/nm^2$) will be used as the nominal standard, respectively. The presented method may be applied in principle to any other supported catalyst of interest.

### 8.5.2.1 Particle size

The powders used for the experiments shown in this section are compared with regard to their particle size distribution as displayed in figure 8.8. It is shown, that 'coated' powders, i.e. those containing a thin layer of $MoO_3$ or $Cr_2O_3$, show the same particle size distribution as the corresponding 'as is' support material. Regarding flow characteristics, $TiO_2$-based systems are rated as cohesive, whereas $Al_2O_3$-based systems are rated as free-flowing.

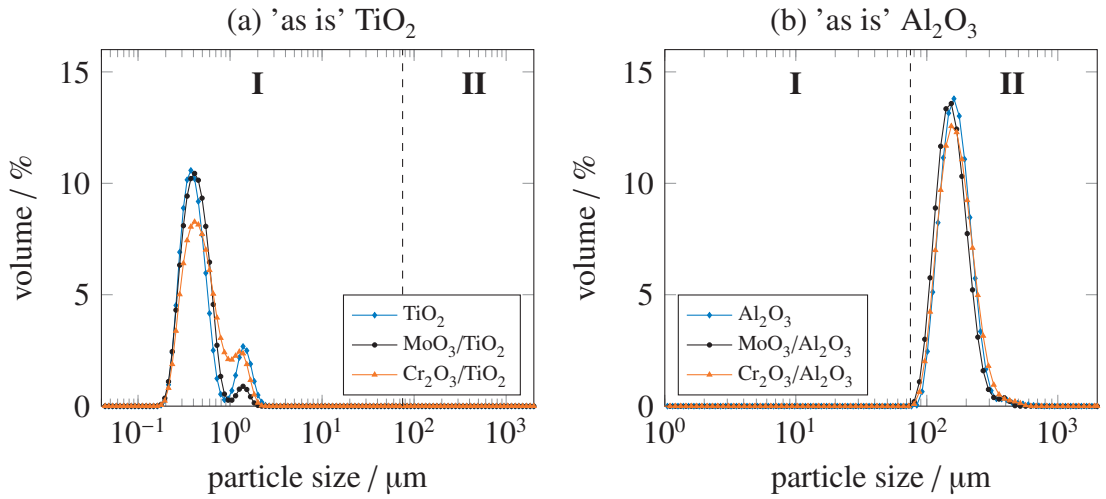


**Figure 8.8:** Particle size analysis of 'as is' $TiO_2$ (a) and 'as is' $Al_2O_3$ (b), coated with a thin layer of $MoO_3$ or $Cr_2O_3$, respectively. The dashed line positioned at 75 µm denotes the boundary value between cohesive (domain I) and free-flowing (domain II) particles.

### 8.5.2.2 Mixing

Figure 8.9 shows the XPS results obtained for $TiO_2$-based materials. Known that the particle sizes of standard and analyte are identical, all introduced mixing procedures (shaking, grinding and dispersing powders in a liquid) should result in a relative standard deviation of $s_{\text{rel}} \leq 7\,\%$, if the experimental errors occur exclusively from the statistics of the XPS analysis. In this case, all mixing techniques should lead to the maximum achievable precision. As the applied $TiO_2$ particles are smaller than 10 µm, the results obtained for grinding and dispersion in ethanol are in line with the expectation outlined in section 8.5.1. However, the striking result of the experiments plotted in figure 8.9 is, that shaking also leads to a similar precision when compared to grinding and dispersion in ethanol. This could not be expected as the energy input by shaking is not enough to separate agglomerates, as was shown in the first set of experiments, discussed in section 8.5.1. It is thus worth emphasizing, that the specific components used here enable high quality mixtures, even if the standard is introduced by shaking. Apparently, both 'coated' systems show a similar agglomeration behavior. Apart from the very low relative standard deviation, the offset in absolute Mo/Cr intensity ratio obtained when applying the shaking, grinding or dispersion in ethanol is however puzzling. Obviously a systematic error must have been introduced in one or two of the mixing techniques leading to a deviation of the absolute $I_{Mo\ 3d}/I_{Cr\ 2p}$ intensity ratio by almost a factor of 2. A detailed discussion regarding this topic is provided further below and in a forth coming paper.

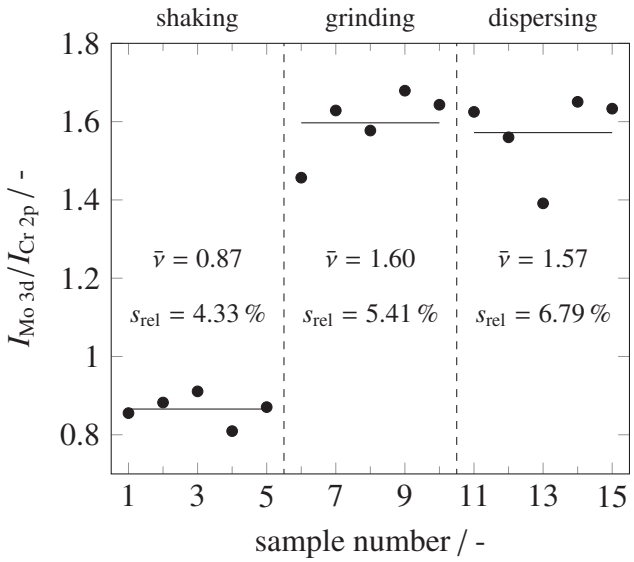


**Figure 8.9:** XPS analysis of $MoO_3/TiO_2$ and $Cr_2O_3/TiO_2$ ($\xi$ = 5/1) mixed by shaking, grinding and dispersing powders in ethanol.

The XPS results obtained from the alternative system, i.e. mixing powders which are supported on 'as is' $Al_2O_3$, are shown in figure 8.10. Similar to the results obtained for $TiO_2$, grinding and dispersion in ethanol result in relative standard deviations below 7 %. The value for shaking is slightly higher at 12 %. It is worth mentioning, that all experiments involving free-flowing powders have so far shown significantly worse precision values. Hence, using 'coated' powders almost entirely solves the problem of segregation even when dealing with particle sizes above 75 µm. Nevertheless, powders supported on 'as is' $Al_2O_3$ also show significant offsets in absolute $I_{Mo\ 3d}/I_{Cr\ 2p}$ intensity ratios between the applied mixing procedures. When the mean values presented in figure 8.10 are evaluated, a factor of 1.06 occurs between shaking and dispersion in a liquid and a factor of 1.54 occurs between shaking and grinding. This systematic deviation as well as the one observed for powders supported on 'as is' $TiO_2$, need to be discussed.

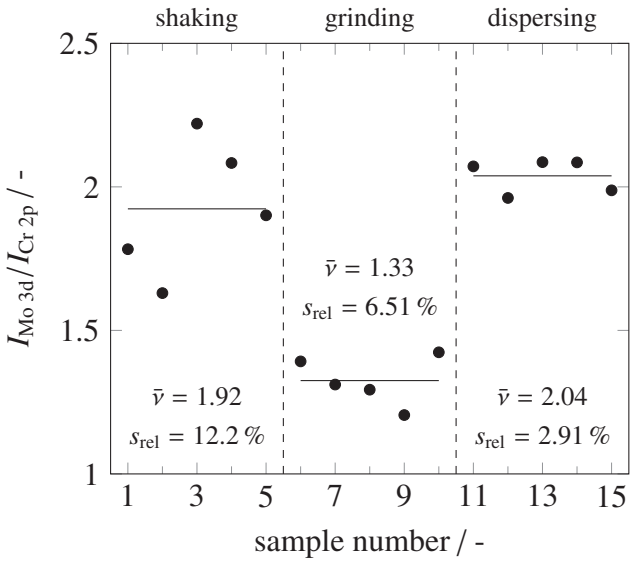


**Figure 8.10:** XPS analysis of $MoO_3/Al_2O_3$ and $Cr_2O_3/Al_2O_3$ ($\xi$ = 5/2) mixed by shaking, grinding and dispersing powders in ethanol.

In order to obtain an idea which effects account for the the observed offsets, it is necessary to clarify the differences between the applied mixing techniques. Shaking can be regarded as the 'least invasive' technique because a minimum amount of energy is used for dispersing the powders that are kept in their dry state. Thus, the arithmetic mean values obtained for shaking are regarded as the most trustworthy. Grinding and dispersing powders in ethanol on the other hand involve a markedly higher input of mechanical energy, whereas the latter is regarded as the 'most invasive' technique, as it additionally involves contacting powders with a liquid. Indeed, it was shown in an additional experiment (described in section 8.7.4), that Cr and Mo species may be dissolved to some degree in ethanol. This effect may have led to a re-dispersion of surface compounds, e.g. by surface deposition upon drying. The monitored increase in $I_{Mo\ 3d}/I_{Cr\ 2p}$ ratio might thus be explained by the removal of $Mo^{6+}$ species from $MoO_3$ surfaces and their re-deposition on $TiO_2$ or $Cr_2O_3$ surfaces during drying. Although grinding does not involve the wetting of powders, mechanical force alone may also trigger the re-dispersion of Mo oxide species. Hence, it has been reported, that $MoO_3$ crystallites can be completely spread over a $\gamma$-$Al_2O_3$ surface by means of ball milling [338]. In our $TiO_2$-supported samples, small amounts of crystalline $Cr_2O_3$ and $MoO_3$ were identified in the coating layer by means of XRD (section 8.7.6) and thus crystalline material might act as a reservoir which is re-dispersed during the mixing procedure. Nonetheless, the exact reason for the increase in $I_{Mo\ 3d}/I_{Cr\ 2p}$ ratio is still subject of ongoing research.

$Al_2O_3$-supported systems show a different behavior as $TiO_2$-supported powders. Hence, the offset between shaking and dispersing powders in ethanol almost vanishes. This may have several reasons, however, it is interesting to note, that no crystalline $MoO_3$ or $Cr_2O_3$ phases were observed on $Al_2O_3$ samples. This seems to be in line with the comparably low coverages of Mo

and Cr atoms per $nm^2$ of support surface. Thus, if the reason for the observed offsets are linked to additional crystalline phases, it seems logically, that $Al_2O_3$-supported powders show lower offsets in comparison with $TiO_2$-supported systems. Of course, this argument does not hold in the case of grinding. However, grinding should be excluded from the above discussion as it involves particle crushing and therefore it might be highly disadvantageous for the intended goal of providing a synthesis route towards a thoroughly mixed powder sample without introducing any unwanted side effects. The offset between grinding and shaking/dispersion in ethanol, may also originate from ill-defined particle sizes and/or the exposure of additional support surface in the form of fracture planes. However, without more detailed information, we back away from a deeper discussion at this point.

## 8.6 Conclusion

It was demonstrated how binary solid mixtures of satisfactory quality for quantitative XPS analysis are obtained. If cohesive powders of a maximum particle size of 10 µm and high stability against re-dispersion effects are used, manual grinding provides a high enough accuracy at a manageable complexity. Dispersion in ethanol is an even more complex mixing technique that also gives highly accurate results. If some effort is put into the synthesis of a tailor-made internal standard, powder mixing is greatly facilitated since the achievable mixing quality turned out to be independent of particle size. Care must be taken with grinding and suspending powders in liquids, as this may lead to re-dispersion of the chemical species used as intensity normal in XPS. Our results open the door for using internal intensity standards for quantitative XPS analysis of technical catalysts on a routine basis.

## 8.7 Supporting Information

### 8.7.1 Mass gain of baked out $Al_2O_3$

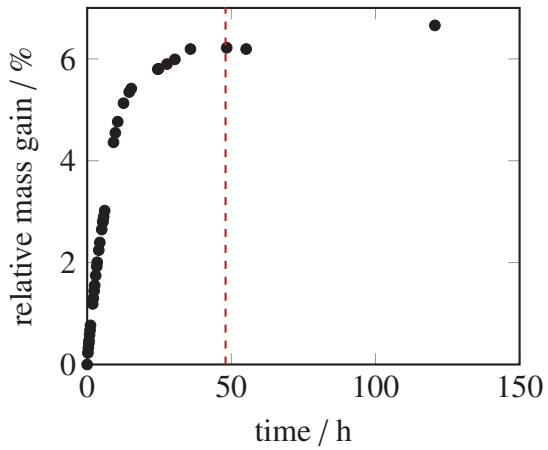


**Figure 8.11:** Mass gain of 'as is' $Al_2O_3$ after bakeout at 450 °C (5 h, 5 K/min). The dashed vertical line at 48 h displays the maximum waiting time before weighing out analyte/standard mixtures.

### 8.7.2 Effect of sonication time on size distributions of $Al_2O_3$, $TiO_2$ and $WO_3$

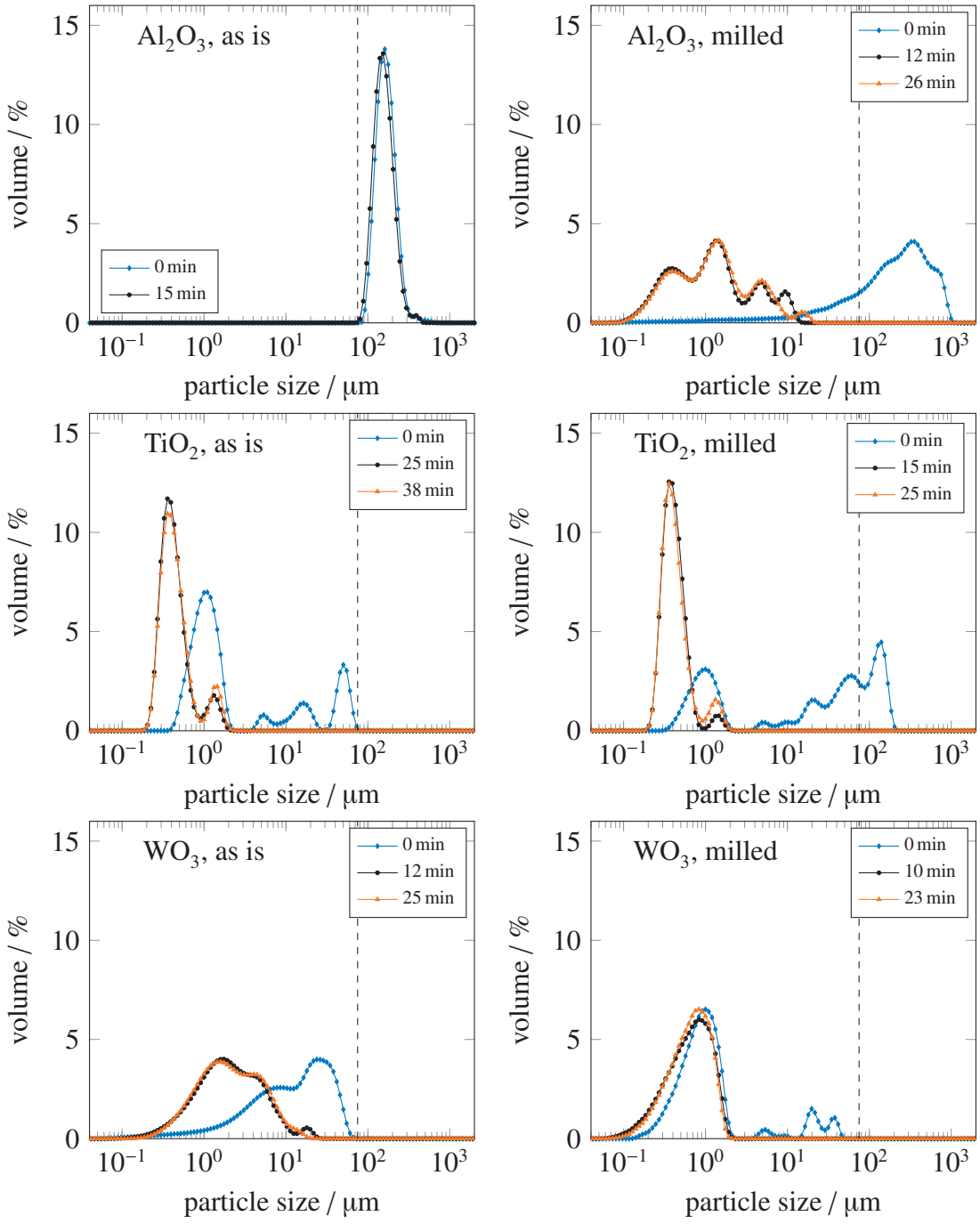


**Figure 8.12:** Size distributions of 'as is' (left) and 'milled' (right) $Al_2O_3$, $TiO_2$ and $WO_3$ powders for varying sonication times in ethanol.

## 8.7.3 Theoretical reference values

### 8.7.3.1 Precision

The uncertainty of an XPS measurement, $u(y)$, can be accessed via Gaussian error propagation according to equation (8.16). Relative uncertainties are defined in equation (8.17).

$$u^2(y) = \sum_{i=1}^{m} \left( \frac{\partial f}{\partial x_i} \right)^2 \cdot u^2(x_i) \tag{8.16}$$

$$u_{\mathrm{rel}} = \frac{u(x_i)}{|x_i|} \tag{8.17}$$

$u(y)$ results from differentiation the intensity ratio $y = I_A/I_S$, with respect to $I_A$ and $I_S$. After simplification, equation (8.18) is obtained.

$$u^2(y) = y^2 \cdot \left( \left( \frac{u(I_A)}{I_A} \right)^2 + \left( \frac{u(I_S)}{I_S} \right)^2 \right) \tag{8.18}$$

If relative uncertainties are introduced, the following expression is obtained:

$$u_{\mathrm{rel}}(y) = \sqrt{u_{\mathrm{rel}}^2(I_A) + u_{\mathrm{rel}}^2(I_S)} \tag{8.19}$$

Hence, the relative uncertainty of the internal standard approach depends on the relative uncertainties of the considered photoelectron intensities. As our measurement routine rules out time-dependent fluctuations of the experimental conditions, we believe that the most error-prone step in the determination of photoelectron intensities is the signal integration procedure. If we assume a value of 5 % for the relative uncertainty of the latter, which seems realistic for technical powder samples, the maximum achievable precision in quantitative XPS analysis is in the region of 7 %.

### 8.7.3.2 Trueness

**Elemental analysis** of an ideal mixture of $Al_2O_3$ and $WO_3$ powders, weight out in a mass ratio $\xi = m_{Al_2O_3}/m_{WO_3}$, gives an absolute value of the tungsten mass fraction, $w_W$, of

$$w_W = \frac{m_W}{m_{WO_3} + m_{Al_2O_3}} = \frac{M_W}{M_{WO_3}} \cdot \frac{1}{1+\xi} \tag{8.20}$$

where $m_i$ is the mass of species i and $M_i$ is the molar mass of species i. For a mass ratio of $\xi = 5/1$, equation (8.20) gives a tungsten mass fraction of $w_W = 13.22\,\text{wt\%}$.

**XPS analysis** of an ideal mixture of analyte (A) and standard (S) gives an absolute value for the relative intensity ratio $I_A/I_S$, of

$$\frac{I_A}{I_S} = \frac{\sigma_A(h\nu)}{\sigma_S(h\nu)} \cdot \frac{L_A(\gamma)}{L_S(\gamma)} \cdot \frac{T(E_A)}{T(E_S)} \cdot \frac{N_A}{N_S} \cdot \frac{f(\lambda_A)}{f(\lambda_S)}. \tag{8.21}$$

The transmission function of a LHS 10 electron analyzer, operated at a constant pass energy, is given by

$$T(E_i) \propto \frac{1}{E_i}, \tag{8.22}$$

where $E_i$ is the kinetic energy the considered photoelectron line of a species i [339]. Furthermore, the applied XPS setup was operated at $\gamma = 54.7$, whereby angular asymmetries, $L_i(\gamma)$, cancel each other out [195]. The amount of photoelectrons which are leaving the sample can be expressed by

$$N_i \cdot f(\lambda_i) = \rho_{i,\,2D} \cdot A \cdot \int_0^\infty e^{-z/\lambda_i(E_i)}, \tag{8.23}$$

where $N_i$ is the amount of atoms of species i which contribute to the regarded photoelectron line, $e^{-z/\lambda_i}$ is the escape probability of emitted photoelectrons in a distance $z$ below the sample surface, $\rho_{i,\,2D}$ is the area density of atoms of species i and $A$ is the illuminated sample surface area. Under the assumption of a similar constitution of the sample surface and the sample bulk, $\rho_{i,\,2D}$ can be expressed by

$$\rho_{i,\,2D} = \rho_{i,\,3D} \cdot z = \frac{\rho_i}{M_i \cdot N_A} \cdot z, \tag{8.24}$$

where $\rho_{i,\,3D}$ is the volume density of atoms of species i, $\rho_i$ is the mass density (per volume) and $N_A$ is Avogdro's constant. Equation (8.23) and (8.24) can be summarized as follows:

$$N_i \cdot f(\lambda_i) = \frac{\rho_i}{M_i \cdot N_a} \cdot A \cdot \int_0^\infty z \cdot e^{-z/\lambda_i(E_i)} = \frac{\rho_i}{M_i \cdot N_a} \cdot A \cdot \lambda_i(E_i)^2 \tag{8.25}$$

In the case of $Al_2O_3$ and $WO_3$ powders, the density ratio of the analyte, $\rho_{Al}$, and standard component, $\rho_W$, can be expressed as follows:

$$\frac{\rho_{Al}}{\rho_W} = \frac{m_{Al}}{m_W} = \frac{n_{Al} \cdot M_{Al}}{n_W \cdot M_W} = \frac{2 \cdot n_{Al_2O_3} \cdot M_{Al}}{n_{WO_3} \cdot M_W} = 2 \cdot \xi \cdot \frac{M_{WO_3}}{M_{Al_2O_3}} \cdot \frac{M_{Al}}{M_W} \tag{8.26}$$

Summarizing equations (8.21) to (8.26) for an ideal mixture of $Al_2O_3$ and $WO_3$ powders, having a mass ratio of $\xi = m_{Al_2O_3}/m_{WO_3} = 5/1$, results in the following equation:

$$\frac{I_{Al\,2p}}{I_{W\,4f}} = 2 \cdot 5 \cdot \frac{\sigma_{Al\,2p}(1253.6\,eV)}{\sigma_{W\,4f}(1253.6\,eV)} \cdot \frac{E_{W\,4f}}{E_{Al\,2p}} \cdot \frac{M_{WO_3}}{M_{Al_2O_3}} \cdot \frac{\lambda^2_{Al_2O_3}}{\lambda^2_{WO_3}} \tag{8.27}$$

If cross-sections from [193] and IMFPs calculated according to [196] are used, an intensity ratio of $I_{Al\,2p}/I_{W\,4f} = 2.50$ is obtained. In the case of a $TiO_2$ analyte, a $Al_2O_3$ standard and $\xi = m_{TiO_2}/m_{Al_2O_3} = 5/1$, the obtained intensity ratio is $I_{Ti\,2p}/I_{Al\,2p} = 23.62$.

### 8.7.4 Solubility of Cr and Mo species in ethanol

The solubility of Cr and Mo species in ethanol was checked by sonicating the following powders for 2 h in ethanol:

- $Cr_2O_3/Al_2O_3$ ($\theta_{Cr} = 2.81\,at/nm^2$)
- $Cr_2O_3/TiO_2$ ($\theta_{Cr} = 11.23\,at/nm^2$)
- $MoO_3/Al_2O_3$ ($\theta_{Mo} = 3.0/nm^2$)
- $MoO_3/TiO_2$ ($\theta_{Mo} = 15.2/nm^2$)

After sonication, suspensions were filtered (Pall, 0.1 µm) to remove all particles from the suspension. The remaining colorless solutions were drop-casted on a $SiO_2$ wafer at 100 °C. Subsequent XPS analysis of the wafers revealed Cr 2p and Mo 3d signals for all samples, i.e. small amounts of Cr or Mo species must have dissolved in the ethanol solution.

## 8.7.5 XRD patterns of reference compounds

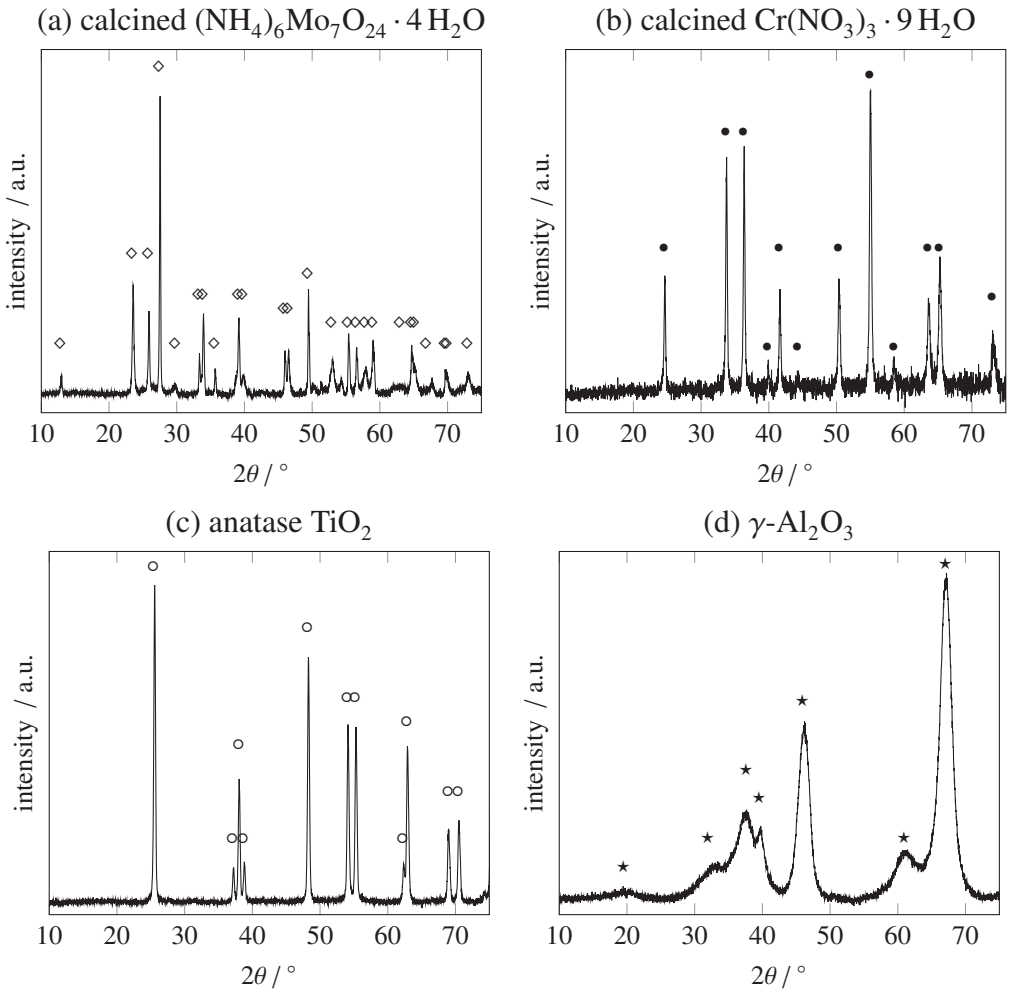


**Figure 8.13:** XRD patterns of calcined ammonium heptamolybdate (a), calcined chromium(III) nitrate (b), milled $TiO_2$ (c) and milled $Al_2O_3$ (d). Indicated reference reflections are for crystalline $MoO_3$ (◇), $Cr_2O_3$ (●), anatase $TiO_2$ (○) and $\gamma$-$Al_2O_3$ (⋆) (JCPDS 76-1003, 38-1479, 84-1286, 10-0425).

## 8.7.6 XRD patterns of $Cr_2O_3$ and $MoO_3$ supported on $TiO_2$ and $Al_2O_3$

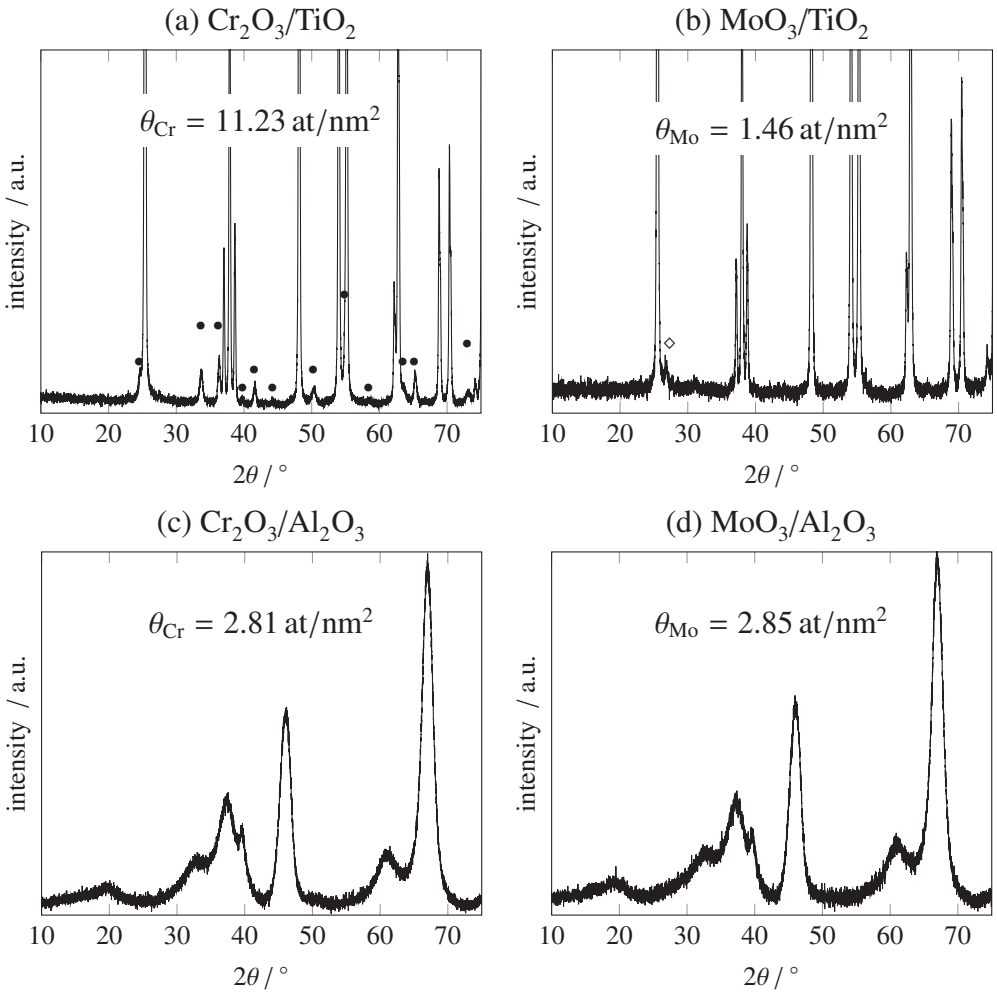


**Figure 8.14:** XRD patterns of $Cr_2O_3/TiO_2$ (a), $Cr_2O_3/Al_2O_3$ (b), $MoO_3/TiO_2$ (c) and $MoO_3Al_2O_3$ (d). Indicated reference reflections are for crystalline $MoO_3$ (◇) and $Cr_2O_3$ (●) (JCPDS 76-1003, 38-1479).

# 9 Closing

## 9.1 Summary

The $CO_2$ methanation is a key step in the Power-to-Gas concept and might as such contribute to the transition of the energy supply system towards 100 % renewable energy. Although the synthesis over Ni-based catalysts has been known from the beginning of the 20$^{th}$ century, its commercialization has not yet been realized and is seriously considered only since a couple of years. Despite the known and severe consequences of sulfur poisoning of Ni catalysts, there is still a lack of systematic investigations of sulfur poisoning of state-of-the-art Ni catalysts operated under $CO_2$ methanation conditions. The thesis at hand provides a solid pool of experimental data which serves as a basis for deducing the general principles of sulfur poisoning and understanding the prevailing mechanisms and kinetics.

In the first part of the thesis, the propagation of a 'poisoning wave' through a fixed-bed microreactor is visualized by near infrared thermography measurements during *in situ* poisoning of a Ni-Al catalyst by 5 ppm of $H_2S$ under equilibrium conditions (400 °C, 1 bar, $H_2/CO_2/Ar$ = 4/1/5). The hot spot, which is initially formed at the reactor entrance due to the exothermal character of the $CO_2$ methanation reaction, starts to migrate at a constant velocity along the reactor axis upon the addition of $H_2S$ to the feed gas mixture. The integral conversion is not affected until the hot spot reaches the reactor outlet because only a fraction of the fixed-bed is needed to achieve the equilibrium product gas composition. The hot spot vanishes at the reactor outlet once the fixed-bed is completely saturated with sulfur. At this point, the methanation activity of the bed is entirely lost. The measured catalyst lifetime roughly correlates with its $H_2$ uptake capacity measured prior to poisoning. It is therefore suggested that the amount of surface nickel atoms determine the lifetime of a Ni-Al catalyst under sulfur poisoning conditions.

Upon studying the *in situ* poisoning behavior of different Ni-Al catalysts, it is indeed found that the $H_2$ uptake of an aged Ni-Al catalyst precisely matches its capacity for S adsorption. Hence, a constant saturation coverage of $\theta_S = 0.73 \pm 0.02$ is obtained independent of the catalyst's Ni loading. Furthermore, no difference in poisoning behavior was monitored for $H_2S$ to $SO_2$ poisoning. Based on the obtained results, it was possible to derive a general applicable model

for the prediction of Ni-Al catalyst lifetimes under sulfur poisoning conditions. Extrapolation of this model to ppb levels of sulfur in the feed led to the conclusion that such experiments are excessively time consuming and will not lead to sulfur coverages below circa $\theta_S = 0.5$. Therefore, an *ex situ* poisoning method, which was able to achieve sulfur coverages between $\theta_S = 0$ and $\theta_S = 0.73$ was chosen. Activities, which were normalized to the non-poisoned state, were found to decrease below 20 % of their initial value ($\theta_S = 0$) for sulfur coverages exceeding $\theta_S = 0.2$. The surprisingly strong dependence of activity on sulfur coverage correlates strongly with the loss of the catalyst's $CO_2$ adsorption capacity and to a lesser extent also with the loss of its $H_2$ adsorption capacity. Based on this data, it was calculated that on average about 10 unoccupied Ni surface atoms are needed for the adsorption of one $CO_2$ molecule. Subsequent evaluation of activation energies of poisoned and non-poisoned samples led to the conclusion that sulfur poisoning is due to mere site-blockage and only to a lesser extent due to electronic effects. The obtained adsorption stoichiometry for $CO_2$ molecules therefore indicates that the $CO_2$ methanation reaction is highly structure-sensitive.

Investigations of sulfur poisoning of Ni-Al catalysts promoted by Fe, Mn, Co, Zn and Cu reveal an increased resistance versus *in situ* $H_2S$ poisoning of promoted systems. The obtained results suggest that the employed promoter metals adsorb $H_2S$ and protect the active $Ni^0$ surface to some degree. Furthermore, Mn- and Fe-promoted catalysts show an increased activity in the non-poisoned state, whereas Co- and Zn-promoted catalysts do not have an impact on activity and Cu decreases it. $H_2$ and $CO_2$ adsorption experiments indicate that the observed trends are due to the adsorption of additional amounts of $CO_2$ on the promoter phase and its conversion to $CH_4$. This behavior is only observed for Mn- and Fe-doped systems. In contrast, Cu adsorbs $CO_2$ but forms CO instead of $CH_4$, causing catalyst deactivation. Co and Zn act as spectator species, which adsorb small (Zn) or negligible (Co) amounts of $CO_2$, and have insignificant impact on catalyst activity.

When studying promoter metals, X, or poisons, S, interacting with Ni-Al catalysts, the analytical complexity is greatly increased as compared to pure Ni-Al systems. On the one hand, this is because additional phases need to be taken into account. Hence, binary Ni-Al systems are extended towards ternary or quaternary (S-)X-Ni-Al systems. On the other hand, the quantity of the added phases, related to the promoter and poison compound, is significantly smaller as compared to the active phase and the support phase. Thus, one readily approaches the analytical limit of common standard methods such as XRD, TPR, TGA and even $H_2$ or $CO_2$ chemisorption. Conclusive evidence about the effect of promoters or poisons, their location on the catalyst surface and possible interactions with the active and/or support phase is therefore greatly impeded. In order to provide an analytical tool, which has the potential to handle these challenges, the last part of this thesis deals with the development of a novel technique for quantitative XPS analysis of technical catalysts. It is demonstrated, that an internal standard, which has substantial benefits, can be introduced to a powder sample by shaking, grinding or

dispersing the powders in a liquid. If the analyte and standard compound are cohesive powders of a maximum particle size of 10 µm, a sufficiently high mixture quality is obtained by manual grinding or dispersing powders in ethanol. If some additional effort is put into the synthesis of a tailor-made internal standard, powder mixing is greatly facilitated since the achievable mixing quality turns out to be independent of particle size and mixing technique. However, care must be taken with applying high shear forces, as this may lead to the re-dispersion of the chemical species used as intensity normal in XPS analysis. The obtained results open the door for using internal intensity standards for quantitative XPS analysis of technical catalysts on a routine basis.

## 9.2 Outlook

Over the course of this thesis, new research questions have emerged and new possibilities have opened up. Thermography provides unique insights into the temperature profile of fixed-beds under working conditions. This information may be used to validate existing computer models describing heat and mass transport phenomena. Also, additional potential remains for studying catalyst deactivation. With regards to (sulfur) poisoning, an adsorber bed might be added to the front end of the reactor. Thus, the observed poisoning effects should be delayed by the lifetime of the adsorber.

Furthermore, the propagation of sulfur gradients along the reactor axis has been thoroughly described. In an industrial reactor, however, particle (i.e. pellet) sizes are larger than employed here. Hence, mass transport limitations in radial position need to be considered. Further experimental and theoretical work on sulfur poisoning of pellets and packed beds would capture these effects and lead to valuable correlations for the industrial operation of catalytic fixed-beds. Also, the regeneration of poisoned catalysts is important for industrial operation. One possible technique is the addition of water vapor at high temperatures [340]. The chances and limitations of this technique might be elucidated and compared to other options such as purging with $H_2$ or treating the catalyst with $O_2$. In general, the applied setup would become more powerful if a sophisticated sulfur analyzer would be attached. Thus, the sulfur balance could be closed and sulfur breakthrough curves could be recorded.

Apart from sulfur poisoning of pure Ni-Al catalysts, the work on promoted Ni-Al systems has revealed a way to increase the sulfur resistance of Ni-Al catalysts. However, elucidating the observed effects is a great analytical challenge. In order to understand the prevailing effect of promoters in more detail, it is suggested to apply sophisticated characterization techniques such as XPS, EXAFS, Mössbauer spectroscopy and others. Furthermore, molydbenum-promoted Ni catalysts have been reported to show great resistance against sulfur poisoning and were even

found to exhibit some residual activity for CO hydrogenation in the sulfided state [149]. Similar effects might be expected from tungsten-promoted systems [220]. As it was shown in chapter 8 of this thesis, $MoO_3$ is easily spread over common support materials such as $TiO_2$ or $Al_2O_3$. It might thus be worth investigating the sulfur resistance of Ni-Al catalysts containing small amounts of Mo or W.

The presented work on quantitative XPS analysis of technical catalysts bridges the gap between surface science and technical chemistry and offers a sophisticated tool to understand surface phenomena such as catalyst activation, deactivation, poisoning or promotion on a deeper level. Some research questions, which are still not fully understood and might be addressed by quantitative XPS analysis are:

- What is the reason for the great stability of Ni-Al catalysts against thermal degradation?
- What is the role of $NiAl_2O_4$ surface species?
- What is the oxidation state of Mn and Fe during activation and does this change under reaction conditions?
- How are Fe and Mn contacted to the active and/or the support phase?
- Which surface species are affected by sulfur poisoning and does this match with chemisorption results?

# A Bibliography


[1] International Energy Agency, *World Energy Outlook 2018*, OECD Publishing, **2017**.

[2] U. N. Framework Convention on Climate Change, Conference of the Parties, *Third Session: 1997a, Kyoto Protocol to the United Nations Framework Convention on Climate Change: Agenda Item 5*, FCCC/CP/1997/L.7/Add.1.

[3] S. Koopmann, S. Nicolai, A. Schnettler in *IEEE PES Innovative Smart Grid Technologies, Europe*, IEEE, **2014**, pp. 1–6.

[4] J. Nitsch, T. Pregger, T. Naegler, D. Heide, D. L. de Tena, F. Trieb, Y. Scholz, K. Nienhaus, N. Gerhardt, M. Sterner, T. Trost, A. von Oehsen, R. Schwinn, C. Pape, H. Hahn, M. Wickert, B. Wenzel, *Langfristszenarien und Strategien für den Ausbau der erneuerbaren Energien in Deutschland bei Berücksichtigung der Entwicklung in Europa und global*, Schlussbericht BMU - FKZ 03MAP146, Bundesministerium für Umwelt, Naturschutz und Reaktorsicherheit, Berlin, **2012**.

[5] W. Leonhard, F. Crotogino, C. Gatzen, W. Glaunsinger, S. Donadei, M. Kleimaier, M. Koenemund, H. Landinger, T. Lebioda, D. Sauer, H. Weber, A. Wenzel, W. Wolf, W. Woyke, S. Zunft, *VDE-Studie: Energiespeicher in Stromversorgungssystemen mit hohem Anteil erneuerbarer Energieträger. Bedeutung, Stand der Technik, Handlungsbedarf. ETG Task Force Energiespeicher*, Verband der Elektrotechnik Elektronik Informationstechnik e.V., Frankfurt, **2009**.

[6] S. Peter, *Modellierung einer vollständig auf erneuerbaren Energien basierenden Stromerzeugung im Jahr 2050 in autarken, dezentralen Strukturen*, UBA - FB001831, Umweltbundesamt, Dessau-Roßlau, **2013**.

[7] B. Dunn, H. Kamath, J.-M. Tarascon, *Science* **2011**, *334*, 928–935.

[8] M. Sterner, I. Stadler, *Energiespeicher – Bedarf, Technologien, Integration*, Springer, Heidelberg, **2014**.

[9] P.-J. Schweizer, O. Renn, W. Köck, J. Bovet, C. Benighaus, O. Scheel, R. Schröter, *Util. Policy* **2016**, *43*, 206–209.

[10] M. Sterner, *Bioenergy and renewable power methane in integrated 100% renewable energy systems: Limiting global warming by transforming energy systems*, Dissertation, Universität Kassel, **2009**.

[11] H. Giouse, *Triennum work report 2009-2012 – Working Committee 2: Underground Gas Storage*, International Gas Union, Kuala Lumpur, **2012**.

[12] International Energy Agency, *World Energy Outlook 2018*, OECD Publishing, **2018**.

[13] S. Ewald, F. Koschany, D. Schlereth, M. Wolf, O. Hinrichsen, *Chem. unserer Zeit* **2015**, *49*, 270–278.

[14] S. Schiebahn, T. Grube, M. Robinius, L. Zhao, A. Otto, B. Kumar, M. Weber, D. Stolten in *Transition to Renewable Energy Systems*, Wiley-VCH, Weinheim, **2013**, pp. 813–848.

[15] M. Bailera, P. Lisbona, L. M. Romeo, S. Espatolero, *Renew. Sust. Energ. Rev.* **2017**, *69*, 292–312.

[16] J. Giesecke, E. Mosonyi, *Wasserkraftanlagen*, Springer, Heidelberg, **2009**.

[17] J. Mergel, M. Carmo, D. Fritz in *Transition to Renewable Energy Systems*, Wiley-VCH, Weinheim, **2013**, pp. 423–450.

[18] M. Specht, J. Brellochs, V. Frick, B. Stuermer, U. Zuberbuehler, M. Sterner, G. Waldstein, *Erdöl Erdgas Kohle* **2010**, *126*, 342–345.

[19] D. Schlereth, O. Hinrichsen, *Chem. Eng. Res. Des.* **2014**, *92*, 702–712.

[20] D. Schlereth, O. Hinrichsen, *Ind. Eng. Chem. Res.* **2014**, *53*, 11550–11556.

[21] D. Schlereth, P. J. Donaubauer, O. Hinrichsen, *Chem. Eng. Technol.* **2015**, *38*, 1845–1852.

[22] D. Schlereth, *Kinetic and Reactor Modeling for the Methanation of Carbon Dioxide*, Dissertation, Technische Universität München, **2015**.

[23] F. Koschany, D. Schlereth, O. Hinrichsen, *Appl. Catal. B* **2016**, *181*, 504–516.

[24] F. Koschany, *Experimentelle Studien zur Methanisierung von $CO_2$ auf Nickelkatalysatoren*, Dissertation, Technische Universität München, **2016**.

[25] T. Burger, F. Koschany, O. Thomys, K. Köhler, O. Hinrichsen, *Appl. Catal. A* **2018**, *558*, 44–54.

[26] T. Burger, F. Koschany, A. Wenng, O. Thomys, K. Köhler, O. Hinrichsen, *Catal. Sci. Technol.* **2018**, *8*, 5920–5932.

[27] K. Köhler, O. Thomys, O. Hinrichsen, F. Koschany, T. Burger, Nickel methanation catalysts doped with iron and manganese, WO 2018/141646 A1, **09.08.2018**.

[28] K. Köhler, O. Thomys, O. Hinrichsen, F. Koschany, T. Burger, Iron-doped nickel-methanation catalysts, WO 2018/141648 A1, **09.08.2018**.

[29] K. Köhler, O. Thomys, O. Hinrichsen, F. Koschany, T. Burger, Manganese-doped nickel-methanation catalysts, WO 2018/141649 A1, **09.08.2018**.

[30] S. Ewald, M. Kolbeck, T. Kratky, M. Wolf, O. Hinrichsen, *Appl. Catal. A* **2019**, *570*, 376–386.

[31] S. Ewald, *Investigation of the deactivation behavior of Ni-Al catalysts for $CO_2$ methanation*, Dissertation, Technische Universität München, **2019**.

[32] T. Y. Yeo, J. Ashok, S. Kawi, *Renew. Sust. Energ. Rev.* **2019**, *100*, 52–70.

[33] C. Schüler, M. Wolf, O. Hinrichsen, *J. $CO_2$ Util.* **2018**, *25*, 158–169.

[34] M. Wolf, C. Schüler, O. Hinrichsen, *J. $CO_2$ Util.* **2019**, *32*, 80–91.

[35] M. Wolf, L. H. Wong, C. Schüler, O. Hinrichsen, *J. $CO_2$ Util.* **2020**, *36*, 276–287.

[36] P. Sabatier, J. B. Senderens, *C. R. Acad. Sci.* **1902**, *134*, 689–691.

[37] S. Abelló, C. Berrueco, D. Montané, *Fuel* **2013**, *113*, 598–609.

[38] J. Gao, Y. Wang, Y. Ping, D. Hu, G. Xu, F. Gu, F. Su, *RSC Adv.* **2012**, *2*, 2358.

[39] Gas infrastructure - Quality of gas - Groupe H; German version EN 16726:2015, Standard, Deutsches Institut für Normung e.V., Berlin, **2016**.

[40] Natural gas - Correlation between water content and water dew point (ISO 18453:2004); German version EN ISO 18453:2005, Standard, Deutsches Institut für Normung e.V., Berlin, **2006**.

[41] K. Altfeld, D. Pinchbeck, *Gas for Energy* **2013**, *2013*, 1–12.

[42] P. Frontera, A. Macario, M. Ferraro, P. L. Antonucci, *Catalysts* **2017**, *7*, 59.

[43] S. Rönsch, J. Schneider, S. Matthischke, M. Schlüter, M. Götz, J. Lefebvre, P. Prabhakaran, S. Bajohr, *Fuel* **2016**, *166*, 276–296.

[44] M. A. A. Aziz, A. A. Jalil, S. Triwahyono, A. Ahmad, *Green Chem.* **2015**, *17*, 2647–2663.

[45] J. Gao, Q. Liu, F. Gu, B. Liu, Z. Zhong, F. Su, *RSC Adv.* **2015**, *5*, 22759–22776.

[46] W. Wang, S. Wang, X. Ma, J. Gong, *Chem. Soc. Rev.* **2011**, *40*, 3703–3727.

[47] W. Wei, G. Jinlong, *Front. Chem. Sci. Eng.* **2011**, *5*, 2–10.

[48] M. Schoder, U. Armbruster, A. Martin, *Chem. Ing. Tech.* **2013**, *85*, 344–352.

[49] K. Yaccato, R. Carhart, A. Hagemeyer, A. Lesik, P. Strasser, A. F. Volpe, H. Turner, H. Weinberg, R. K. Grasselli, C. Brooks, *Appl. Catal. A* **2005**, *296*, 30–48.

[50] J. Kopyscinski, T. J. Schildhauer, S. M. A. Biollaz, *Fuel* **2010**, *89*, 1763–1783.

[51] T. Riedel, M. Claeys, H. Schulz, G. Schaub, S.-S. Nam, K.-W. Jun, M.-J. Choi, G. Kishan, K.-W. Lee, *Appl. Catal. A* **1999**, *186*, 201–213.

[52] E. Vesselli, J. Schweicher, A. Bundhoo, A. Frennet, N. Kruse, *J. Phys. Chem. C* **2010**, *115*, 1255–1260.

[53] G. Weatherbee, C. H. Bartholomew, *J. Catal.* **1981**, *68*, 67–76.

[54] K. B. Kester, E. Zagli, J. L. Falconer, *Appl. Catal.* **1986**, *22*, 311–319.

[55] J. Liu, C. Li, F. Wang, S. He, H. Chen, Y. Zhao, M. Wei, D. G. Evans, X. Duan, *Catal. Sci. Technol.* **2013**, *3*, 2627–2633.

[56] D. C. D. da Silva, S. Letichevsky, L. E. P. Borges, L. G. Appel, *Int. J. Hydrogen Energy* **2012**, *37*, 8923–8928.

[57] S. Tada, T. Shimizu, H. Kameyama, T. Haneda, R. Kikuchi, *Int. J. Hydrogen Energy* **2012**, *37*, 5527–5531.

[58] N. Takezawa, H. Terunuma, M. Shimokawabe, H. Kobayashib, *Appl. Catal.* **1986**, *23*, 291–298.

[59] G. Du, S. Lim, Y. Yang, C. Wang, L. Pfefferle, G. L. Haller, *J. Catal.* **2007**, *249*, 370–379.

[60] W. Zhen, B. Li, G. Lu, J. Ma, *Chem. Comm.* **2015**, *51*, 1728–1731.

[61] H. Muroyama, Y. Tsuda, T. Asakoshi, H. Masitah, T. Okanishi, T. Matsui, K. Eguchi, *J. Catal.* **2016**, *343*, 178–184.

[62] W. Wang, W. Chu, N. Wang, W. Yang, C. Jiang, *Int. J. Hydrogen Energy* **2016**, *41*, 967–975.

[63] F.-W. Chang, T.-J. Hsiao, S.-W. Chung, J.-J. Lo, *Appl. Catal. A* **1997**, *164*, 225–236.

[64] C. K. Vance, C. H. Bartholomew, *Appl. Catal.* **1983**, *7*, 169–177.

[65] D. Pandey, G. Deo, *J. Ind. Eng. Chem.* **2016**, *33*, 99–107.

[66] G. D. Lee, M. J. Moon, J. H. Park, S. S. Park, S. S. Hong, *Korean J. Chem. Eng.* **2005**, *22*, 541–546.

[67] Y. Li, Q. Zhang, R. Chai, G. Zhao, Y. Liu, Y. Lu, *ChemCatChem.* **2015**, *7*, 1427–1431.

[68] S. Abello, C. Berrueco, F. Gispert-Guirado, D. Montane, *Catal. Sci. Technol.* **2016**, *6*, 2305–2317.

[69] L. He, Q. Lin, Y. Liu, Y. Huang, *J. Energy Chem.* **2014**, *23*, 587–592.

[70] B. Mutz, M. Belimov, W. Wang, P. Sprenger, M.-A. Serrer, D. Wang, P. Pfeifer, W. Kleist, J.-D. Grunwaldt, *ACS Catal.* **2017**, *7*, 6802–6814.

[71] X. Wang, T. Zhen, C. Yu, *Appl. Petrochem. Res.* **2016**, *6*, 217–223.

[72] S. Hwang, U. G. Hong, J. Lee, J. G. Seo, J. H. Baik, D. J. Koh, H. Lim, I. K. Song, *J. Ind. Eng. Chem.* **2013**, *19*, 2016–2021.

[73] J. Sehested, K. E. Larsen, A. L. Kustov, A. M. Frey, T. Johannessen, T. Bligaard, M. P. Andersson, J. K. Nørskov, C. H. Christensen, *Top. Catal.* **2007**, *45*, 9–13.

[74] M. P. Andersson, T. Bligaard, A. Kustov, K. E. Larsen, J. Greeley, T. Johannessen, C. H. Christensen, J. K. Nørskov, *J. Catal.* **2006**, *239*, 501–506.

[75] K. Zhao, Z. Li, L. Bian, *Front. Chem. Sci. Eng.* **2016**, *10*, 273–280.

[76] A. Zhao, W. Ying, H. Zhang, M. Hongfang, D. Fang, *J. Nat. Gas Chem.* **2012**, *21*, 170–177.

[77] Y. Yu, G. Jin, Y. Wang, X. Y. Guo, *Catal. Comm.* **2013**, *31*, 5–10.

[78] S. Rahmani, M. Rezaei, F. Meshkani, *J. Ind. Eng. Chem.* **2014**, *20*, 4176–4182.

[79] A. Zhao, W. Ying, H. Zhang, H. Ma, D. Fang, *Energ. Source. Part A* **2014**, *36*, 1049–1056.

[80] Y.-X. Pan, C.-J. Liu, Q. Ge, *J. Catal.* **2010**, *272*, 227–234.

[81] Q. Pan, J. Peng, T. Sun, S. Wang, S. Wang, *Catal. Commun.* **2014**, *45*, 74–78.

[82] G. Weatherbee, C. H. Bartholomew, *J. Catal.* **1982**, *77*, 460–472.

[83] M. Araki, V. Ponec, *J. Catal.* **1976**, *44*, 439–448.

[84] M. P. Andersson, F. Abild-Pedersen, I. N. Remediakis, T. Bligaard, G. Jones, J. Engbæk, O. Lytken, S. Horch, J. H. Nielsen, J. Sehested, J. R. Rostrup-Nielsen, J. K. Nørskov, I. Chorkendorff, *J. Catal.* **2008**, *255*, 6–19.

[85] M. A. Vannice, *J. Catal.* **1975**, *37*, 462–473.

[86] D. E. Peebles, D. W. Goodman, J. M. White, *J. Phys. Chem.* **1983**, *87*, 4378–4387.

[87] J. L. Falconer, A. E. Zağli, *J. Catal.* **1980**, *62*, 280–285.

[88] S. Fujita, H. Terunuma, M. Nakamura, N. Takezawa, *Ind. Eng. Chem. Res.* **1991**, *30*, 1146–1151.

[89] H. Nakano, S. Kawakami, T. Fujitani, J. Nakamura, *Surf. Sci.* **2000**, *454*, 295–299.

[90] H. P. Steinrück, M. P. D'evelyn, R. J. Madix, *Surf. Sci. Lett.* **1986**, *172*, L561–L567.

[91] H. S. Bengaard, J. K. Nørskov, J. Sehested, B. S. Clausen, L. P. Nielsen, A. M. Molenbroek, J. R. Rostrup-Nielsen, *J. Catal.* **2002**, *209*, 365–384.

[92] V. Sanchez-Escribano, M. L. Vargas, E. Finocchio, G. Busca, *Appl. Catal. A* **2007**, *316*, 68–74.

[93] J. W. E. Coenen, P. F. M. T. Van Nisselrooy, M. H. J. M. De Croon, P. F. H. A. Van Dooren, R. Z. C. Van Meerten, *Appl. Catal.* **1986**, *25*, 1–8.

[94] E. Vesselli, M. Rizzi, L. De Rogatis, X. Ding, A. Baraldi, G. Comelli, L. Savio, L. Vattuone, M. Rocca, P. Fornasiero, A. Baldereschi, M. Peressi, *J. Phys. Chem. Lett.* **2009**, *1*, 402–406.

[95] C. Schild, A. Wokaun, A. Baiker, *J. Mol. Catal.* **1991**, *69*, 347–357.

[96] C. Vogt, E. Groeneveld, G. Kamsma, M. Nachtegaal, L. Lu, C. J. Kiely, P. H. Berben, F. Meirer, B. M. Weckhuysen, *Nat. Catal.* **2018**, *1*, 127.

[97] J. Sehested, *J. Catal.* **2003**, *217*, 417–426.

[98] T. W. Hansen, J. B. Wagner, P. L. Hansen, S. Dahl, H. Topsøe, C. J. H. Jacobsen, *Science* **2001**, *294*, 1508–1510.

[99] J. A. Moulijn, A. E. van Diepen, F. Kapteijn, *Appl. Catal. A* **2001**, *212*, 3–16.

[100] M. S. Spencer, *Nature* **1986**, *323*, 685.

[101] J. Zieliński, *J. Mol. Catal.* **1993**, *83*, 197–206.

[102] J. Zielinski, *Appl. Catal. A* **1993**, *94*, 107–115.

[103] R. Lamber, G. Schulz-Ekloff, *Surf. Sci.* **1991**, *258*, 107–118.

[104] J. Sehested, J. A. P. Gelten, I. N. Remediakis, H. Bengaard, J. K. Nørskov, *J. Catal.* **2004**, *223*, 432–443.

[105] W. M. Shen, J. A. Dumesic, C. G. Hill, *J. Catal.* **1981**, *68*, 152–165.

[106] C. H. Bartholomew, *Catal. Rev. Sci. Eng.* **1982**, *24*, 67–112.

[107] B. Mutz, P. Sprenger, W. Wang, D. Wang, W. Kleist, J.-D. Grunwaldt, *Appl. Catal. A* **2018**, *556*, 160–171.

[108] J. R. Rostrup-Nielsen, D. L. Trimm, *J. Catal.* **1977**, *48*, 155–165.

[109] D. L. Trimm, *Catal. Rev. Sci. Eng.* **1977**, *16*, 155–189.

[110] C. H. Bartholomew, P. K. Agrawal, J. R. Katzer, *Adv. Catal.* **1982**, *31*, 135–242.

[111] T. Rosenquist, *J. Iron Steel Inst.* **1954**, *176*, 37.

[112] J. L. Oliphant, R. W. Fowler, R. B. Pannel, *J. Catal.* **1978**, *51*, 229–242.

[113] J. R. Rostrup-Nielsen, *J. Catal.* **1968**, *11*, 220–227.

[114] J. G. McCarty, H. Wise, *J. Chem. Phys.* **1980**, *72*, 6332–6337.

[115] C. H. Bartholomew, R. B. Pannel, *J. Catal.* **1980**, *65*, 390–401.

[116] M. Perdereau, J. Oudar, *Surf. Sci.* **1970**, *20*, 80–98.

[117] I. B. Alstrup, J. R. Rostrup-Nielsen, S. Røen, *Appl. Catal.* **1981**, *1*, 303–314.

[118] M. Argyle, C. H. Bartholomew, *Catalysts* **2015**, *5*, 145–269.

[119] J. E. Demuth, D. W. Jepsen, P. M. Marcus, *Phys. Rev. Lett.* **1974**, *32*, 1182.

[120] J. Oudar, *Catal. Rev. Sci. Eng.* **1980**, *22*, 171–195.

[121] A. Grossmann, W. Erley, H. Ibach, *Surf. Sci.* **1995**, *337*, 183–189.

[122] L. Ruan, I. Stensgaard, F. Besenbacher, E. Lægsgaard, *Phys. Rev. Lett.* **1993**, *71*, 2963.

[123] C. H. Bartholomew, *Appl. Catal. A* **2001**, *212*, 17–60.

[124] T. Edmonds, J. J. McCarroll, R. C. Pitkethly, *J. Vac. Sci. Technol.* **1971**, *8*, 68–74.

[125] J. J. McCarroll, T. Edmonds, R. C. Pitkethly, *Nature* **1969**, *223*, 1260.

[126] L. Ruan, F. Besenbacher, I. Stensgaard, E. Lægsgaard, *Phys. Rev. Lett.* **1992**, *69*, 3523.

[127] E. J. Erekson, C. H. Bartholomew, *Appl. Catal.* **1983**, *5*, 323–336.

[128] K. D. Rendulic, A. Winkler, *Surf. Sci.* **1978**, *74*, 318–320.

[129] W. Erley, H. Wagner, *J. Catal.* **1978**, *53*, 287–294.

[130] W. D. Goodman, M. Kiskinova, *Surf. Sci.* **1981**, *105*, L265–L270.

[131] M. Kiskinova, D. W. Goodman, *Surf. Sci.* **1981**, *108*, 64–76.

[132] S. Johnson, R. J. Madix, *Surf. Sci.* **1981**, *108*, 77–98.

[133] R. J. Madiz, M. Thornburg, S.-B. Lee, *Surf. Sci. Lett.* **1983**, *133*, L447–L451.

[134] E. L. Hardegree, P. Ho, J. M. White, *Surf. Sci.* **1986**, *165*, 488–506.

[135] P. Ho, E. L. Hardegree, J. M. White, *Surf. Sci.* **1986**, *165*, 507–519.

[136] C. H. Rochester, R. J. Terrell, *J. Chem. Soc. Faraday Trans. 1* **1977**, *73*, 609–621.

[137] R. W. Fowler, C. H. Bartholomew, *Ind. Eng. Chem. Prod. Res. Dev.* **1979**, *18*, 339–347.

[138] C. H. Bartholomew, R. B. Pannell, *Appl. Catal.* **1982**, *2*, 39–49.

[139] R. A. Dalla Betta, A. G. Piken, M. Shelef, *J. Catal.* **1975**, *40*, 173–183.

[140] C. H. Bartholomew, G. D. Weatherbee, G. A. Jarvi, *J. Catal.* **1979**, *60*, 257–269.

[141] J. R. Rostrup-Nielsen, K. Pedersen, *J. Catal.* **1979**, *59*, 395–404.

[142] P. W. Wentrcek, J. G. McCarty, C. M. Ablow, H. Wise, *J. Catal.* **1980**, *61*, 232–241.

[143] W. D. Fitzharris, J. R. Katzer, W. H. Manogue, *J. Catal.* **1982**, *76*, 369–384.

[144] J. R. Rostrup-Nielsen, *J. Catal.* **1984**, *85*, 31–43.

[145] E. B. Maxted, *Adv. Catal.* **1951**, *3*, 129–178.

[146] E. F. G. Herington, E. K. Rideal, *Trans. Faraday Soc.* **1944**, *40*, 505–516.

[147] J. R. Rostrup-Nielsen, *Stud. Surf. Sci. Catal.* **1991**, *68*, 85–101.

[148] N. Andersen, F. Topsøe, I. Alstrup, J. R. Rostrup-Nielsen, *J. Catal.* **1987**, *104*, 454–465.

[149] P. Y. Hou, H. Wise, *J. Catal.* **1985**, *93*, 409–416.

[150] C. Hulteberg, *Int. J. Hydrogen Energ.* **2012**, *37*, 3978–3992.

[151] G. Hochgesand, *Ind. Eng. Chem.* **1970**, *62*, 37–43.

[152] K. J. Andersson, M. S. Rasmussen, P. E. H. Nielsen, *Fuel* **2017**, *203*, 1026–1030.

[153] K. Müller, M. Fleige, F. Rachow, D. Schmeißer, *Energy Procedia* **2013**, *40*, 240–248.

[154] W. A. W. A. Bakar, R. Ali, N. S. Mohammad, *Arab. J. Chem.* **2015**, *8*, 632–643.

[155] M. Neubert, P. Treiber, C. Krier, M. Hackel, T. Hellriegel, M. Dillig, J. Karl, *Fuel* **2017**, *207*, 253–261.

[156] J. Guilera, J. del Valle, A. Alarcón, J. A. Díaz, T. Andreu, *J. $CO_2$ Util.* **2019**, *30*, 11–17.

[157] F. Schüth, M. D. Ward, J. M. Buriak, *Chem. Mater.* **2018**, *30*, 3599–3600.

[158] J. W. Olesik, *Anal. Chem.* **1991**, *63*, 12A–21A.

[159] W. Friedrich, P. Knipping, M. Laue, *Ann. Phys.* **1913**, *346*, 971–988.

[160] W. H. Bragg, W. L. Bragg, *Proc. R. Soc. London A* **1913**, *88*, 428–438.

[161] W. L. Bragg, *Proc. R. Soc. London A* **1913**, *89*, 248–277.

[162] L. Spieß, G. Teichert, R. Schwarzer, H. Behnken, C. Genzel, *Moderne Röntgenbeugung*, Vieweg+Teubner, Wiesbaden, **2009**.

[163] P. Debye, P. Scherrer, *Phys. Z.* **1916**, *17*, 277.

[164] P. Scherrer, *Göttinger Nachrichten Math. Phys.* **1918**, *2*, 98–100.

[165] U. Holzwarth, N. Gibson, *Nat. Nanotechnol.* **2011**, *6*, 534.

[166] H. P. Klug, L. E. Alexander, *X-Ray Diffraction Procedures: For Polycrystalline and Amorphous Materials*, Wiley-VCH, Weinheim, **1974**.

[167] A. K. Singh, *Advanced X-ray Techniques in Research and Industry*, IOS Press, Amsterdam, **2005**.

[168] K. S. W. Sing, D. H. Everett, R. A. W. Haul, L. Moscou, R. A. Pierotti, J. Rouquérol, T. Siemieniewska, *Pure Appl. Chem.* **1985**, *57*, 603–619.

[169] S. Brunauer, P. H. Emmett, E. Teller, *J. Am. Chem. Soc.* **1938**, *60*, 309–319.

[170] Determination of the specific surface area of solids by gas adsorption - BET method (ISO 9277:2010), Standard, International Organization for Standardization, Geneva, **2014**.

[171] R. B. Pannell, K. S. Chung, C. H. Bartholomew, *J. Catal.* **1977**, *46*, 340–347.

[172] Determination of the dispersion degree of metals using gas chemisorption - Part 1: Principles, Standard, Deutsches Institut für Normung e.V., Berlin, **2017**.

[173] F. Solymosi, *J. Mol. Catal.* **1991**, *65*, 337–358.

[174] H.-J. Freund, M. W. Roberts, *Surf. Sci. Rep.* **1996**, *25*, 225–273.

[175] G. Martin, M. Primet, J. A. Dalmon, *J. Catal.* **1978**, *53*, 321–330.

[176] B. Bartos, H.-J. Freund, H. Kuhlenbeck, M. Neumann, H. Lindner, K. Müller, *Surf. Sci.* **1987**, *179*, 59–89.

[177] J. H. Taylor, C. H. Amberg, *Can. J. Chem.* **1961**, *39*, 535–539.

[178] L. H. Little, C. H. Amberg, *Can. J. Chem.* **1962**, *40*, 1997–2006.

[179] L. H. Little, *Infrared spectra of adsorbed species*, Academic Press, Michigan, **1966**.

[180] M. León, E. Díaz, S. Bennici, A. Vega, S. Ordónez, A. Auroux, *Ind. Eng. Chem. Res.* **2010**, *49*, 3663–3671.

[181] A. W. Coats, J. P. Redfern, *Analyst* **1963**, *88*, 906–924.

[182] D. A. M. Monti, A. Baiker, *J. Catal.* **1983**, *83*, 323–335.

[183] P. Malet, A. Caballero, *J. Chem. Soc. Faraday Trans. 1* **1988**, *84*, 2369.

[184] J. F. Watts, J. Wolstenholme, *An Introduction to Surface Analysis by XPS and AES*, John Wiley & Sons, Chichester, England, **2003**.

[185] T. Gros, *Entwicklung einer Methode zum homogenen Beimischen eines internen Standards zu pulverförmigen Katalysatorproben für die quantitative XPS-Analyse*, Forschungspraktikum, Technische Universität München, **2017**.

[186] G. Ertl, J. Küppers, *Low Energy Electrons and Surface Chemistry*, Verlag Chemie, Weinheim, **1974**.

[187] D. Briggs, M. P. Seah, *Practical Surface Analysis, Auger and X-ray Photoelectron Spectroscopy*, John Wiley & Sons, New Jersey, **1990**.

[188] J. F. Moulder, W. F. Stickle, P. E. Sobol, K. D. Bomben, *Handbook of X-Ray Photoelectron Spectroscopy*, Perkin-Elmer Corporation Physical Electronics Division, Eden Prairie, MN, **1992**.

[189] G. Johansson, J. Hedman, A. Berndtsson, M. Klasson, R. Nilsson, *J. Electron Spectrosc. Relat. Phenom.* **1973**, *2*, 295–317.

[190] M. P. Seah, W. A. Dench, *Surf. Interface Anal.* **1979**, *1*, 2–11.

[191] H. P. C. E. Kuipers, H. C. E. van Leuven, W. M. Visser, *Surf. Interface Anal.* **1986**, *8*, 235–242.

[192] M. P. Seah, S. J. Spencer, *J. Electron Spectrosc. Relat. Phenom.* **2006**, *151*, 178–181.

[193] J. H. Scofield, *J. Electron Spectrosc. Relat. Phenom.* **1976**, *8*, 129–137.

[194] J. J. Yeh, I. Lindau, *At. Data Nucl. Data Tables* **1985**, *32*, 1–155.

[195] R. F. Reilman, A. Msezane, S. T. Manson, *J. Electron Spectrosc. Relat. Phenom.* **1976**, *8*, 389–394.

[196] S. Tanuma, C. J. Powell, D. R. Penn, *Surf. Interface Anal.* **2003**, *35*, 268–275.

[197] C. D. Wagner, *Anal. Chem.* **1977**, *49*, 1282–1290.

[198] C. D. Wagner, *J. Electron Spectrosc. Relat. Phenom.* **1983**, *32*, 99–102.

[199] G. Mie, *Ann. Phys.* **1908**, *330*, 377–445.

[200] Particle size analysis - Laser diffraction methods (ISO 13320:2009-10), Standard, International Organization for Standardization, Geneva, **2009**.

[201] S. E. Bott, W. E. Hart, Particle size analysis utilizing Polarization Intensity Differential Scattering, US005104221A, **14.04.1992**.

[202] I. Zimmermann, *Chem. Ing. Tech.* **1996**, *68*, 422–425.

[203] B. Mutz, H. W. P. Carvalho, S. Mangold, W. Kleist, J.-D. Grunwaldt, *J. Catal.* **2015**, *327*, 48–53.

[204] A. P. Grosvenor, M. C. Biesinger, R. S. C. Smart, N. S. McIntyre, *Surf. Sci.* **2006**, *600*, 1771–1779.

[205] A. N. Mansour, *Surf. Sci. Spectra* **1994**, *3*, 231–238.

[206] S. J. Mills, P. S. Whitfield, A. R. Kampf, S. A. Wilson, G. M. Dipple, M. Raudsepp, G. Favreau, *J. Geosci.-Czech.* **2012**, 273–279.

[207] D. C. Puxley, I. J. Kitchener, C. Komodromos, N. D. Parkyns, *Stud. Surf. Sci. Catal.* **1983**, *16*, 237–271.

[208] R. D. Shannon, *Acta Crystallogr. A* **1976**, *32*, 751–767.

[209] R. B. Shalvoy, B. H. Davis, P. J. Reucroft, *Surf. Interface Anal.* **1980**, *2*, 11–16.

[210] Bundesministerium für Wirtschaft und Energie, *Die Energiewende: unsere Erfolgsgeschichte*, Bundesministerium für Wirtschaft und Energie, Berlin, **2017**.

[211] European Commission, *A Roadmap for Moving to a Competetive Low Carbon Economy in 2050*, European Commission, Brussels, **2011**.

[212] Climeworks Press Release, World-First Climeworks Plant: Capturing $CO_2$ from Air to Boost Growing Vegetables, **2017**.

[213] M. Marwood, F. Van Vyve, R. Doepper, A. Renken, *Catal. Today* **1994**, *20*, 437–448.

[214] J. M. Rynkowski, T. Paryjczak, A. Lewicki, M. I. Szynkowska, T. P. Maniecki, W. K. Jóźwiak, *React. Kinet. Catal. Lett.* **2000**, *71*, 55–64.

[215] E. Zagli, J. L. Falconer, *J. Catal.* **1981**, *69*, 1–8.

[216] G. Weatherbee, C. H. Bartholomew, *J. Catal.* **1984**, *87*, 352–362.

[217] S. Scirè, C. Crisafulli, R. Maggiore, S. Minicò, S. Galvagno, *Catal. Lett.* **1998**, *51*, 41–45.

[218] D. Li, N. Ichikuni, S. Shimazu, T. Uematsu, *Appl. Catal. A* **1998**, *172*, 351–358.

[219] M. Kuśmierz, *Catal. Today* **2008**, *137*, 429–432.

[220] G. A. Mills, F. W. Steffgen, *Catal. Rev.* **1974**, *8*, 159–210.

[221] S. Toemen, W. A. W. A. Bakar, R. Ali, *J. $CO_2$ Util.* **2016**, *13*, 38–49.

[222] A. Beuls, C. Swalus, M. Jacquemin, G. Heyen, A. Karelovic, P. Ruiz, *Appl. Catal. B* **2012**, *113*, 2–10.

[223] M. Jacquemin, A. Beuls, P. Ruiz, *Catal. Today* **2010**, *157*, 462–466.

[224] H. Kusama, K. K. Bando, K. Okabe, H. Arakawa, *Appl. Catal. A* **2000**, *197*, 255–268.

[225] É. Novák, K. Fodor, T. Szailer, A. Oszkó, A. Erdöhelyi, *Top. Catal.* **2002**, *20*, 107–117.

[226] R. Wijayapala, F. Yu, C. U. Pittman, T. E. Mlsna, *Appl. Catal. A* **2014**, *480*, 93–99.

[227] P. Albers, J. Pietsch, S. F. Parker, *J. Mol. Catal. A* **2001**, *173*, 275–286.

[228] A. Borodziński, G. C. Bond, *Catal. Rev.* **2006**, *48*, 91–144.

[229] Y.-G. Chen, K. Tomishige, K. Yokoyama, K. Fujimoto, *Appl. Catal. A* **1997**, *165*, 335–347.

[230] J. Martins, N. Batail, S. Silva, S. Rafik-Clément, A. Karelovic, D. P. Debecker, A. Chaumonnot, D. Uzio, *Catal. Comm.* **2015**, *58*, 11–15.

[231] E. Kok, J. Scott, N. Cant, D. Trimm, *Catal. Today* **2011**, *164*, 297–301.

[232] M. A. A. Aziz, A. A. Jalil, S. Triwahyono, S. M. Sidik, *Appl. Catal. A* **2014**, *486*, 115–122.

[233] J. Fournier, L. Carreiro, Y. T. Qian, S. Soled, R. Kershaw, K. Dwight, A. Wold, *J. Solid State Chem.* **1985**, *58*, 211–220.

[234] J. Kirchner, J. K. Anolleck, H. Lösch, S. Kureti, *Appl. Catal. B* **2018**, *223*, 47–59.

[235] C. Fukuhara, K. Hayakawa, Y. Suzuki, W. Kawasaki, R. Watanabe, *Appl. Catal. A* **2017**, *532*, 12–18.

[236] F. Ocampo, B. Louis, A. Kiennemann, A. C. Roger, *IOP Conf. Ser.-Mater. Sci. Eng.* **2011**, *19*.

[237] S. Furukawa, M. Okada, Y. Suzuki, *Energy Fuels* **1999**, *13*, 1074–1081.

[238] G. M. Shashidhara, M. Ravindram, *React. Kinet. Catal. Lett.* **1988**, *37*, 451–456.

[239] F. Song, Q. Zhong, Y. Yu, M. Shi, Y. Wu, J. Hu, Y. Song, *Int. J. Hydrogen Energy* **2017**, *42*, 4174–4183.

[240] D. Wierzbicki, R. Baran, R. Dębek, M. Motak, T. Grzybek, M. E. Gálvez, P. Da Costa, *Int. J. Hydrogen Energy* **2017**, *42*, 23548–23555.

[241] A. I. Anastasov, *Chem. Eng. J.* **2002**, *86*, 287–297.

[242] G. Aparicio-Mauricio, R. S. Ruiz, F. López-Isunza, C. O. Castillo-Araiza, *Chem. Eng. J.* **2017**, *321*, 584–599.

[243] L. Kiewidt, J. Thöming, *Chem. Eng. Sci.* **2015**, *132*, 59–71.

[244] O. Korup, S. Mavlyankariev, M. Geske, C. F. Goldsmith, R. Horn, *Chem. Eng. Process.* **2011**, *50*, 998–1009.

[245] R. J. van Welsenaere, G. F. Froment, *Chem. Eng. Sci.* **1970**, *25*, 1503–1516.

[246] I. Gräf, A.-K. Rühl, B. Kraushaar-Czarnetzki, *Chem. Eng. J.* **2014**, *244*, 234–242.

[247] I. Gräf, G. Ladenburger, B. Kraushaar-Czarnetzki, *Chem. Eng. J.* **2016**, *287*, 425–435.

[248] R. Horn, K. A. Williams, N. J. Degenstein, L. D. Schmidt, *Chem. Eng. Sci.* **2007**, *62*, 1298–1307.

[249] R. Horn, O. Korup, M. Geske, U. Zavyalova, I. Oprea, R. Schlögl, *Rev. Sci. Instrum.* **2010**, *81*, 064102.

[250] O. Korup, C. F. Goldsmith, G. Weinberg, M. Geske, T. Kandemir, R. Schlögl, R. Horn, *J. Catal.* **2013**, *297*, 1–16.

[251] D. Türks, H. Mena, U. Armbruster, A. Martin, *Catalysts* **2017**, *7*, 152.

[252] L. Basini, *Catal. Today* **2006**, *117*, 384–393.

[253] M. Simeone, L. Salemme, L. Menna, *Int. J. Hydrogen Energy* **2012**, *37*, 9049–9057.

[254] M. Frey, T. Romero, A.-C. Roger, D. Edouard, *Catal. Today* **2016**, *273*, 83–90.

[255] A. Russell, C. Henry, N. W. Currier, A. Yezerets, W. S. Epling, *Appl. Catal. A* **2011**, *397*, 272–284.

[256] O. Shakir, A. Yezerets, N. W. Currier, W. S. Epling, *Appl. Catal. A* **2009**, *365*, 301–308.

[257] C. Schüler, O. Hinrichsen, *Chem. Ing. Tech.* **2016**, *88*, 1693–1702.

[258] M. Bosco, F. Vogel, *Catal. Today* **2006**, *116*, 348–353.

[259] J. Kopyscinski, T. J. Schildhauer, F. Vogel, S. M. A. Biollaz, A. Wokaun, *J. Catal.* **2010**, *271*, 262–279.

[260] R. A. Sheldon, *Catal. Today* **1987**, *1*, 351–355.

[261] T. Abe, M. Tanizawa, K. Watanabe, A. Taguchi, *Energ. Environ. Sci.* **2009**, *2*, 315.

[262] S. Eckle, H.-G. Anfang, R. J. Behm, *J. Phys. Chem. C* **2010**, *115*, 1361–1367.

[263] S. Sharma, Z. Hu, P. Zhang, E. W. McFarland, H. Metiu, *J. Catal.* **2011**, *278*, 297–309.

[264] J.-N. Park, E. W. McFarland, *J. Catal.* **2009**, *266*, 92–97.

[265] N. Perkas, G. Amirian, Z. Zhong, J. Teo, Y. Gofer, A. Gedanken, *Catal. Lett.* **2009**, *130*, 455–462.

[266] P. Forzatti, *Catal. Today* **1999**, *52*, 165–181.

[267] M. D. Kaufman Rechulski, T. J. Schildhauer, S. M. A. Biollaz, C. Ludwig, *Fuel* **2014**, *128*, 330–339.

[268] M. Gatti, E. Martelli, F. Marechal, S. Consonni, *Appl. Therm. Eng.* **2014**, *70*, 1123–1140.

[269] A. Aksoylu, A. Akin, Z. Onsan, D. Trimm, *Appl. Catal. A* **1996**, *145*, 185–193.

[270] R. Maatman, S. Hiemstra, *J. Catal.* **1980**, *62*, 349–356.

[271] T. van Herwijnen, H. van Doesburg, W. A. de Jong, *J. Catal.* **1973**, *28*, 391–402.

[272] S. Potter, M. Cabbage, L. McCarthy, *National Aeronautics and Space Administration (NASA)* **2017**.

[273] O. Edenhofer, R. Pichs-Madruga, Y. Sokona, E. Farahani, S. Kadner, K. Seyboth, A. Adler, I. Baum, S. Brunner, P. Eickemeier, B. Kriemann, J. Savolainen, S. Schlömer, C. von Stechow, T. Zwickel, J. C. Minx, *Climate Change 2014: Mitigation of Climate Change. Contribution of Working Group III to the Fifth Assessment Report of the Intergovernmental Panel on Climate Change*, IPCC, New York, **2014**.

[274] A. J. Hunt, E. H. K. Sin, R. Marriott, J. H. Clark, *ChemSusChem* **2010**, *3*, 306–322.

[275] M. Peters, B. Koehler, W. Kuckshinrichs, W. Leitner, P. Markewitz, T. E. Müller, *ChemSusChem* **2011**, *4*, 1216–1240.

[276] J. H. Kwak, L. Kovarik, J. Szanyi, *ACS Catal.* **2013**, *3*, 2449–2455.

[277] H. Y. Kim, H. M. Lee, J.-N. Park, *J. Phys. Chem. C* **2010**, *114*, 7128–7131.

[278] I. A. Fisher, A. T. Bell, *J. Catal.* **1996**, *162*, 54–65.

[279] W. Gac, W. Zawadzki, M. Rotko, G. Słowik, M. Greluk, *Top. Catal.* **2019**, 1–11.

[280] P. H. M. De Korte, E. B. M. Doesburg, C. P. J. De Winter, L. L. Van Reijen, *Solid State Ionics* **1985**, *16*, 73–80.

[281] L. E. Alzamora, J. R. H. Ross, E. C. Kruissink, L. L. Van Reijen, *J. Chem. Soc. Faraday Trans. 1* **1981**, *77*, 665–681.

[282] M. Gabrovska, R. Edreva-Kardjieva, D. Crişan, P. Tzvetkov, M. Shopska, I. Shtereva, *React. Kinet. Mech. Catal.* **2012**, *105*, 79–99.

[283] B. Dragoi, A. Ungureanu, A. Chirieac, C. Ciotonea, C. Rudolf, S. Royer, E. Dumitriu, *Appl. Catal. A* **2015**, *504*, 92–102.

[284] A. Carrero, J. A. Calles, A. J. Vizcaıno, *Appl. Catal. A* **2007**, *327*, 82–94.

[285] H. J. Jung, M. A. Vannice, L. N. Mulay, R. M. Stanfield, W. N. Delgass, *J. Catal.* **1982**, *76*, 208–224.

[286] Z. Yu, D. Chen, M. Rønning, T. Vrålstad, E. Ochoa-Fernández, A. Holmen, *Appl. Catal. A* **2008**, *338*, 136–146.

[287] S. Ewald, O. Hinrichsen, *Appl. Catal. A* **2019**, *580*, 71–80.

[288] C. A. Bernardo, I. Alstrup, J. R. Rostrup-Nielsen, *J. Catal.* **1985**, *96*, 517–534.

[289] T. A. Le, J. Kim, Y. R. Jeong, E. D. Park, *Catalysts* **2019**, *9*, 599.

[290] J. A. Rodriguez, J. Hrbek, *Acc. Chem. Res.* **1999**, *32*, 719–728.

[291] J. Bayer, K. C. Stein, L. J. E. Hofer, R. B. Anderson, *J. Catal.* **1964**, *3*, 145–155.

[292] D. Beierlein, D. Häussermann, M. Pfeifer, T. Schwarz, K. Stöwe, Y. Traa, E. Klemm, *Appl. Catal. B* **2019**, *247*, 200–219.

[293] C. J. Powell, *J. Vac. Sci. Technol. A* **2003**, *21*, S42–S53.

[294] F. Reniers, C. Tewell, *J. Electron Spectrosc. Relat. Phenom.* **2005**, *142*, 1–25.

[295] C. J. Powell, A. Jablonski, *Nucl. Instr. Methods Phys. Res. A* **2009**, *601*, 54–65.

[296] J. S. Brinen, *Acc. Chem. Res.* **1980**, *9*, 86–92.

[297] D. Briggs, *Appl. Surf. Sci.* **1980**, *6*, 188–203.

[298] D. R. Baer, J. E. Amonette, M. H. Engelhard, D. J. Gaspar, A. S. Karakoti, S. Kuchibhatla, P. Nachimuthu, J. T. Nurmi, Y. Qiang, V. Sarathy, S. Seal, A. Sharma, P. G. Tratnyek, C.-M. Wang, *Surf. Interface Anal.* **2008**, *40*, 529–537.

[299] A. T. Bell, *Science* **2003**, *299*, 1688–1691.

[300] F. Gao, D. W. Goodman, *Annu. Rev. Phys. Chem.* **2012**, *63*, 265–286.

[301] M. F. Ebel, H. Ebel, *J. Electron Spectrosc. Relat. Phenom.* **1974**, *3*, 169–180.

[302] A. Cros, *J. Electron Spectrosc. Relat. Phenom.* **1992**, *59*, 1–14.

[303] T. L. Barr, S. Seal, *J. Vac. Sci. Technol. A* **1995**, *13*, 1239–1246.

[304] B. R. Cuenya, S.-H. Baeck, T. F. Jaramillo, E. W. McFarland, *J. Am. Chem. Soc.* **2003**, *125*, 12928–12934.

[305] G. Hopfengärtner, D. Borgmann, I. Rademacher, G. Wedler, E. Hums, G. W. Spitznagel, *J. Electron Spectrosc. Relat. Phenom.* **1993**, *63*, 91–116.

[306] M. P. Seah, *J. Vac. Sci. Technol. A* **1997**, *15*, 485–492.

[307] M. P. Seah, M. E. Jones, M. T. Anthony, *Surf. Interface Anal.* **1984**, *6*, 242–254.

[308] C. D. Wagner, L. E. Davis, M. V. Zeller, J. A. Taylor, R. H. Raymond, L. H. Gale, *Surf. Interface Anal.* **1981**, *3*, 211–225.

[309] H. W. van der Marei, *Contr. Mineral. and Petrol.* **1966**, *12*, 96–138.

[310] J. P. Baltrus, L. E. Makovsky, J. M. Stencel, D. M. Hercules, *Anal. Chem.* **1985**, *57*, 2500–2503.

[311] T. Rundlöf, M. Mathiasson, S. Bekiroglu, B. Hakkarainen, T. Bowden, T. Arvidsson, *J. Pharm. Biomed. Anal.* **2010**, *52*, 645–651.

[312] P. Swift, D. Shuttleworth, M. P. Seah in *Practical Surface Analysis, Auger and X-ray Photoelectron Spectroscopy*, John Wiley & Sons, New Jersey, **1990**, pp. 437–443.

[313] W. Swartz, D. M. Hercules, *Anal. Chem.* **1971**, *43*, 1774–1779.

[314] G. D. Nichols, D. M. Hercules, R. C. Peek, D. J. Vaughan, *Appl. Spectrosc.* **1974**, *28*, 219–222.

[315] D. M. Wyatt, J. C. Carver, D. M. Hercules, *Anal. Chem.* **1975**, *47*, 1297–1301.

[316] E. Paparazzo, *Appl. Surf. Sci.* **1986**, *25*, 1–12.

[317] E. Paparazzo, *J. Electron Spectrosc. Relat. Phenom.* **1987**, *43*, 97–112.

[318] A. W. Nienow, N. Harnby, M. F. Edwards in *Mixing in the Process Industries*, Butterworth-Heinemann, Oxford, England, **1997**, pp. 1–23.

[319] K. Kendall, *Science* **1994**, *263*, 1720–1725.

[320] J. M. Ottino, D. V. Khakhar, *Annu. Rev. Fluid Mech.* **2000**, *32*, 55–91.

[321] J. W. Carson, T. A. Royal, G. D. J., *Bulk Solids Handl.* **1986**, *6*, 139–144.

[322] P. Tang, V. M. Puri, *Particul. Sci. Technol.* **2004**, *22*, 321–337.

[323] J. C. Williams in *Priniciples of Powder Technology*, John Wiley & Sons, Chichester, England, **1990**, pp. 71–91.

[324] P. M. C. Lacey, *J. Appl. Chem.* **1954**, *4*, 257–268.

[325] M. Cherian, M. S. Rao, W.-T. Yang, J.-M. Jehng, A. M. Hirt, G. Deo, *Appl. Catal. A* **2002**, *233*, 21–33.

[326] D. S. Zingg, L. E. Makovsky, R. E. Tischer, F. R. Brown, D. M. Hercules, *J. Phys. Chem.* **1980**, *84*, 2898–2906.

[327] M. R. Querry, *Optical Constants*, Contractor Report, US Army Chemical Research, Development and Engineering Center (CRDC), Aberdeen Proving Ground, MD, **1985**.

[328] J. R. DeVore, *J. Opt. Soc. Am.* **1951**, *41*, 416–419.

[329] M. Rubin, K. von Rottkay, S.-J. Wen, N. Özer, J. Slack, *Sol. Energ. Mat. Sol. Cells* **1998**, *54*, 49–57.

[330] J. Rheims, J. Köser, T. Wriedt, *Meas. Sci. Technol.* **1997**, *8*, 601.

[331] G. Gottschalk, *Fresenius Z. Anal. Chem.* **1962**, *187*, 164–182.

[332] W. Merz, W. Pfab, *Mikrochim. Acta* **1969**, *57*, 905–920.

[333] B. E. H. Saxberg, B. R. Kowalski, *Anal. Chem.* **1979**, *51*, 1031–1038.

[334] S. Günther, M. Marsi, A. Kolmakov, M. Kiskinova, M. Noeske, E. Taglauer, G. Mestl, U. A. Schubert, H. Knözinger, *J. Phys. Chem. B* **1997**, *101*, 10004–10011.

[335] L. Wang, W. K. Hall, *J. Catal.* **1982**, *77*, 232–241.

[336] R. Margraf, J. Leyrer, H. Knözinger, E. Taglauer, *Surf. Sci.* **1987**, *189*, 842–850.

[337] J. Leyrer, R. Margraf, E. Taglauer, H. Knözinger, *Surf. Sci.* **1988**, *201*, 603–623.

[338] G. Mestl, H. Knözinger, *Langmuir* **1998**, *14*, 3964–3966.

[339] A. Van Eenbergen, E. Bruninx, *J. Electron Spectrosc. Relat. Phenom.* **1984**, *33*, 51–60.

[340] J. R. Rostrup-Nielsen, *J. Catal.* **1971**, *21*, 171–178.

# Publication list

## Publications

- S. Ewald, F. Koschany, D. Schlereth, M. Wolf, O. Hinrichsen, *Katalyse und Reaktionstechnik: Power-to-Gas*, Chemie in unserer Zeit, **2015**, *49*, 270-278.

- C. Schüler, M. Wolf, O. Hinrichsen, *Contactless temperature measurements under static and dynamic reaction conditions in a single-pass fixed bed reactor for $CO_2$ methanation*, Journal of $CO_2$ Utilization, **2018**, *25*, 158-169.

- S. Ewald, M. Kolbeck, T. Kratky, M. Wolf, O. Hinrichsen, *On the deactivation of Ni-Al catalysts in $CO_2$ methanation*, Applied Catalysis A, **2019**, *570*, 376-386.

- M. Wolf, C. Schüler, O. Hinrichsen, *Sulfur poisoning of co-precipitated Ni-Al catalysts for the methanation of $CO_2$*, Journal of $CO_2$ Utilization, **2019**, *32*, 80-91.

- M. Wolf, L. H. Wong, C. Schüler, O. Hinrichsen, *$CO_2$ methanation on transition-metal-promoted Ni-Al catalysts: Sulfur poisoning and the role of $CO_2$ adsorption capacity for catalyst activity*, Journal of $CO_2$ Utilization, **2020**, *36*, 276-287.

- M. Wolf, T. Kratky, T. Gros, S. Günther, O. Hinrichsen, *Novel synthesis route towards internal intensity standards for quantitative analysis of technical catalysts by X-ray photoelectron spectroscopy*, in preparation.

## Selected conference contributions

### Oral presentations

- M. Wolf, O. Hinrichsen, *Comparing the sulfur resistance of $NiAlO_x$ catalysts for the methanation of $CO_2$*, 51. Jahrestreffen Deutscher Katalytiker (Weimar, Germany, **2018**)

### Poster presentations

- M. Wolf, E. Fritzler, O. Hinrichsen, *$CO_2$ methanation: deactivation due to sulfur poisoning*, European Symposium on Chemical Reaction Engineering (Fürstenfeldbruck, Germany, **2015**).

- M. Wolf, E. Fritzler, O. Hinrichsen, *$CO_2$ methanation: deactivation due to sulfur poisoning*, 49. Jahrestreffen Deutscher Katalytiker (Weimar, Germany, **2016**).

- M. Wolf, E. Fritzler, O. Hinrichsen, *Impact of sulfur poisoning on the kinetics of $CO_2$ methanation*, 16$^{th}$ International Congress on Catalysis (Beijing, China, **2016**).

- M. Wolf, L. Schönfeld, O. Hinrichsen, *Selective ex-situ poisoning of co-precipitated $NiAlO_x$ catalysts*, 50. Jahrestreffen Deutscher Katalytiker (Weimar, Germany, **2017**).

- M. Wolf, L. Schönfeld, O. Hinrichsen, *Selective ex-situ poisoning of co-precipitated $NiAlO_x$ catalysts*, 13$^{th}$ European Congress on Catalysis (Florence, Italy, **2017**).

- C. Schüler, M. Wolf, O. Hinrichsen, *Contactless temperature measurements under static and dynamic reaction conditions in a single-pass fixed bed reactor for $CO_2$ methanation*, 51. Jahrestreffen Deutscher Katalytiker (Weimar, Germany, **2018**).

- M. Wolf, C. Schüler, T. Burger, O. Hinrichsen, *Sulfur poisoning of co-precipitated Ni-Al catalysts for the methanation of $CO_2$*, 52. Jahrestreffen Deutscher Katalytiker (Weimar, Germany, **2019**).